SYNTHESIS AND STRUCTURE-PROPERTY RELATIONSHIPS IN SELECTED METAL FLUORIDES

Sandra Ann Reisinger

A Thesis Submitted for the Degree of PhD
at the
University of St Andrews

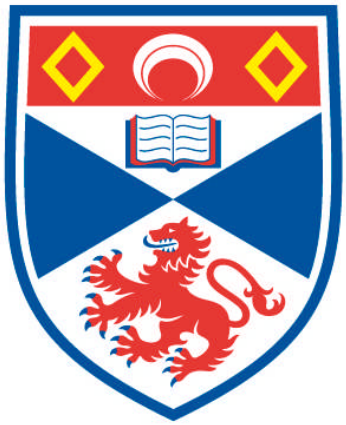

2011

Synthesis and Structure-Property Relationships in Selected Metal Fluorides

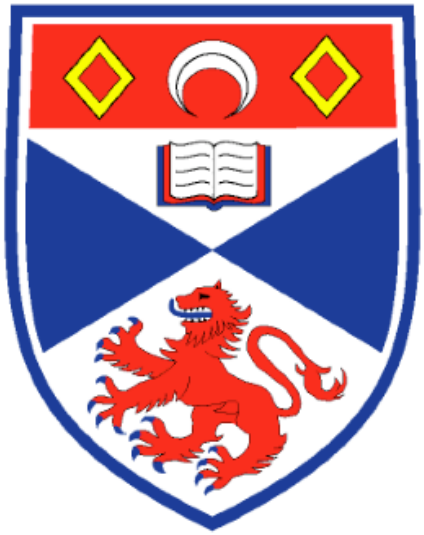

University
of
St Andrews

A thesis presented for the degree of

Doctor of Philosophy

in the Faculty of Science of the University of St Andrews

by Sandra Ann Reisinger, MSc, AMRSC

August 2011

Declaration

I, Sandra Reisinger, hereby certify that this thesis, which is approximately 35,000 words in length, has been written by me, that it is the record of work carried out by me and that it has not been submitted in any previous application for a higher degree.

I was admitted as a research student in October 2008 and as a candidate for the degree of PhD in October 2009; the higher study for which this is a record was carried out in the University of St Andrews between 2008 and 2011.

Date ……..… Signature of candidate ……..…

Supervisor's Declaration

I hereby certify that the candidate has fulfilled the conditions of the Resolution and Regulations appropriate for the degree of PhD in the University of St Andrews and that the candidate is qualified to submit this thesis in application for that degree.

Date ……..… Signature of supervisor ……..…

Signature of supervisor ……..…

In submitting this thesis to the University of St Andrews I understand that I am giving permission for it to be made available for use in accordance with the regulations of the University Library for the time being in force, subject to any copyright vested in the work not being affected thereby. I also understand that the title and the abstract will be published, and that a copy of the work may be made and supplied to any bona fide library or research worker, that my thesis will be electronically accessible for personal or research use unless exempt by award of an embargo as requested below, and that the library has the right to migrate my thesis into new electronic forms as required to ensure continued access to the thesis. I have obtained any third-party copyright permissions that

may be required in order to allow such access and migration, or have requested the appropriate embargo below.

The following is an agreed request by candidate and supervisor regarding the electronic publication of this thesis:

Embargo on both the printed copy and electronic copy for the same fixed period of two years on the following ground(s): publication would preclude future publication.

Date ……..… Signature of candidate ……..…

Signature of supervisor ……..…

Signature of supervisor ……..…

Abstract

There has been an increase in the interest in fluoride materials over the last decade. This interest has focused on multiferroic materials and kagome lattices, to name but a few areas. This thesis focuses on the synthesis and crystallographic characterisation of selected transition metal fluorides and oxyfluorides. Work is presented on the tetragonal tungsten bronze solid solutions of K_xFeF_3, where x = 0.58 and x ≈ 0.5, and the copper analogue, $K_3Cu_3Fe_2F_{15}$; the kagome structure of $Cs_2ZrCu_3F_{12}$; and hydrothermal reactions using vanadium, manganese, or molybdenum as the transition metals in the formation of new fluorides and oxyfluorides.

The tetragonal tungsten bronze compounds K_xFeF_3 (x = 0.58 and x ≈ 0.5) are both tetragonal at 500 K. In the variant with the lower K-content, there is a clear phase separation into two tetragonal phases even at this temperature. The $K_{0.58}FeF_3$ sample separates into two distinct phases below 340 K to possess one tetragonal and one orthorhombic phase. Then at roughly 300 K, both samples undergo a phase transition where the tetragonal phase in the *P4/mbm* space group in $K_{0.58}FeF_3$ changes to an orthorhombic phase with a larger unit cell; and the tetragonal phase in $P4_2bc$ for the $K_{0.5}FeF_3$ sample changes to the same orthorhombic model, whilst the *P4/mbm* model remains unchanged. The evolution of the lattice parameters and phase fractions is studied in detail using synchrotron powder X-ray diffraction (sPXRD).

The kagome structure investigated, $Cs_2ZrCu_3F_{12}$, possesses the "ideal" kagome lattice at room temperature, but previous work has suggested that there is a phase transition at 225 K. The two structures are determined by single crystal X-ray diffraction at 300 K and 125 K. Variable temperature sPXRD studies are performed between these two temperature ranges to determine the phase evolution as a function of temperature. The structure changes from a rhombohedral to a monoclinic phase at low temperature. This is the result of the buckling of the kagome layers at the phase transition. The Zr^{4+} ion changes from 6 to 7 coordinate and this is seen as the main driving force for the distortion of the kagome layer from its "ideal" planar arrangement.

The phase transition is first-order as seen from the electrical impedance measurements.

The hydrothermal reactions presented reveal seven new materials and their crystal structures. $Sr_2V_2F_{10}·H_2O$ is new and found to be isostructural to $Sr_2Fe_2F_{10}·H_2O$. $BaVO_2F_3$ is a cubic material that is potentially piezoelectric. Two hybrid organic inorganic manganese compounds are reported. The ladder structure $(C_3N_2H_5)[Mn_2F_6(H_2O)_2]$ crystallises in a polar space group and shows promise as a candidate for multiferroic studies. The second hybrid material, $(C_7NH_{16})_2[MnF_5(H_2O)]·2H_2O$, crystallises in a centrosymmetric space group. The Mo hybrid materials are all centrosymmetric and possess isolated molybdenum-centred monomeric or dimeric octahedral units.

Acknowledgements

First and foremost, I want to thank my supervisors, Professor Philip Lightfoot and Dr Finlay Morrison, for giving me the opportunity to do the research that I have. You have both supported me in my work and I am truly thankful for that.

Thank you Phil for all the encouragement and support that you have given me over the years. I have learnt many a valuable lesson with regards to synthesis and analysis. And also a lesson or two on travel advice and fund management. Thank you Finlay for broadening my horizons with regards to analytical methods. Your patience and support have proven invaluable.

Several collaborations with Professor Marc Leblanc and Dr Anne-Marie Mercier at the Université du Maine, and with Professor Robert Blinc at the "Jožef Stefan" Institute have yielded several samples that were used in the course of this work. Thank you so much for supplying these.

The synthetic work reported in this thesis would not have been possible had Dr Anne-Marie Mercier and Professor Marc Leblanc from the Université du Maine not synthesised several vital samples for me. Thank you Anne-Marie, you truly are an angel. Marc, thank you for making my stay with your group so memorable and wonderful.

The analytical aspects of this work would not have been possible without the assistance of several beam line scientists at the Diamond Light Source Synchrotron. Thank you Dr Chiu Tang, Dr Julia Parker, and Dr Stephen Thompson on beam line I11 for the discussions about my work and the assistance at all hours of the day when problems arose at the beam line.

A special thank you also to Professor Alexandra Slawin. Without your assistance and training I would not have been able to do much of the work presented here. And therefore also thank you to the Mini.

Members of the Lightfoot group, both past and present, have also been of assistance during the course of my PhD. Thank you Alexandra Gibbs for the countless gingerbread men and cups of tea, Dr David Aldous for inspiring the work that I did and then reading through the results that came of it, Lewis

Downie and Martin Peel for being there when I needed a mind or two to bounce ideas off of, or complain about the slowness of my computer, and Dr Karen Johnston, the one person who always knows the answers to my questions, no matter how obscure. Thank you also for reading the various drafts of my thesis.

Thank you also to Phoebe Allan for just being you. This thesis would not have come into being if you had not been the wonderful and supportive person that you are. I count myself very lucky to have you as a friend. Your assistance with data collection has been greatly appreciated. Katharina, Yann, Brian, and Ken, and so many others are responsible for keeping me sane throughout these years. Rina, thank you for teaching me the deeper meaning of anatidaephobia.

Last, but definitely not least, I want to thank my parents, Herbert and Ingrid Reisinger, for all that they have done for me. Without your endless support and love I would never have had the chance to find my passion and go so far. I am eternally grateful. My siblings, Walter and Astrid, have kept my morale going and have entertained me to see me through the ups and downs of this work. Thank you.

Table of Contents

List of Abbreviations

θ	Bragg angle
λ	Wavelength
χ^2	Goodness-of-fit for a Rietveld refinement
CCD	Charge-coupled device
CFC	Chlorofluorocarbon
cif	Crystallographic information file
CSL	Classical spin liquid
d	d-spacing
F_{hkl}	Structure factor
f_n	Scattering factor
GOF	Goodness-of-fit for a single crystal refinement
GSAS	General Structure Analysis Software
HTB	Hexagonal tungsten bronze
MAC	Multi-analysing crystal detectors
ODF	Orientation distribution function
PTFE	Polytetrafluoroethylene
PXRD	Powder X-ray diffraction
QSL	Quantum spin liquid
R_p	R-factor
RAM	Random access memory
RVB	Resonating valence bond state
SCXRD	Single crystal X-ray diffraction
sXRD	Synchrotron X-ray diffraction
T_C	Curie temperature
T_N	Neel temperature
TB	Tungsten bronze
TTB	Tetragonal tungsten bronze
VBS	Valence bond solid
wR_p	Weighted R-factor
XRD	X-ray diffraction

Chapter 1

Introduction and Background

1.1 Brief Background on Fluorine and Fluorides[1]

Fluorine is the most electronegative element in the periodic table. Thus it is a very reactive element and the only natural occurrence of it is in the form of fluorides. In fact, it is so reactive that it forms compounds with the heavier noble gases, an achievement initially thought impossible.[2] Because of this extreme reactivity, although the element was known to exist from the mid eighteenth century, it was only isolated in 1886 by Henri Moissan; a feat for which he received the 1906 Nobel Prize in Chemistry,[3] before dying in 1907. One of the main suspects for the cause of his death was fluorine poisoning. This is a common fate suffered by most of the scientists who have worked on fluorine.

The strongest, most common oxidising agent known to date is fluorine.[4] This is because fluorine has seven electrons in its outer shell, one short of the eight electrons that would completely fill its 2p electron shell. Thus, it will scavenge any electrons it can find from other atoms to fill its electron shell. The consequence is that fluoride ions favour forming bonds with other compounds. Due to its high electronegativity it has a rather small ionic radius of 1.33 Å, much smaller than the remaining halides (for example chloride at 1.81 Å), and similar in size to oxides at 1.40 Å.[5] This means that the lattice energies for fluorides are higher than for the remaining halides, making fluorides the more stable compounds. The small size of the fluoride ions, as well as the large electronegativity, leads to the ions having a weak covalent character. This makes it easy for oxides, or other ions of suitable size, to displace the fluorides in compounds, a common occurrence.

This property has been put to use in many ways to make better materials for various applications. It has also been used for more nefarious purposes such as to kill intentionally as in the case of Cola Lemming who added the pest killer

sodium fluoride to a cup of coffee to kill her husband's mistress;[6] but also to kill accidentally, as is the case when the same poison, sodium fluoride, was accidentally added to the scrambled eggs in a hospital in the USA (in place of sodium chloride) and 163 patients were taken ill and 47 died.[6]

The improvement of materials for applications has been achieved in many fields, for example it has shown to be successful in the synthesis of fluoride phosphates for use in catalysis, in fluoride borates in lasers, or in fluoride silicates for thermal stability.[7] The most well-known materials to date that contain fluorine are the non-stick material Teflon (a fluorocarbon) and the refrigerant Freon (a chlorofluorocarbon, CFC). These two materials show both the advantages and disadvantages of fluorides. Whilst Teflon has improved many aspects of life such as the non-stick frying pan or the creation of inert reaction vessels for extremely reactive reactions, Freon has been banned from use in industrial instruments such as refrigerators and air conditioners as it depletes the ozone layer. Coincidentally, the CFC Freon was developed by Thomas Midgley Jr., the same man who discovered that adding tetraethylead to petrol stopped the 'knocking' sound in car engines.[8]

1.2 The Chemistry and Structures of Inorganic Fluorides[1, 7, 9, 10]

As mentioned in the previous section, fluorides form very stable compounds due to their high electronegativity. This high electronegativity makes fluorides capable of forcing metals into their highest oxidation states available, such as the +7 oxidation state for rhenium in ReF_7.

Although the fluorides are extremely stable, they are easily transformed into oxyfluorides when some, or most, of the fluoride ions are replaced by oxide ions, which are of a comparable size. This brings with it a need to increase the charge on the cation counter-ions, or to add new cation counter-ions to balance the change in the charges for the fluorides (-1) and oxides (-2).

In the solid state, fluorides can from metal complexes and network structures. The metal complexes are beyond the scope of this work and will not be discussed or elaborated on further in this work. Instead, the focus shall be on various network structures and their resultant properties.

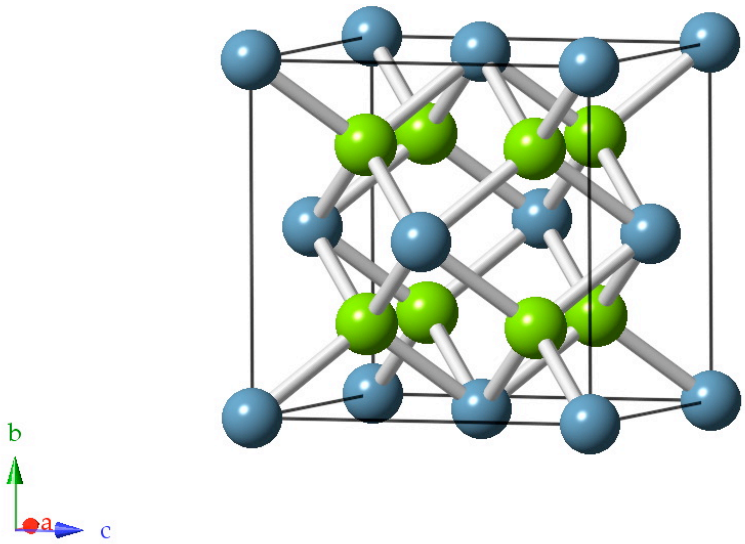

Figure 1.1: Fluorite structure of CaF_2 with the Ca^{2+} in blue and the F^- in green

Fluorides form many different framework structures. The earliest reported structure was that of fluorite, or fluorospar, first reported in the early sixteenth century. The most common use for it is as a flux agent, a material that aids in the formation of the flux growth of compounds. Fluorite has the chemical formula CaF_2 and crystallises in the cubic structure shown in Figure 1.1.[11]

The fluorite structure type is different to most other network structures in that the cations are used to define the structure, rather than the anions, which is the norm. This arrangement, however, can be reversed to give the antifluorite structure, where the anions define the structure, as is the case for Na_2O.

The fluorides can have the metals bonded to the fluoride ions in a continuous manner to form a network structure, as in the fluorite structure, or they can form isolated units, as in $[C_4N_2H_{12}]_3[V_2O_2F_8][VOF_4(H_2O)]_2$, which is a hybrid structure showing the isolated $[V_2O_2F_8]$ dimers and the monomers $[VOF_4(H_2O)]$, Figure 1.2.[12] A hybrid structure is one in which there are isolated organic units and inorganic units. This is the distinction between hybrid structures and complexes, which combine the organic and inorganic constituents into one. This compound also illustrates the concept of sharing of ions amongst octahedra. In the abovementioned compound, $[C_4N_2H_{12}]_3[V_2O_2F_8][VOF_4(H_2O)]_2$, the dimers share two fluoride ions to form two

bridges between the two V-centred octahedra. This leads to one of the edges on each of the octahedra to be shared and thus they are referred to as edge-sharing octahedra. Corner-sharing and face-sharing polyhedra are the other possible forms of sharing bonded atoms amongst polyhedra, examples of which are shown in Figure 1.3.

The given examples show the polyhedra connecting to one another in zero dimensions (the monomers and dimers shown in Figure 1.2), and one dimension (the linked chains of the corner-sharing octahedra in Figure 1.3). These dimensionalities are common in these materials.

1.2.1 Zero-Dimensional (Oxy)Fluorides

1.2.1.1 Quasi-Isolated Fluorides, or Monomeric Units

When metal octahedra form and do not coordinate to one another but only form hydrogen bonds to one another, they are referred to as quasi-isolated,[13] or monomeric units. The isolated nature of the octahedra prevents any transfer of electrical charge or magnetic moment and as such these compounds tend to be electrically and magnetically inert.

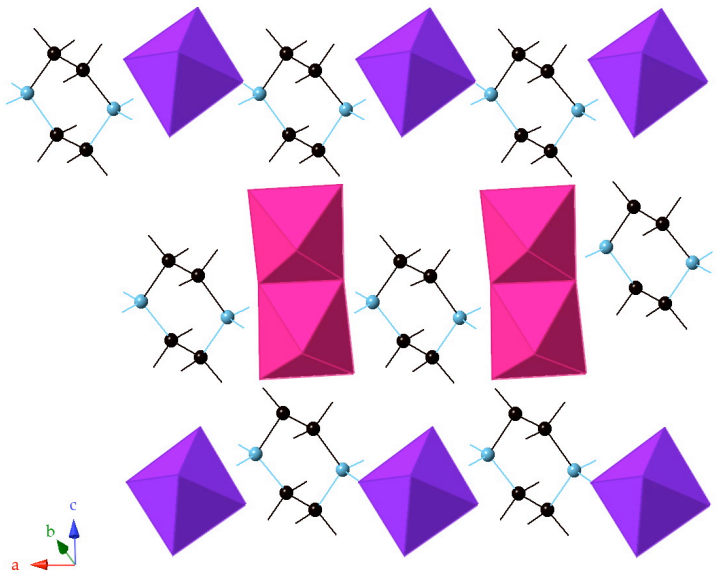

Figure 1.2: Structure of $[C_4N_2H_{12}]_3[V_2O_2F_8][VOF_4(H_2O)]_2$ showing isolated $[VOF_4(H_2O)]$ monomers (purple) and the edge-sharing dimers $[VO_2F_8]$ (pink)

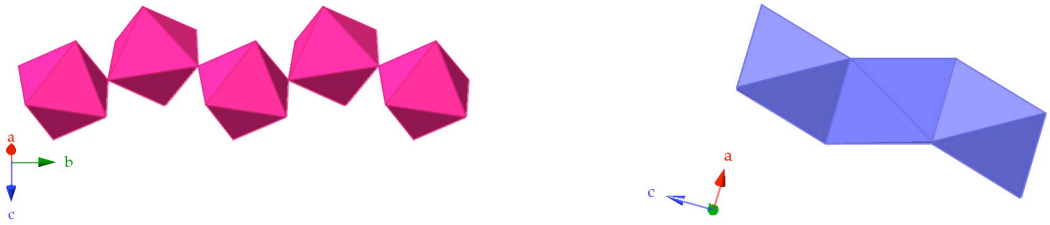

Figure 1.3: Portions of the structure of $[C_4N_2H_6][VF_5].H_2O$ showing corner-sharing octahedra (left),[14] and $CsNiF_3$ showing face-sharing octahedra (right)[15]

1.2.1.2 Dimeric Units

The dimeric unit is defined as a set of two octahedra that share one, two, or three ligands to be corner-, edge-, or face-sharing octahedra, respectively. There are many examples of these materials in the literature. These dimers can be purely fluoride-based as is the case for $[(CH_3)_4N]_3(Cr_2F_9)$,[16] Figure 1.4. They can also contain oxide anions or water molecules, both of which are observed in the structure of $Cs[C_4H_{12}N][V_2O_2F_8(H_2O)]$,[17] Figure 1.4. This dimer is interesting as the two linked octahedra are very different. One of the octahedra has a water molecule in one of its apical positions and an oxide ion in the other, whilst the second octahedron has the bridging fluoride ion and its sole oxide ion at its apical position. This is an extremely rare occurrence, as most dimers tend to consist of two octahedra that are chemically the same.

In most if not all cases the bridging bonds, be they oxide- or fluoride-based, are elongated compared to the remaining bonds. This is because the bridging atoms now share more bonds with two metal atoms and this weakens the bond strength of these atoms.

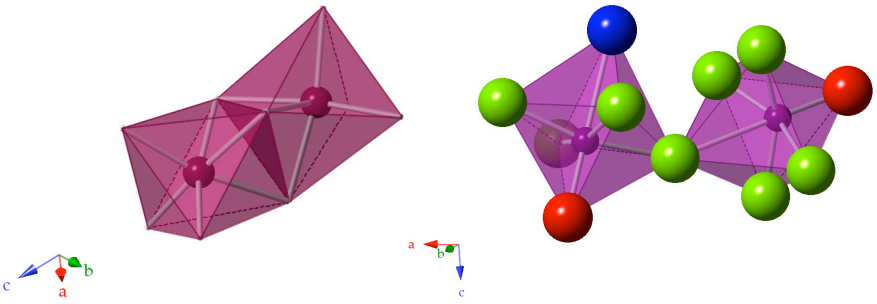

Figure 1.4: Dimeric units of the fluoride-only (Cr_2F_9) in $[(CH_3)_4N]_3(Cr_2F_9)$ on the left, and the oxyfluoride dimer $[V_2O_2F_8(H_2O)]$ in $Cs[C_4H_{12}N][V_2O_2F_8(H_2O)]$ showing the oxide ions in red and the water oxygen in blue on the right

1.2.2 One-Dimensional (Oxy)Fluorides

One-dimensional materials are formed when the octahedra link up to one another in chains or ladders. They most frequently do so by sharing corners.

Chain structures are by far the more common of the one-dimensional structures. These chains are divided into *trans*- or *cis*- chains, where the orientation of the adjoining octahedra defines which type of the chain it is.

Certain organic templates favour the formation of these chains. This has been shown, for example, for the manganese fluorides with the templates ethylenediamine, 1,3-diaminopropane, 1,4-diaminobutane, and 1,6-diaminohexane.[13] In addition to the elongation of the bridging bonds the axial bonds are elongated due to a Jahn-Teller distortion.

The nature of the bridges formed is not only dictated by the metal ion and the bonds it forms, but also by the size and nature of the cationic counter-ion species.

A further type of one-dimensional material can be formed when dimers link to one another to form one-dimensional ladder structures. These are much less common than the chain structures, but may provide more interesting magnetic and electrical properties. An example of a ladder structure is $RbVOF_3$,[18] Figure 1.5. This material, along with $CsVOF_3$ and NH_4VOF_3, is antiferromagnetic.[19]

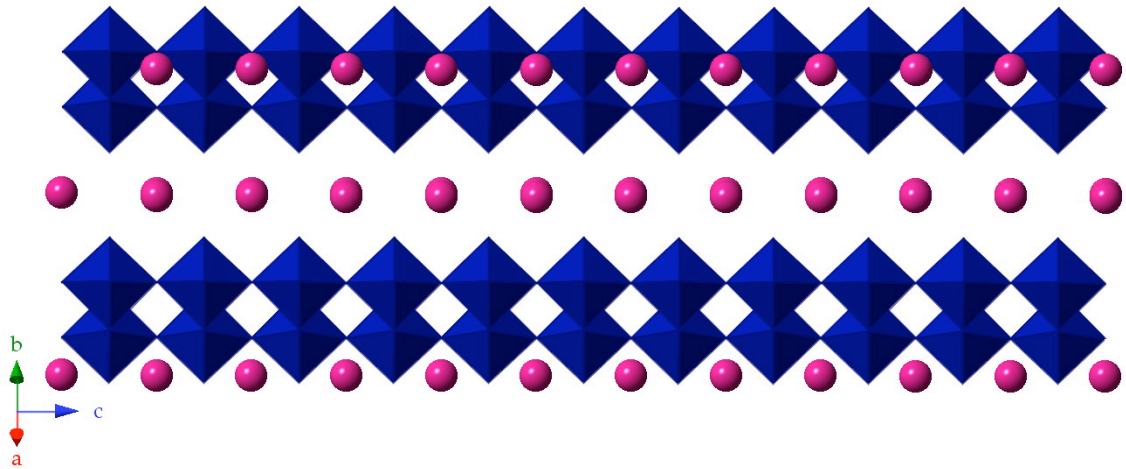

Figure 1.5: Ladder structure of $RbVOF_3$ indicting the linked $[VOF_3]$ dimers that connect to one another to form the ladders along the c-axis

1.2.3 Two-Dimensional (Oxy)Fluorides

If a two-dimensional network structure is desired, the polyhedra must link to one another in a plane to form sheets, as is the case for kagome structures such as the naturally occurring mineral jarosite, $KFe_3(SO_4)_2(OH)_6$, Figure 1.6.[20] This structure is a two-dimensional solid as the layers formed by the $Fe_3(OH)_6$ extend in the *ab*-plane, but the individual sheets are separated from one another by K^+ cations and sulphate anions as shown in Figure 1.6.

As the kagome structure type is of interest in the later part of this work, a brief description of its origin and structural arrangement is now given. A kagome lattice is defined as a two-dimensional pattern of "interlaced triangles whose points each have four neighbouring points".[21] Its name is derived from Japanese with *kage* meaning a bamboo basket and woven pattern, *me*, as shown in the traditional woven kagome basket in Figure 1.7.[21, 22]

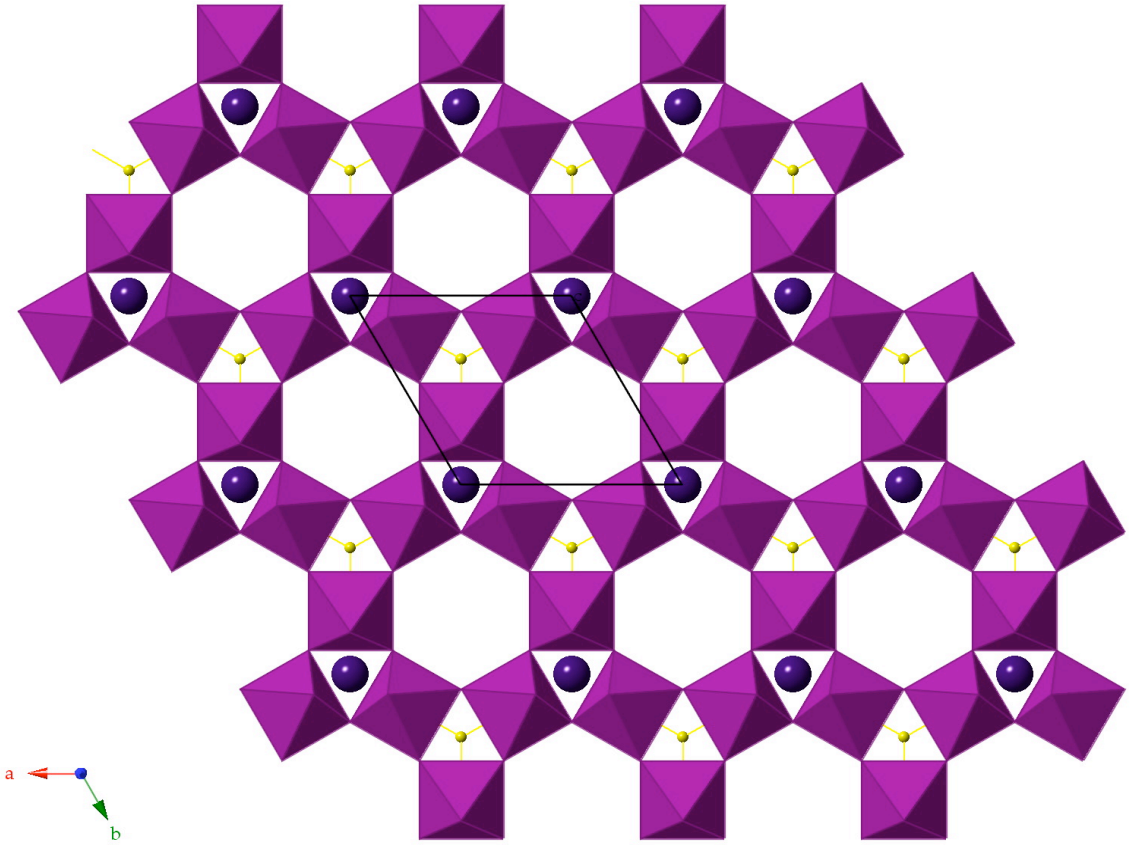

Figure 1.6: Kagome structure of the mineral jarosite, $KFe_3(SO_4)_2(OH)_6$ viewed along the c-axis with the K^+ cations shown in purple and the sulphate ions in yellow[20]

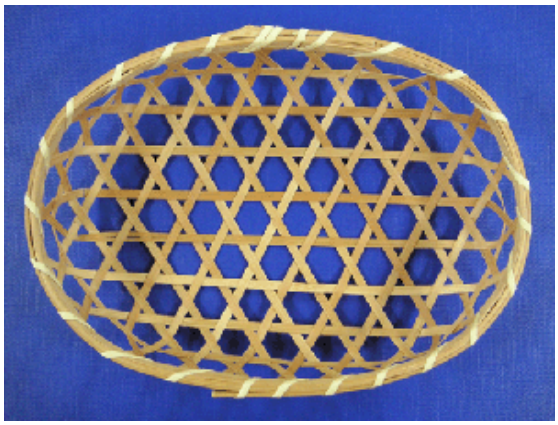

Figure 1.7: Kagome basket giving rise to the name for the structure type[23]

The kagome lattice is the most geometrically frustrated system possible. A frustrated system is defined as a system where preferred interactions of the magnetic moments or spins cannot be simultaneously. As such, it is of interest to physicists and chemists as the magnetic or electrical frustrations arising from the structural arrangement necessarily lead to the creation of compounds that may be magnetoelectric, or possibly even multiferroic. There is no set general chemical formula for this structure type as it is described by the overall arrangement of the atoms in sheets and the spin moment of the metal ions making up these sheets.

A network structure is continuously connected in all three dimensions and so to get from any two-dimensional structure to a three-dimensional network structure, one takes these two-dimensional sheets and connects them directly to one another to form a three-dimensional network.

For example, if one takes the kagome structure and connects these sheets directly to one another, one obtains the hexagonal tungsten bronze structure (HTB), Figure 1.8, where selected cations occupy the interstitial sites.

This structure type is a member of the tungsten bronze (TB) family. Tungsten bronzes were first isolated, analysed, and reported in 1824 by Friedrich Wöhler,[24] a man best known for his later synthesis of urea.[25] Members of the initially reported TB family are notable for their intense shades of bronze that arise as a result of their composition, M_xWO_3.

Initially the terminology for tungsten bronzes only applied to compounds of the formula M_xWO_3, where M is usually an alkaline metal and the value of x lies between 0 and 1.

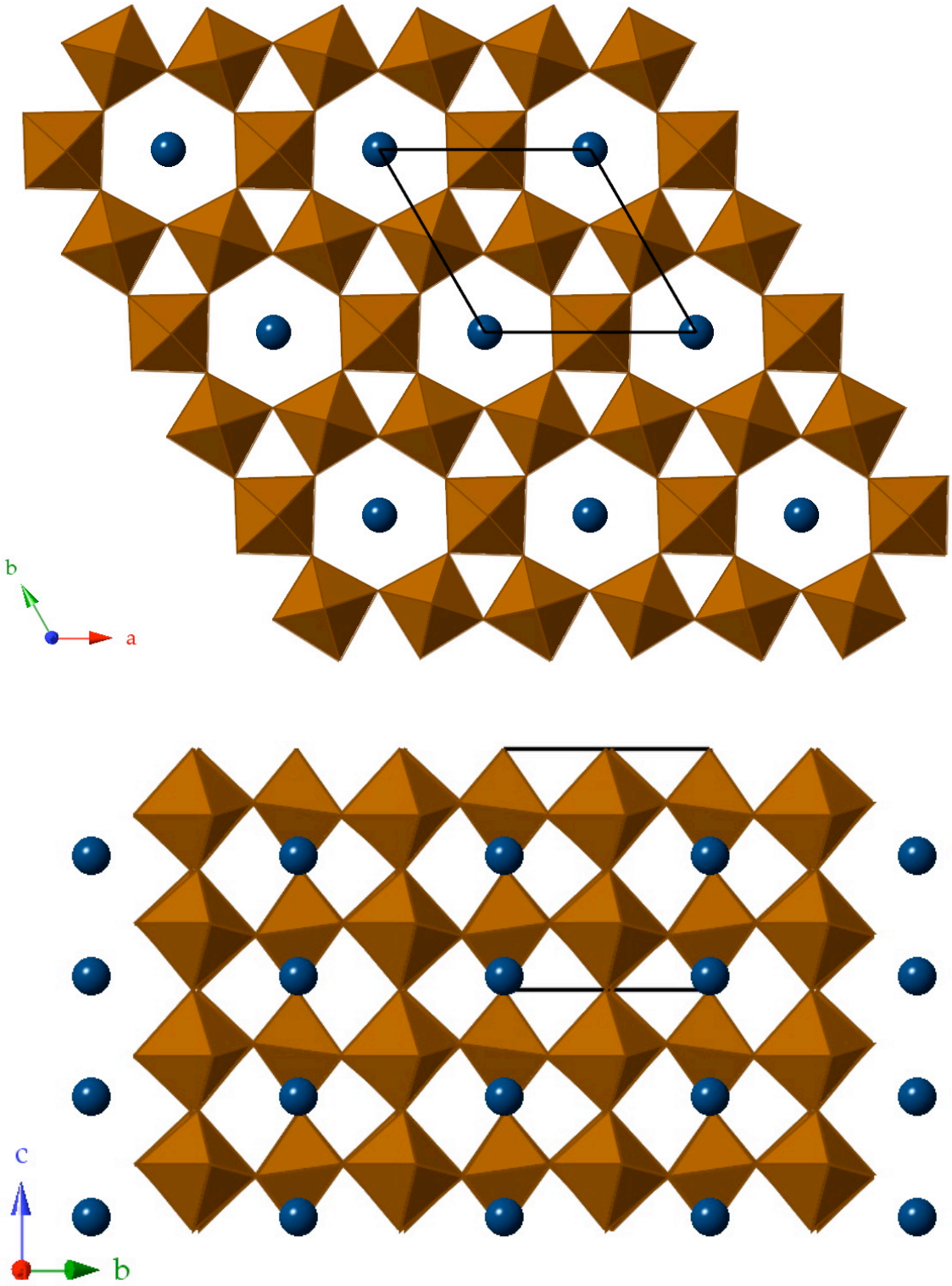

Figure 1.8: Hexagonal tungsten bronze structure of $K_{0.26}WO_3$ as reported by Schultz and Horiuchi[26] viewed along the c-axis (top) and in a side-on view along the a-axis to show the connection of the sheets in three dimensions (bottom)

There are several different TB structure types possible. These depend, for the most part, on the value of x. The general trend for these structures is as follows: at very low values of x, the compound will most likely be of the HTB type. The next lowest in crystallographic symmetry is then the tetragonal tungsten bronze (TTB) structure, Figure 1.9, and finally the lowest symmetry is the monoclinic distorted ReO_3 type structure, Figure 1.10. This last structure type is similar to the perovskite structure, ABX_3, although none of the interstitial holes are filled (i.e. all of the A sites are vacant). The exact limits of the value of x for the various phases depend on the nature of the metals used.

The structure type of particular interest in the course of this work is the TTB structure type. The TTB structure was first reported Magnéli on $K_{0.57}WO_3$ in 1949.[27] The general formula for a TTB is defined as $A_2BC_2M_5X_{15}$. Large cations occupy the 15-coordinate A sites (pentagonal tunnels) and 12-coordinate B sites (square tunnels), whilst smaller cations occupy the nine-coordinate C sites (trigonal tunnels). The positions of these sites are illustrated in Figure 1.9. By introducing vacancies on the B and C sites, a range of solid solutions can be prepared.

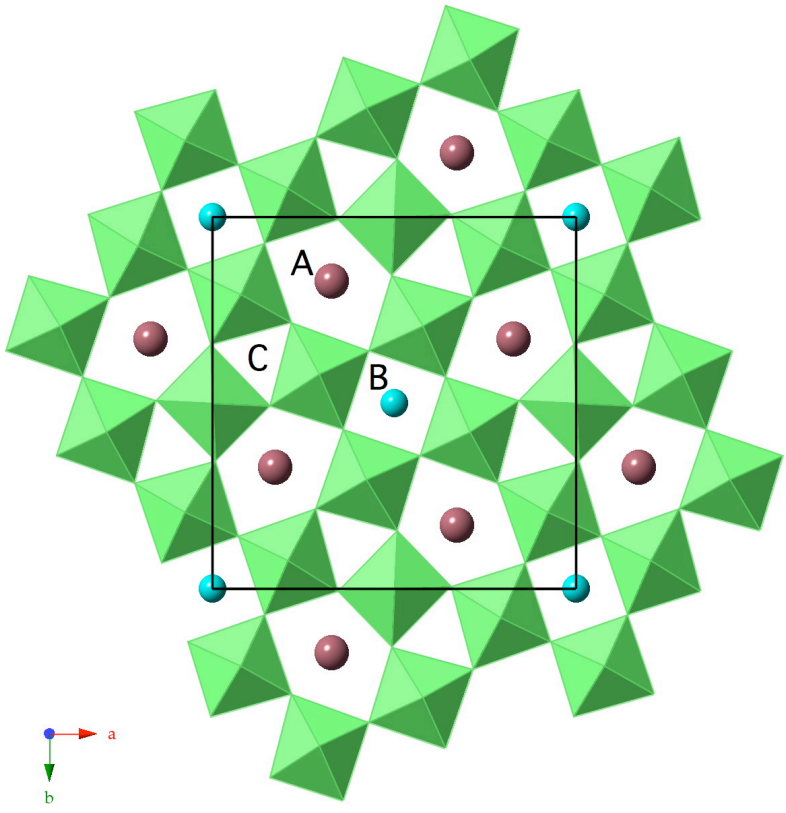

Figure 1.9: Tetragonal tungsten bronze structure of $Ba_2NaNb_5O_{15}$ as reported by Foulon et al.[28] viewed along the c-axis (with the A, B and C sites indicated)

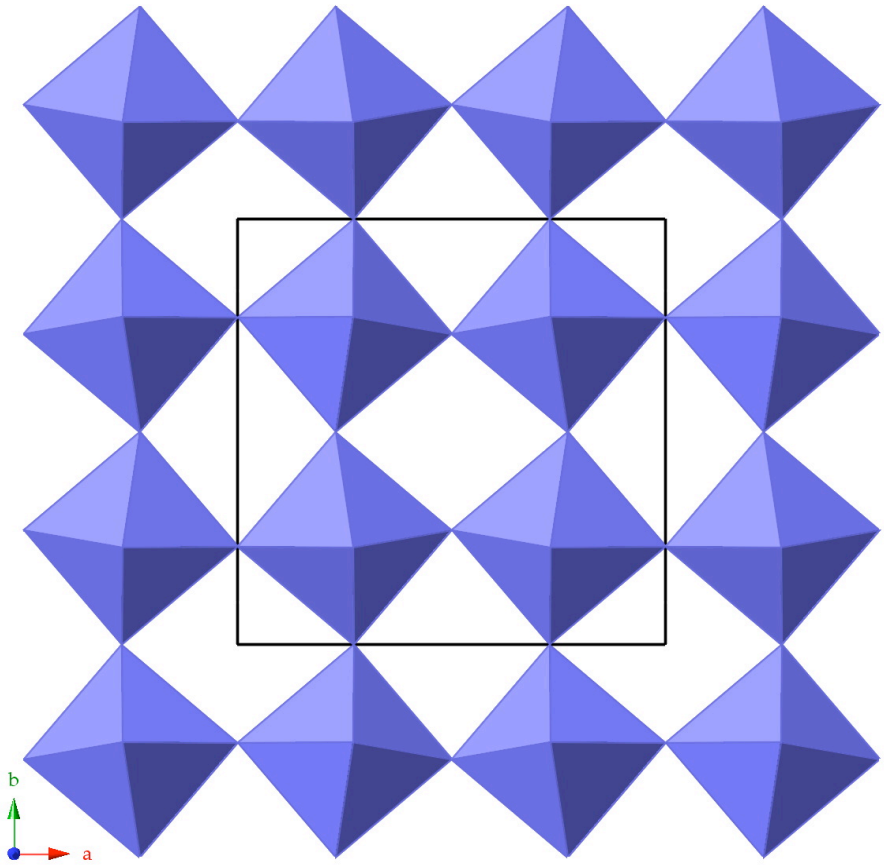

Figure 1.10: ReO_3 structure as reported by Jorgensen et al.[29] viewed along the c-axis

1.3 Selected Physical Properties of Fluorides

There are many properties that are commonly found in fluorides and oxyfluorides. All fluorides have much higher melting points than their analogues of the remaining halides. This is because fluorides possess much higher lattice energies. This is a result of the high electronegativity of the fluorides.

A very well known property exhibited by many fluorides and some oxyfluorides is fluorescence, named after the luminescent property first observed in fluorite doped with small amounts of europium. This property has found a widespread application in fluorescent lamps and plasma display panels.[30] A particularly good candidate for this is Eu^{3+}-doped $KGdF_4$.[30-32] $KGdF_4$ alone does not fluoresce, it is the addition of the dopant Eu^{3+}, that leads to this property.

Another property of fluorides that is desirable is that fluoride aids the hardening of tooth enamel. This is most frequently achieved by the addition of

sodium fluoride (NaF), fluorosilicic acid (H_2SiF_6), or sodium fluorosilicate (Na_2SiF_6) to drinking water. Fluoride-containing toothpastes are a further form of tooth protection that is readily available and used.

The properties most relevant to the work presented in the course of this thesis are magnetic and electrical properties. A brief overview of the relevant properties and the reasons for interest in this work are given.

The two structure types described in more detail in the previous section, namely the kagome and TTB structures, are chemically frustrated structures. Chemically frustrated structures are properly defined in Chapter 4. This frustration leads to several different properties arising for these compounds: they may be magnetoelectric, or possibly even multiferroic.

A magnetoelectric compound is a material that possesses both magnetically and electrically polarisable moments; in addition, one of these polarisations drives the other.[33] That is to say that the two effects are coupled to one another.[34] In most cases the magnetic polarisation drives the electrical polarisation.

This coupling is frequently observed in frustrated materials, because the inability of these compounds to balance adjacent spin or magnetic moments leads to the creation of a magnetic polarisation in the material and this can then in turn induce an electric polarisation.

1.3.1 Magnetic Polarisability[1, 35]

There are several different modes of magnetic polarisation that can occur in materials, and a selected few that are relevant to the work covered in this thesis are briefly described. The discussion of magnetic polarisations is limited to those that are present even in the absence of a magnetic field.

1.3.1.1 Ferromagnetism[35]

A material that exhibits spontaneous magnetisation in the absence of an external applied magnetic field with all dipole moments aligned at absolute

zero is referred to as a ferromagnetic material. This spontaneous magnetisation can be switched hysteretically by an applied magnetic field. This property is only present below a certain temperature, called the Curie temperature, T_C. The magnetic moments of the sample are all arranged in the same direction within the solid, Figure 1.11.

The arrangement of the magnetic moments need not be the same throughout the entire sample. The sample may consist of several domains that each have their moments aligned in the same direction within that domain but the alignment of the different domains may be non-uniform.

Below T_C the sample is magnetised by its own molecular magnetic field only and the thermal fluctuation of the sample does not annul this interaction. As the temperature of the sample is increased from absolute zero towards T_C, the thermal fluctuations within the sample become stronger and cause excitations, which disrupt the ferromagnetic order. At T_C this interference is strong enough to annul the magnetisation and an ordered state is no longer present above T_C.

1.3.1.2 Antiferromagnetism

The most likely magnetisation for the frustrated materials is an antiferromagnetic one.

An antiferromagnetic material is defined as a compound that has magnetic moments that are aligned in an antiparallel manner, Figure 1.12, with the magnitudes of the opposing magnetic moments being equal. The antiparallel sets of magnetic moments can effectively be separated into two distinct subsets of magnetic interactions as indicated in Figure 1.12. The nearest neighbour of each spin moment is thus not its direct neighbour on the complete lattice but rather is direct neighbour on the separate sublattice.

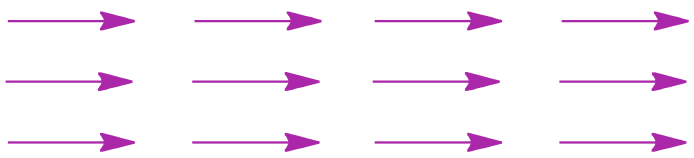

Figure 1.11: Arrangement of magnetic moments in a ferromagnetic compound

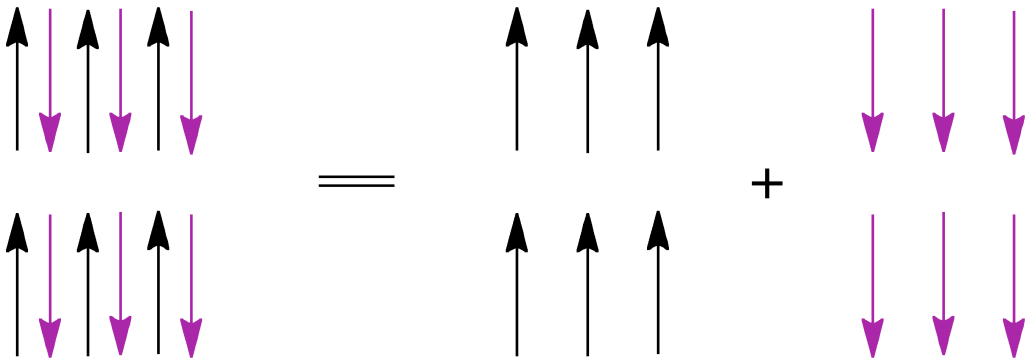

Figure 1.12: Arrangement of magnetic moments in an antiferromagnetic compound[36]

The magnetic moments in the material give rise to a spontaneous magnetic field below the Neel temperature, T_N, but no net magnetisation of the material. In the case of the ferromagnetic compounds the direction of the magnetic field is not relevant; but in the antiferromagnetic materials this is not the case. Here, the direction of the magnetic field is important, as there are two separate sublattices that need to be optimised energetically.

In both ferromagnetic and antiferromagnetic materials, above T_C or T_N respectively they are paramagnetic. Thus they have zero net magnetisation if there is no applied magnetic field above these temperatures.

1.3.2 Electrical Polarisability[37]

There are also several different modes of electrical polarisation that a material may be subject to. Only selected polarisations are elaborated upon in this section.

1.3.2.1 Ferroelectricity

A ferroelectric material is defined as a material that, upon going from a dielectric high-temperature phase to a low-temperature phase, exhibits spontaneous electric polarisation. This spontaneous polarisation can be switched hysteretically by an applied electric field. This requires that the low-temperature phase crystallise in a polar space group. This is necessary as the

dipoles are subject to the same symmetry requirements as the crystal, and so an inversion centre cancels each electric dipole by generating an antiparallel partner of the same magnitude.

A simpler version of this definition is analogous to that for ferromagnetism; but in this case the focus is on electric dipole moments in the material, rather than magnetic moments. That is to say, a ferroelectric material is one that generates a spontaneous electric field below the Curie temperature, due to the parallel arrangement of its dipole moments.

1.3.2.2 Antiferroelectricity

A material is defined as antiferroelectric if it has dipole moments that are aligned in an antiparallel manner. The magnitudes of the two opposing dipoles are equal and so there is net neutrality in the compound. Below its Neel temperature, the compound experiences localised electric fields on a microscopic scale, but the net effect is neutral on a macroscopic scale. The antiparallel dipole moments can be separated into two sublattices and so the nearest neighbour for each dipole is not the direct neighbour on the complete lattice, but rather the next neighbour on the sublattice, just as for an antiferromagnetic material.

1.3.3 Multiferroics

As noted previously, under extraordinary circumstances, a geometrically frustrated material can be a multiferroic. A multiferroic material is a material that has at least two ferroic properties simultaneously present in the same solid state phase.[38] This definition has now also been expanded to allow magnetoelectrics to be classified as multiferroic, even though in these materials one polarisability drives the other, rather than the two existing independently of one another.[34, 39, 40]

1.3.4 Applications

Several applications of fluorides have already been discussed in the course of this chapter, such as the addition of certain fluorides to drinking water or toothpaste to prevent the formation of tooth cavities.

Fluorides have been used historically as refrigerants as was noted with CFCs. This, however, is no longer an application that fluorides are used for. One of the largest industrial uses for the element fluorine is in the production of nuclear fuels via the synthesis of UF_6.

The most famous application of fluorides, though, must be the non-adhesive material Teflon (polytetrafluoroethylene, or PTFE). It has many different applications from its non-stick properties to its inert nature and as such it is ideally suited as a reaction vessel. These Teflon reaction vessels are frequently used in synthetic processes involving fluorine or fluorides, as it is one of the few materials that do not react with either.

The materials discussed in the course of this work are all potential or known magnetoelectrics or multiferroics. Thus, they are suitable candidates to be used in random access memory (RAM) drives in computing technology. This is because multiferroics have been shown to be ideal candidates for this application as they have the ability to store data magnetically and electrically, and read it in the same manner. This increases the rate at which the data can be read and stored.[39] This has been done using oxide-based multiferroics, but there is no reason why fluoride-based multiferroics should not be equally suitable candidates for further study.

1.4 Aims and Objectives

Initially, the aim of this thesis was to focus on the work presented by Aldous in the course of his PhD.[19] The hydrothermal reactions involving vanadium in its various oxidation states provided many new materials, several of which showed promise as ferroic materials. This work should thus extend this field of research by using alkaline metals in place of the alkaline earth metals presented by Aldous.

Simultaneously, a solid state synthetic route is used to synthesise known multiferroic and other magnetically interesting materials. The aim of this approach is to understand the effect of the synthetic approach on the production of multiferroic materials, and to answer certain questions that have been raised in the literature concerning these compounds. All of the samples are made by following or modifying reported procedures for these compounds. The materials studied in this manner are selected for two reasons: in one case there is a disagreement in the reported crystal structures (for the TTB members of the solid solution of K_xFeF_3), and in the other case there has been a report of a phase transition for a material, $Cs_2ZrCu_3F_{12}$, but the crystal structure for this new low temperature phase is unknown.

A third aim is to perform hydrothermal reactions to make hybrid organic inorganic materials. These have been studied in a limited manner in the literature and if a suitable transition metal can be selected, it is assumed that several potentially ferroic materials can be produced. Transition metals used are molybdenum (again, this is an expansion on the work done by Aldous[19] for his thesis), and manganese. The latter has been selected as it has an ideal electron configuration for electrically and magnetically active materials.

1.5 Thesis Overview

In the course of this work, the synthesis and structural analysis of selected solid state fluorides and oxyfluorides by high-resolution powder X-ray diffraction and single crystal X-ray diffraction are presented. No measurements of magnetic properties are made for any of the compounds, but a simple electrical experiment is performed for one of the samples.

The relevant experimental techniques are described and defined in Chapter 2. Particular emphasis is paid to diffraction techniques and the associated problems that may arise as a result of the samples analysed. Both single crystal X-ray diffraction and powder X-ray diffraction are covered, with a short description and comparison of these two techniques as well as synchrotron radiation. This chapter also contains an explanation of the experimental methods used to synthesise the various samples, from hydrothermal methods to solid state methods.

Chapters 3 to 5 are results chapters. Chapter 3 focuses on the crystallographic study of the tetragonal tungsten bronze K_xFeF_3 solid solution system with particular emphasis on $K_{0.6}FeF_3$ (a known multiferroic) and $K_{0.5}FeF_3$. The relevant literature is covered and the scope of the analysis done explained. These materials are studied over a 400 K temperature range from 100 K to 500 K. They both show clear phase separations and phase transitions that have not been reported to date. These conclusions are only possible due to the use of high-resolution synchrotron powder X-ray diffraction experiments. A Cu-doped version, $K_3Cu_3Fe_2F_{15}$, synthesised by a collaborating research group is also presented by single crystal X-ray diffraction and powder diffraction.

Chapter 4 is a report of the structural analysis and phase transition of the kagome material $Cs_2ZrCu_3F_{12}$. The chapter contains an introduction to the relevant physical concepts and the work done to date on this material and similar analogues. The synthesis and characterisation of this material is presented. Single crystals are obtained that confirm the room temperature structure as reported in the literature, but the low temperature structure is new. Synchrotron high-resolution X-ray diffraction experiments confirm the structural phase transition and the models used. An electrical impedance measurement confirms the first order phase transition and correlates with the observed magnetic anomaly reported in the literature.

Chapter 5 includes a collection of single crystal structures obtained from hydrothermal and slow evaporation reactions. Both inorganic and hybrid organic inorganic structures are presented. The two inorganic structures are vanadium-based: one being an oxyfluoride, whilst the other is a hydrated fluoride. The hybrid structures are hydrated fluorides or oxyfluorides and have either manganese or molybdenum as the transition metal ions. One of these structures, $(C_3N_2H_5)[Mn_2F_6(H_2O)_2]$, is a potential multiferroic as it crystallises in a polar space group and the structure consists of ladders of Mn-centred octahedra. The Mo-centred structures are all centrosymmetric. All but one of the structures consists of the same Mo-centred dimers.

Chapter 6 gives a summary of all the results chapters and combines all of the conclusions reached for the individual samples into a coherent whole for fluoride-based structures by relating them to the chemical and physical concepts presented in this chapter.

1.6 References

1. P. Hagenmuller, in *Inorganic Solid Fluorides : Chemistry and Physics*, Academic Press, Orlando, Fla., 1985.
2. N. Bartlett, *Proc. Chem. Soc., London*, 1962, 218.
3. The Nobel Foundation, *The Nobel Prize in Chemistry 1906*, http://nobelprize.org/nobel_prizes/chemistry/laureates/1906, Accessed 12 July 2011, 2011.
4. D. F. Shriver and P. W. Atkins, *Inorganic Chemistry*, Third edition, Oxford University Press, Oxford, 2002.
5. R. Shannon, *Acta Crystallogr., Sect. A: Fundam. Crystallogr.*, 1976, **32**, 751-767.
6. J. Emsley, *Elements of Murder : A History of Poison*, Oxford University Press, Oxford ; New York, 2005.
7. T. Nakajima, B. Zemva and A. Tressaud, *Advanced Inorganic Fluorides : Synthesis, Characterization, and Applications*, Elsevier, Amsterdam; New York, 2000.
8. B. Bryson, *A Short History of Nearly Everything*, 1st Edition, Broadway Books, New York, 2003.
9. W.-K. Li, G.-d. Zhou and T. C. W. Mak, *Advanced Structural Inorganic Chemistry*, Oxford University Press, Oxford ; New York, 2008.
10. K. Adil, M. Leblanc, V. Maisonneuve and P. Lightfoot, *Dalton Trans.*, 2010, **39**, 5983-5993.
11. E. A. Zhurova, B. A. Maximov, V. I. Simonov and B. P. Sobolev, *Kristallografiya*, 1996, **41**, 438-443.
12. D. W. Aldous, N. F. Stephens and P. Lightfoot, *Dalton Trans.* , 2007, 4207-4213.
13. U. Bentrup, M. Feist and E. Kemnitz, *Progr. Solid State Chem.*, 1999, **27**, 75-129.
14. D. W. Aldous, N. F. Stephens and P. Lightfoot, *Inorg. Chem.*, 2007, **46**, 3996-4001.
15. C. Jørgensen, J. Neilands, R. Nyholm, D. Reinen, R. Williams and D. Babel, in *Structure and Bonding*, Springer Berlin / Heidelberg, 1967, vol. 3, 1-87.

16. L. Kiriazis and R. Mattes, *Z. Anorg. Allg. Chem.*, 1991, **593**, 90-98.
17. M. Hilbers, M. Leimkuehler and R. Mattes, *Z. Naturforsch., B: Anorg. Chem. Org. Chem.*, 1989, **44**, 383-388.
18. D. W. Aldous, R. J. Goff, J. P. Attfield and P. Lightfoot, *Inorg. Chem.*, 2007, **46**, 1277-1282.
19. D. Aldous, *Solvothermal Chemistry of Early Transition Metal Fluorides*, PhD thesis, University of St Andrews, 2008.
20. U. Becker and B. Gasharova, *Physics and Chemistry of Minerals*, 2001, **28**, 545-556.
21. M. Mekata, *Phys. Today*, 2003, **56**, 12-13.
22. I. Syôzi, *Progress of Theoretical Physics*, 1951, **6**, 306.
23. Z. Hiroi and et al., *J. Phys.: Condens. Matter*, 2007, **19**, 140301.
24. P. G. Dickens and M. S. Whittingham, *Quart. Rev. (London)*, 1968, **22**, 30-44.
25. F. Wöhler, *Annalen der Physik*, 1828, **88**, 253-256.
26. A. J. Schultz and H. Horiuchi, *Acta Crystallogr., Sect. C: Cryst. Struct. Commun.*, 1986, **42**, 641-644.
27. A. Magneli, *Arkiv foer Kemi*, 1949, **1**, 213-221.
28. G. Foulon, M. Ferriol, A. Brenier, G. Boulon and S. Lecocq, *European Journal of Solid State Inorganic Chemistry*, 1996, **33**, 673-686.
29. J. E. Jorgensen, W. G. Marshall, R. I. Smith, J. S. Olsen and L. Gerward, *J. Appl. Crystallogr.*, 2004, **37**, 857-861.
30. M. Karbowiak, A. Mech, L. Kepinski, W. Mielcarek and S. Hubert, *J. Alloys Compd.*, 2005, **400**, 67-75.
31. M. Karbowiak, A. Mech, A. Bednarkiewicz and W. Strek, *J. Alloys Compd.*, 2004, **380**, 321-326.
32. F. You, S. Huang, S. Liu and Y. Tao, *J. Lumin.*, 2004, **110**, 95-99.
33. W. Eerenstein, N. D. Mathur and J. F. Scott, *Nature*, 2006, **442**, 759-765.
34. M. Fiebig, *J. Phys. D: Appl. Phys.*, 2005, **38**, R123.
35. J.-M. Dance and A. Tressaud, in *Inorganic Solid Fluorides : Chemistry and Physics*, Academic Press, Orlando, Fla., 1985.
36. S. Blundell, *Magnetism in Condensed Matter*, Oxford University Press, Oxford ; New York :, 2001.

37. M. E. Lines and A. M. Glass, *Principles and Applications of Ferroelectrics and Related Materials*, Clarendon Press ; Oxford University Press, New York, 2001.
38. H. Schmid, *J. Phys.: Condens. Matter*, 2008, **20**, 434201.
39. N. A. Spaldin and M. Fiebig, *Science*, 2005, **309**, 391-392.
40. J. van den Brink and D. I. Khomskii, *J. Phys.: Condens. Matter*, 2008, **20**.

Chapter 2

Experimental Techniques

2.1 Symmetry in Crystals

2.1.1 Lattices and Systems in Crystals[1-3]

The formation of solids is governed by the electrostatic interactions and bonds within the compound. Once the ideal interactions have been found, the structure is at an energy minimum and stable. The asymmetric unit is then the smallest, most simple repeating unit in the structure that can be rotated, translated, or reflected to give the unit cell. The unit cell is defined as the smallest repeating unit within a structure that shows each of the symmetry elements present. The unit cell can be translated in all three dimensions to yield the crystal lattice. This lattice is defined as an infinite array of symmetry-equivalent points, known as lattice points. The lattice does not indicate the position of the atoms in the structure, but rather the symmetry elements that define them. This also applies to the lattice points; they do not indicate the presence of an atom, merely the symmetry that relates it to the atoms surrounding it. These symmetry interactions, in addition to the unit cell dimensions, lead to the possible crystal classes.

The unit cell can be classed in one of seven different crystal systems, Figure 2.1. The symmetry requirements for these crystal systems are also given in Table 2.1. Each unit cell can be described in terms of three axes *a*, *b*, and *c*, and three angles α, β, and γ. The angle α is defined as the angle formed between the axes *b* and *c*; the angle β is defined as the angle formed between the axes *a* and *c*; and the angle γ is defined as the angle formed between the axes *a* and *b*.

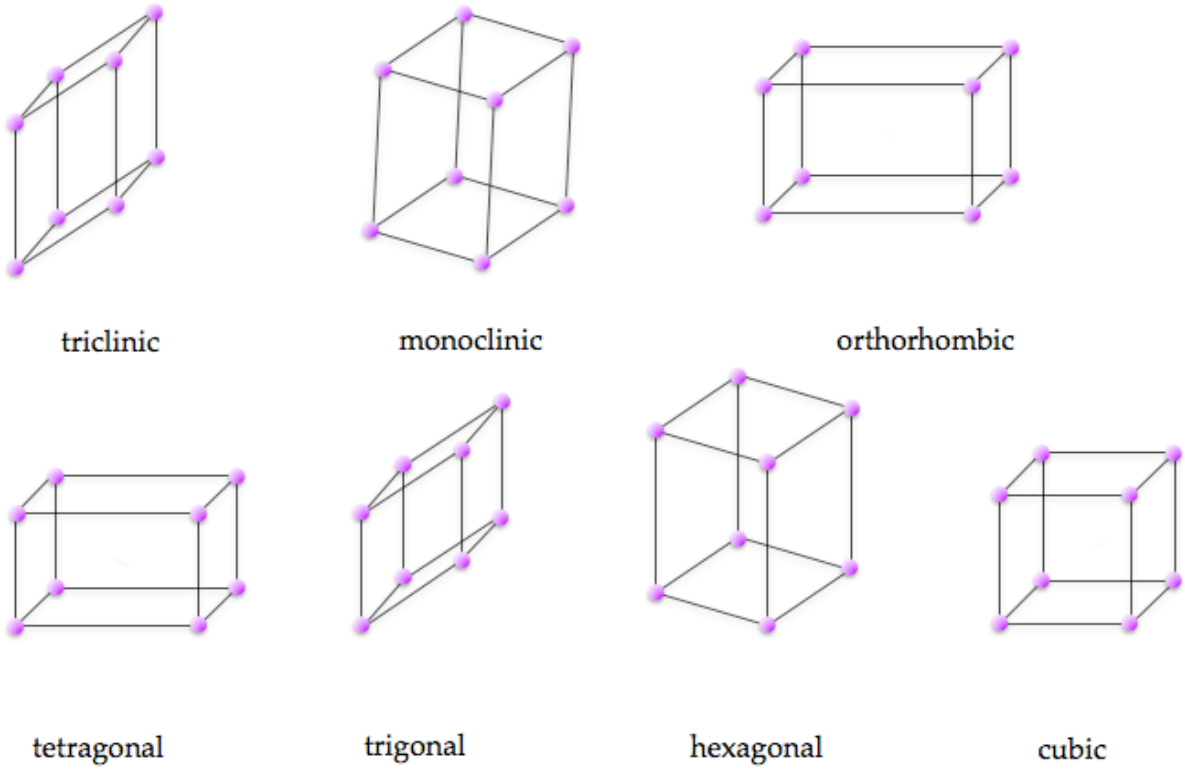

Figure 2.1: The seven crystal systems

The possible lattice types for these crystal systems are also given in Table 2.1. These refer to the possible centring in the unit cell. It is possible that the lattice points are only found at the corners of the unit cell (primitive, P); at the corners of the unit cell and in the centre of each face, (face-centred, F); at the corners of the unit cell and in the centre of it (body-centred, I); at the corners of the unit cell and one side, usually the *ab* plane (side-centred, C). These lattice types are shown in Figure 2.2. The combination of the seven crystal systems and four lattice types leads to fourteen unique Bravais lattices.

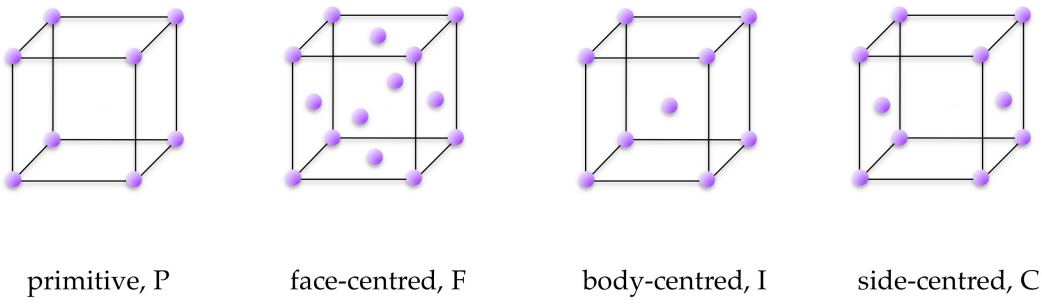

Figure 2.2: The four lattice types

Table 2.1: The seven crystal systems with symmetry and unit cell requirements

Crystal system	Unit cell dimensions	Required symmetry	Possible lattice types
triclinic	None	None	P
monoclinic	$a \neq b \neq c$ $\alpha = \gamma = 90°, \beta \neq 90°$	One two-fold axis or one mirror plane	P, C
orthorhombic	$a \neq b \neq c$ $\alpha = \beta = \gamma = 90°$	Three mutually perpendicular two-fold axes or mirror planes	P, F, I, C
tetragonal	$a = b \neq c$ $\alpha = \beta = \gamma = 90°$	One four-fold axis	P, I
trigonal	$a = b = c$ $\alpha = \beta = \gamma \neq 90°$ or $a = b \neq c$ $\alpha = \beta = 90°, \gamma = 120°$	One three-fold axis One three-fold axis	P (R)
hexagonal	$a = b \neq c$ $\alpha = \beta = 90°, \gamma = 120°$	One six-fold axis	P
cubic	$a = b = c$ $\alpha = \beta = \gamma = 90°$	Three four-fold axes at 109.28° to one another	P, F, I

2.1.2 Point Groups[2-5]

A point group is defined as the complete collection of symmetry operations for a fragment or molecule. Each point group is assigned its own symbol. In total, there are 32 possible crystallographic point groups, Table 2.2.

Table 2.2: The 32 crystallographic point groups

Crystal system	Allowed point groups						
triclinic	*1*	***$\bar{1}$***					
monoclinic	*2*	*m*	***2/m***				
orthorhombic	*222*	*mm2*	***mmm***				
tetragonal	*4*	*$\bar{4}$*	***4/m***	*422*	*4mm*	*$\bar{4}$2m*	***4/mmm***
trigonal	*3*	***$\bar{3}$***	*32*	*3m*	***$\bar{3}$m***		
hexagonal	*6*	*$\bar{6}$*	***6/m***	*622*	*6mm*	*$\bar{6}$2m*	***6/mmm***
cubic	*23*	***m$\bar{3}$***	*432*	*$\bar{4}$3m*	***m$\bar{3}$m***		

The point groups indicated in bold type are centrosymmetric

All point symmetry operations can be divided into two groups: proper rotations, which are rotations through a particular fraction of 360° about a rotation axis, and improper rotations, which are rotations through a particular fraction of 360° with a simultaneous reflection in a plane perpendicular to the rotation axis. All improper rotations lead to a change in the handedness of the fragment or molecule that is being acted upon. This is not the case for proper rotations, where the original handedness is retained.

The number of rotations that must be done to do one complete rotation through 360° gives the order of the rotation axis. Due to the symmetry constraints in crystals, the only possible numbers are 2, 3, 4, and 6 for both proper and improper rotations. The symbol *m* designates an improper rotation accompanied by a mirror plane (which is an inversion in crystallographic terms).

If the inversion centre is preserved in the point group, it is called centrosymmetric. The remaining point groups are noncentrosymmetric. This lack of a centre of symmetry is required as a prerequisite for optical activity, piezoelectricity, and ferroelectricity.[4]

2.1.3 Space Groups[4, 6]

The 32 point groups, in combination with the 14 Bravais lattices, give a total of 230 unique space groups. Space groups are created by adding translational elements, specifically screw axes or glide planes, to the point groups. These translational operations are merely rotations or reflections with an additional translation in space. A full list of the space groups along with their symmetry operations and notation can be found in the *International Tables for Crystallography, Volume A*.[5]

The space group is written as a combination of several symbols. The first character indicates the lattice type and the remaining symbols give the symmetry operations, with those relating to the principal axis (if present) coming first.

2.1.4 Miller Planes[7]

Due to the ordered, and thus regular, arrangement of the atoms in crystalline materials, they can be regarded as equivalent to a diffraction grating. This diffraction grating works only for waves of a wavelength similar to the distances between lattice points (in the 1 to 100 Å region). Thus, for simplification, the crystal can be regarded as a set of layers of atoms or planes, referred to as Miller planes. The distance between these planes is called the d-spacing, d_{hkl}. Each Miller plane is denoted (hkl).

William H. Bragg and his son William Lawrence Bragg made use of this analogy to develop a simple and concise law[8] that relates the incident radiation and the diffracted radiation as follows

$$n\lambda = 2d_{hkl}\sin\theta \qquad (2.1)$$

This is known as Bragg's law. The wavelength of the radiation used, λ, is related to the d-spacing, d_{hkl}, and the diffraction angle, θ. The letter n refers to the plane that the radiation is diffracted from. It is usually set to a value of 1, but if the number is greater than 1, the d_{hkl}-spacing is divided by that same number.[1]

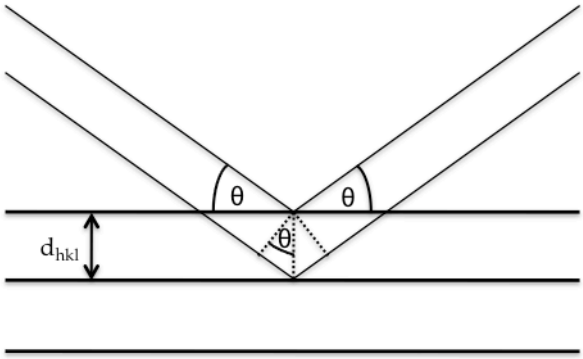

Figure 2.3: Schematic representation of Bragg's law

A diagrammatic representation is given in Figure 2.3. The incident beam of radiation is diffracted by the surface of the material at an angle, θ. A further beam of incident radiation penetrates the sample to a different Miller plane. This beam now has to travel a further distance than the first beam to remain in phase with the first beam so that the diffraction requirement is met. This difference in distance is equal to $2d_{hkl}\sin\theta$.

2.1.5 Reciprocal Space and the Reciprocal Lattice[3, 9]

It is important to remember that the diffraction pattern generated by a solid is not a depiction of the real reflections from that solid, but rather a set of vectors generated in reciprocal space. This three-dimensional pattern of points is known as the reciprocal lattice, and each is generated from a particular Bravais lattice. Each point in the pattern can be assigned to the end point of the vectors generated by a combination of the vector perpendicular to a Miller plane and the intensity of the diffracted beam in that plane. The magnitude of each of these vectors is equal to the inverse of the Bragg interplanar d-spacing, d_{hkl}. Thus, the lattice parameters can be calculated directly from these points. The reciprocal lattice is related to the real or direct lattice of the crystal by a Fourier transform.

2.2 Diffraction Techniques

Several types of X-ray diffraction experiments are covered in this work: conventional laboratory single crystal X-ray diffraction (SCXRD), conventional laboratory powder X-ray diffraction (PXRD), and high-resolution synchrotron powder diffraction (sPXRD).

2.2.1 A Brief History of X-rays

In 1895 Wilhelm Konrad Röntgen discovered a hitherto unidentified form of electromagnetic radiation (with a wavelength of ~ 1 Å) that he labelled X-radiation due to its unknown nature at the time. Max von Laue and Paul Knipping, in 1912,[3] then proceeded to show that this radiation was ideal for diffraction studies, thus conducting the first X-ray diffraction (XRD) experiment. The ability of this radiation to interact with atoms so as to give an indication of the structure of solids was further developed by William Bragg and his son William Lawrence Bragg through the derivation of Bragg's law in the same year (described in Section 2.1.4), for which they received the Nobel Prize in 1915.

2.2.2 X-ray Generation[10]

X-rays are generated when electrons strike a material. Upon impact, the electrons are slowed down or stopped by the target material, and some of the kinetic energy lost is converted into electromagnetic radiation. This radiation has a wide range of wavelengths and is commonly referred to as white radiation, or Bremsstrahlung. The lowest possible wavelengths for which radiation can be emitted are those that correspond to the highest energy X-rays.

Monochromatic radiation is preferred for XRD experiments. This radiation is generated when a metal target is bombarded with electrons of a particular energy. The electrons possess sufficient energy to ionise and excite an electron in the metal. An electron from a different shell will then replace the

excited electron in that shell. This loss in energy when going from a higher energy outer shell to a lower energy inner shell is converted into X-ray radiation. An example is the ionisation of copper, a common metal target in diffraction experiments. A *1s* electron (in the K shell) can become excited and then either a *2p* or *3p* electron can replace it. These transitions are labelled K_α and K_β, respectively. The K_α transition can be separated into $K_{\alpha 1}$ and $K_{\alpha 2}$ as the *2p* electron can have two possible spin orientations, up or down. These transitions are seen as spikes in the emission spectrum of the metal, Figure 2.4. Each metal has its unique emission spectrum and thus the different metal targets each have a unique X-ray spectrum with specific wavelengths corresponding to particular K transitions, Table 2.3.

A diffraction experiment requires three essential elements: the radiation source (the aforementioned metal target), the sample, and a detector.

The most frequently encountered detector type in XRD experiments at the moment is the charge-coupled device or CCD detector. This detector consists of a semi-conductor that is induced to produce electron-hole pairs when struck by radiation. The electrons are trapped in potential energy wells and are registered as a current.

Table 2.3: Selected X-ray wavelengths in Ångstrom (Å) of some common target metals[1]

Target metal	$K_{\alpha 1}$	$K_{\alpha 2}$
Iron, Fe	1.9360	1.9399
Copper, Cu	1.5405	1.5443
Molybdenum, Mo	0.7093	0.7135
Silver, Ag	0.5594	0.5638

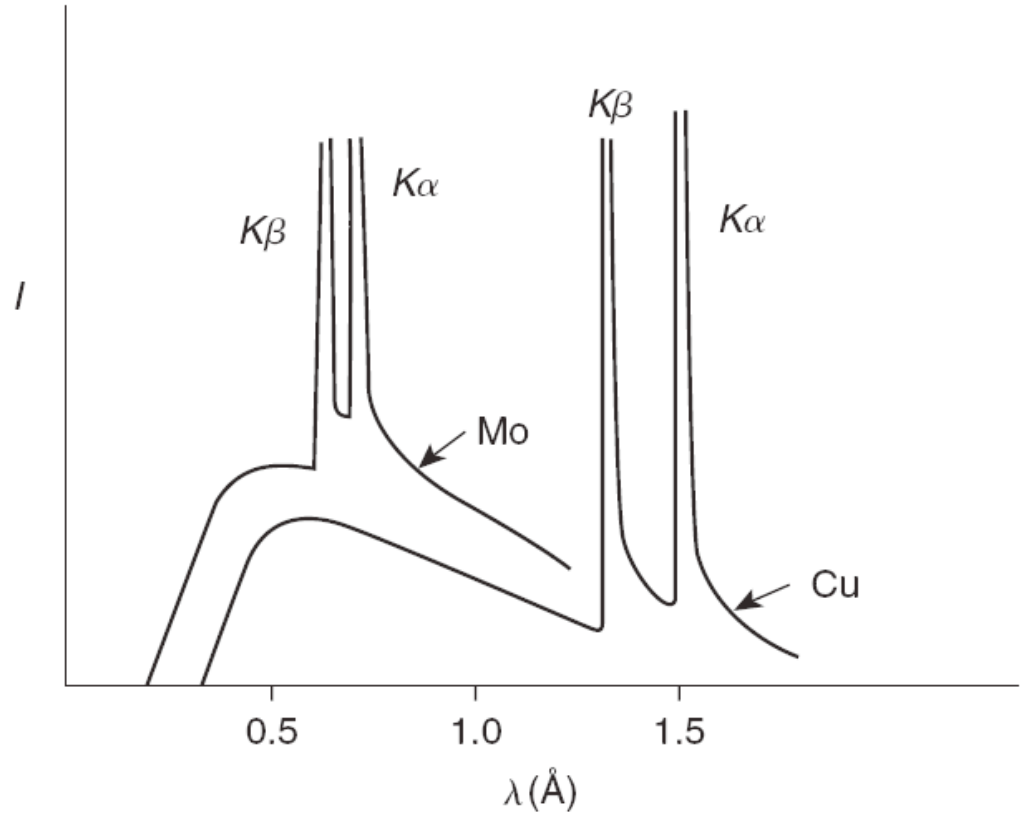

Figure 2.4: Parts of the emission spectra of copper and molybdenum[11]

2.2.3 X-ray Diffraction[1, 3, 12]

The intensity of the diffracted beam is dependent upon the electron density in each of the Miller planes. Each atom scatters a different amount of X-rays. This relationship is given in the scattering factor, f_n, for each atom n. The electron density is a measurement of the density over the complete crystal, i.e. it is a factor that gives information on the entire structure, not merely a particular point. For the centrosymmetric case, the electron density at any point xyz, ρ(xyz), in the crystal is given by

$$\rho(xyz) = \frac{1}{V}\sum F_{hkl} \cos 2\pi(hx + ky + lz) \qquad (2.2)$$

The structure factor, F_{hkl}, for a particular Miller plane hkl is directly related to the intensity, I_{hkl}, of the associated hkl Miller plane as follows

$$I_{hkl} \propto (F_{hkl})^2 \tag{2.3}$$

By applying a Fourier transform to equation 2.2 one obtains the equation to solve for the structure factor

$$F_{hkl} = \sum f_n \cos 2\pi(hx + ky + lz) \tag{2.4}$$

2.2.4 Single Crystal X-Ray Diffraction Techniques[12-15]

In SCXRD experiments, a single crystal is mounted in the path of the incident X-ray beam. Under ideal circumstances the single crystal consists of an infinite array of uniform unit cells. This, in turn, leads to all Miller planes being aligned in the same manner within the crystal. Each unique set of Miller planes will diffract the incident beam in a different direction in three-dimensional space. By rotating the crystal and obtaining as many unique reflections as possible, a three-dimensional model of reciprocal space is obtained. The large number of reflections, many of which are degenerate, enable fast indexing of the unit cell.

2.2.4.1 Structure Solution by Direct Methods[12-14, 16]

Direct methods are types of structure determination that ideally lead from the measured X-ray data directly to the full solution of the structure in simple and logical steps.[13]

Diffraction is essentially the measurement of the interference of a beam; the emergent, or diffracted, beams each have a unique phase and amplitude. The amplitude is easily measured as the number of counts, or the intensity, at the detector. The phase, on the other hand, is practically unmeasurable. It is this phase that is assigned using direct methods solutions.

The Fourier transform of the diffraction pattern is the electron density map. The electron density can only be positive or zero. Thus all negative phases from the diffraction pattern are essentially 'lost'. By using various

statistical models that relate the relationships of the diffracted phase to the electron density map, one can find a set of phases that give the best fit to the experimental data.

2.2.4.2 Structure Refinement by Least-Squares Fitting[15, 17, 18]

The positions of the atoms generated by direct methods solutions are not necessarily the actual positions of the atoms within the unit cell. In addition, it is quite common that not all of the atoms have been located by the solution. This is particularly true of lighter atoms such as hydrogen. It is thus important to refine the initial solution to give a new electron density map that is a better reflection of the observed reflections. From this new map further atoms, if there are any, can be located.

A least-squares refinement compares the observed intensities, F_o, in the diffraction pattern with the calculated intensities, F_c. That is to say, the refinement attempts to find a minimum, M, using the equation

$$M = \sum w(F_o^2 - F_c^2)^2 \tag{2.5}$$

where w is a weighting factor and is defined by equation 2.6 in the SHELXL-97 structure solution program used during the course of this work.[19]

$$w = \frac{1}{\sigma^2(F_o^2) + (aP)^2 + bP} \tag{2.6}$$

P is a summation used to reduce the bias, $\sigma^2(F_o^2)$ is the standard uncertainty of the intensity, and a and b are adjustable parameters that aim to keep the fit to an optimum by maintaining the goodness of fit, GOF or S,

$$GOF = S = \left\{ \frac{\sum [w(F_o^2 - F_c^2)]^2}{n - p} \right\}^{1/2} \tag{2.7}$$

where n is the number of reflections observed and p is the total number of parameters that are being refined, as close to 1.0 as possible.

2.2.4.3 Experimental Aspects of Structure Determination

A Rigaku SCX Mini diffractometer and a Rigaku Mercury CCD diffractometer were used to collect all SCXRD data. All diffractometers are fitted with area detectors allowing faster data collection times via the collection of multiple diffraction spots in a single image. The Rigaku SCX Mini diffractometer collects images twice to remove any spurious peaks that may appear due to cosmic radiation. The data are analysed by direct methods[16] and refined using SHELXL-97.[19]

2.2.5 Powder X-Ray Diffraction Techniques[1, 3, 20]

In a polycrystalline powder sample, there are millions of tiny crystallites and each of these diffracts the incident beam at a slightly different angle as one assumes that all of the crystallites are randomly orientated. The consequence of this is that instead of generating just one spot on the detector, there are many spots, and they are all closely spaced leading to diffraction rings rather than spots. Essentially, each crystallite diffracts the beam in a slightly different direction, which gives rise to diffraction cones that are registered as rings at the detector. The angle between the incident and diffracted beam is 2θ, where θ is the Bragg angle.

As a consequence of this diffraction smearing, PXRD experiments are conducted in a different manner to SCXRD experiments. In a SCXRD experiment, the sample is rotated in the X-ray beam and the diffracted beam collected at a fixed detector. In a PXRD experiment, the sample is stationary and the detector is moved through space measuring the 2θ angle mentioned above. The result is a plot of the intensity versus 2θ.

The powder pattern obtained is unique for each compound, and can thus be used as a form of identification.

2.2.5.1 The Rietveld Analysis Method[20-22]

The output of a PXRD experiment is a plot of intensity versus 2θ. Peaks in the data are indexed to particular hkl planes. It is common to have several of these planes occurring at similar 2θ values, leading to peak overlap. This is one factor complicating the analysis of powder patterns.

The Rietveld method was developed by Hugo Rietveld and first used in 1966.[21] The Rietveld method is a method of analysis that attempts to fit a calculated model to the experimental data. Subsequently, least-squares refinements are performed to minimize the difference between the two, S_y.

$$S_y = \sum_i \frac{1}{y_i}(y_{oi} - y_{ci})^2 \tag{2.8}$$

where y_{oi} is the observed intensity at the i^{th} step, and y_{ci} is the calculated intensity at the i^{th} step. The inverse of y_i is used to prevent any peak of larger intensity from dominating the calculation.

Unlike in a SCXRD solution where no model is required as a starting point, the Rietveld method requires a basic model with the unit cell parameters, space group, and approximate atomic coordinates. This model is then refined in subsequent steps.

There are several key factors that affect a powder pattern: the peak positions depend on the unit cell parameters; the peak intensities depend on the atomic number, atomic positions and the atomic displacement parameters of each atom; and the peak shape depends on the crystallinity of the sample, as well as the degree of disorder, strain, and size of the particles, and any possible crystal defects.

The R-factor is used as a measure of how well the calculated and observed patterns agree. It is denoted by R_p, and is given by

$$R_p = \frac{\sum_i |y_{oi} - y_{ci}|}{\sum_i y_{oi}} \tag{2.9}$$

This is a fair approximation but the strength of Rietveld analysis lies in its ability to shape the profiles of the models by analysing each peak in a weighted manner so that all peaks give an equal contribution to the R-factor and this is better reflected in the weighted R-factor, wR_p,

$$wR_p = \left[\frac{\sum_i \frac{1}{y_i} \left(y_{oi} - y_{ci} \right)}{\sum_i \frac{1}{y_i} (y_{oi})^2} \right]^{\frac{1}{2}} \tag{2.10}$$

The final parameter that is used to estimate the quality of the fit is the χ^2 value. It gives a goodness of fit

$$\chi^2 = \frac{\sum_i \frac{1}{y_i} \left(y_{oi} - y_{ci} \right)^2}{N - P + C} \tag{2.11}$$

where N denotes the number of observations, P is the number of refined parameters, and C is the number of constraints. χ^2 is equivalent to the goodness of fit, GOF, in SCXRD refinements. An ideal value is close to 1.0.

2.2.5.2 Experimental Aspects of Structure Determination

X-ray powder diffraction data were collected in house on a Stoe diffractometer with Ge monochromated Cu $K_{\alpha 1}$ radiation (λ = 1.5406 Å).[23] Prior to analysis, each sample was ground into a fine powder and mounted on Mylar discs. The sample was then examined in transmission geometry. Theoretical powder patterns were simulated using the Stoe WinXPow software.

Occasionally, X-ray powder diffraction data were collected on a PANalytical X'Pert Pro diffractometer (Le Mans) with Ge(111) monochromated Cu $K_{\alpha 1}$ radiation (λ = 1.5406 Å).[23] In this case, the sample was examined in Bragg–Brentano reflection geometry (θ-2θ). Theoretical powder patterns were simulated using the PANalytical X'Pert Highscore Plus software.

All data were analysed using the General Structure Analysis System (GSAS) software package.[24]

2.2.6 Synchrotron Powder X-Ray Diffraction[25]

In a synchrotron electrons are emitted and accelerated close to the speed of light in a linear accelerator, or linac. These electrons are then bent using magnets so that they can circulate around a booster synchrotron. In this synchrotron, the electrons are accelerated so that they reach a particular energy. Once attained, they are injected into the storage ring. As the electron beam passes around the storage ring, it is bent by magnets and in the process of doing so very intense electromagnetic radiation is generated, known as synchrotron light. This light spans the X-ray, ultraviolet, and infrared regions of the electromagnetic spectrum.

Some of this synchrotron light is then split from the storage ring and sent to the experimental beamlines, experimental chambers that channel and filter the light to suit the particular experimental conditions for each beamline. A schematic of a synchrotron is given in Figure 2.5.

2.2.6.1 Synchrotron X-ray Diffraction Data Collection

The beamline used for all high-resolution X-ray powder diffraction experiments is I11 at the Diamond Light Source Synchrotron, Figure 2.5.[26] This is a high–resolution powder diffractometer. Variable temperature studies were performed between 90 K and 500 K. All measurements from 100 K to 500 K (excluding room temperature experiments) were completed using an Oxford Cryostream Plus cryostat.

All samples were filled into 0.5 mm diameter borosilicate capillaries and mounted on brass capillary spinners. These were in turn mounted on magnetic bases that could be attached to the diffractometer.

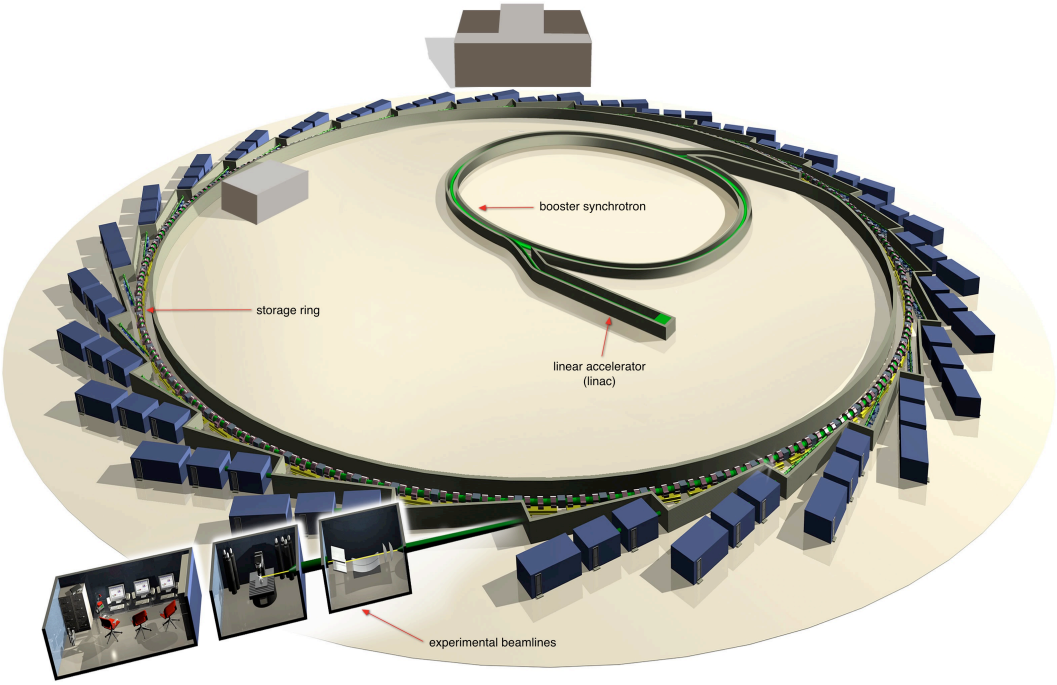

Figure 2.5: Schematic of a synchrotron[27]

All data were collected from 0° to 145° using five multi-analysing crystal detectors, known as MACs. Each of these detectors consists of nine silicon (111) analysing crystals and nine detectors. All data were analysed between 5° and 80° or 90° in 2θ, depending on the sample. Refinements were performed using the GSAS software package.[24]

2.2.7 Comparison of Diffraction Techniques

SCXRD and PXRD are complementary techniques that give a detailed structural understanding of a compound.

SCXRD techniques generate a three-dimensional pattern of reciprocal space and this allows for accurate placement of the atoms and their atomic displacement parameters within the structure. Absolute configurations, stereochemistry, coordination environments, and non-bonded interactions can all readily be obtained. Furthermore, the placement of hydrogen atoms can also be achieved, if the electron density map is of sufficient resolution.

In contrast, PXRD techniques do not have the above-mentioned properties as their strengths. The strength of this method lies in its ability to give a far more accurate determination of the unit cell parameters. Furthermore, PXRD experiments can give a more accurate picture of the overall composition of a sample: the entire sample is studied at once, rather than a single, and possibly unrepresentative, crystal. Thus phase separations, impurities, and degradation products can be studied.

2.3 Preferred Orientation

Under ideal circumstances, a powdered or polycrystalline sample will have all particles in a random orientation. This is not always the case. Some samples, by virtue of their anisotropy, are predisposed to align along a particular direction, Figure 2.6. This is very common for samples that consist of crystallites in the form of platelets or fibres. In these samples, no matter how finely the sample is ground, the anisotropy will remain.

This leads the Miller planes along one direction diffracting more of the incident radiation than other Miller planes. The consequence of this is that the corresponding hkl peaks in the powder pattern will be more intense than they should be and the peaks that are particularly underrepresented are of a far weaker intensity than expected.

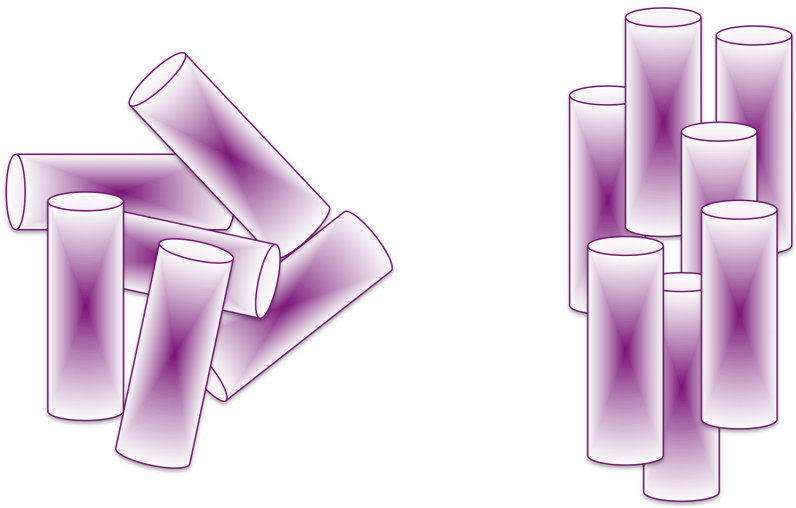

Figure 2.6: A randomly orientated sample on the left and a sample showing preferred orientation on the right

2.3.1 Preferred Orientation Correction[28, 29]

In order to analyse the powder XRD data and obtain a more accurate description of the peak intensities, a correction must be introduced for the Miller planes that are being over- or under-represented in the diffraction pattern.

The first step is to assign a set of Cartesian coordinates to all of the possible crystallite orientations. Several of these orientations may be degenerate due to the crystal symmetry.

Each of the non-degenerate orientations is then assigned a set of Euler angles θ, ψ, and ϕ. The first two define the rotation of the crystallite's z-axis, whilst the latter defines the rotation about the z-axis.[28] These angles define the orientation of the crystallite within a sphere. The angles are measured relative to a standard or normal direction and then all crystallites are defined relative to it. For example, if the (100) hkl plane is set as the normal plane, then all (100) directions for the remaining crystallites are measured relative to this defined direction. Each of the directions for the remaining crystallites is called a pole. Each orientation g can therefore be represented by a pole figure, which is a contour plot of the poles, Figure 2.7.

The volume fraction of all crystallites that have orientation g is then given by the orientation distribution function (ODF) described by

$$ODF(g) = \frac{1}{V}\frac{dV(g)}{dg} \tag{2.12}$$

where V is the volume of the sample, and dV(g) is the volume of all the crystallites with orientation g in the area dg.

Although the ODF looks deceptively easy to calculate from experimental data, this is not the case. The ODF can only be calculated from the difference between the observed intensity Y_o and the calculated intensity, Y_c.

$$Y_c = Y_b + \sum_h SKF_h^2 P(\Delta T_h) \tag{2.13}$$

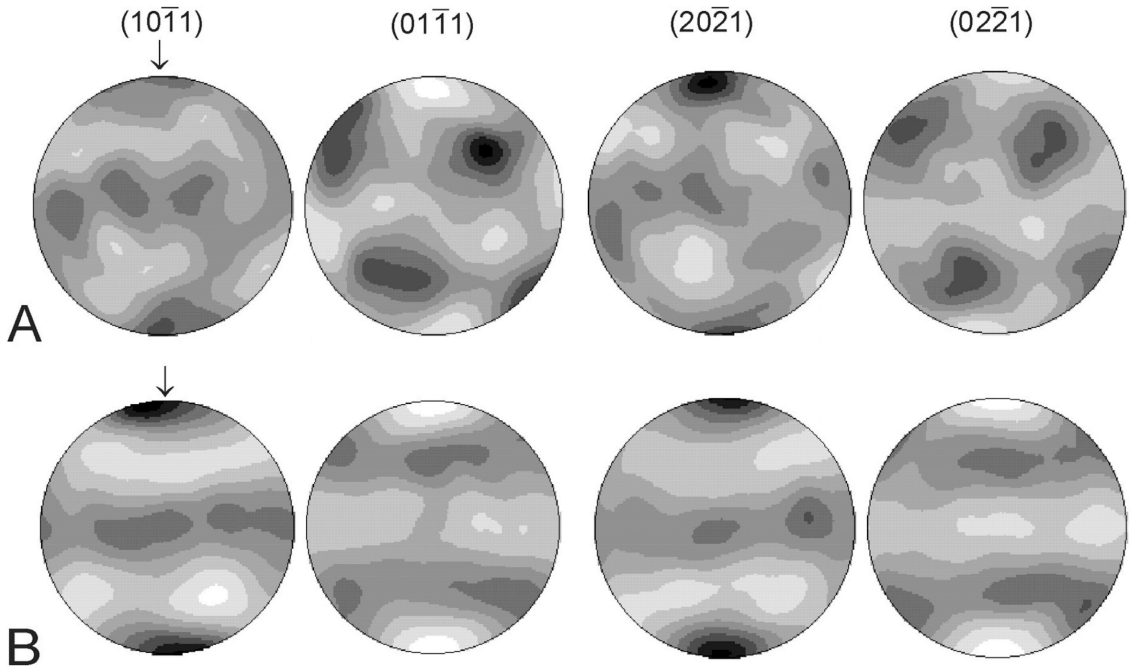

Figure 2.7: Pole figures for rhombohedral lattice planes of quartz, recalculated from orientation distribution.
(Figure taken from H.-R. Wenk et al., Geology, *2005, **33**, page 275, Figure 4)*[30]

Y_b is the intensity contribution from the background and the summation is the contribution from the diffracted beam.[29] The Bragg intensity of each of the diffracted beams is composed of the structure factor F_h^2 which has been modified by some scale factor, S, a product of several correction factors, K, and the profile function $P(\Delta T_h)$, which is determined by the displacement ΔT_h, of the profile point from the reflection position. The correction factor K consists of several factors, but one of these is of particular interest when performing spherical harmonics corrections. The term in question, A(h,g), is a general description of the texture, or preferred orientation, of the sample, and is given in equation 2.14. It describes the preferred orientation of the sample at the orientation ***g***.

$$A(h,g) = 1 + \sum_{l=2}^{L} \frac{4\pi}{2l+1} \sum_{m=-l}^{l} \sum_{n=-l}^{l} C_l^{mn} k_l^m(h) k_l^n(g) \qquad (2.14)$$

C_l^{mn} is a coefficient, and $k_l^m(h)$ and $k_l^n(g)$ are the harmonic terms. They relate to the crystal and sample symmetries respectively.[29] This indicates that the two inner sums only work for even numbers of l as all other contributions are zero.

Equation 2.14 is similar to a Taylor series and thus, in order to obtain the most accurate solution, the more terms used, the better. Hence, under ideal circumstances, one would let L, the upper limit of the first summation term, tend to infinity to obtain the most accurate result, but this is computationally unrealistic.

The sum is truncated to anywhere between 2 and 34 terms in the GSAS software package.[29] This contribution is the factor that is optimised to give the best fit for equation 2.13. This type of preferred orientation correction is referred to as a spherical harmonic correction (SHC).

2.4 Bond Valence Sums[31, 32]

The bond valence method, also referred to as the bond valence sum method (BVS), is a method of analysis used in coordination chemistry to determine the oxidation states of the anions and cations in a material.[32]

It is based on the assumption that the measure of the strength of a bond is related to its length and the oxidation state of the metal involved. The method assumes that the bond lengths around each metal ion are an indication of the oxidation state of that ion. So the total bond valence, V_i, of an atom i can be calculated by determining the individual bond valences, v_{ij}, of each contributing bond to i from the remaining atoms j, as follows

$$\sum_j v_{ij} = V_i \tag{2.15}$$

The individual valence contributions, v_{ij}, are calculated by looking at the bond length, d_{ij}, and finding its variation from the ideal reference value, R_{ij}, as shown in the equation

$$v_{ij} = \exp\left[\frac{(R_{ij} - d_{ij})}{b}\right] \tag{2.16}$$

b is a constant that is generally set to 0.37.[31] The reference bond length values of R_{ij} are usually calculated from the ionic radii presented in the work done by Shannon.[33]

2.5 Preparative Methods

Two main preparative methods are used in the course of this thesis: solid state methods and hydrothermal methods. A brief introduction to both follows in this section.

2.5.1 The Solid State Reaction Method[34]

A solid state reaction is defined as a reaction in which the solid starting materials are mixed and directly reacted without the addition of a solvent, or melting of the starting materials. In all but a few cases this requires high temperatures, in excess of 500 °C for fluorides. The reaction proceeds slowly and so the reaction time is usually longer than for a "wet" reaction.

These reactions are slow because they require that ions move across grain boundaries to interact with the other starting materials. Due to the lack of any available reaction medium, the ions must move from their starting material to the neighbouring material to form the new compound. This initially leads to a fast reaction on the surfaces but as the ions must move from further within the material to the reaction surface, the rate of reactions slows down. A further problem is that one of the reactants may react faster and thus there is a faster formation of the product on that particle. This again hinders the rate of reaction. A schematic of this reaction scheme is given in Figure 2.8.

This immediately provides one important point for any solid state reaction: the surface area or grain size. The finer the sample, the larger the surface area and thus the faster the rate of reaction is found to be. It is therefore imperative that the sample is well ground and mixed so that as many different surfaces touch as possible.

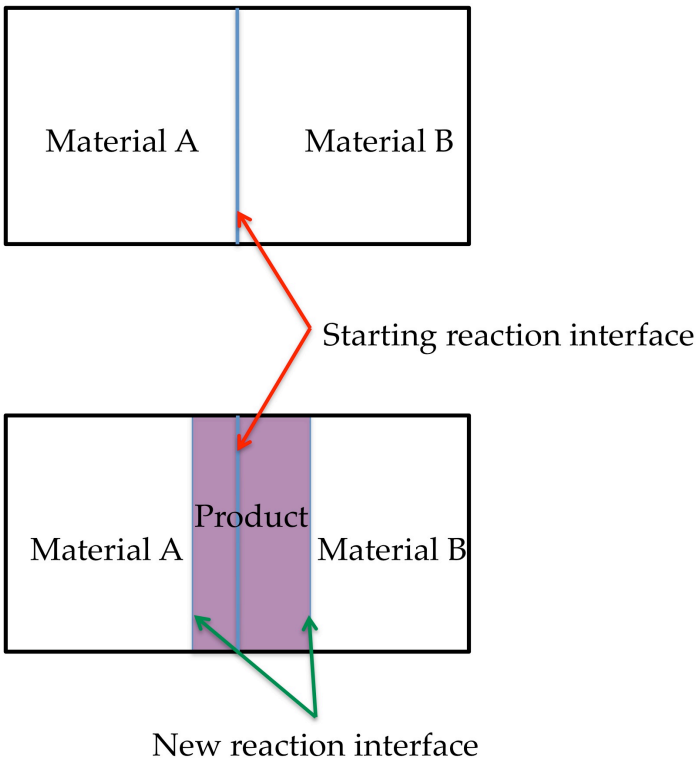

Figure 2.8: Reaction interface for a solid state reaction[32]

2.5.1.1 Solid State Reaction Experiments

All starting materials in this work are moisture and air sensitive, so they are handled in a glove box. The starting materials are weighed out and combined in the glove box. Whilst still handling the materials in the glove box, they are then sealed in a gold tube, Figure 2.9, to avoid unwanted reactions with the reaction vessel and the surrounding atmosphere. This is because the starting materials readily react with air, water, and surfaces that are not noble metals. The sealed gold tube is then placed in the furnace and the reaction done under a positive argon flow to ensure no oxygen enters the system.

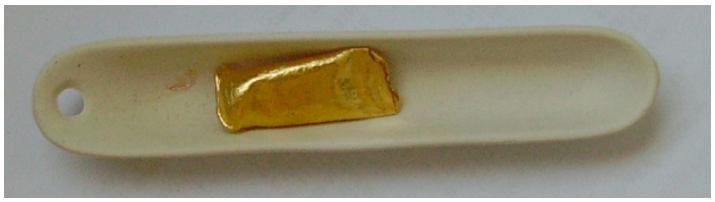

Figure 2.9: Gold tube used for solid state reactions involving fluoride starting materials

2.5.2 The Hydrothermal Method[34]

The hydrothermal method refers to reactions that are performed in a sealed vessel, referred to as an autoclave, and at temperatures exceeding the boiling point of the solvent system used. This leads to a strong increase in pressure above ambient and this high pressure adds to, and frequently drives, the reaction mechanism leading to the formation of new materials.

The high pressures enable reactions to occur at much lower temperatures than if the same reaction were performed at ambient pressure. This means that many new materials and otherwise inaccessible phases of materials can be made because the starting materials remain stable and do not decompose at these comparatively low reaction temperatures, which they would otherwise do if attempting to make the desired materials under other conditions. Most of these reactions are performed between 100 °C and 200 °C, although it is possible to perform reactions at much higher temperatures if the suitable equipment is available.

A further advantage of using hydrothermal methods is that many of the materials synthesised can be crystallised during the reaction and this makes phase and structure identification easier. The fact that the materials are in solution also increases the rate of reaction when compared to the solid state reactions and this means that this method is ideal for studies of phase diagrams for materials as several of these reactions can be done simultaneously and for short reaction times.

A more detailed historical overview of the hydrothermal method and its development is given in Chapter 5.

2.5.2.1 Hydrothermal Reaction Experiments

The reaction vessel used in hydrothermal reactions is called an autoclave. In this particular instance, the type used is referred to as a bomb autoclave, Figure 2.10. It consists of a stainless steel outer shell that has a Teflon

Figure 2.10: Bomb autoclave showing the stainless steel outer and Teflon inner containers

steel bomb, and the bomb is then sealed tightly so that all components are firmly locked in place. All reactions occur in the Teflon container, and its inert nature makes for a stable and desirable reaction vessel.

In all hydrothermal reactions performed for this thesis, metal salts were combined with other metal salts or organic templates in the presence of HF (acting as the fluoride ion source), and water was added as the solvent.

2.6 References

1. A. R. West, in *Solid State Chemistry and Its Applications*, Wiley, Chichester, 1984, Chapter 5.
2. W. Clegg, The 12th BCA/CCG Intensive Teaching School in X-Ray Structure Analysis, Chapter 2, Trevelyan College, University of Durham, 2009.
3. R. Jenkins, R. Snyder and Editors, *Introduction to X-Ray Powder Diffractometry*, Wiley, 1996.
4. A. R. West, in *Solid State Chemistry and Its Applications*, Wiley, Chichester, 1984, Chapter 6.

5. *International Tables for Crystallography, Volume A, Space-Group Symmetry*, Fourth, Published for the International Union of Crystallography by D. Reidel Pub. Co., Dordrecht, Holland ; Boston, U.S.A. :, 1995.
6. W. Clegg, The 12th BCA/CCG Intensive Teaching School in X-Ray Structure Analysis, Chapter 4, Trevelyan College, University of Durham, 2009.
7. W. H. Bragg and W. L. Bragg, *The Crystalline State*, G. Bell, London,, 1933.
8. W. H. Bragg, *Nature (London, U. K.)*, 1912, **90**, 410.
9. A. D. Bond, The 12th BCA/CCG Intensive Teaching School in X-Ray Structure Analysis, Chapter 5, Trevelyan College, University of Durham, 2009.
10. U. Shmueli and International Union of Crystallography., *Theories and Techniques of Crystal Structure Determination*, Oxford University Press, Oxford, 2007.
11. U. Shmueli, in *International Union of Crystallography - 9*, Oxford University Press, Oxford, Editon edn., 2007, p. 92.
12. D. Watkin, The 12th BCA/CCG Intensive Teaching School in X-Ray Structure Analysis, Chapter 1, Trevelyan College, University of Durham, 2009.
13. P. Main, The 12th BCA/CCG Intensive Teaching School in X-Ray Structure Analysis, Chapter 10, Trevelyan College, University of Durham, 2009.
14. W. Clegg, *Crystal Structure Determination*, Oxford University Press, Oxford ; New York, 1998.
15. P. Müller, *Crystal Structure Refinement : a Crystallographer's Guide to SHELXL*, Oxford University Press, Oxford ; New York, 2006.
16. G. M. Sheldrick, *Acta Crystallogr., Sect. A: Fundam. Crystallogr.*, 1990, **46**, 467-473.
17. P. Main, The 12th BCA/CCG Intensive Teaching School in X-Ray Structure Analysis, Chapter 12, Trevelyan College, University of Durham, 2009.
18. D. Watkin, The 12th BCA/CCG Intensive Teaching School in X-Ray Structure Analysis, Chapter 13, Trevelyan College, University of Durham, 2009.

19. *SHELXS-97 - A Program for Automatic Solution of Crystal Structures*, G. M. Sheldrick, Version 97-2, 1997.
20. V. K. Pecharsky and P. Y. Zavalij, *Fundamentals of Powder Diffraction and Structural Characterization of Materials*, 2nd, Springer, New York, 2009.
21. R. A. Young, *The Rietveld method*, International Union of Crystallograhy ; Oxford University Press, Chester, England, 1993.
22. R. E. Dinnebier and S. J. L. Billinge, *Powder Diffraction : Theory and Practice*, Royal Society of Chemistry, Cambridge, 2008.
23. A. R. West, in *Solid State Chemistry and Its Applications*, Wiley, Chichester, 1984, Chapter 3.
24. *General Structure Analysis System GSAS*, A. C. Larson and R. B. von Dreele, Report No. La-UR-86-748, 1987.
25. G. Margaritondo, *Elements of Synchrotron Light : for Biology, Chemistry, and Medical Research*, Oxford University Press, Oxford ; New York, 2002.
26. S. P. Thompson, J. E. Parker, J. Potter, T. P. Hill, A. Birt, T. M. Cobb, F. Yuan and C. C. Tang, *Rev. Sci. Instr.*, 2009, **80**, 075107-075109.
27. Diamond Light Source 2011 Ltd, *About Diamond - Diamond at a glance*, http://diamond.ac.uk/Home/About/Facts.html, Accessed 05/05/2011, 2011.
28. R.-J. Roe, *J. Appl. Phys.*, 1965, **36**, 2024-2031.
29. R. Von Dreele, *J. Appl. Crystallogr.*, 1997, **30**, 517-525.
30. H.-R. Wenk, I. Lonardelli, S. C. Vogel and J. Tullis, *Geology*, 2005, **33**, 273-276.
31. N. E. Brese and M. O'Keeffe, *Acta Crystallogr., Sect. B: Struct. Sci.*, 1991, **47**, 192-197.
32. A. R. West, in *Solid State Chemistry and Its Applications*, Wiley, Chichester, 1984, Chapter 8.
33. R. Shannon, *Acta Crystallogr., Sect. A: Fundam. Crystallogr.*, 1976, **32**, 751-767.
34. A. R. West, in *Solid State Chemistry and Its Applications*, Wiley, Chichester, 1984, Chapter 2.

Chapter 3

The Phase Separations and Phase Transitions of Selected Tetragonal Tungsten Bronze-Type Fluorides

3.1 Introduction to Tetragonal Tungsten Bronze Compounds

Tetragonal tungsten bronzes (TTB) have been defined and described in Chapter 1.

Most TTBs are oxide-based, and much work has been done on these compounds as many of them possess ferroelectric, piezoelectric, pyroelectric or ferromagnetic properties. This prevalence of oxide analogues is mainly due to the originally synthesised compounds for the tungsten bronzes being oxides and furthermore, the starting materials are readily available and stable. The first of these to be studied in detail were solid solutions of barium strontium niobate, $Ba_{1-x}Sr_xNb_2O_6$,[1, 2] and barium sodium niobate, $Ba_{4+x}Na_{2-2x}Nb_{10}O_{30}$.[3]

Many TTBs have been shown to be ferroelectric.[2, 4, 5] Most of these compounds undergo a transition from a ferroelectric phase to a paraelectric one by going from the noncentrosymmetric *4mm* point group to the centrosymmetric *4/mmm* one.[6] With many of these materials there is also a ferroelastic to paraelastic transition, albeit it in a transition from one crystal class to another, as is the case for $K_3Fe_5F_{15}$, where the sample changes from *4/mmm* to *mm2*.[7]

Ferroelectric materials can be separated into two distinct groups: displacive ferroelectrics and order-disorder ferroelectrics. An example of a displacive ferroelectric is $Ba_2KNb_5O_{15}$, where the ferroelectricity arises from a displacement of the M cation (in this case Nb^{5+}) from the ideal octahedron. A special case of an order-disorder ferroelectric may occur when there is localised charge ordering of some M cations. An example of this type is $K_3Fe_5F_{15}$, where the Fe^{2+} and Fe^{3+} cations can selectively order below T_C.[7] This compound is a rare example of a fluoride-based TTB.

3.2 Solid Solutions of K_xFeF_3

Solid solutions of K_xFeF_3 were first reported by de Pape in 1965.[8] He found there to be three distinct phases in the region $0 < x < 1$. For values of x below 0.18, the structure is that of the hexagonal tungsten bronze (HTB) type with some residual FeF_3 starting material. This changes to the pure HTB for $0.18 \leq x \leq 0.25$. The phase then changes to that of the TTB in addition to the HTB for $0.25 < x < 0.40$. For the interval $0.40 \leq x \leq 0.60$, only the TTB is observed. For $0.60 < x < 0.95$, the TTB coexists with a perovskite phase that is isostructural to $KFeF_3$. Above $x = 0.95$ only this phase is observed. Only the TTB phase will be focused upon in this chapter. In the TTB phase, the Fe^{2+} and Fe^{3+} cations are found to be disordered in the $[MF_6]$ octahedra that make up the framework of the structure. The K^+ cations occupy positions in the square and pentagonal tunnels. All pentagonal tunnels are occupied, but the occupancy of the square tunnels is what defines the limits of the solid solution, Figure 3.1. In each unit cell, there are four K^+ cations that occupy the pentagonal tunnels, whilst there can be anything from zero to two K^+ cations in the square tunnels.

$K_{0.6}FeF_3$, or $K_3Fe_5F_{15}$ (Figure 3.1), is a reported multiferroic.[7] It is both ferromagnetic and ferroelastic. It was first reported to crystallise in the tetragonal space group *P4/mbm* with $a = 12.73(1)$ Å and $c = 3.996(4)$ Å.[8] It was thereafter reported by Hardy *et al.*[9] that the compound crystallises in the orthorhombic distortion of the TTB with $a = 12.750(2)$ Å, $b = 12.637(2)$ Å, and $c = 3.986(2)$ Å in *Pba2*. The most likely cause for the distortion was that the Fe sites became charge-ordered, thus leading the different sites for the $[FeF_6]$ octahedra and therefore *a* and *b* were of different lengths. Figure 3.2 shows this orthorhombic cell. This led to the prediction that the compound is ferroelectric as the space group is polar.[10] This was further supported when the dielectric permittivity was analysed and found to have a characteristic ferroelectric-paraelectric phase transition.[7, 11] The compound's T_C is 490 K.[7] Below this temperature the material is both ferroelectric and ferroelastic. A weak ferromagnetic transition occurs at a T_C of approximately 122 K.[12] This ferromagnetic transition is a very common property of TTBs as the low temperature structures are predisposed to be magnetically frustrated.[13]

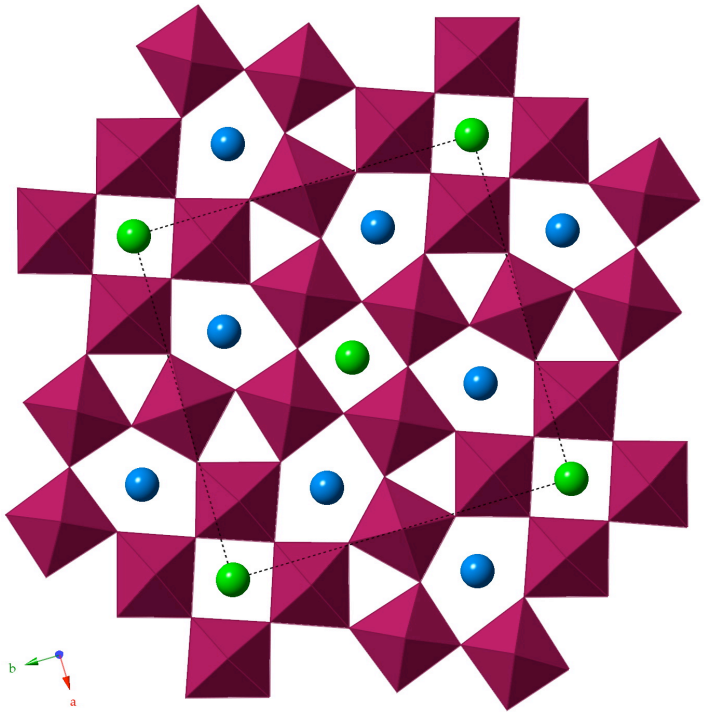

Figure 3.1: TTB structure of K_xFeF_3 viewed along the c-axis showing the two K^+ sites (blue and green), with the occupancy of the green cations in the square tunnels defining the value of x

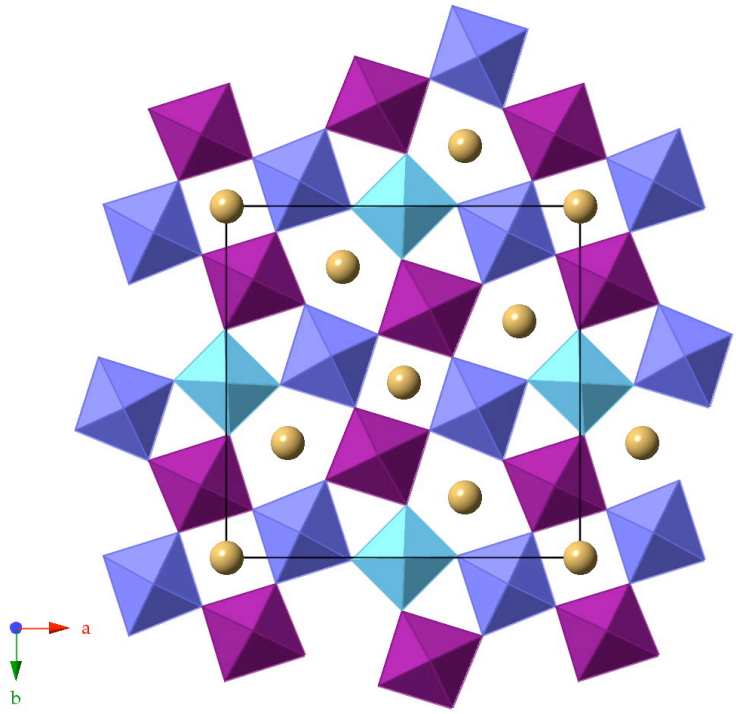

Figure 3.2: Orthorhombic distortion of the TTB structure of K_xFeF_3 viewed along the c-axis showing the three iron sites, with the charge-ordering of these sites leading to different bond lengths for the octahedra

In a subsequent study by Ishihara *et al.* polarised light microscopy on single crystals of the compound indicated that there was an orthorhombic to monoclinic transition at approximately 290 K.[14]

In the last few years, there has been a renewed interest in fluoride-based multiferroics[15, 16] and several new investigations of the K_xFeF_3 system have been reported, although the emphasis of this resurgence has been focused on $K_{0.6}FeF_3$.[12, 17-19]

Fabbrici *et al*.[17] have used transmission electron microscopy (TEM) and single crystal data to postulate a set of possible phases for samples of $K_{0.525}FeF_3$. These include the non-centrosymmetric *P4bm* model, the ferroelectric structure (FES) model in *Bbm2*, and the charge-ordered structure (COS) model in $P4_2bc$. A summary of these is given in Table 3.1. Both the FES and COS structures are based on the observation of satellite reflections in the TEM pattern of the standard TTB model. The COS supercell is attributed to the ordering of the Fe^{2+} and Fe^{3+} cations in layers along the *c*-axis and this leads to adjacent layers becoming non-equivalent. This non-equivalence is directly proportional to the K^+ content of the sample as this defines the Fe^{2+}/Fe^{3+} ratio. The authors report this phase in a non-centrosymmetric space group as they assume that the compound is ferroelectric. The FES structure is based upon that reported for $Ba_2NaNb_5O_{15}$.[3] It relates the quasi-commensurate modulation along the $[110]_{TTB}$ direction to the doubling of the c axis parameter. The structure has the parameters $a \approx 2a_{TTB}\sqrt{2}$, $b \approx a_{TTB}\sqrt{2}$, and $c = 2c_{TTB}$.[17] This phase is determined to be commensurate for the fluoride TTBs. The $[FeF_6]$ octahedra tilt in a sinusoidal

Table 3.1: The proposed phases of $K_{0.525}FeF_3$ as given by Fabbrici et al.[17]

	Standard TTB model	FES model	COS model
Crystal system	Tetragonal	Orthorhombic	Tetragonal
Space group	*P4bm*	*Bbm2*	$P4_2bc$
Unit cell dimensions	a = 12.634(1) Å b = 12.634(1) Å c = 3.9515(3) Å	a = 35.730(3) Å b = 17.872(1) Å c = 7.9030(6) Å	a = 12.634(1) Å b = 12.634 (1) Å c = 7.9030(6) Å

wave-like manner leading to the octahedra tilting out of the ideal TTB plane and thus producing an elongation of both the *a* and *b* axes, and the iron atoms are displaced from the standard positions in the octahedra. In this structure there should be no charge ordering, although there is an apparent preference by the Fe^{2+} for the octahedra around the square tunnel sites. Fabbrici *et al.*[17] also indicate that these observations are a common trait of the K_xFeF_3 solid solution for $0.4 \leq x \leq 0.6$. This was not always observed in the analogues, where either some, or all, of the Fe^{2+} or Fe^{3+} was replaced by Mn^{2+} or In^{3+},[17, 20] indicating that this is a property of this particular solid solution only.

In a subsequent study by Mezzadri *et al.*,[18] the authors present further evidence of charge ordering in the orthorhombic distortion of the TTB model with Fe^{2+} and Fe^{3+} octahedra alternating along the *c* axis to minimise distortions. This however leads to a doubling of the *c* axis, giving a model in *Pba2* with *a* = 12.751(1) Å, *b* = 12.660(1) Å, and *c* = 7.975(1) Å. They also present temperature ranges over which the above structures will be observed. Between 0 K and 290 K, the FES structure is the prevalent superstructure; from 290 K to 490 K, the COS structure replaces the FES structure; and above 490 K, the orthorhombic TTB model is observed. They indicate that the tetragonal TTB model only appears at temperatures above 570 K.

Blinc and co-workers have also reported doped analogues of $K_{0.6}FeF_3$, where either Fe^{2+} has been replaced by Cu^{2+} to give $K_3Cu_3Fe_2F_{15}$,[21] or Fe^{3+} by Cr^{3+} to give $K_3Cr_2Fe_3F_{15}$.[22] The compound $K_3Cu_3Fe_2F_{15}$ is reported to be a standard TTB in *P4/mbm* with *a* = 12.5925 Å and *c* = 3.9406 Å.[21] There appears to be no preferred location for the Cu^{2+} ion in any particular octahedra and as a consequence there is no evidence of a Jahn-Teller distortion in any of the octahedra. The material shows antiferromagnetic behaviour below T_N = 85 K. The other compound reported, $K_3Cr_2Fe_3F_{15}$,[22] is also solved in *P4/mbm* with identical lattice parameter values for $K_3Cu_3Fe_2F_{15}$. Again, there seems to be no evidence that the $[CrF_6]$ octahedra have a preferred position within the structure. There is evidence of antiferromagnetic behaviour below 37 K, and a further transition, which is antiferromagnetic in character, at 17 K.

In this work, we present a variable temperature study of two solid solutions of K_xFeF_3 with $x \approx 0.6$ and $x \approx 0.5$. Synchrotron powder X-ray diffraction (sPXRD) experiments were performed at the Diamond Light Source

synchrotron between 500 K and 100 K. Scanning electron microscopy (SEM) images were collected to elucidate details regarding the morphology of the samples to explain certain observations made during the data refinement. Due to the difficulties in preparing sufficiently large samples, no neutron experiments are performed. The doped analogue, $K_3Cu_3Fe_2F_{15}$, is also studied over the 300 K to 100 K temperature range. Single crystal experiments at low temperature are also presented.

3.3 Experimental

3.3.1 Synthesis

Several attempts were made in house to synthesise the compounds in question. This was not possible, and so the samples used were synthesised by Dr Anne-Marie Mercier at the Université du Maine in Le Mans, France.

Samples of K_xFeF_3 with $x \approx 0.6$ and $x \approx 0.5$ were prepared by combining the KF, FeF_2, and FeF_3 in the ratios given below and placing them in a sealed Pt tube. The samples were weighed out and mixed in a glove box under a dry nitrogen atmosphere. The sealed tube was dehydrated and degassed at 120 °C overnight, and then heated to 710 °C for 48 hours.

The reaction mixture for the synthesis of $K_{0.6}FeF_3$ consists of 0.58 g KF, 0.60 g FeF_2, and 0.41 g FeF_3. The reaction mixture for the synthesis of $K_{0.5}FeF_3$ consists of 0.91 g KF, 1.00 g FeF_2, and 0.95 g FeF_3.

The $K_3Cu_3Fe_2F_{15}$ sample was provided by Professor Robert Blinc from the "Jožef Stefan" Institute, Ljubljana, Slovenia, although no further experimental details were given.

3.3.2 Synchrotron Powder X-ray Diffraction

Standard room temperature PXRD experiments were performed using a Stoe diffractometer (in house) with Ge monochromated Cu $K_{\alpha 1}$ radiation (λ = 1.54056 Å).[23] The high-resolution X-ray powder diffraction beamline I11 at the

Diamond Light Source Synchrotron (λ = 0.828698(2) Å for the $K_{0.6}FeF_3$ sample, and λ = 0.825558(2) Å for the $K_{0.5}FeF_3$ sample) was used for all variable temperature high-resolution X-ray powder diffraction experiments between 500 K and 100 K. All diffraction data were analysed and refined using the GSAS software package.[24] Parameters refined include the background coefficients, the detector zero point, instrumental parameters, lattice parameters, profile parameters, isotropic and anisotropic atomic displacement parameters, atomic occupancies, and atomic position parameters.

3.3.3 Scanning Electron Microscopy

The crystal morphology of the two K_xFeF_3 samples was investigated in house by scanning electron microscopy, SEM, using a Jeol JSM-600 microscope operating at 20 – 30 kV equipped with an Oxford INCA system for energy-dispersive X-ray spectroscopy, EDX.

3.4 Results and Discussion

All cifs and powder XRD data for all samples are located in Appendix B.

3.4.1 $K_{0.6}FeF_3$

The sample was initially investigated by standard PXRD. The refinement indicated the presence of some impurities, but they were not identifiable at that point. sPXRD data were then collected at room temperature and indicated the impurities to be K_2FeF_5 (*Pbcn*, a = 7.4059(4) Å, b = 12.8771(9) Å, c = 20.4282(13) Å) as reported by Le Bail *et al.*;[25] and α-Fe_2O_3 or hematite ($R\bar{3}ch$, a = 5.0346(3) Å, c = 13.7533(13) Å) as reported by Pailhe *et al.*[26]

Both the tetragonal $P4_2bc$ (Fabbrici)[17] and the orthorhombic *Pba2* (Mezzadri)[18] models could be fitted to the room temperature data. It was thus decided to fit both models to the data at 500 K, Figure 3.3 and Table 3.2, and

proceed through the entire temperature range down to 100 K to see if either of the models gave a better fit in a particular temperature range.

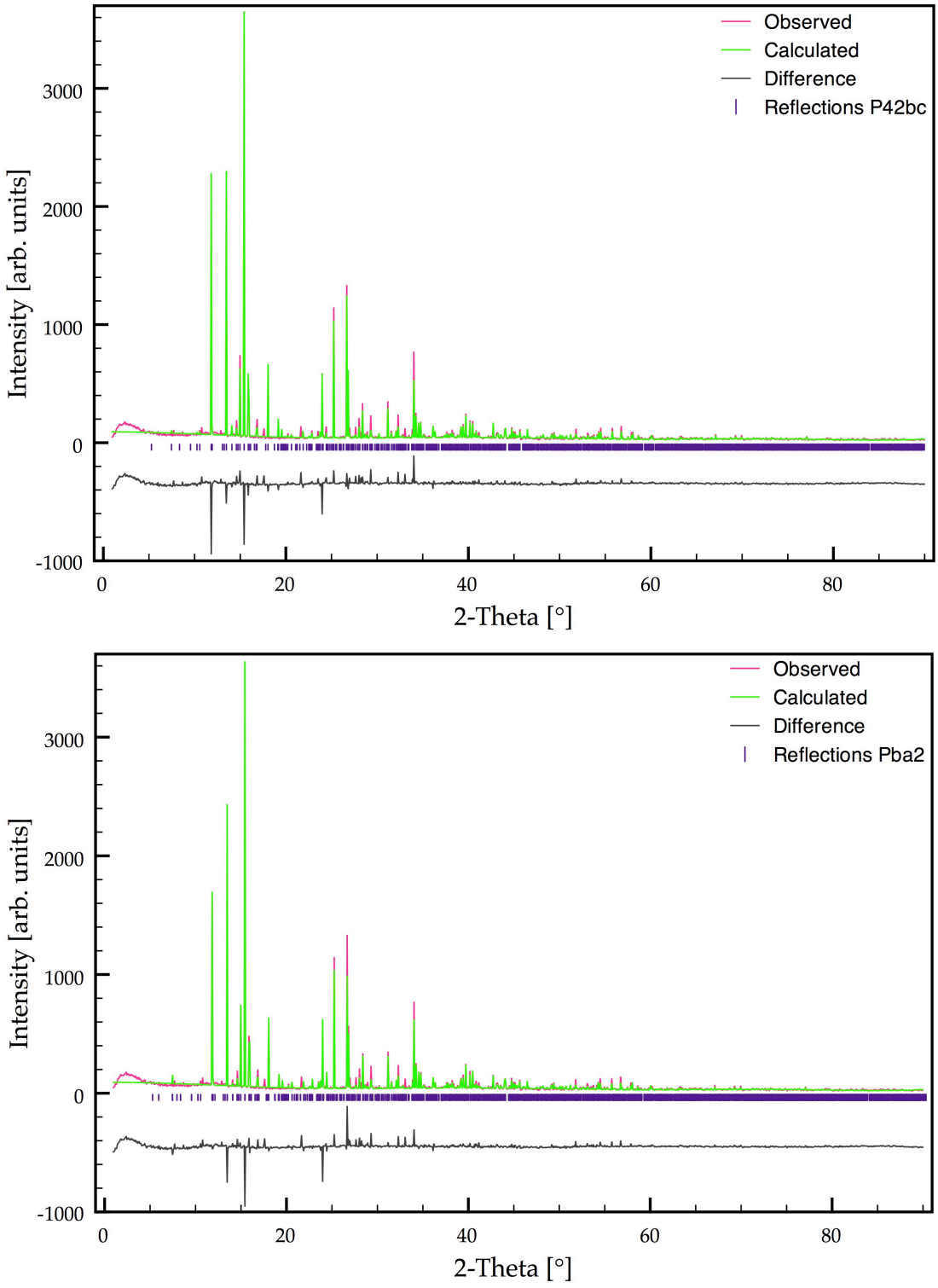

Figure 3.3: Single phase refinements of sPXRD data for $K_{0.6}FeF_3$ at 500 K using tetragonal $P4_2bc$ (top) and orthorhombic Pba2 (bottom) structural models

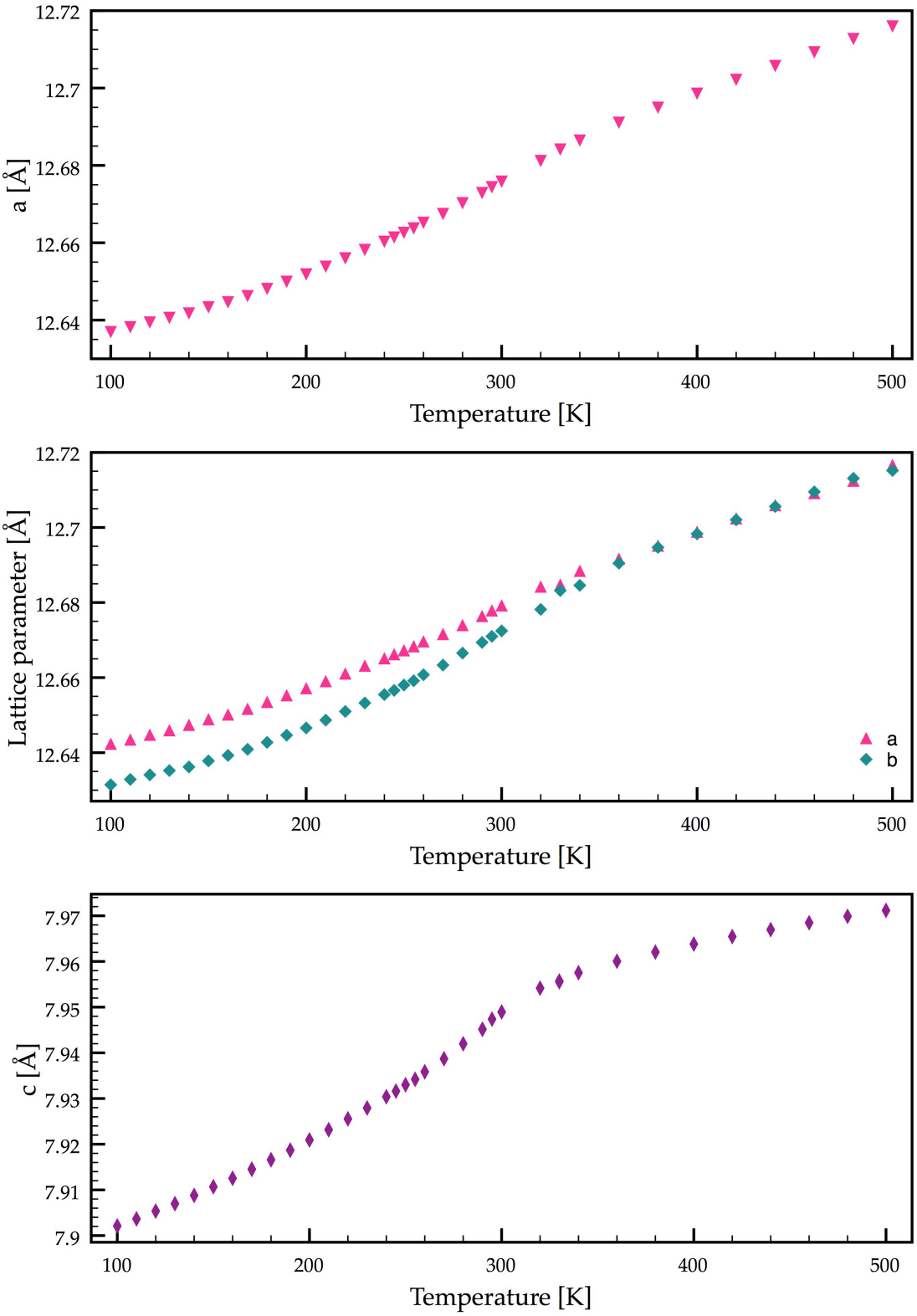

Figure 3.4: Change in the unit cell parameter a for the $P4_2bc$ model (top), a and b for Pba2 (middle) and the c parameter for both, which are essentially identical (bottom)

Table 3.2: The refinement details for $K_{0.6}FeF_3$ at 500 K using both the tetragonal and orthorhombic models as given by Fabbrici[17] and Mezzadri[18] respectively

	$P4_2bc$	*Pba2*
Unit cell parameters	a = 12.71599(2) Å c = 7.971191(15) Å	a = 12.7166(3) Å b = 12.7153(3) Å c = 7.971173(14) Å
χ^2	2.838	2.698
wR_p	21.01 %	20.49 %
R_p	16.27 %	15.77 %

Above 360 K, the tetragonal model gave the best fit when the difference plots were analysed, although the statistical values favoured the orthorhombic model. Between 360 K and 320 K, there was no preference for either. Below 320 K the orthorhombic model was the preferred model. This was mirrored in the lattice parameters for both models, in particular in the *c* lattice parameter. Figure 3.4 gives the plots of the lattice parameters versus temperature.

As stated at the start of the chapter, the initial model proposed for the sample was the tetragonal *P4/mbm*.[8] This model has the simple one octahedron-deep 3.9 Å *c*-axis (1c). This model was then also fitted to the 500 K data, Table 3.3. There was only one peak within the entire pattern that could be fitted by the *$P4_2bc$* (2c) model but not the (1c) model. It was not immediately clear as to whether or not the "peak" is an actual peak or merely a part of the background, as highlighted in Figure 3.5. Due to the lack of any further evidence other than this one weak peak, it was decided that the (2c) model be discarded and the *P4/mbm* model used. In order to obtain an estimate of the actual sample composition, the site occupancy of the two distinct potassium sites were refined and the atomic displacement parameters constrained to have the same value so that they did not mask the freely refining variables. The K1 site refined to a value greater than 1, and so it was reset to 1 and not refined further. The K2 site was left to refine. This led to the sample being determined to be of the composition $K_{0.58}FeF_3$.

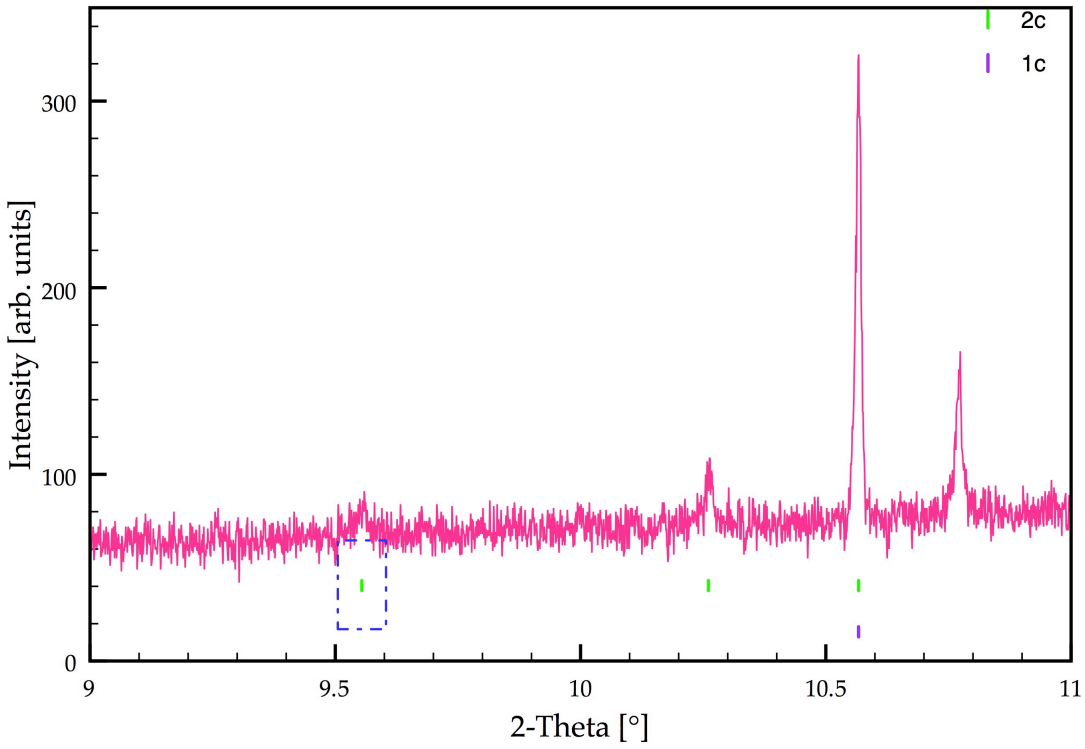

Figure 3.5: Excerpt from the $K_{0.6}FeF_3$ sPXRD data showing the sole "peak" that cannot be indexed by the (1c) model but can be by the (2c) model (the peak at 10.25 ° can be assigned to an impurity phase, K_2FeF_5)

The very same procedure was then applied to the noncentrosymmetric equivalent space group *P4bm*, which has also been reported as a solution.[17] This would be in line with the reported ferroelectric behaviour of the material, as this requires a noncentrosymmetric space group as a prerequisite. Again, the same restraints as for the *P4/mbm* model were used and the resultant Rietveld refinement summarised in Table 3.4. The sole change in the two models was that in *P4bm* there was no constraint that the *z* coordinate had to be either 0 or 0.5. In order to be able to compare the two models, the Fe1 site was constrained to the special position (0.5, 0, 0.5) in the noncentrosymmetric model so as to be one the same position as in the centrosymmetric model. All other atoms then moved relative to it. The second iron site, Fe2, did not move appreciably away from its starting point. The same could be said of the axial fluoride ions (F4 and F5), but there was a noticeable change in the equatorial fluoride ions, Table 3.5. The change indicated that there may be some distortion of the octahedra in the

Table 3.3: Structural parameters for $K_{0.58}FeF_3$ at 500 K using the *P4/mbm* model (a = 12.716290(15) Å, c = 3.985722(6) Å, and V = 644.507(2) Å^3, χ^2 = 2.146, wR_p = 13.8%, R_p = 18.1%) with isotropic atomic displacement parameters and spherical harmonics preferred orientation correction

Atom	Site	Site occupancy	x	y	z	U_{iso}x100 Å^2
Fe1	2c	1	0.5	0	0.5	0.95(3)
Fe2	8j	1	0.21378(6)	0.07509(7)	0.5	1.104(18)
K1	4h	1	0.17259(12)	0.32741(12)	0	4.15(5)
K2	2a	0.902(4)	0	0	0	4.15(5)
F1	8j	1	0.1433(2)	-0.0679(2)	0.5	2.94(9)
F2	4h	1	0.2780(3)	0.2220(3)	0.5	3.33(14)
F3	8j	1	0.3443(2)	-0.0080(2)	0.5	3.13(9)
F4	2d	1	0.5	0	0	4.6(2)
F5	8i	1	0.2075(2)	0.0773(3)	0	2.53(8)

Table 3.4: Structural parameters for $K_{0.58}FeF_3$ at 500 K using the *P4bm* model (a = 12.716282(15) Å, c = 3.985724(6) Å, and V = 644.507(2) Å^3, χ^2 = 2.130, wR_p = 14.1%, R_p = 18.0%) with isotropic atomic displacement parameters and spherical harmonics preferred orientation correction

Atom	Site	Site occupancy	x	y	z	U_{iso}x100 Å^2
Fe1	2b	1	0.5	0	0.5	0.89(3)
Fe2	8d	1	0.21363(6)	0.07510(7)	0.4913(12)	1.059(18)
K1	4c	1	0.17249(12)	0.32751(12)	-0.023(2)	4.17(6)
K2	2a	0.921	0	0	-0.005(3)	4.17(6)
F1	8d	1	0.1443(2)	-0.0679(2)	0.516(2)	2.89(11)
F2	4c	1	0.2784(2)	0.2216(2)	0.539(2)	2.20(16)
F3	8d	1	0.3446(2)	-0.0076(2)	0.527(2)	2.49(10)
F4	2b	1	0.5	0	-0.007(7)	4.9(2)
F5	8d	1	0.2076(2)	0.0774(3)	-0.024(3)	2.73(12)

ab plane, or merely that the increased degrees of freedom for the model were affected by the preferred orientation correction and showed no real effect at all. From that, no clear preference for the noncentrosymmetric model above the centrosymmetric model could be conclusively determined. Therefore, all further refinements were performed using the centrosymmetric *P4/mbm*.

On closer inspection of the fit of the model to the experimental data, it became apparent that there was a discrepancy between the intensity of the (h10) peaks that was not being accounted for properly by the calculated model used. These peaks were more intense in the experimental data than the calculated intensities. The corresponding (h12) peaks were observed to be less intense than calculated. A spherical harmonics preferred orientation correction was then applied to the data and the fit of the model increased markedly. Initially only 12 order terms were used in the spherical harmonics correction but there was still a notable improvement when adding further terms and hence the maximum number of allowed order terms in GSAS, namely 34, were used during the refinements. After adding in the K_2FeF_5 and α-Fe_2O_3 impurities the reduced χ^2 was 2.146 as compared to 2.310 for no preferred orientation correction, Figure 3.6. Detailed Rietveld plots of the entire 2-θ range are given in Figures 3.7 and 3.8.

Table 3.5: Comparison of z-coordinates for $K_{0.58}FeF_3$ at 500 K indicating the change between the constrained *P4/mbm* and the freely moving *P4bm* models

Atom	z-coordinate in *P4/mbm*	z-coordinate in *P4bm*	Difference | *P4/mbm* – *P4bm* |
Fe1	0.5	0.5	0
Fe2	0.5	0.4913(12)	0.0087
K1	0	-0.023(2)	0.023
K2	0	-0.005(3)	0.005
F1	0.5	0.516(2)	0.016
F2	0.5	0.539(2)	0.039
F3	0.5	0.527(2)	0.027
F4	0	-0.007(7)	0.007
F5	0	-0.024(3)	0.024

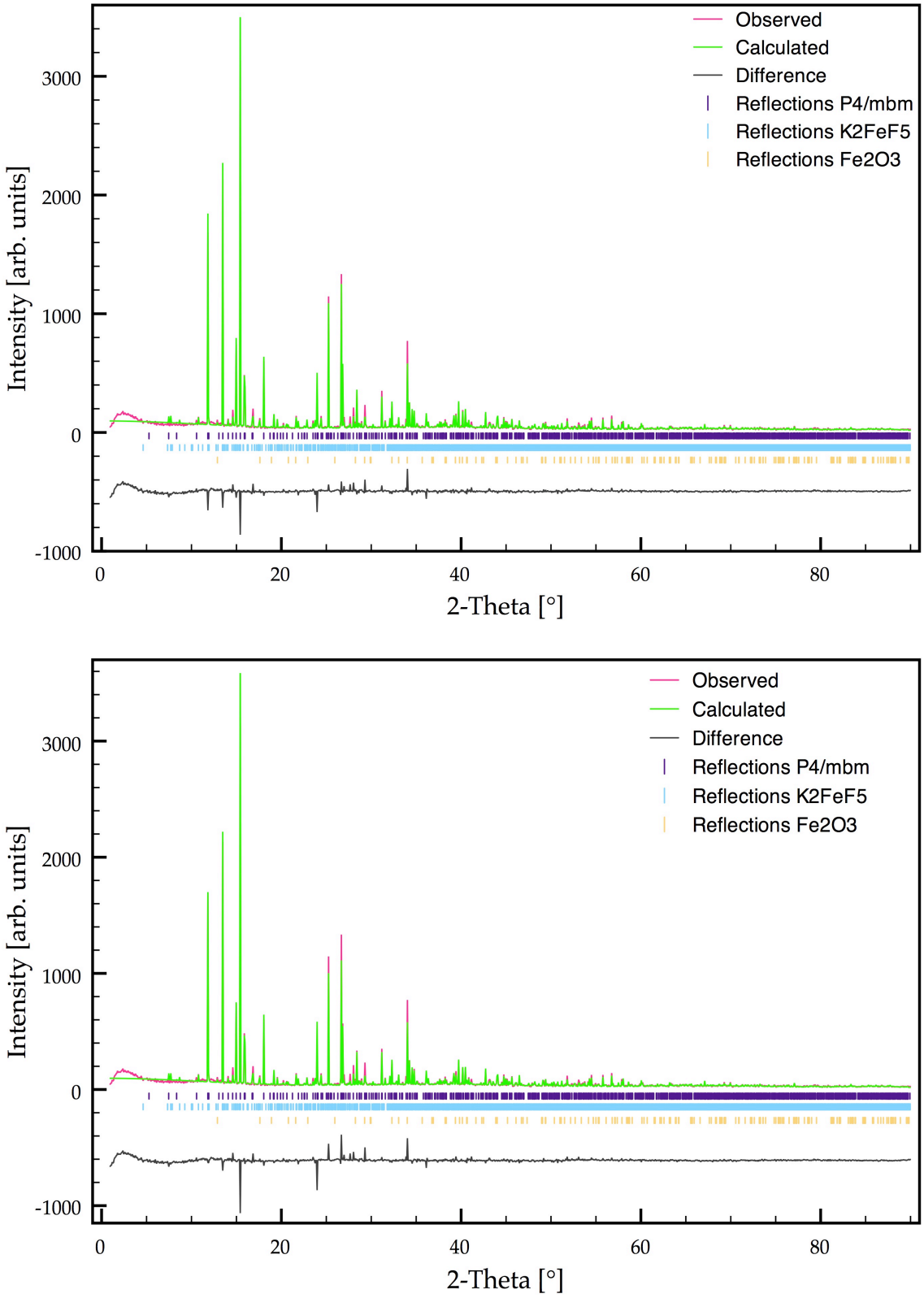

Figure 3.6: Rietveld plots for $K_{0.58}FeF_3$ in P4/mbm at 500 K with spherical harmonic preferred orientation correction (top) and without any preferred orientation correction (bottom)

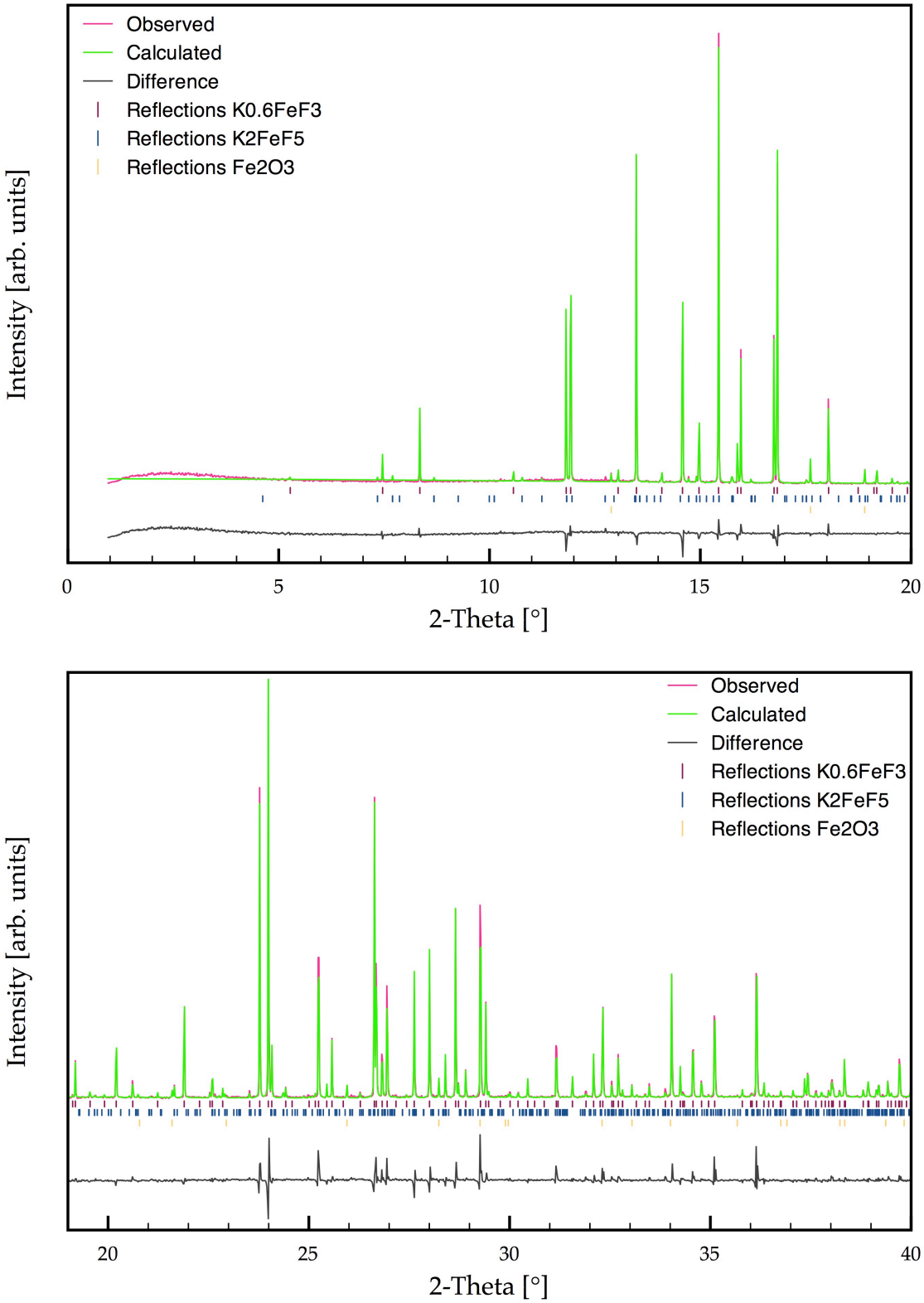

Figure 3.7: Detailed Rietveld plots for $K_{0.58}FeF_3$ in P4/mbm with spherical harmonic preferred orientation correction at 500 K showing the 0 to 20° 2-theta range (top) and the 20 to 40° 2-theta range (bottom)

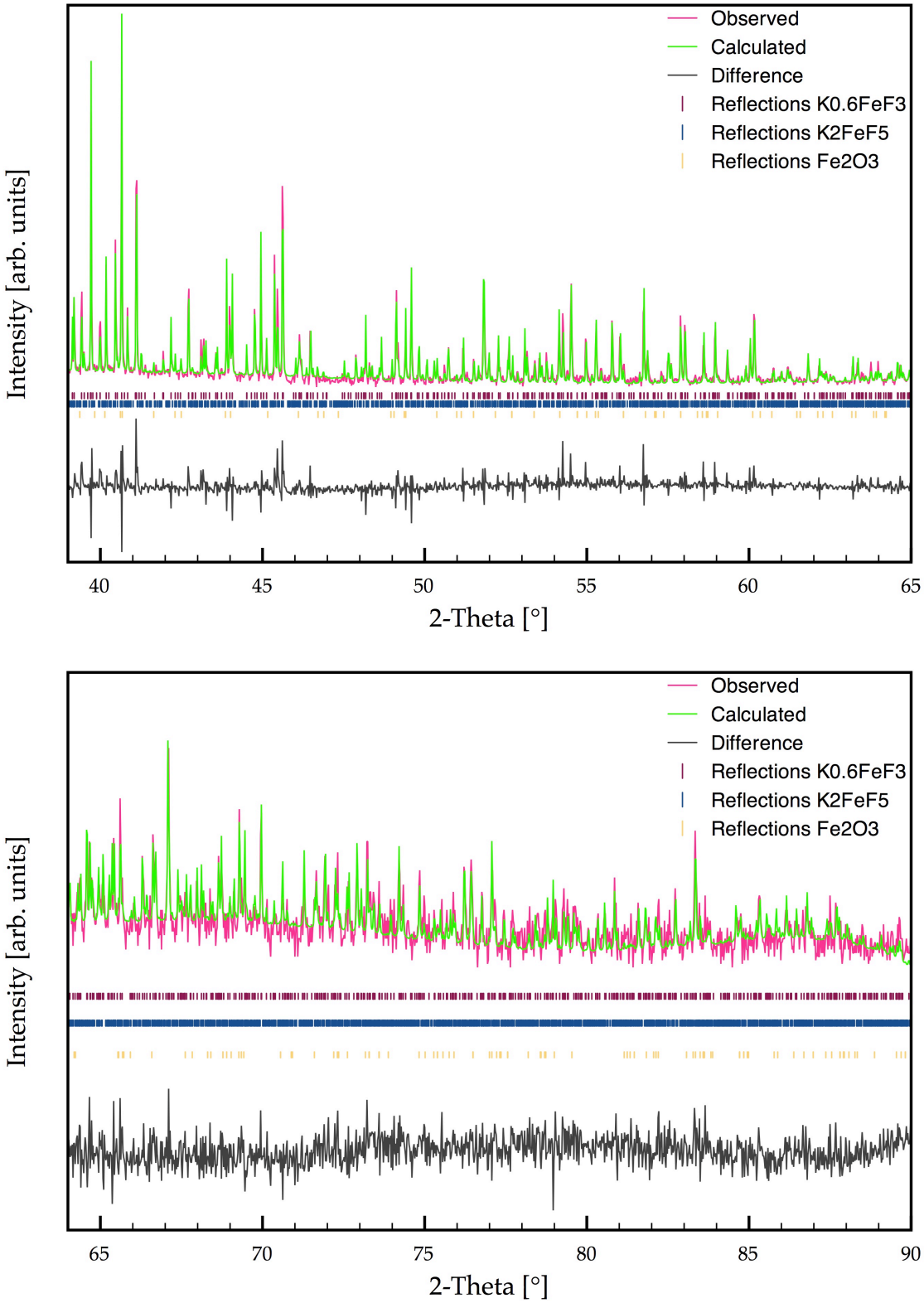

Figure 3.8: Detailed Rietveld plots for $K_{0.58}FeF_3$ in P4/mbm with spherical harmonic preferred orientation correction at 500 K showing the 40 to 65° 2-theta range (top) and the 65 to 90° 2-theta range (bottom)

To confirm that the discrepancy in intensities was due to a preferred orientation problem SEM measurements were conducted on the sample and these indicated that the sample consisted of fine platelets that were determined by EDX to be the TTB phase, whilst the randomly shaped remainders of the sample were the impurities, Figure 3.9.

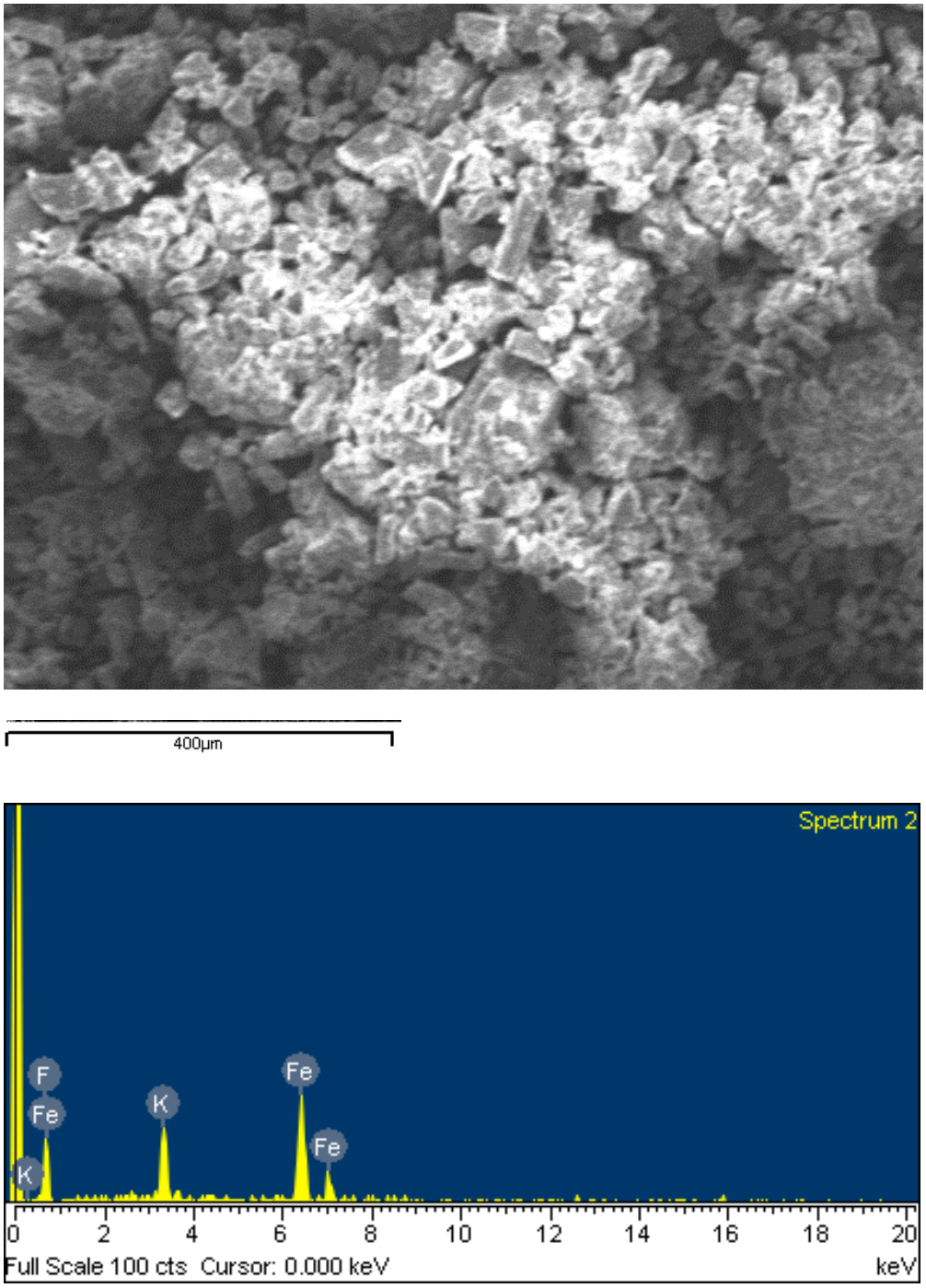

Figure 3.9: SEM image of $K_{0.58}FeF_3$ and the associated EDX spectrum

For all subsequent refinements the following parameters were refined: the background (using a cosine Fourier series with 9 terms); the detector zero point; the scale factor; and the phase fractions. For the tetragonal TTB phase, specifically, the following were also included: lattice parameters; atom positions; site occupancy of K2; isotropic atomic displacement parameters; pseudo-Voigt profile parameters - GW (for the Gaussian contribution) and LY (for the Lorentzian contribution); and all 34 order terms of the spherical harmonics ODF. The lattice parameters and profile parameters, GW and LY, were also refined for each of the impurity phases.

The two impurity phases, K_2FeF_5 and α-Fe_2O_3, were well defined. The cifs as given in the International Crystallographic Structural Database (ICSD) were used and the atomic positions not refined. The isotropic atomic displacement parameters were set to be 0.00500 $Å^2$ for both. The major impurity was K_2FeF_5 with a 3% weight fraction, followed by α-Fe_2O_3 with a weight fraction of 1.6%. The TTB phase made up the remaining 95.4%. This ratio did not change throughout the studied temperature range, Figure 3.10. The lattice parameters for both phases changed continuously and showed no divergences that might indicate a phase change or an inappropriate model, Figures 3.11 and 3.12. The impurities were good fit throughout the temperature range and are not discussed further.

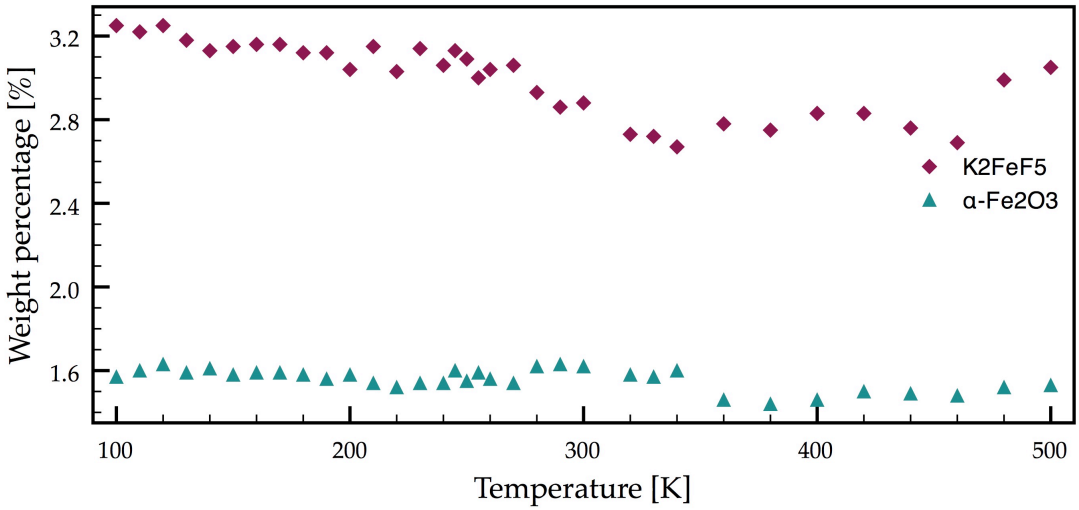

Figure 3.10: Weight fractions of the impurity phases, K_2FeF_5 (purple) and α-Fe_2O_3 (teal), versus temperature

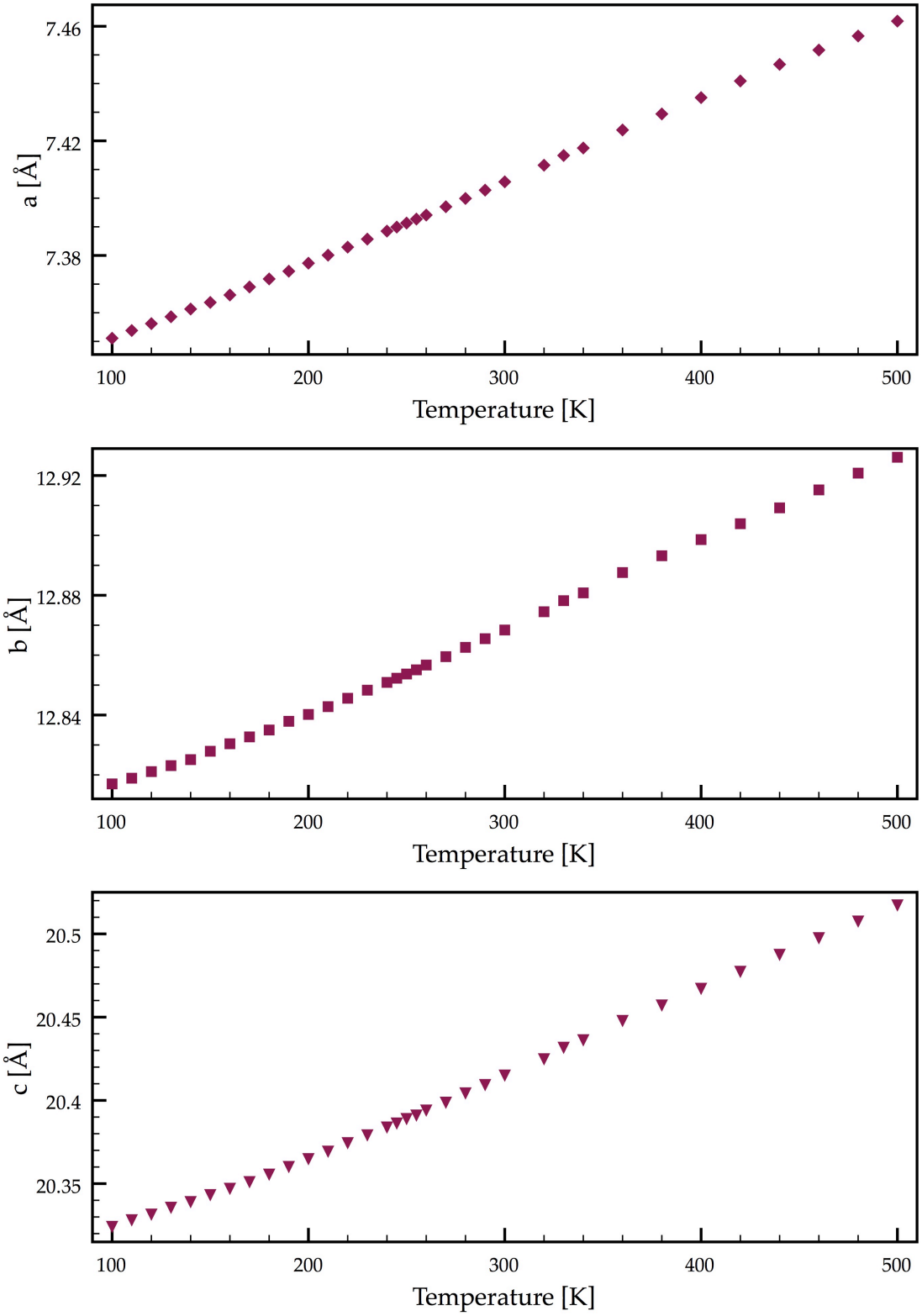

Figure 3.11: Lattice parameters of the impurity phase K_2FeF_5 versus temperature showing no outliers or anomalies

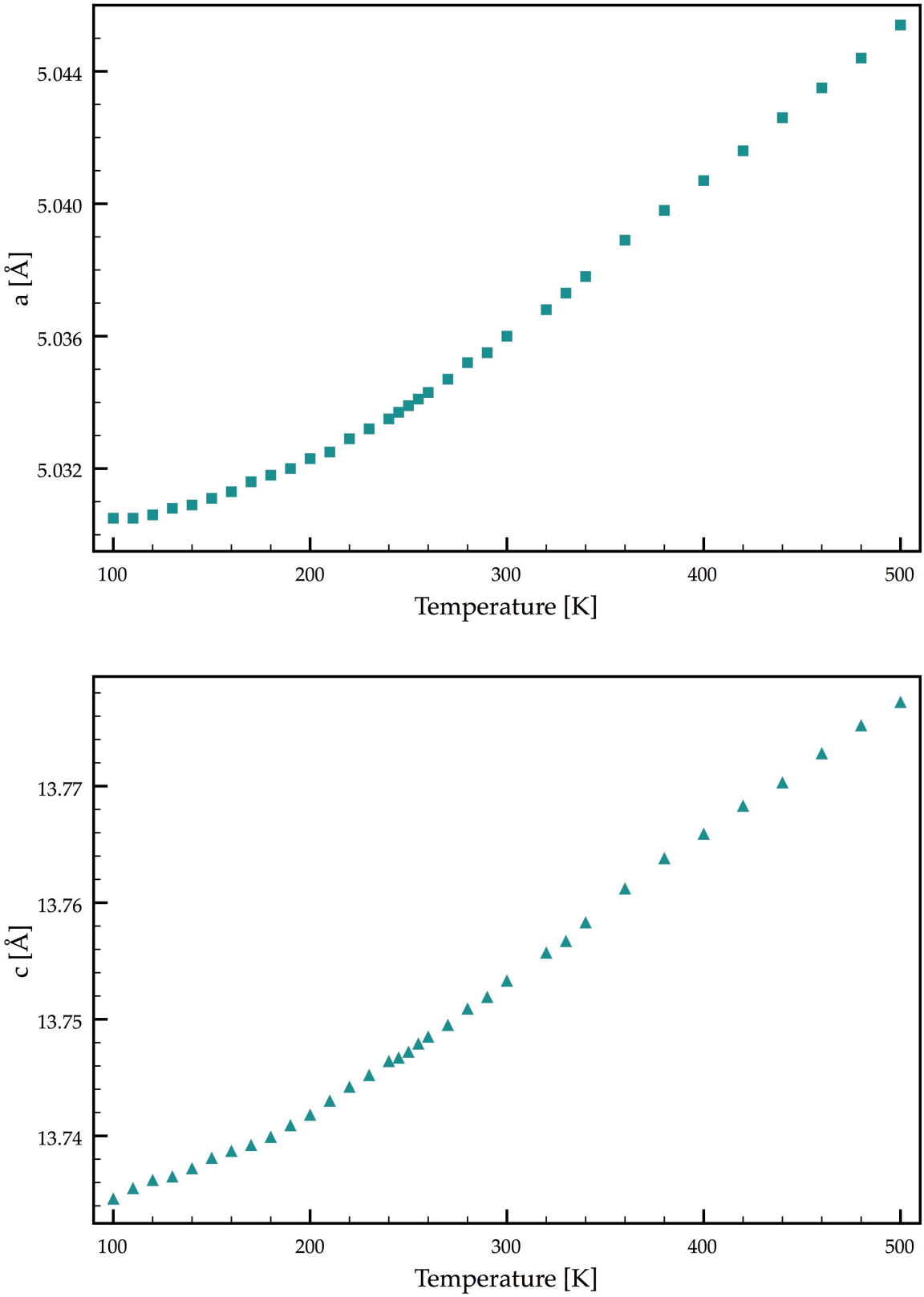

Figure 3.12: Lattice parameters of the impurity phase α-Fe_2O_3 versus temperature showing no outliers or anomalies

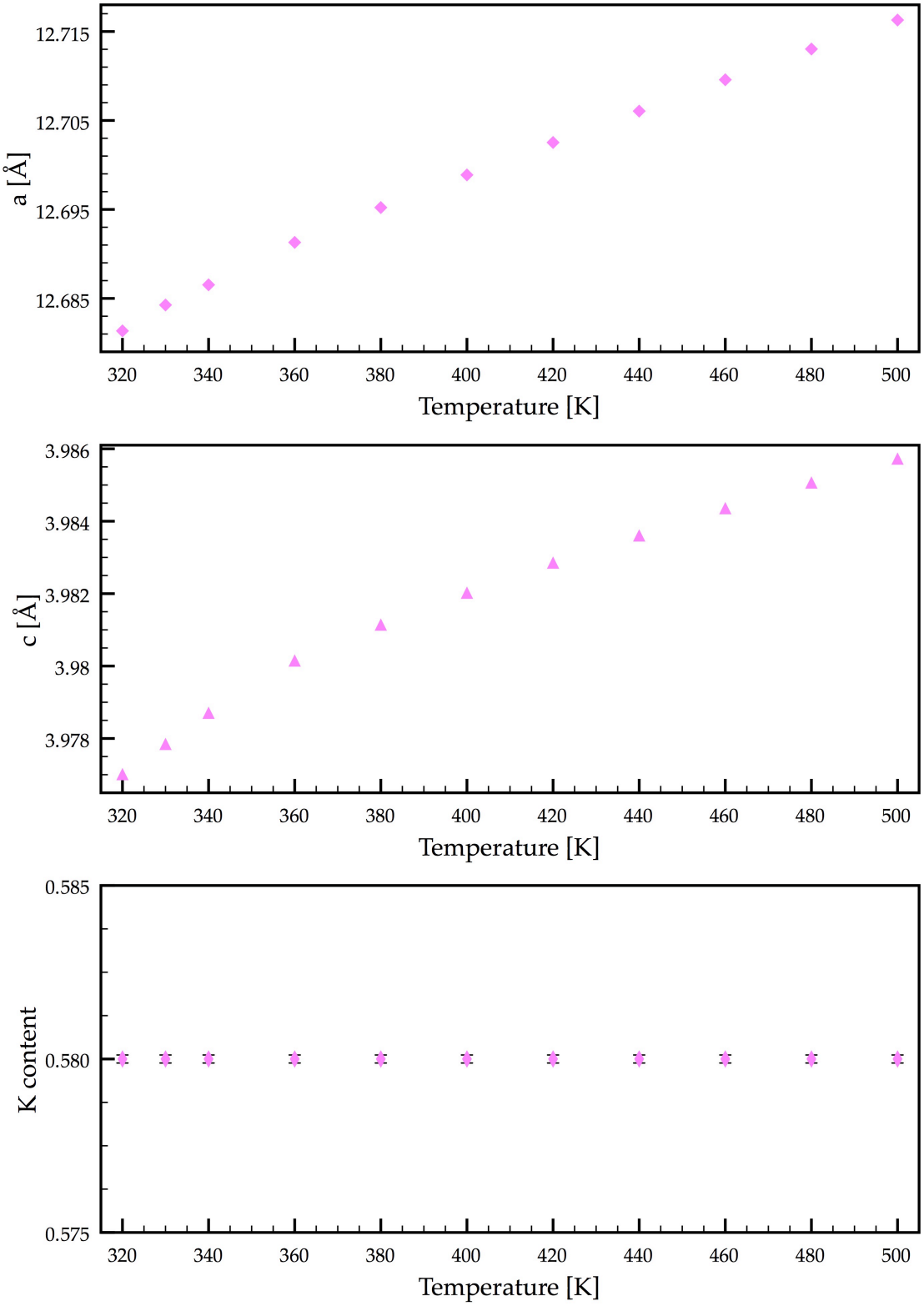

Figure 3.13: Lattice parameters (top) a and (middle) c, of tetragonal $K_{0.58}FeF_3$ versus temperature, and (bottom) the potassium content of the sample versus temperature

The lattice parameters for the TTB phase were analysed and found to follow the same smooth contraction between 500 K and 320 K; that is to say, there were no outliers, Figure 3.13. The value of x in K_xFeF_3 was also monitored and found to be constant at 0.58, Figure 3.13. The sample will henceforth be referred to as $K_{0.58}FeF_3$.

The bond lengths around the iron sites were found to indicate that there was a preference by the Fe^{2+} ions to occupy the (8j) site. The (8j) site makes up the four octahedra that maintain the perovskite template within the TTB structure, Figure 3.14. The (2c) site is the site that links the pentagonal channels and does not form part of the "perovskite-like" core. The average bond length around the Fe1 site (the 2c site) was 1.99 Å, and 2.01 Å for the Fe2 (8j) site, Table 3.6 and Figure 3.15.

Shannon's ionic radii were then used to calculate average bond lengths.[27] The average calculated bond length for a high-spin Fe^{II}-F bond is 2.11 Å, and 1.94 Å for the low-spin state. The high-spin Fe^{III}-F calculated bond average is 1.975 Å and 1.88 Å for the low-spin state. Thus, the bonds around the Fe2 ion were most likely the result of high-spin Fe^{2+} ions. The Fe1 site must thus be the preferred site for the Fe^{3+} ions. The fact that several of the bond lengths for the Fe2 ion, namely the Fe2-Fe3 and Fe2-F5 bonds, were much shorter than the remainder, Figure 3.15, indicated that the site was not purely occupied by the Fe^{2+} ion, but that that was, by far, the preferred site for it. This conclusion was confirmed when bond valence sums for the two iron sites were calculated as described by Brese and O'Keefe.[28] The calculated bond valences were 2.62 for Fe1 and 2.26 for Fe2.

Fabbrici *et al*.[17] indicated that the M^{2+} and Fe^{3+} shared the "perovskite" sites in an alternating manner and the remaining site was an equal mixture of the two ions. This same result was obtained by Banks *et al*. for the TTB $KMnCrF_6$.[13] Both of these reports used a doubling of the *c*-axis to account for the ordering of the ions around the "perovskite" site. This was not the case for the current analysis of $K_{0.58}FeF_3$ as there was no need to double the *c*-axis and so the conventional *P4/mbm* model was maintained.

Table 3.6: Bond lengths [Å] for $K_{0.58}FeF_3$ in the *P4/mbm* model over the 500 K to 360 K temperature range obtained from the Rietveld refinements of the sPXRD data

Temperature [K]	Fe1-F3	Fe1-F4	Average
500	1.983(3)	1.993(2)	1.988
480	1.976(3)	1.993(2)	1.985
460	1.980(3)	1.992(2)	1.986
440	1.977(3)	1.992(2)	1.985
420	1.978(3)	1.991(2)	1.985
400	1.983(3)	1.991(2)	1.987
380	1.978(3)	1.991(2)	1.985
360	1.980(3)	1.990(2)	1.985

Temperature [K]	Fe2-F1	Fe2-F1	Fe2-F2	Fe2-F3	Fe2-F5	Average
500	2.027(3)	2.048(3)	2.038(2)	1.967(3)	1.99465(15)	2.015
480	2.031(3)	2.043(3)	2.038(2)	1.973(3)	1.99426(14)	2.016
460	2.026(3)	2.044(3)	2.036(2)	1.971(3)	1.99392(14)	2.014
440	2.024(3)	2.042(3)	2.037(2)	1.973(3)	1.99353(14)	2.014
420	2.023(3)	2.042(3)	2.034(2)	1.971(3)	1.99314(14)	2.013
400	2.023(3)	2.041(3)	2.039(2)	1.966(3)	1.99272(14)	2.012
380	2.026(3)	2.037(3)	2.039(2)	1.968(3)	1.99218(13)	2.012
360	2.025(3)	2.037(3)	2.037(2)	1.969(3)	1.99167(13)	2.012

In the temperature range 500 K to 340 K, the data were well described by the tetragonal *P4/mbm* TTB model. Below 360 K, the (h00) peaks (which overlap with the (0k0) peaks) began to broaden at the base, Figure 3.16. These shoulders could not be accounted for using the tetragonal model alone.

The fact that this only affected the (h00) peaks was indicative of a distortion that led to a lowering of the space group symmetry and the *a* and *b* lattice parameters becoming non-equivalent. An investigation of the maximal

non-isomorphic subgroups of *P4/mbm* indicated that the most likely distortion was an orthorhombic one. In order to obtain starting cifs to eliminate some, if not all, of the subgroups the online program ISODISTORT[29] was used. Of these files, the most suitable was found to be the orthorhombic *Pbam*. This model accounted for all the observed shoulders in the diffraction pattern, Figure 3.16.

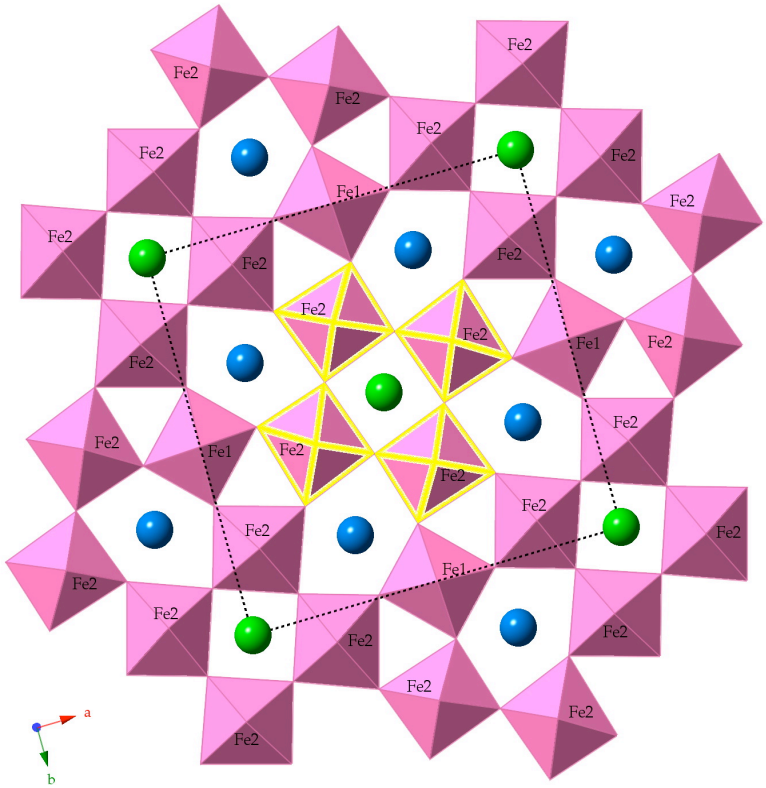

Figure 3.14: $K_{0.58}FeF_3$ viewed along the c-axis with labels for the two Fe sites, with the Fe1 site probably occupied mostly by Fe^{3+} and the Fe2 site by Fe^{2+}, and the perovskite sites highlighted

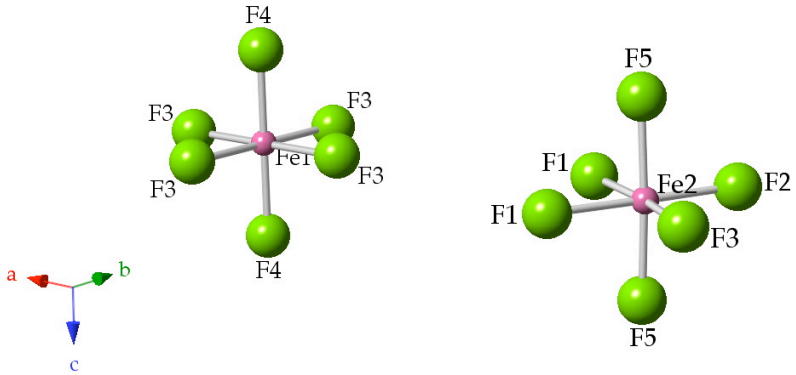

Figure 3.15: Coordination environments for the sites Fe1 and Fe2 in $K_{0.58}FeF_3$ obtained from the 380 K Rietveld refinement of the sPXRD data

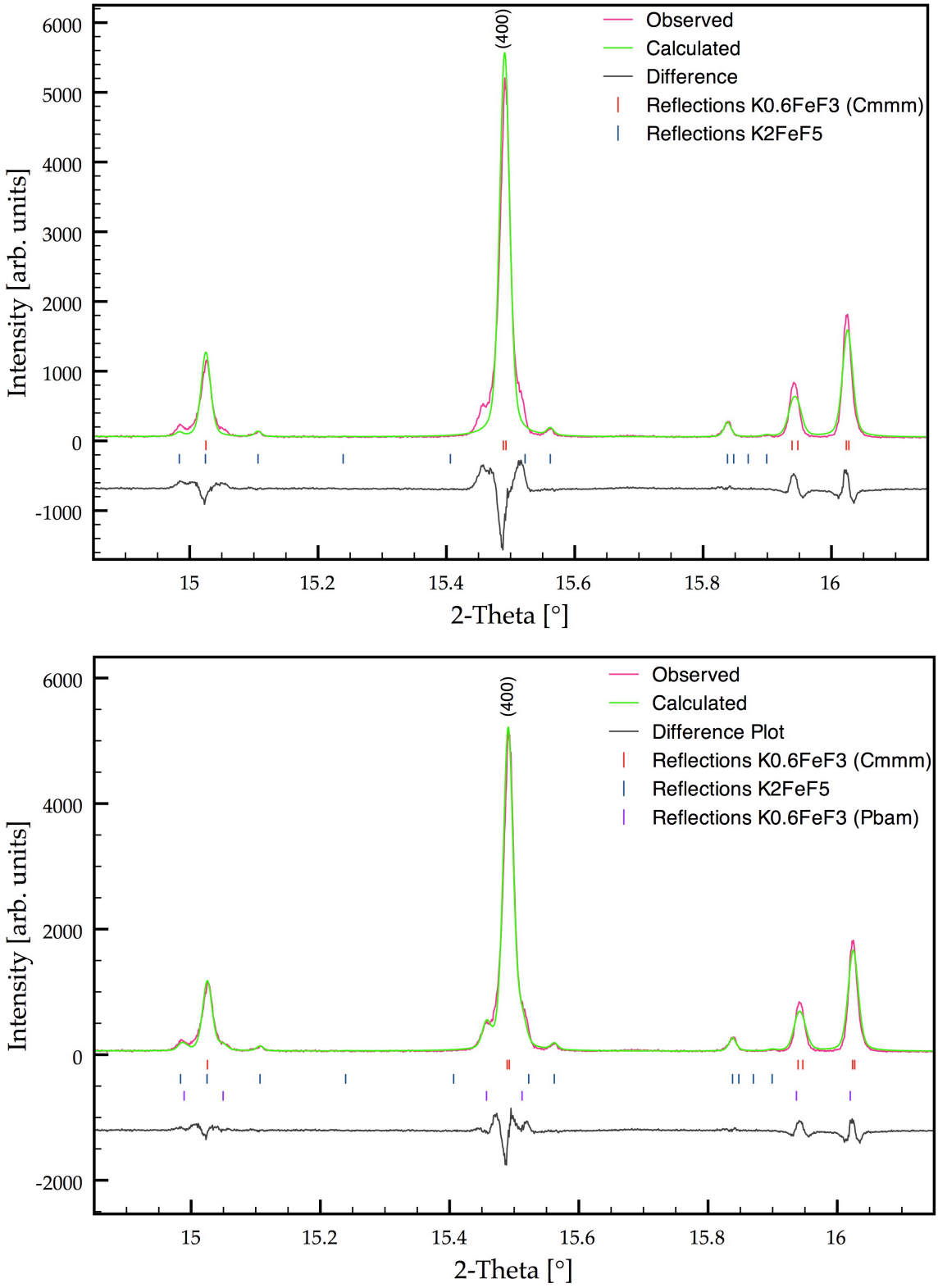

Figure 3.16: Excerpt from the sPXRD pattern of $K_{0.58}FeF_3$ below 360 K indicating the appearance of shoulders on the (h00) peaks (in this case the (400) peak at approx. 15.5°) that cannot be fitted by the tetragonal TTB (top) and that can be accounted for by adding the orthorhombic Pbam model to the already present model (bottom)

The phase fraction of *Pbam* grew in quickly from 0% at 340 K to roughly 10% at 300 K and remained constant after that, Figure 3.17. Due to the fact that the model used is an approximation model, no atom parameters are refined. The atoms in the unit cell were derived from the 380 K *P4/mbm* refinement, as this was a data set that clearly had no evidence of the orthorhombic phase. Only the lattice parameters, the pseudo-Voigt profile parameters GW and LY, and the phase fraction were refined. The ODF terms for the spherical harmonics preferred orientation correction were also taken from the 380 K data set and not refined further. The *Pbam* model is an orthorhombic distortion of the tetragonal starting model. The lattice parameters are of the same magnitude, with the sole difference that the *a* and *b* lattice parameters are no longer required to be equal.

The *a* and *b* lattice parameters were significantly different, Figure 3.17, whilst the *c* lattice parameter, Figure 3.17, remained very similar to that of the tetragonal model. There was no evidence that the two *a* and *b* parameters were tending to converge prior to the sample going through the phase transition and becoming tetragonal. The data subsequently refined well with both phases present, Figure 3.18 (with detailed plots given in Figures 3.20 and 3.21).

It soon became apparent from the diffraction patterns that the tetragonal model was inadequate below 300 K as had been previously noted when the initial starting models were used. The (660) hkl peak changed from a single peak into two distinct separate peaks, Figure 3.19. This could only be accounted for by a lowering of the symmetry from tetragonal to orthorhombic or monoclinic. The full-width half maxima (FWHM) of the (660) "peak" were measured and compared to the (002) reference peak that remained unchanged. At higher temperatures, both of the peaks had similar values of around 0.024° and 0.023° respectively. Below 300 K, the value of the FWHM for the (660) peak increased to a maximum of 0.049° at 110 K. At 100 K, it was possible to measure the FWHM of the two separate peaks and they were found to have values of approximately 0.026°. This indicated that the peaks were of the same phase as the (002) reference peak. Figure 3.22 gives a plot of the FWHM versus temperature.

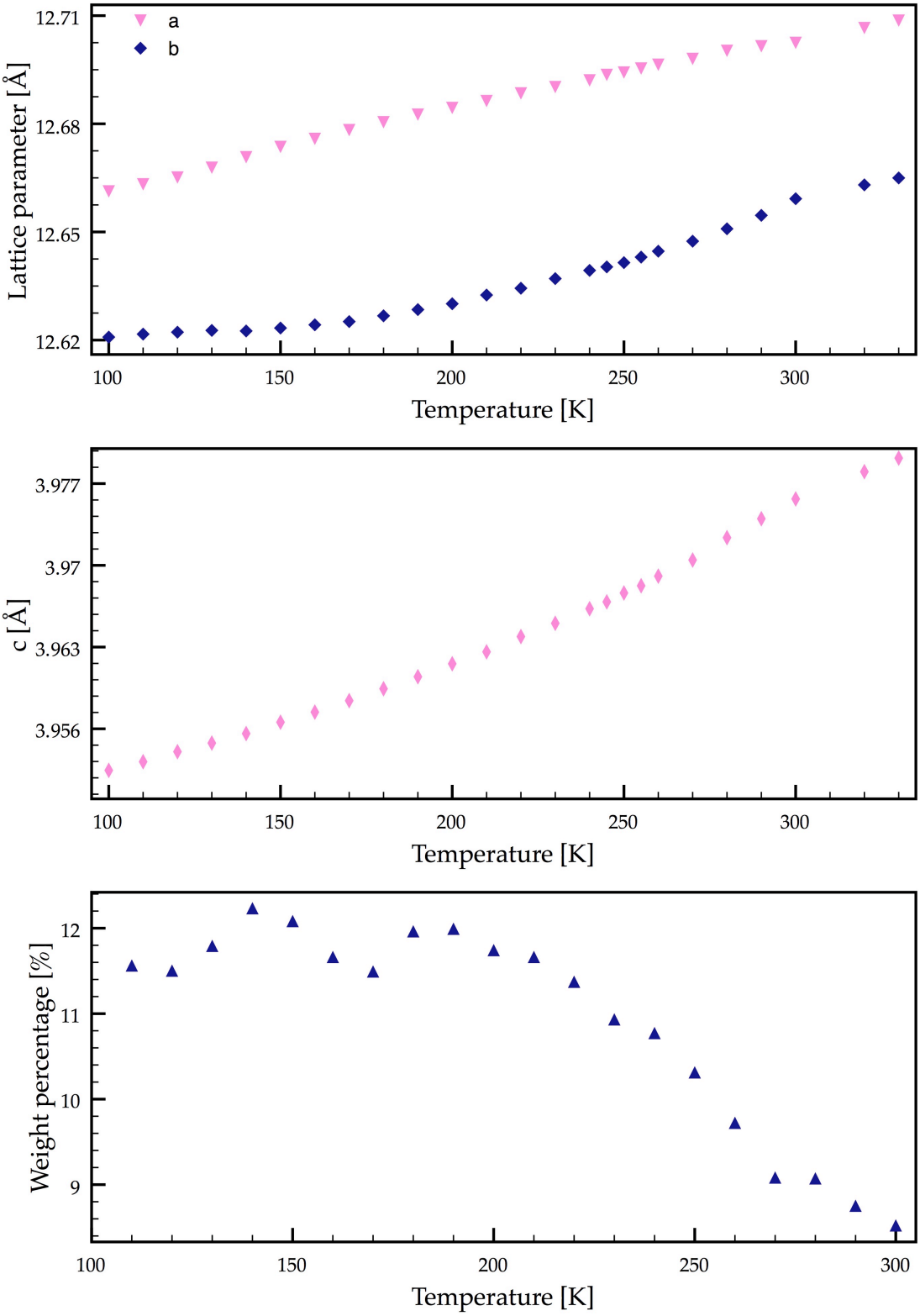

Figure 3.17: Lattice parameters (top) a and b, and (middle) c, of orthorhombic $K_{0.58}FeF_3$ in Pbam versus temperature, and (bottom) the percentage (by weight) of the orthorhombic phase versus temperature

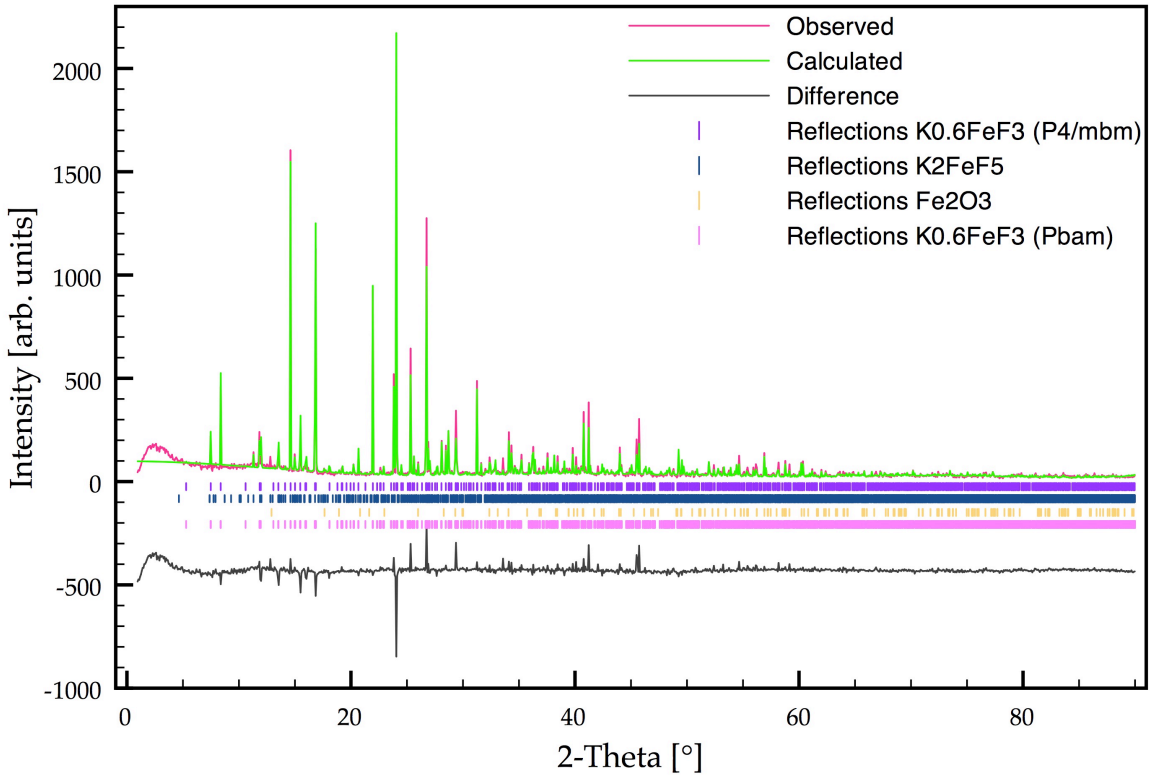

Figure 3.18: Rietveld plot for $K_{0.58}FeF_3$ at 320 K with the P4/mbm and Pbam models

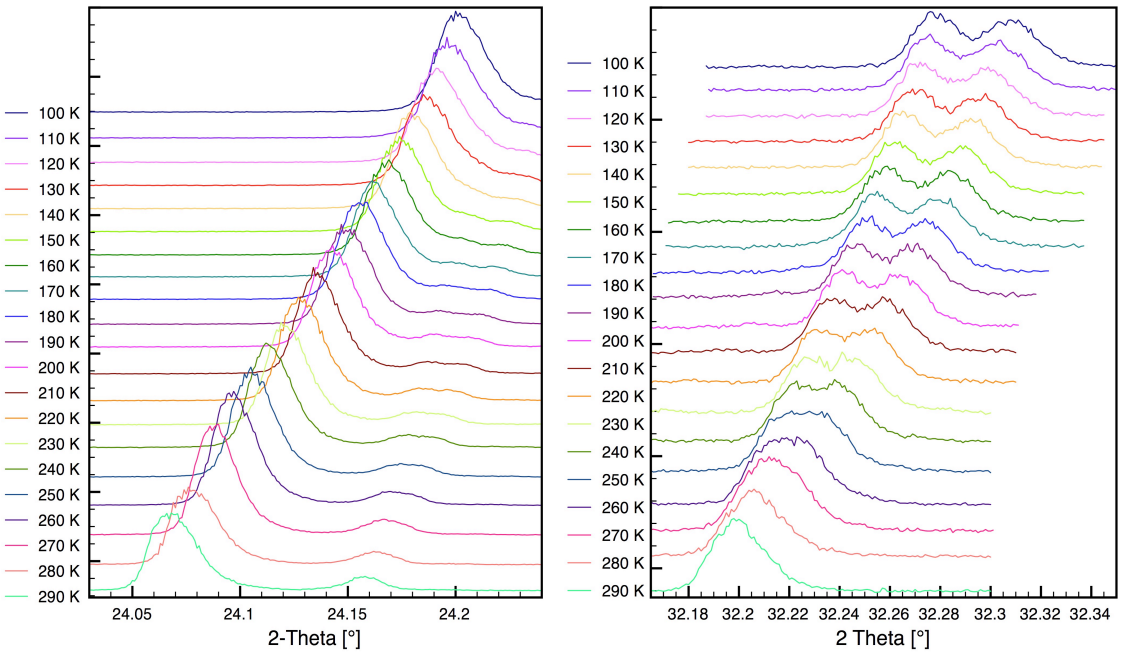

Figure 3.19: Excerpts from the sPXRD patterns of $K_{0.58}FeF_3$ as a function of temperature indicating the constant nature of the (002) reference peak on the left, and the splitting of the "(660)" peak of the tetragonal model on the right

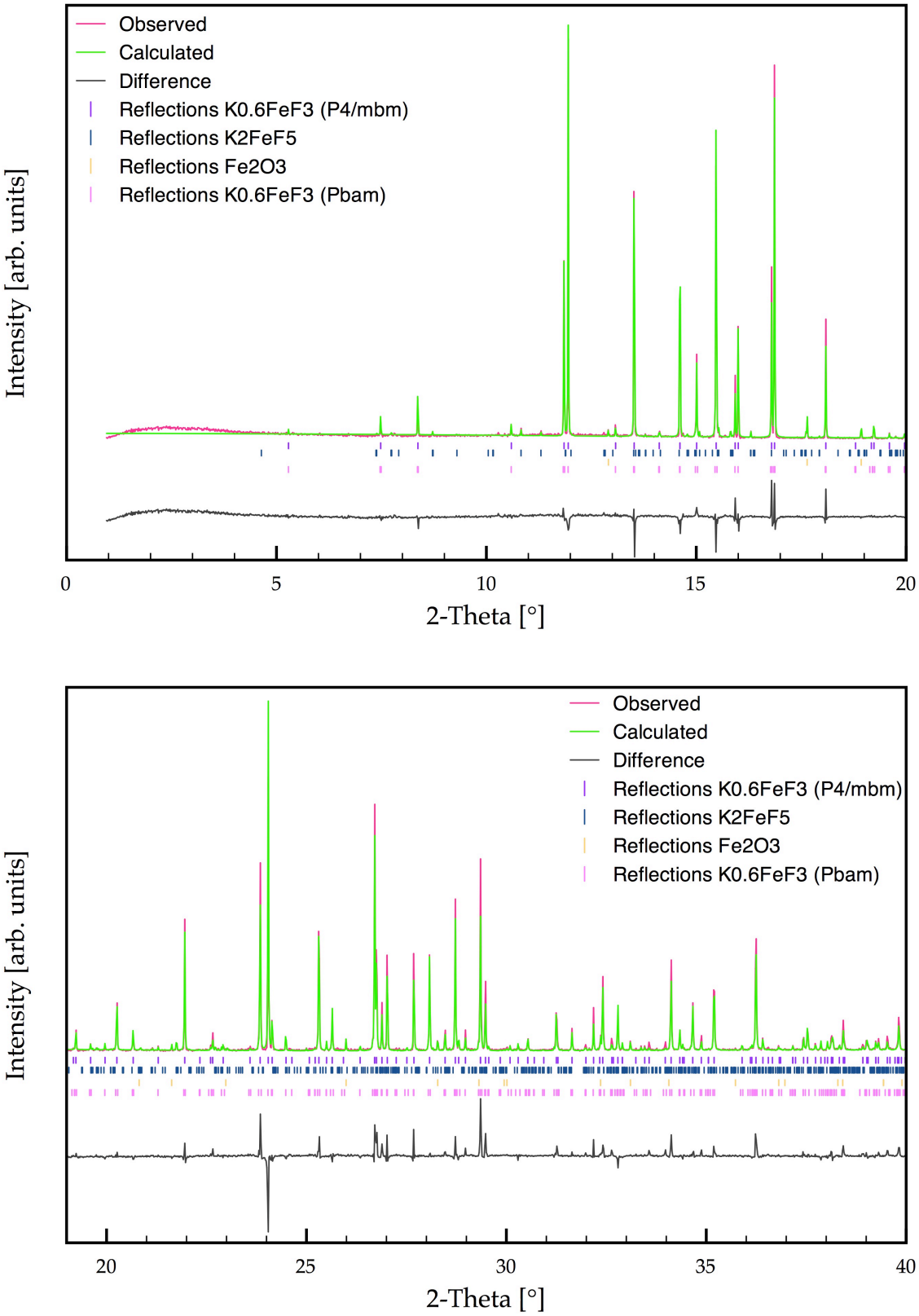

Figure 3.20: Detailed Rietveld plots for $K_{0.58}FeF_3$ in P4/mbm and Pbam at 320 K showing the 0 to 20° 2-theta range (top) and the 20 to 40° 2-theta range (bottom)

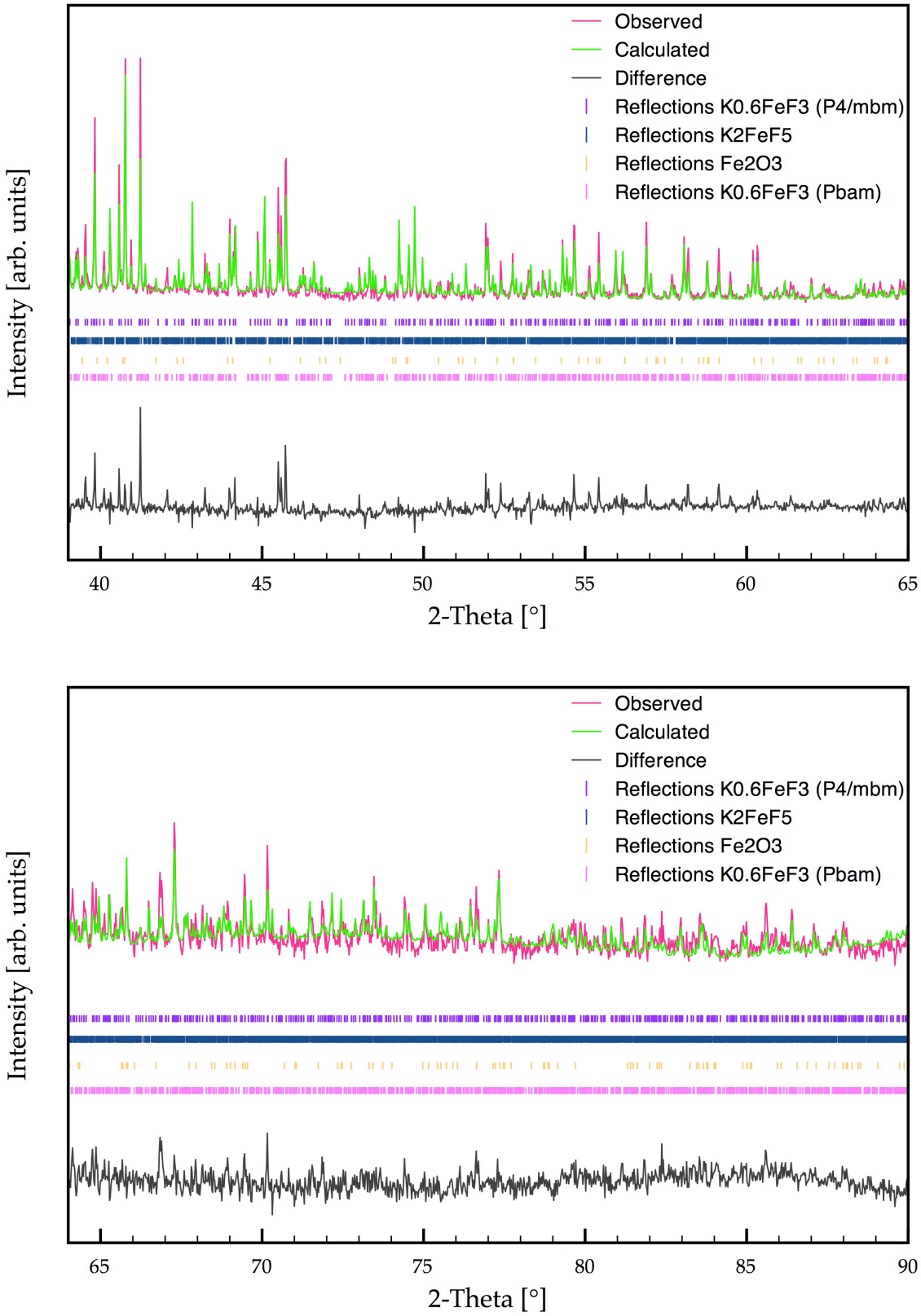

Figure 3.21: Detailed Rietveld plots for $K_{0.58}FeF_3$ in P4/mbm and Pbam at 320 K showing the 40 to 65° 2-theta range (top) and the 65 to 90° 2-theta range (bottom)

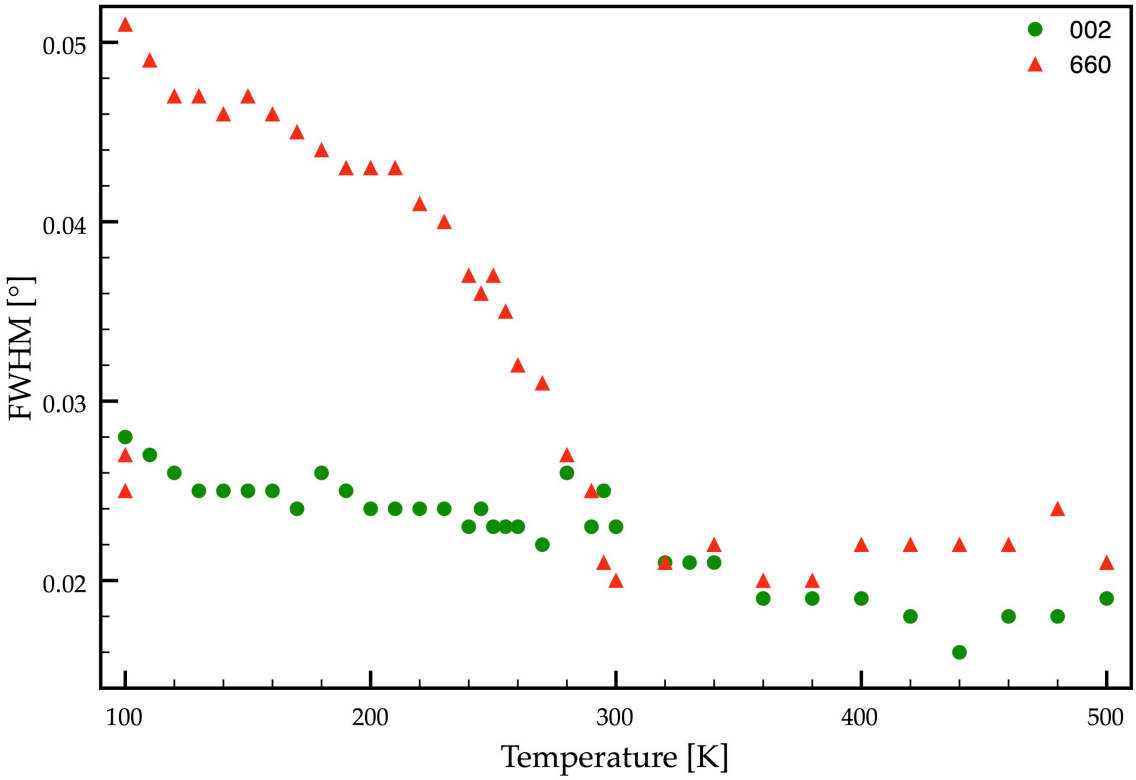

Figure 3.22: FWHM of the (002) reference and (660) peaks versus temperature indicating the transition of the (660) peak from one peak into two

Yet again, the simplest solution to the observed anomaly was that the remainder of the tetragonal phase was going through a phase transition to a lower symmetry phase whilst the first orthorhombic phase, *Pbam*, remained. Thus, orthorhombic and monoclinic models that have been reported for this compound below room temperature were investigated.

The simplest distortion would be that akin to the orthorhombic distortion already mentioned. But this was not the case seeing as the same peaks were not splitting. In the simple 12x12x4 orthorhombic distortion model, *Pbam*, the (h00) peaks were affected the most. This was not true for this phase transition. Thus, other models were considered. The first model that was investigated was the FES model as reported by Fabbrici *et al.*[17] This has a unit cell with $a \approx a_t2\sqrt{2} = 35.730(3)$ Å, $b \approx a_t\sqrt{2} = 17.872(1)$ Å, and $c \approx c_t2 = 7.9030(6)$ Å. Several attempts were made to refine this model, but they all diverged, and so it was discarded as an option. A reinvestigation of the maximal non-isomorphic subgroups of *P4/mbm* was done and the best fit was obtained by using the space

group *Cmmm*. This new unit cell was defined by a distortion in the *ab* plane of the tetragonal model leading to the new unit cell axes being defined along the diagonals of the old structure, Figure 3.23. The cif for this distortion was obtained from the online program ISODISTORT.[29] The new *a* and *b* lattice lengths were longer than the 12 Å ones, as they needed to be multiplied by √2. After this phase transition, the percentage of the initial orthorhombic *Pbam* phase did not change. It remained constant throughout the remainder of the refinements to 100 K. A Rietveld plot of the refinement is given in Figure 3.24 with detailed plots in Figures 3.25 and 3.26. The lattice parameters and weight percentage confirmed this, Figure 3.17.

The atomic parameters were not refined for the *Cmmm* model. This was done for the same reason as for the *Pbam* model: both models are approximation models. There was no evidence to indicate that these were in fact the full and correct solution to the phase transition, but they provided the best solution given the data we had, and the lack of single crystal data to indicate the actual positions of the ions at low temperatures. The spherical harmonics preferred orientation correction ODFs were used from the 380 K tetragonal data set, as they accounted for the preferred orientation observed. Also, because the model used was only an approximation, it was hoped that using a predefined set of ODFs would not mask any further structural observations as, or if, they arose during the refinements.

The lattice parameters were plotted as a function of temperature and showed that the sample was well behaved and did not show any outliers or anomalies throughout the rest of the temperature range, Figure 3.27. The graph showing the plot of the *a* and *b* lattice parameters versus temperature clearly showed that the two axes tended to convergence as the phase transition temperature around 320 K was approached.

Initially the profile parameters were fixed to those of the tetragonal phase, but below 230 K they could be refined freely. Subsequently, the averages of the values between 230 K and 100 K were taken and used to re-refine the data sets above 230 K.

A further anomaly observed was that the (12,0,0) and (0,12,0) peaks appeared very slightly shifted compared to the remainder of the peaks once the *Cmmm* model was fitted, Figure 3.28. This shift only appeared at low

temperatures towards 100 K. This shift in selected peaks might be attributed to an in-plane incommensurate distortion in the *ab* plane. However due to the small size of the shift, no further analysis was done.

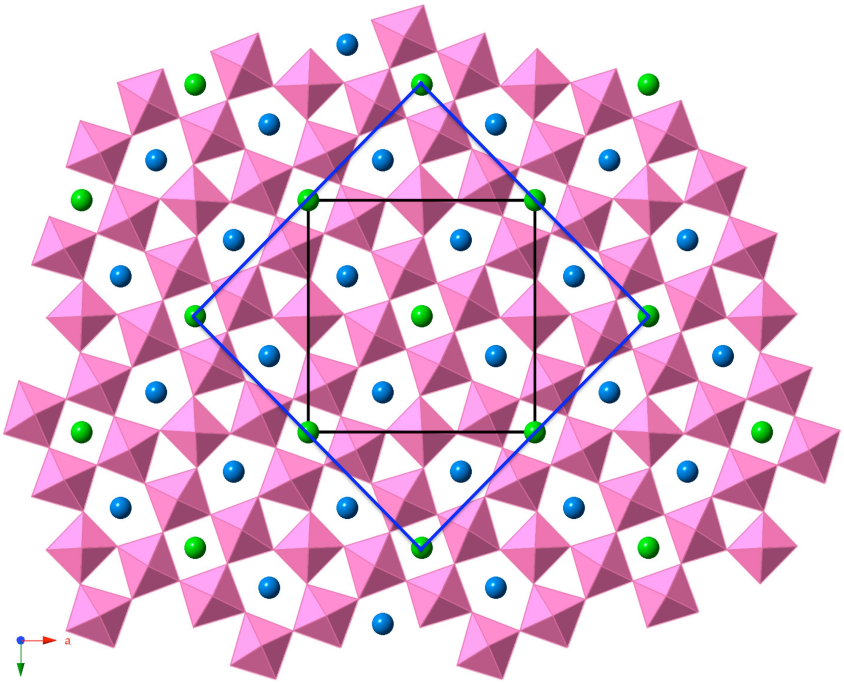

Figure 3.23: Unit cells of $K_{0.58}FeF_3$, with the P4/mbm and Pbam unit cells given in black and the Cmmm unit cell in blue

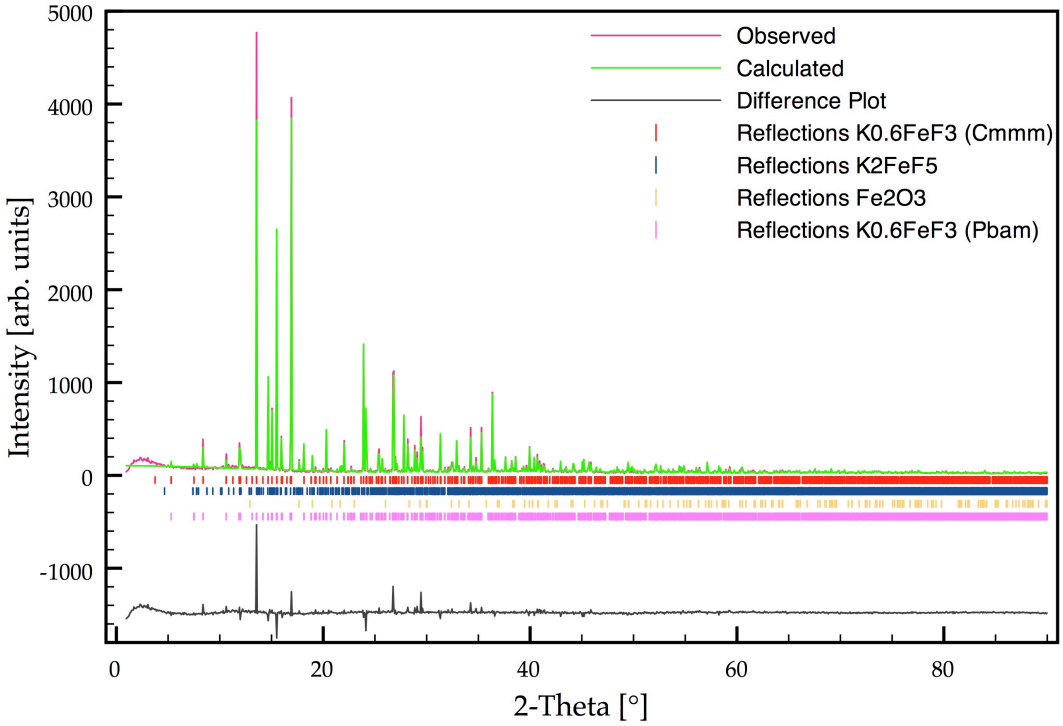

Figure 3.24: Rietveld plot at 100 K for $K_{0.58}FeF_3$ with both the Cmmm and Pbam models

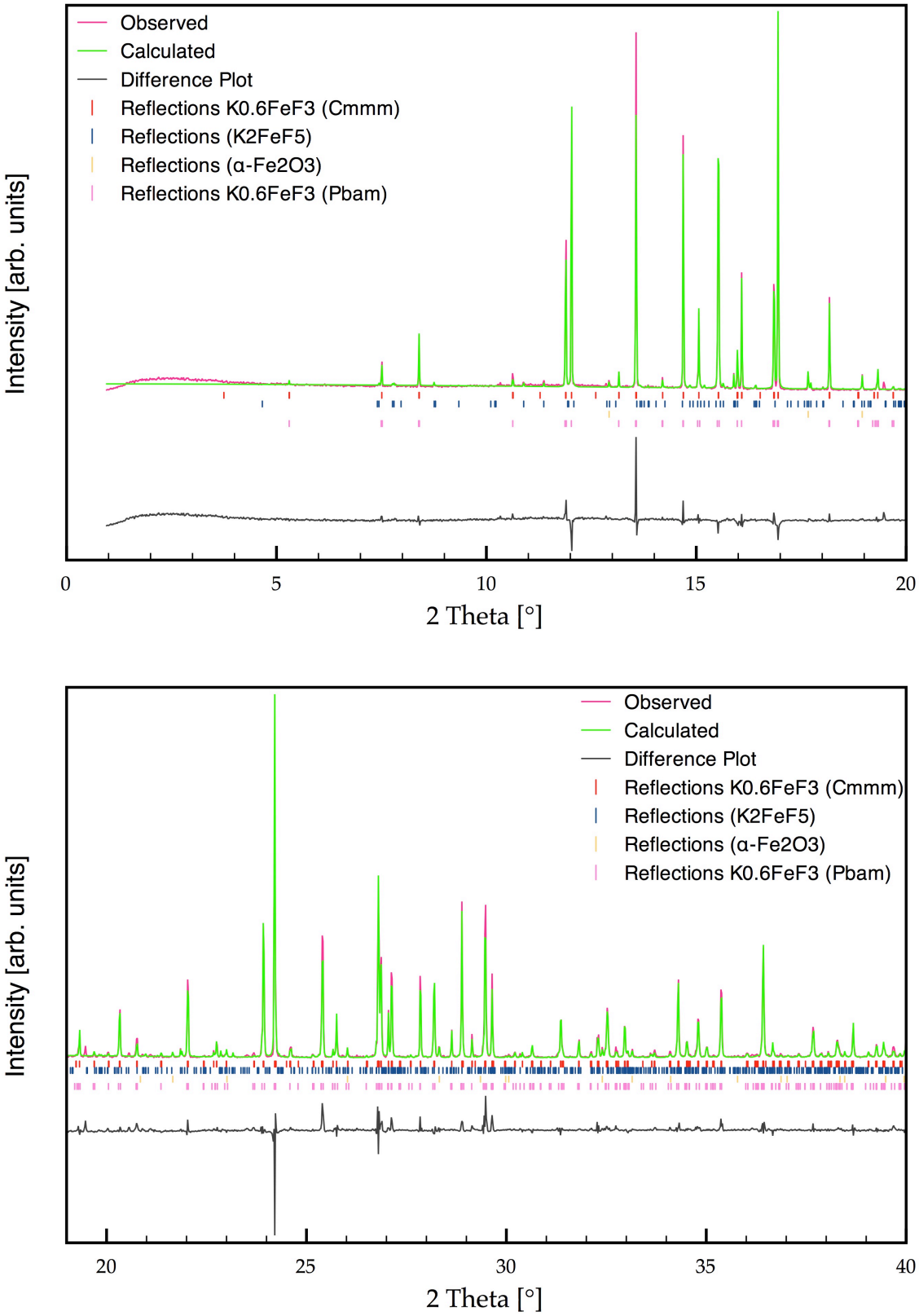

Figure 3.25: Detailed Rietveld plot for $K_{0.58}FeF_3$ in Cmmm and Pbam at 100 K showing the 0 to 20° 2-theta range (top) and the 20 to 40° 2-theta range (bottom)

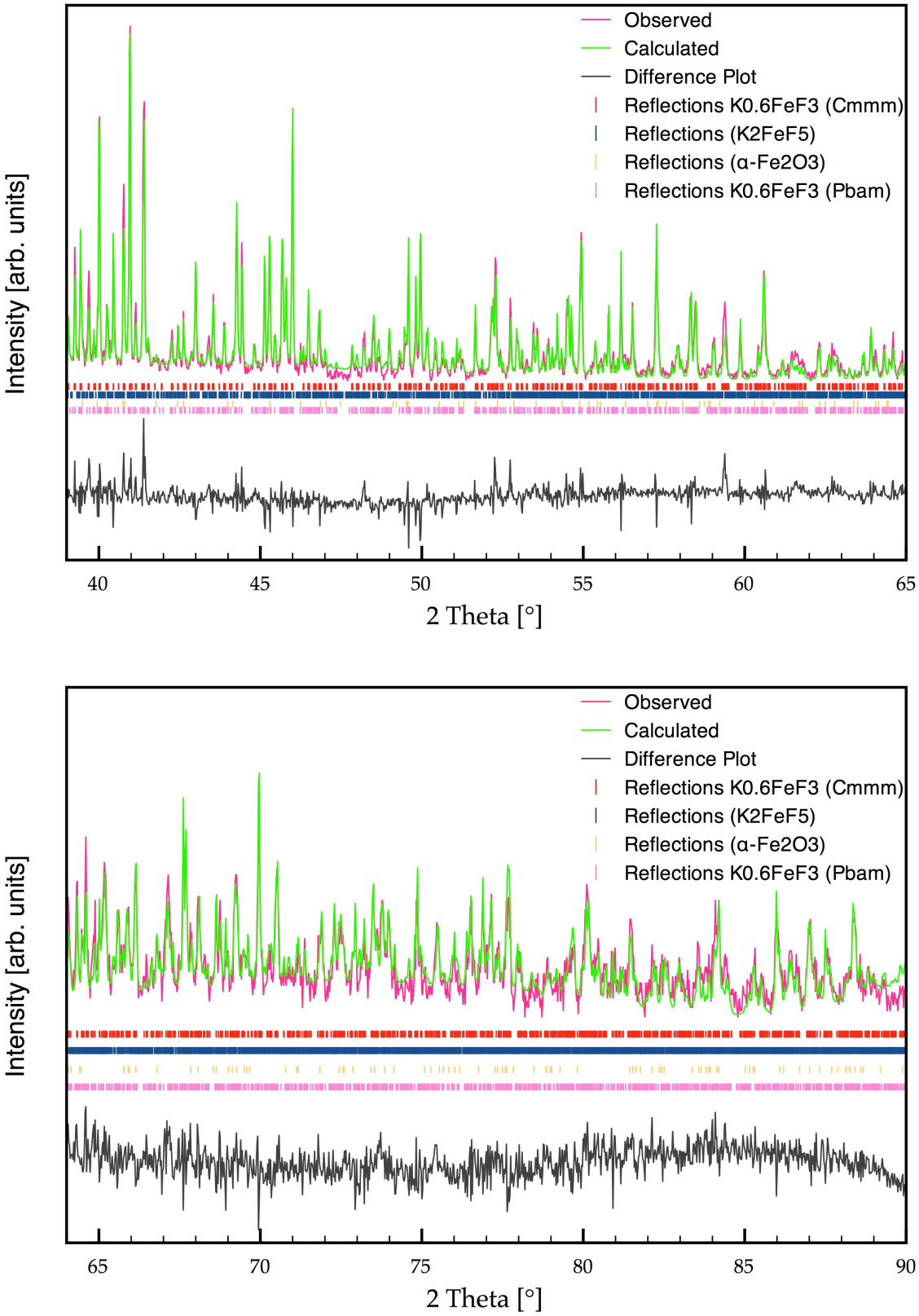

Figure 3.26: Detailed Rietveld plot for $K_{0.58}FeF_3$ in Cmmm and Pbam at 100 K showing the 40 to 65° 2-theta range (top) and the 65 to 90° 2-theta range (bottom)

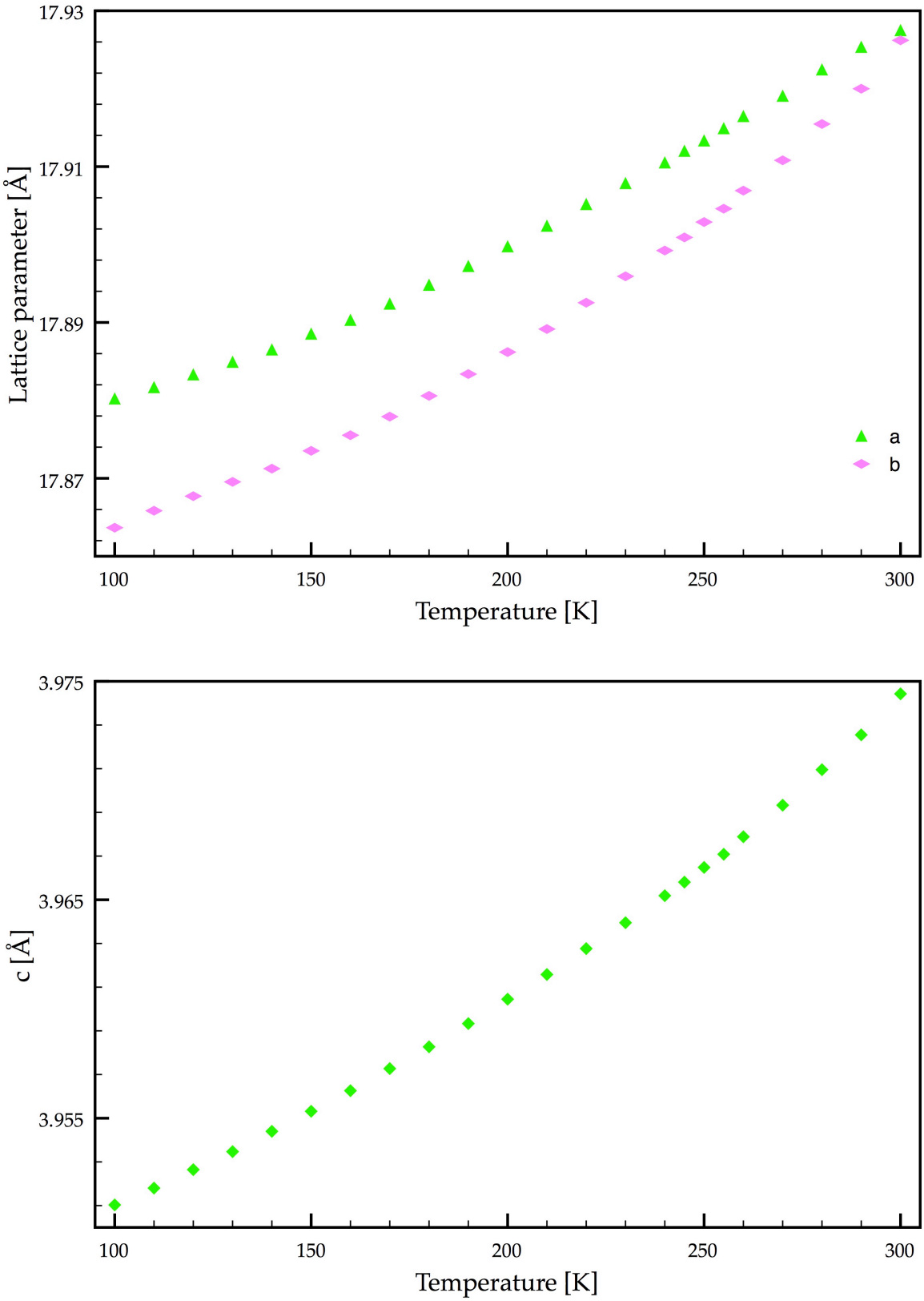

Figure 3.27: Lattice parameters (top) a and b, and (bottom) c, versus temperature for $K_{0.58}FeF_3$ in orthorhombic Cmmm

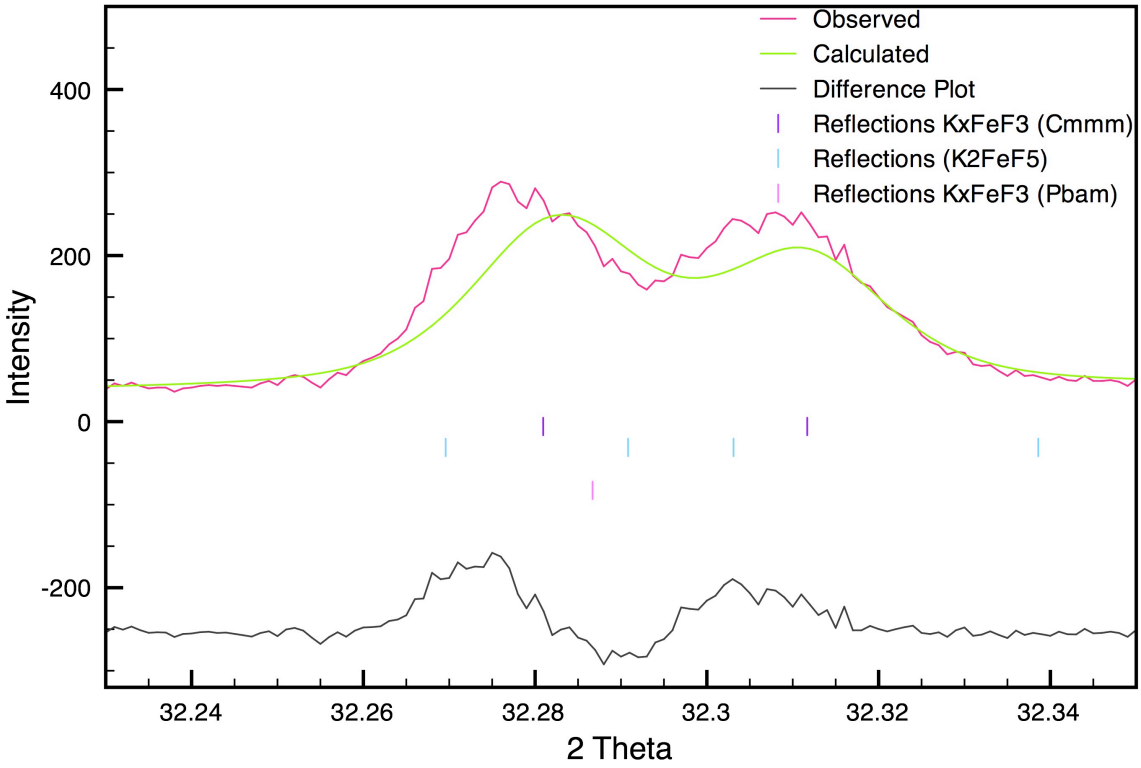

Figure 3.28: Excerpt from the 100 K sPXRD pattern of $K_{0.58}FeF_3$ solved in the Cmmm model indicating the slight shift of the (12,0,0) and (0,12,0) hkl peaks leading to the conclusion that there might be an in-plane incommensurate distortion

Several TTB solid solution compounds, in particular the solid solutions of sodium barium niobate $Ba_2Na_{1-x}Nb_5O_{15}$,[30] also show an incommensurate distortion at low temperatures. These distortions in the other TTBs were attributed to octahedral tilting and dipolar order.[31, 32]

Thus, an investigation of the 100 K to 500 K temperature range for the compound $K_{0.58}FeF_3$ indicated a hitherto unreported phase separation and a new approximation model for the tetragonal to orthorhombic phase transition. The plot of the lattice parameters, Figure 3.29, for all three phases as a function of temperature showed that the tetragonal model changed smoothly into the orthorhombic *Cmmm* model and the *Pbam* model was distinctly different from the two other phases in the *ab* plane distortion. The *c* lattice parameters were unaffected by the phase change, although there was a change in the rate at which the parameter changed during the tetragonal to orthorhombic phase transition.

There was no evidence of a monoclinic distortion as reported by Ishihara *et al*.[14] although this did not indicate the absence thereof. It could merely be a pseudo-orthorhombic model.

Further experiments were conducted to determine if the growth of the *Pbam* phase could be influenced. The sample was reheated to 380 K and then quenched, or slow cooled at different rates. Neither of these approaches affected the weight percentage of either phase. Thus, it seems that the phase separation is thermodynamically driven rather than a kinetically driven property, most likely a result of the tetragonal phase splitting into two phases with different potassium contents. This could not be confirmed to date.

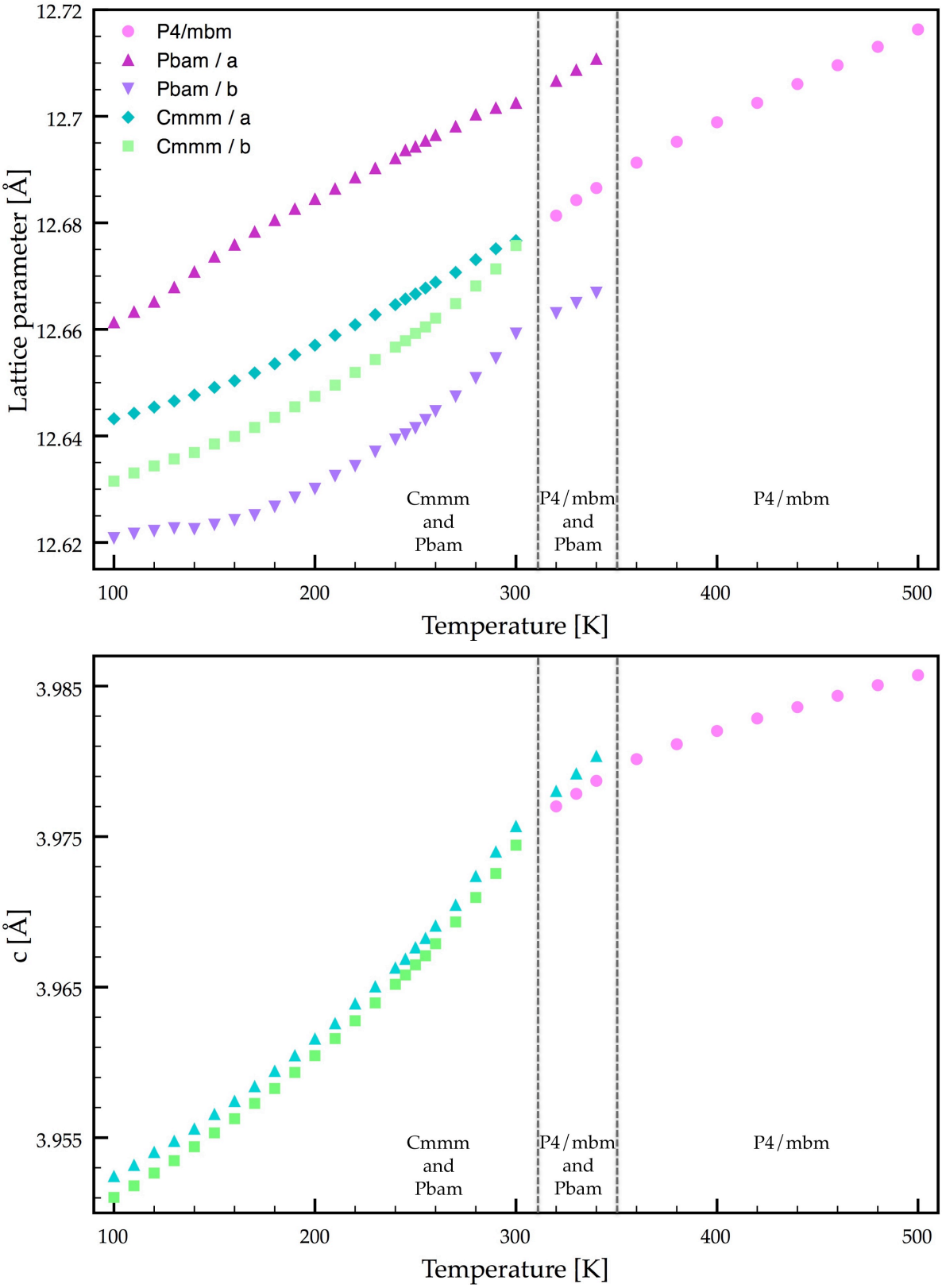

Figure 3.29: Lattice parameters (top) a and b, and (bottom) c, for all phases of $K_{0.58}FeF_3$ with the lattice parameters a and b for Cmmm divided by √2 to allow them to be plotted on the same scale as the remaining phases

3.4.2 $K_{0.5}FeF_3$

This sample was investigated by standard PXRD but, again, it was noted that the fine resolution of high-resolution sPXRD was needed to fully characterise the sample. sPXRD data were thus collected in the temperature range from 100 K to 500 K. Three structural models were presented for this composition in the ICSD. These were the same models as for the $K_{0.6}FeF_3$ model and summarised in Table 3.1. The 295 K data set was used as a starting point to fit or exclude any or all of these reported variants. The orthorhombic *Bbm2* model (a = 35.730(3) Å, b = 17.872(1) Å, c = 7.9030(6) Å) did not match the observed intensities and many predicted peaks were absent, and so was discarded. Consequently, both of the tetragonal models, one with the simple 4 Å c axis and the other with the doubled one, were used. The *P4bm* (a = 12.634(1) Å, c = 3.9515(3) Å) model gave a good fit, but there were several small peaks that were indexed by the doubled c axis but not the simple c axis, Figure 3.30. Therefore, the tetragonal $P4_2bc$ (a = b = 12.634(1) Å, c = 7.9030(6) Å) referred to as the COS model by Fabbrici *et al.*[17] was used in further refinements. It was also apparent from the room temperature data that there was a co-existence of at least two TTB phases as the peaks seemed to have shoulders on one side, Figure 3.31, that could not be accounted for by using only a single-phase model.

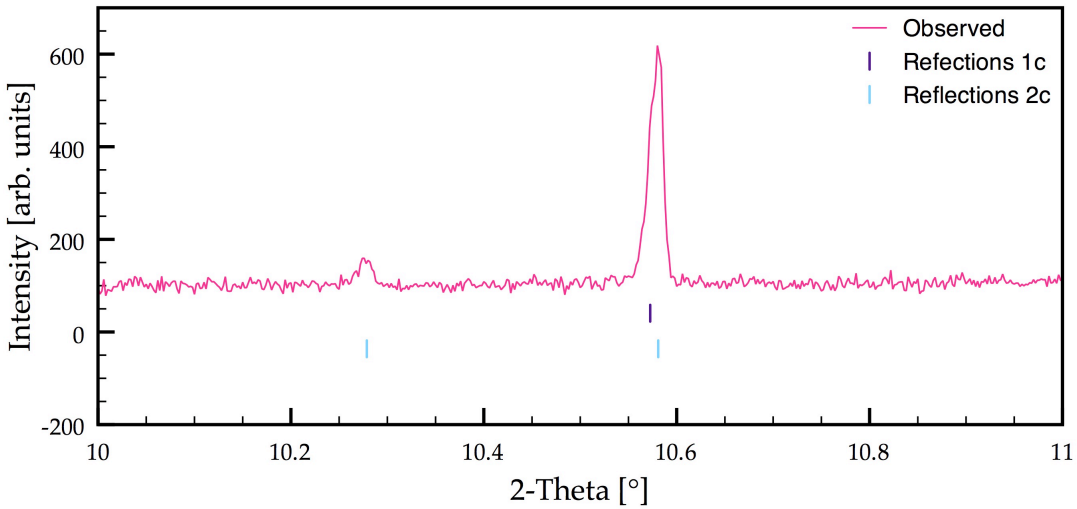

Figure 3.30: Excerpt from the 500 K $K_{0.5}FeF_3$ sPXRD data showing a peak that can be indexed by the (2c) model but not by the (1c) model

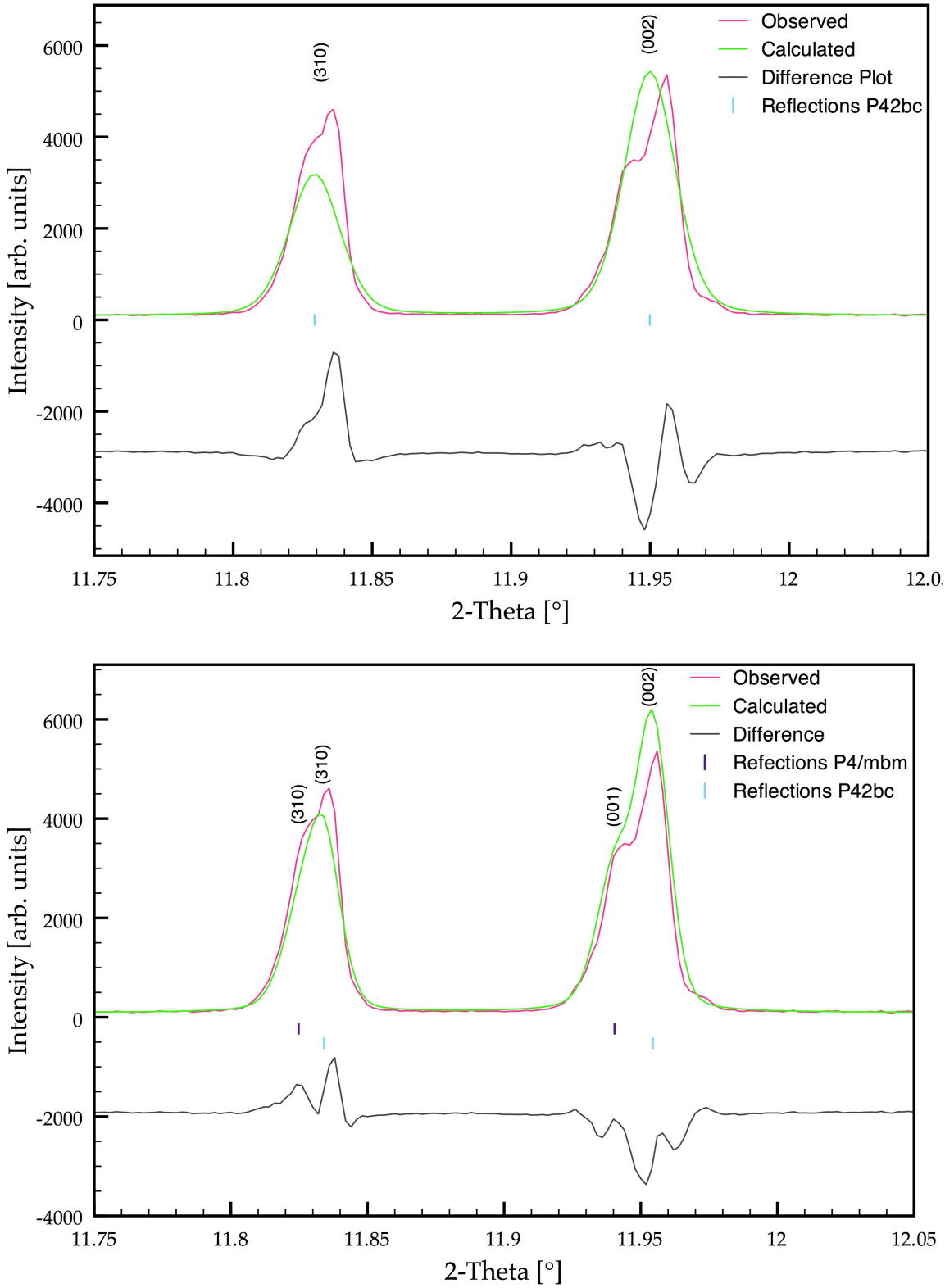

Figure 3.31: Excerpt from the sPXRD pattern of $K_{0.5}FeF_3$ at 500 K indicating the shoulders on the peaks that cannot be fitted by only the $P4_2bc$ TTB model (top) but can be fitted by adding the P4/mbm model (bottom)

Due to the fact that the high temperature data for $K_{0.58}FeF_3$ showed only the existence of one phase (see Section 3.4.1), it was decided to start the refinements using the *P4₂bc* model as a starting point. The 500 K data set still showed the shoulders on the peaks. Due to the fact that the shoulders appeared on only one side of the peak, a second tetragonal phase was added. This second phase was set to the default *P4/mbm* ideal TTB model as determined for the previous compound. This model accounted well for the observed shoulders. The resultant Rietveld refinement is shown in Figure 3.32 (with detailed fits in Figures 3.33 and 3.34), and Tables 3.7 and 3.8 list the structural parameters for both phases.

For all refinements in this discussion the following were refined: the background (a shifted Chebyschev function with 9 terms), the detector zero point, the scale factor, and the phase fractions. For the *P4/mbm* tetragonal TTB phase the following were also refined: the lattice parameters, atom positions, site occupancy of K2, isotropic atomic displacement parameters, and pseudo-Voigt profile parameters GW (for the Gaussian contribution) and LY (for the Lorentzian contribution). For the second tetragonal phase, *P4₂bc*, the following were also refined: the lattice parameters, site occupancy of K2, isotropic atomic displacement parameters of the K^+ ions, and pseudo-Voigt profile parameters GW (for the Gaussian contribution) and LY (for the Lorentzian contribution). For each of the two phases, the atomic displacement parameters for the two potassium ions were constrained to be the same to prevent any correlation effects affecting the site occupancy values.

All of the peaks were indexed by the two models but the reduced χ^2 value remained high at 3.745 for the 500 K data set. This indicated that the models used were merely approximations. However, due to a lack of other suitable models, these two were used as a starting point to gauge the phase behaviour of the compound. The lattice parameters, Figure 3.35, of the both the *P4/mbm* and *P4₂bc* phases were plotted as a function of temperature. The same was done for the potassium content and the weight fraction, Figure 3.36.

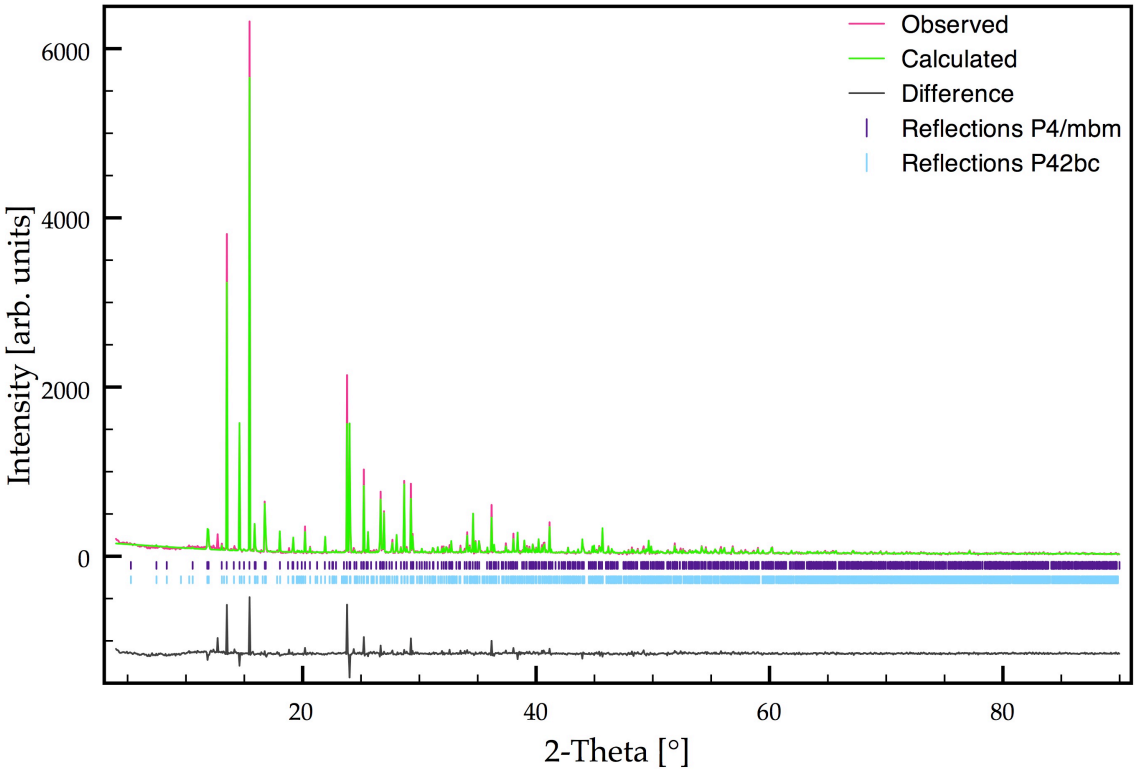

Figure 3.32: Rietveld plot for $K_{0.5}FeF_3$ at 500 K with both the P4/mbm and $P4_2bc$ models

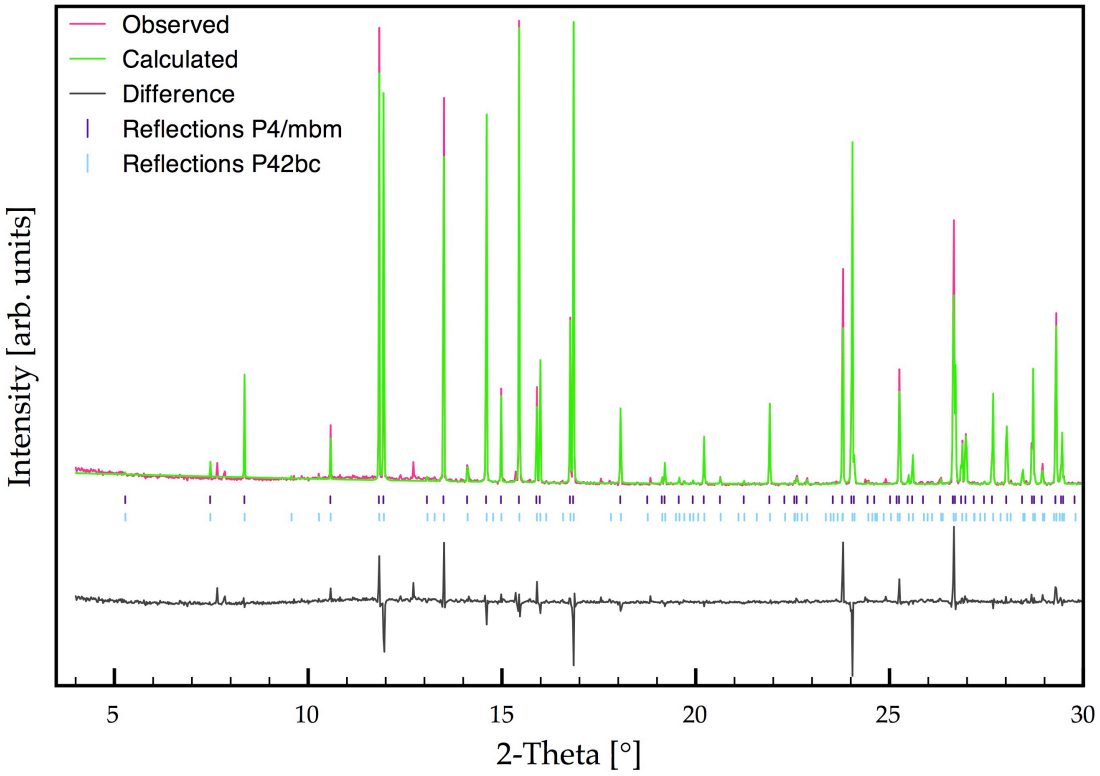

Figure 3.33: Detailed Rietveld plot for $K_{0.5}FeF_3$ in P4/mbm and $P4_2bc$ at 500 K showing the 3 to 30° 2-theta range

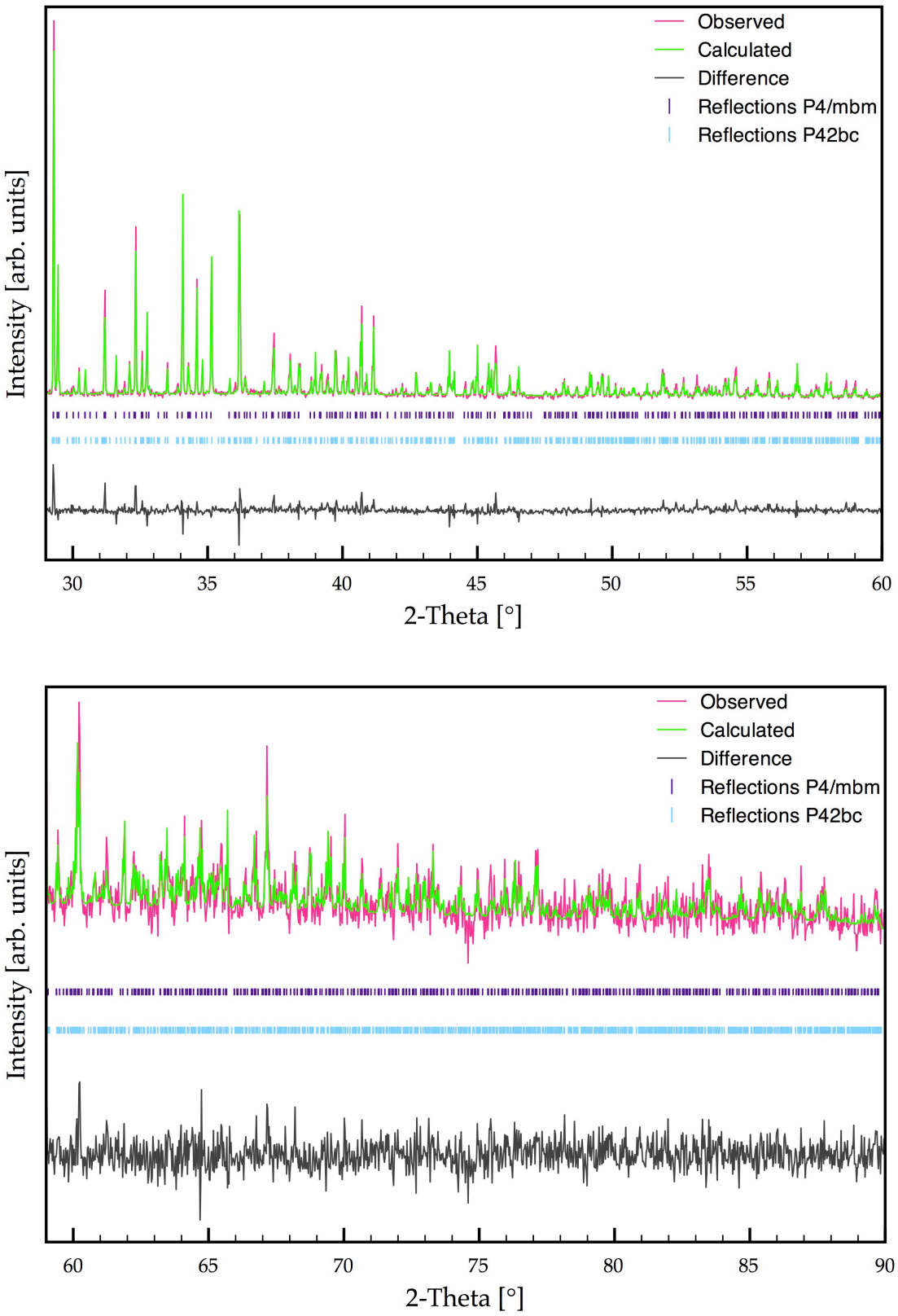

Figure 3.34: Detailed Rietveld plot for $K_{0.5}FeF_3$ in P4/mbm and $P4_2bc$ at 500 K showing the 30 to 60° 2-theta range (top) and the 60 to 90° 2-theta range (bottom)

Table 3.7: Structural parameters for the *P4/mbm* model in $K_{0.5}FeF_3$ at 500 K (a = 12.67087(3) Å, c = 3.968235(13) Å, and V = 637.104(4) Å^3, χ^2 = 3.745, wR_p = 12.98%, R_p = 16.09%) with isotropic atomic displacement parameters

Atom	Site	Site occupancy	x	y	z	U_{iso}x100 Å^2
Fe1	2c	1	0.5	0	0.5	0.49(7)
Fe2	8j	1	0.21226(12)	0.07456(12)	0.5	0.48(3)
K1	4h	1	0.1721(2)	0.3279(2)	0	4.02(6)
K2	2a	0.660(8)	0	0	0	4.02(6)
F1	8j	1	0.1442(4)	-0.0710(5)	0.5	3.10(18)
F2	4h	1	0.2826(4)	0.2174(4)	0.5	2.0(2)
F3	8j	1	0.3440(5)	-0.0066(4)	0.5	3.24(18)
F4	2d	1	0.5	0	0	4.3(4)
F5	8i	1	0.2083(4)	0.0760(4)	0	2.06(13)

Table 3.8: Structural parameters for the *$P4_2bc$* model in $K_{0.58}FeF_3$ at 500 K (a = 12.66096(3) Å, c = 7.927206(19) Å, and V = 1270.731(7) Å^3, χ^2 = 3.745, wR_p = 12.98%, R_p = 16.09%) with isotropic atomic displacement parameters

Atom	Site	Site occupancy	x	y	z	U_{iso} x 100 Å^2
Fe1	4b	1	0.5	0	0.2104	1.151
Fe2	8c	1	0.21305	-0.07416	0.7105	1.151
Fe3	8c	1	0.21096	-0.07425	0.2096	1.150
K1	8c	1	0.1719	-0.3273	0.4597	* 4.02(6)
K2	4a	* 0.623(6)	0	0	-0.0394	* 4.02(6)
F1	8c	1	0.27590	-0.21431	0.2055	2.30
F2	8c	1	0.34418	-0.00107	0.2036	4.05
F3	8c	1	0.51460	-0.15305	0.2101	2.94
F4	8c	1	0.1490	0.0672	0.2052	3.28
F5	8c	1	0.07321	-0.13734	0.2049	3.08
F6	8c	1	0.2077	-0.0747	0.4482	4.4
F7	8c	1	0.2102	-0.0783	-0.0394	4.2
F8	4b	1	0.5	0	0.4573	5.26

* refined variables; all other variables taken from the COS cif from the ICSD

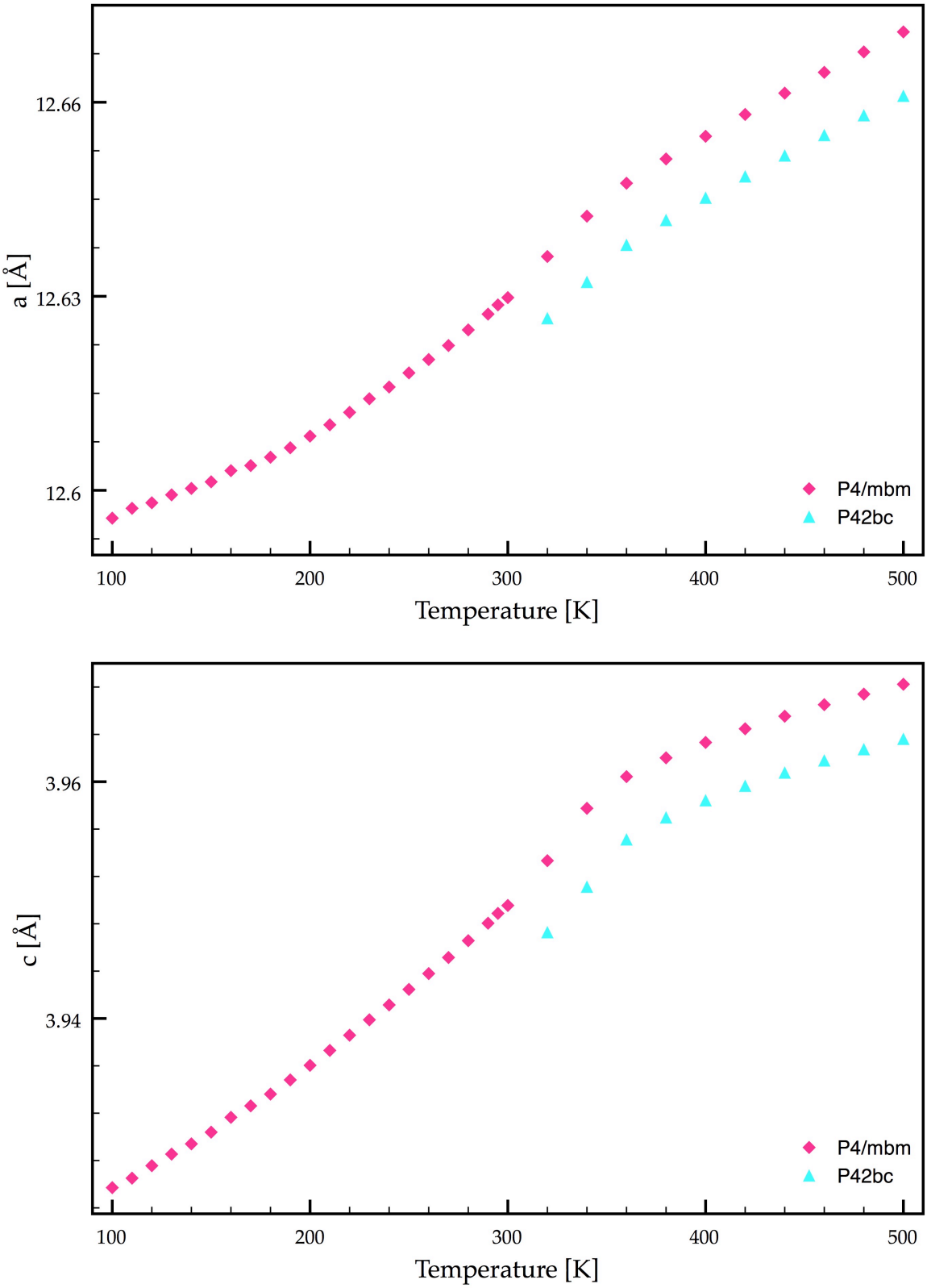

Figure 3.35: Lattice parameters a (top) and c (bottom) of the P4/mbm and $P4_2bc$ phases, with the c lattice parameter for $P4_2bc$ divided by two to plot it on the same scale as P4/mbm versus temperature

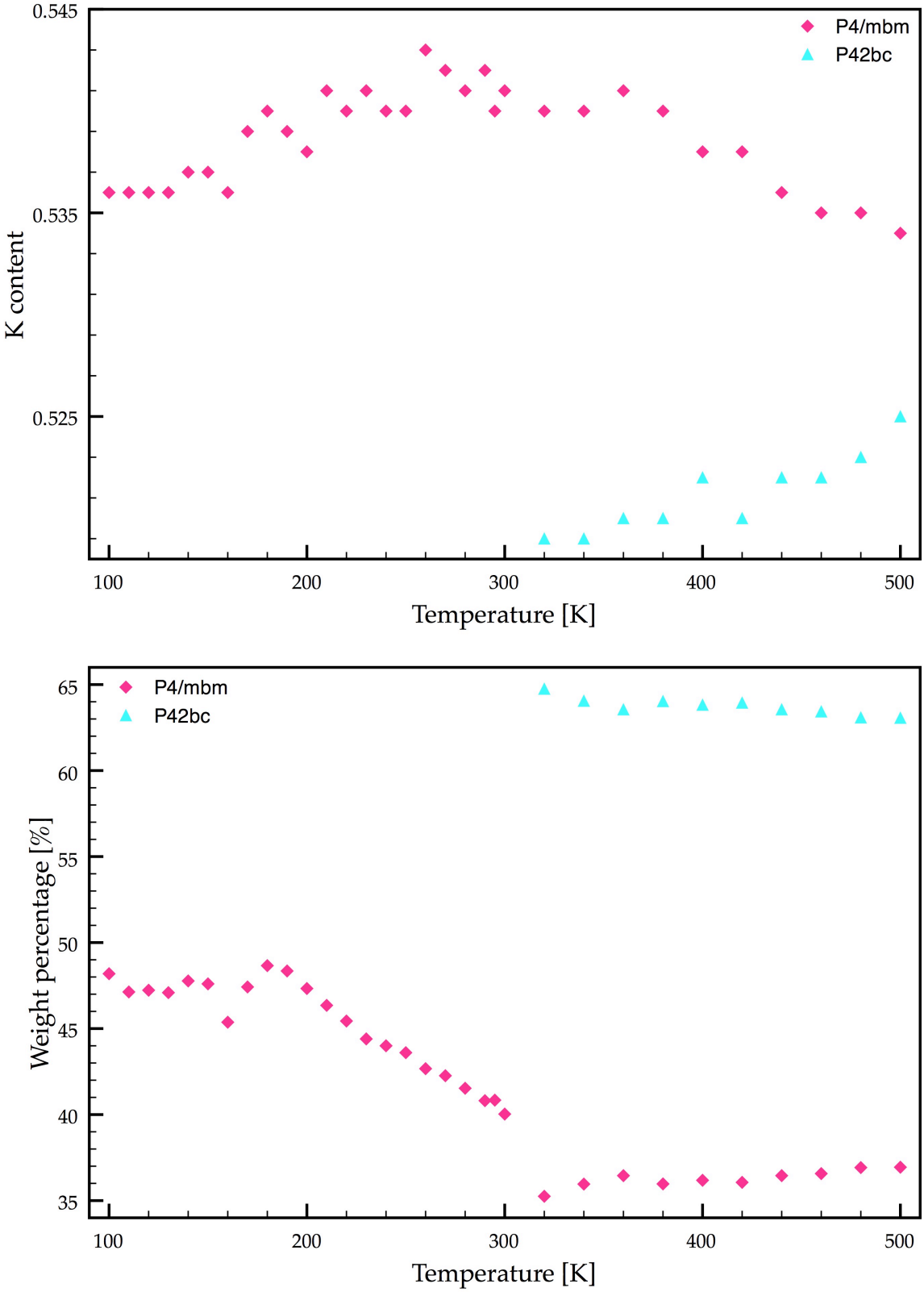

Figure 3.36: Potassium content (top) and percentage (by weight) (bottom) of the P4/mbm and $P4_2bc$ phases versus temperature

The potassium content of the *P4/mbm* phase was on average 0.54, and 0.52 for the $P4_2bc$ model. Consequently, the *P4/mbm* model will referred to as being $K_{0.54}FeF_3$, and the $P4_2bc$ model as $K_{0.52}FeF_3$.

Although there were several long bond lengths in the [FeF_6] octahedra in the *P4/mbm* model, Table 3.9, there was no clear preference by either Fe ion for a particular site. The $P4_2bc$ model is the reported charge-ordered structure model, and thus the ions did selectively order although this could not be confirmed from the experimental data, as the atom positions were not refined. The Fe2 sites were occupied by the Fe^{2+} ions, the Fe3 site by Fe^{3+} ions, and the Fe1 site was a mixture of both ions. Figure 3.37 indicates the various sites in the TTB structure.

Below 400 K, the profile parameters for *P4/mbm* were constrained to be the average of the values from the refinements from 500 K to 400 K.

The (hk0) peaks for $P4_2bc$ began to broaden at 320 K and so an orthorhombic model was fitted to the data. The best fit was obtained by taking the *Cmmm* model as described in Section 3.4.1. This model had only a (1c) *c*-axis, but as it was merely an approximation model, it was deemed sufficient as a starting point. The other tetragonal phase, *P4/mbm*, remained unchanged to 100 K. The lattice parameters, site occupancy of K2, isotropic displacement parameters of the two K^+ ions (constrained to be the same), and the pseudo-Voigt profile parameters GW and LY were refined for the *Cmmm* model. A Rietveld fit for the data is given in Figure 3.38 with detailed plots in Figures 3.39 and 3.40.

The lattice parameters indicated that the sample was well defined by the model, Figure 3.41. Both the orthorhombic *a* and *b* lattice parameters diverged from the tetragonal model to distinctly different values at low temperatures. The *c* lattice parameter followed on smoothly from the high temperature tetragonal model. The K^+ content and the weight fraction as shown in Figure 3.42, on the other hand, showed a great variation with temperature. This was attributed to the *P4/mbm* model which most likely did not really stay tetragonal at low temperatures, but the change was so subtle that it could not be pinpointed. Also, there seemed to be a bug in the GSAS programme suite, as the error bars on the orthorhombic model became zero for most values. This

could not be remedied and so it was not clear if the data were agreeing within the error bars, but it is likely that they do.

Table 3.9: Bond lengths [Å] for $K_{0.54}FeF_3$ in the tetragonal *P4/mbm* model over the temperature range 500 K to 320 K obtained from the Rietveld refinements of the sPXRD data

Temperature [K]	Fe1-F3	Fe1-F4	Average
500	1.979(7)	1.98412(1)	1.989
480	1.973(6)	1.98370(1)	1.977
460	1.976(6)	1.98326(1)	1.978
440	1.979(6)	1.98277(1)	1.980
420	1.986(7)	1.98224(1)	1.985
400	1.989(6)	1.98166(1)	1.987
380	1.982(7)	1.98101(1)	1.982
360	1.973(7)	1.98022(1)	1.975
340	1.977(7)	1.97888(1)	1.978
320	1.978(7)	1.97667(1)	1.978

Temperature [K]	Fe2-F1	Fe2-F1	Fe2-F2	Fe2-F3	Fe2-F5	Average
500	2.035(6)	1.996(7)	2.017(3)	1.961(6)	1.98483(16)	1.996
480	2.039(6)	1.991(6)	2.019(3)	1.969(6)	1.98429(14)	1.998
460	2.035(6)	1.995(6)	2.018(3)	1.964(6)	1.98384(14)	1.997
440	2.030(6)	2.000(6)	2.021(3)	1.962(6)	1.98349(16)	1.997
420	2.030(6)	2.000(6)	2.018(3)	1.957(6)	1.98309(17)	1.995
400	2.022(6)	2.007(6)	2.020(3)	1.945(6)	1.98259(18)	1.993
380	2.017(6)	2.007(6)	2.022(3)	1.954(6)	1.98204(19)	1.994
360	2.018(6)	2.007(6)	2.022(3)	1.963(6)	1.98097(16)	1.995
340	2.014(7)	2.008(7)	2.020(3)	1.953(6)	1.9800(2)	1.993
320	2.011(7)	2.009(7)	2.020(3)	1.953(6)	1.9777(2)	1.991

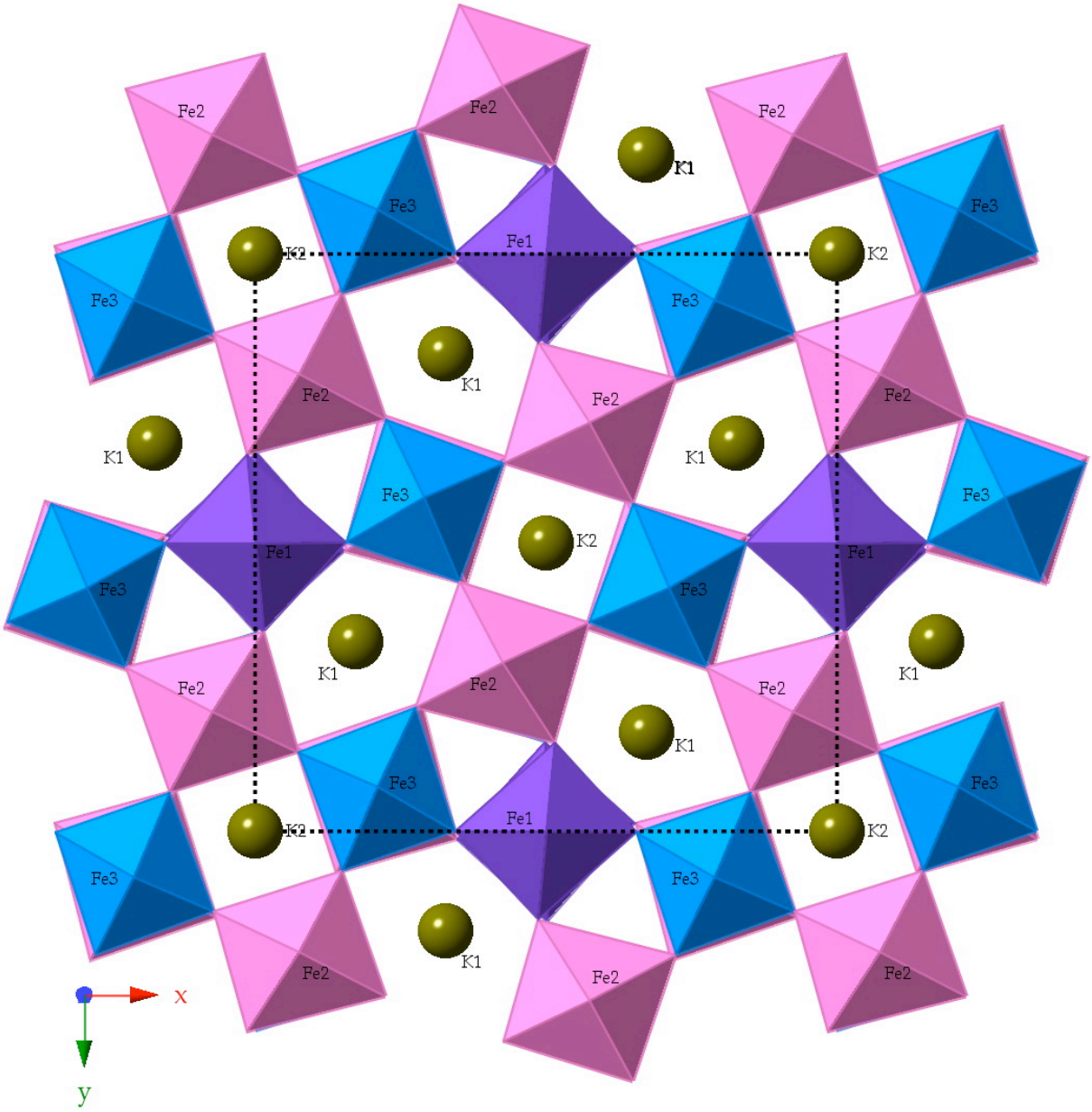

Figure 3.37: Unit cell of the $K_{0.52}FeF_3$ in $P4_2bc$ with the Fe1 site (purple) hosting both Fe^{2+} and Fe^{3+} ions, the Fe2 site (pink) the Fe^{2+} ions, and the Fe3 site (blue) the Fe^{3+} ions

A schematic summary of the lattice parameters is given in Figure 3.43. The investigation of this sample in the temperature range yielded an unknown phase separation for the entire temperature range and a new phase transition at 320 K. The coexistence of the two tetragonal phases is probably defined by their different potassium contents and this seems to be a thermodynamic phase separation, although this is yet to be confirmed.

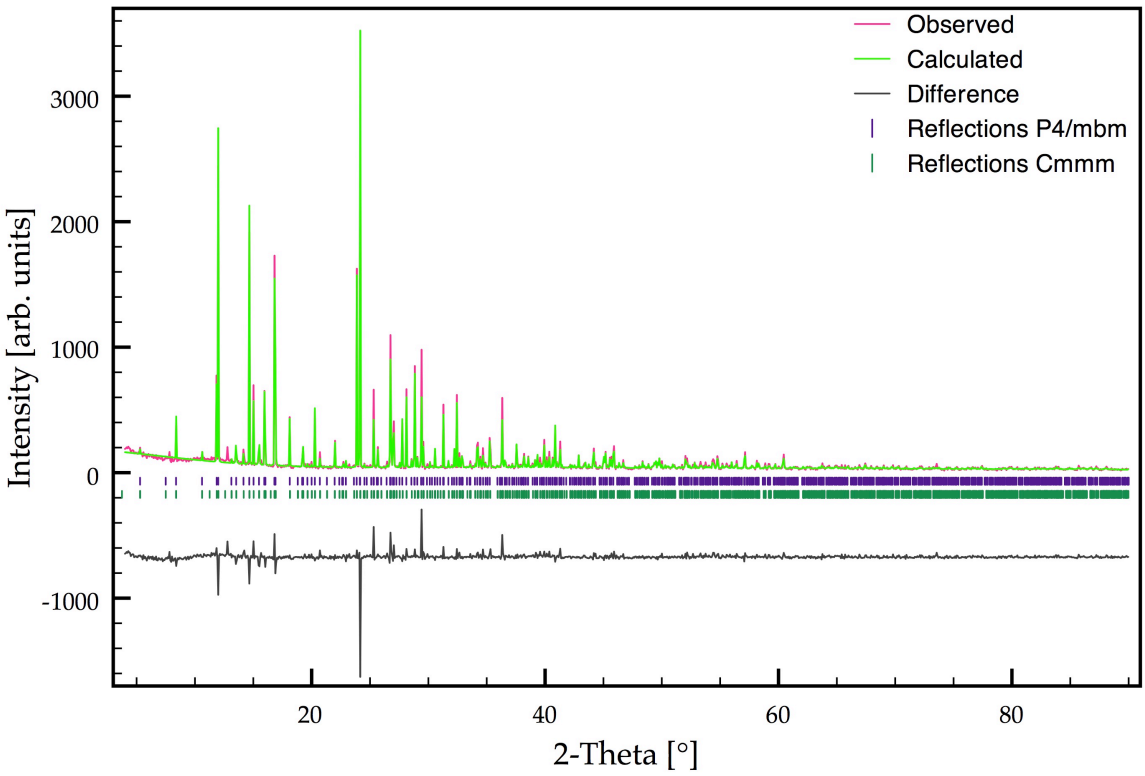

Figure 3.38: Rietveld plot for $K_{0.5}FeF_3$ at 300 K with both the P4/mbm and Cmmm

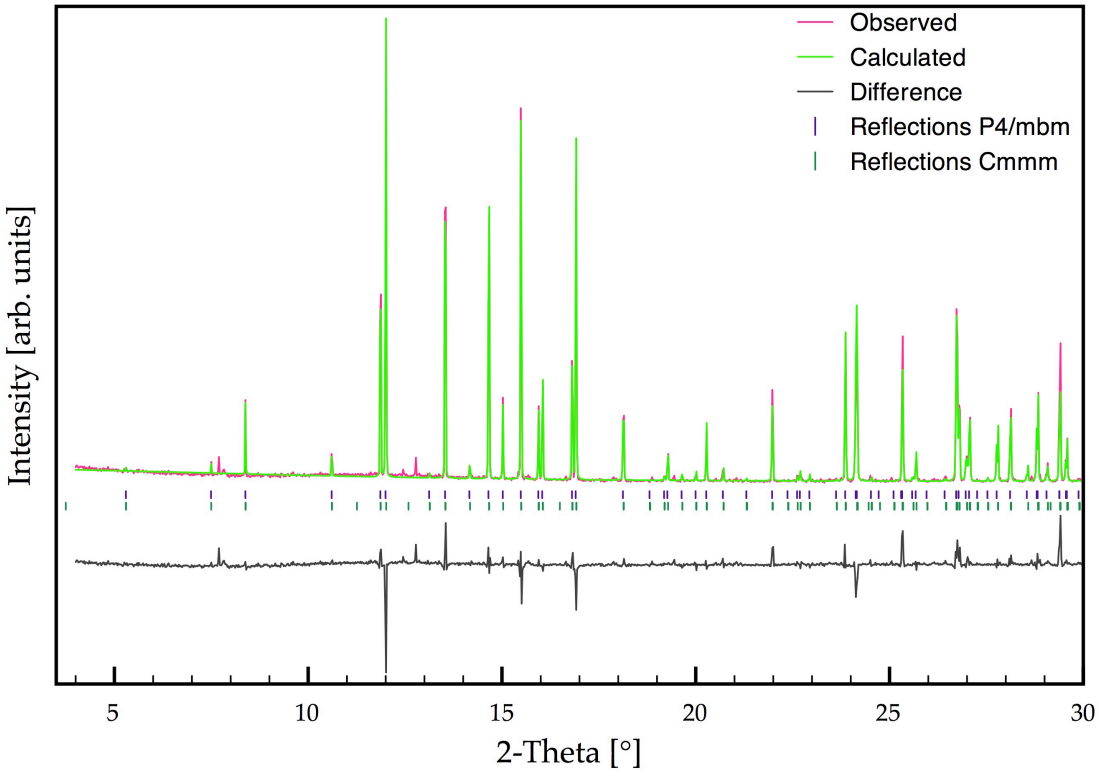

Figure 3.39: Detailed Rietveld plot for $K_{0.5}FeF_3$ in P4/mbm and Cmmm at 300 K showing the 3 to 30° 2-theta range

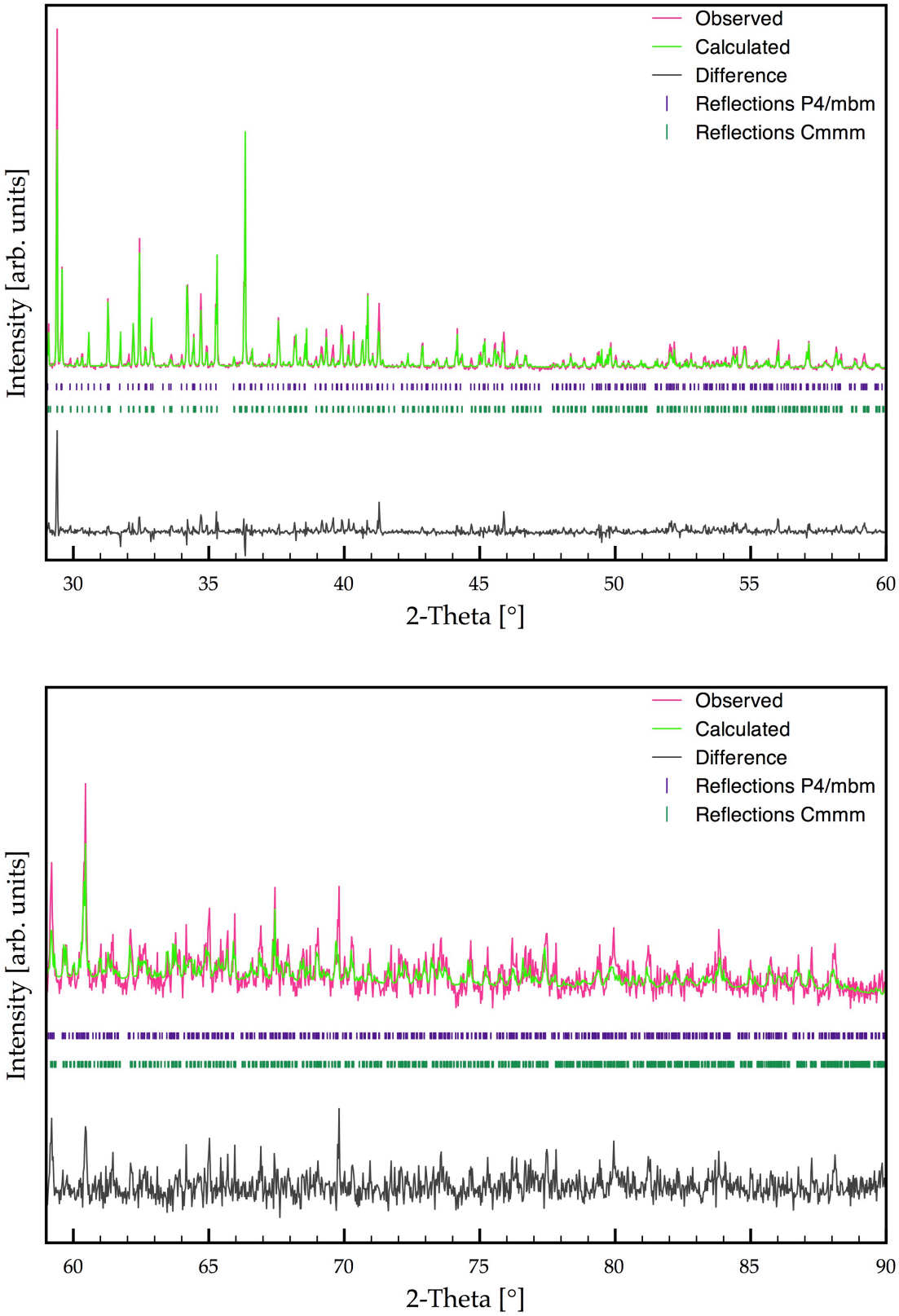

Figure 3.40: Detailed Rietveld plot for $K_{0.5}FeF_3$ in P4/mbm and Cmmm at 300 K showing the 30 to 60° 2-theta range (top) and the 60 to 90° 2-theta range (bottom)

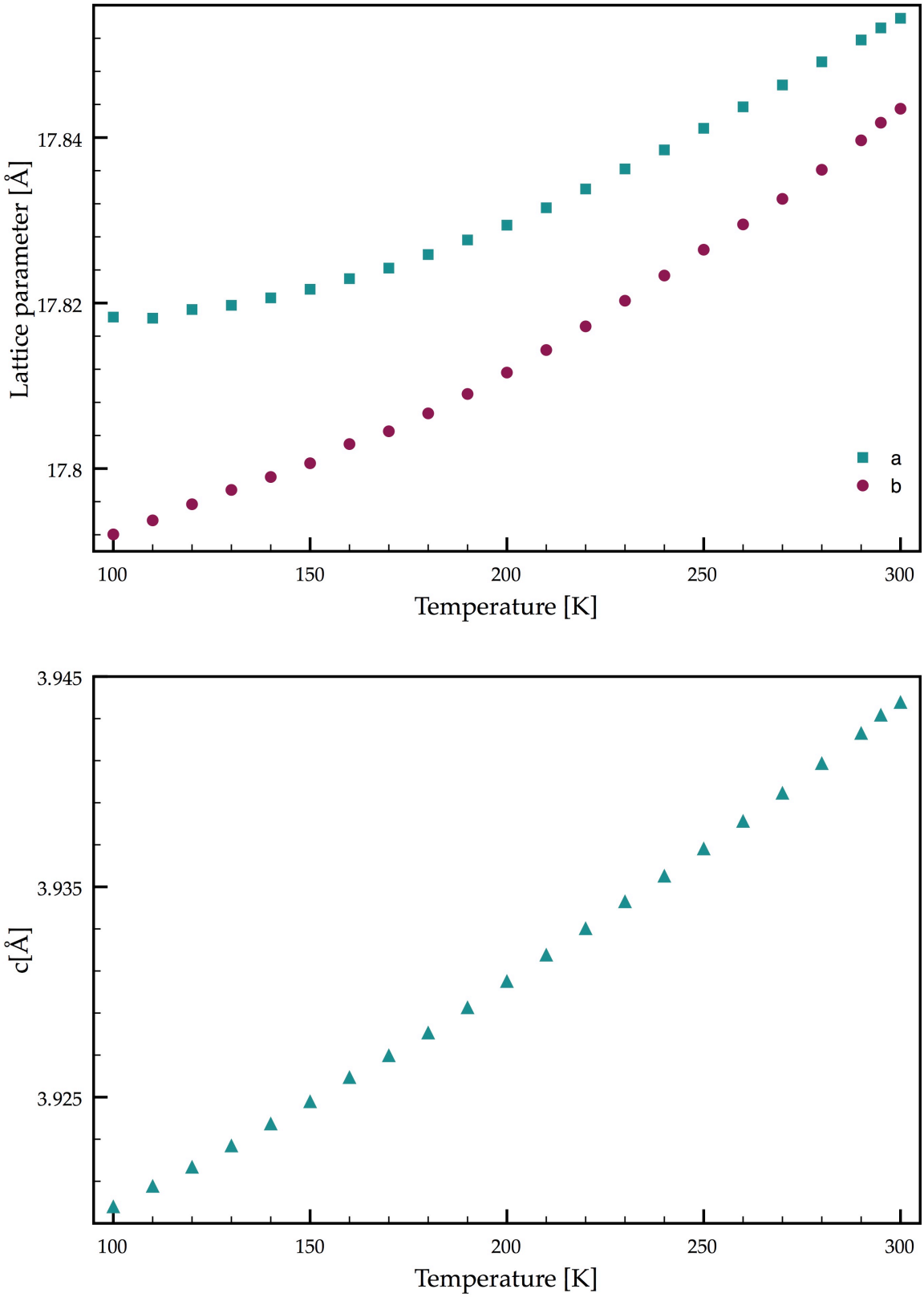

Figure 3.41: Lattice parameters a and b (top), and c (bottom) of the Cmmm phase versus temperature

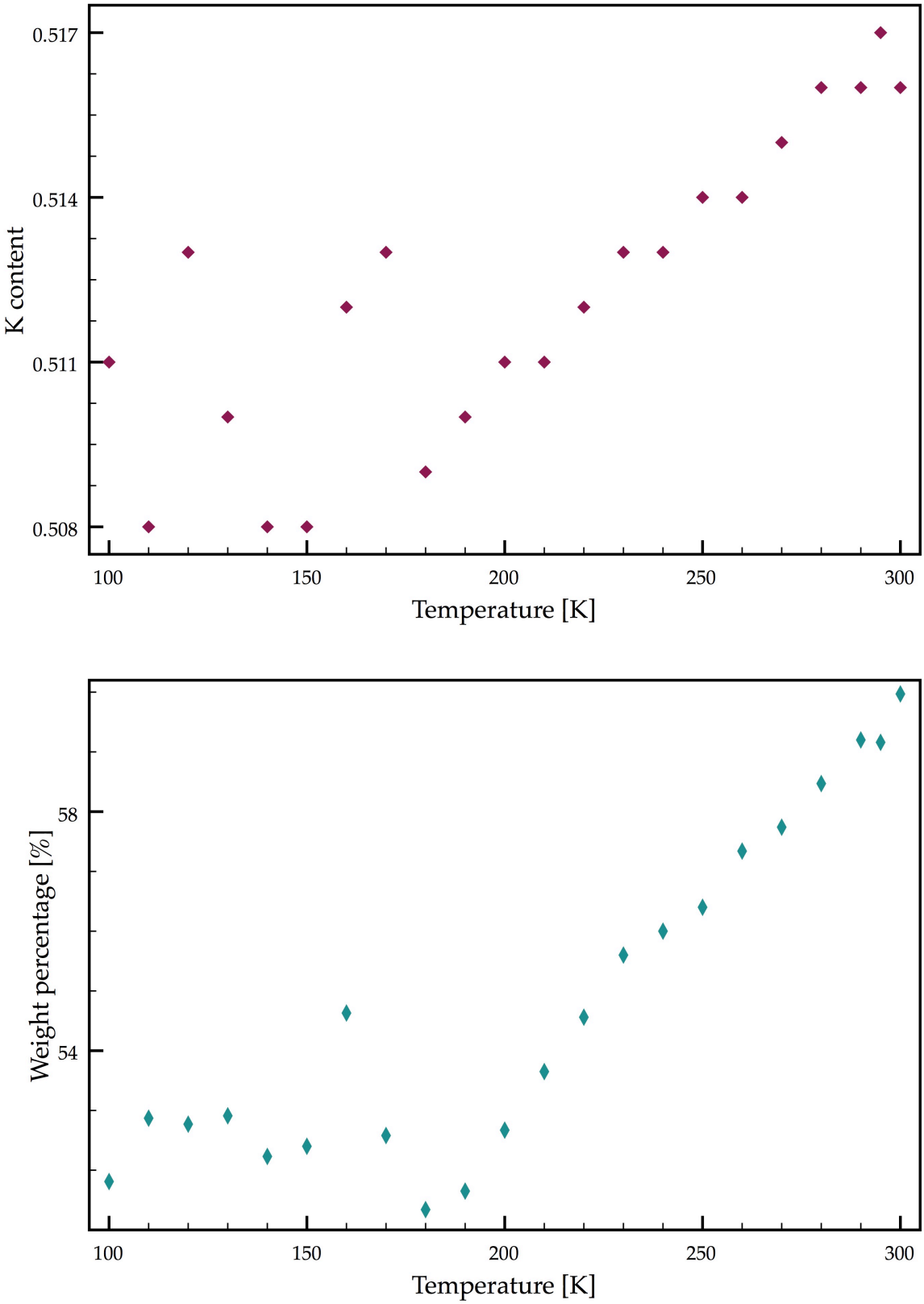

Figure 3.42: Potassium content (top), and phase percentage (by weight) (bottom) of the Cmmm phase as a function of temperature

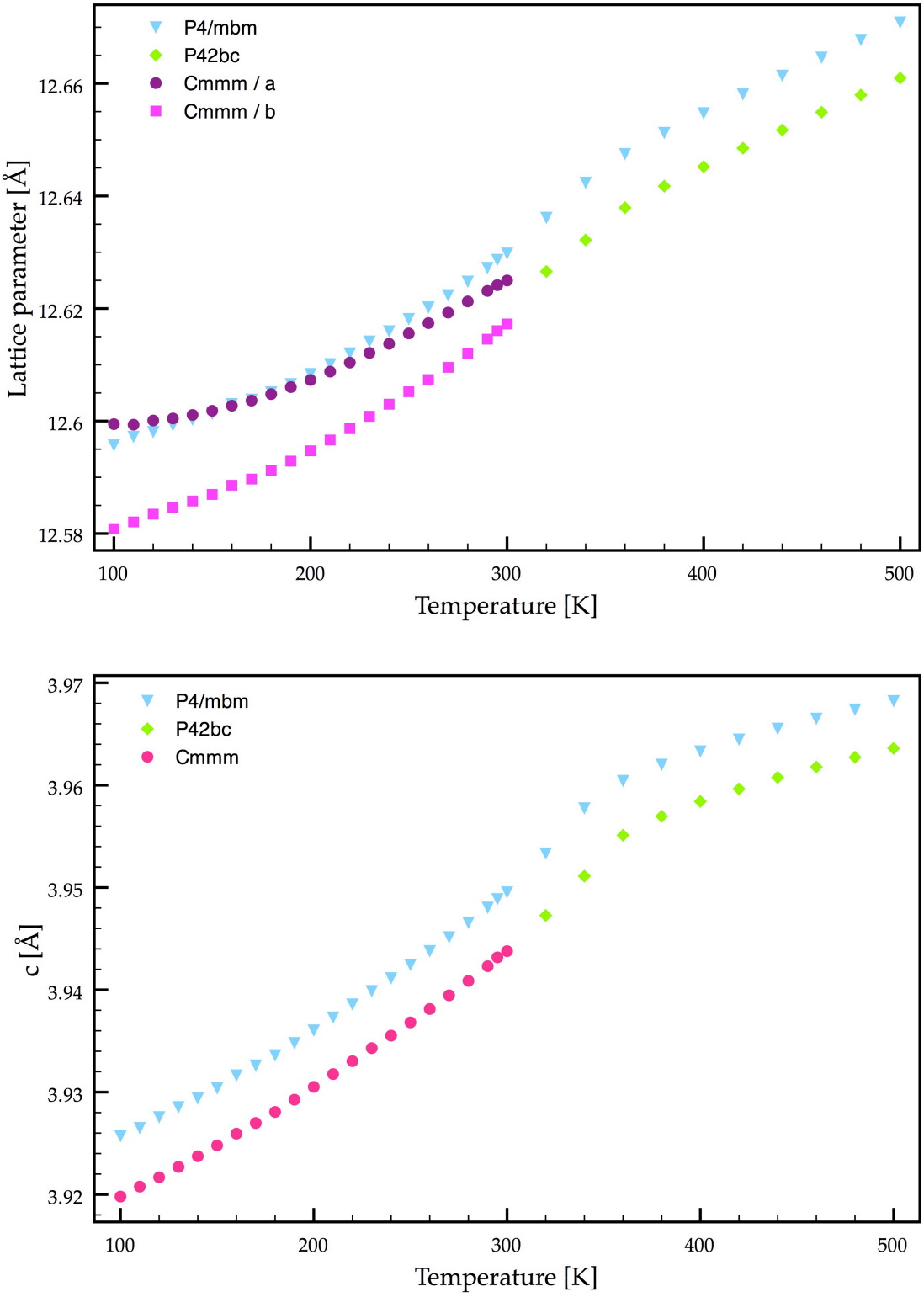

Figure 3.43: Combined lattice parameters for $K_{0.5}FeF_3$ showing a and b (top), and c (bottom) with the lattice parameters a and b for Cmmm divided by √2 allow them to be plotted on the same scale as the remaining phases

3.4.3 $K_3Cu_3Fe_2F_{15}$

This sample was initially investigated by standard PXRD. The lab X-ray data was of very poor resolution and so no starting models could be created. As with the two previous samples, it was noted that the fine resolution of high-resolution sPXRD was needed to fully characterise the sample. sPXRD data were hence collected in the temperature range from 100 K to 300 K in 50 K steps. Only one structural model has been reported for this compound: in the tetragonal standard TTB setting in *P4/mbm*. This model was presented by the collaborating research group (Blinc *et al*., Slovenia).

Two impurity phases were immediately identified: CuO (Stergiou *et al*.[33] *C2/c*, a = 4.794(3) Å, b = 3.362(1) Å, c = 5.228(2) Å, β = 99.74(4)°) and $KFeF_3$ (Miyata *et al*.[34] $Pm\bar{3}m$, a = 4.1198(1) Å). At room temperature, the main phase fitted the model given by Blinc *et al*.[21] (*P4/mbm*, a = 12.5925 Å and c = 3.9406 Å).

Single crystals of the TTB were also obtained and these were analysed on the Diamond beam line I19 at 150 K. A summary of the crystal data and refinement are given in Table 3.10, and the structure in Figure 3.44.

Table 3.10: Crystal data for $K_3Cu_3Fe_2F_{15}$ at 150 K

Formula	$K_3Cu_3Fe_2F_{15}$
Crystal system	Tetragonal
Space group	*P4/mbm*
Unit cell dimensions [Å}	a = 12.5787(6) Å c = 3.9086(2) Å
Volume [Å^3]	618.43(5)
Z	2
ρ(calc) [Mg/m^3]	3.784
Crystal size [mm]	0.020 x 0.040 x 0.040
Goodness-of-fit on F^2	1.098
Final R indices [I>2sigma(I)]	R_1 = 0.0494, wR_2 = 0.1124
R indices (all data)	R_1 = 0.0554, wR_2 = 0.1167

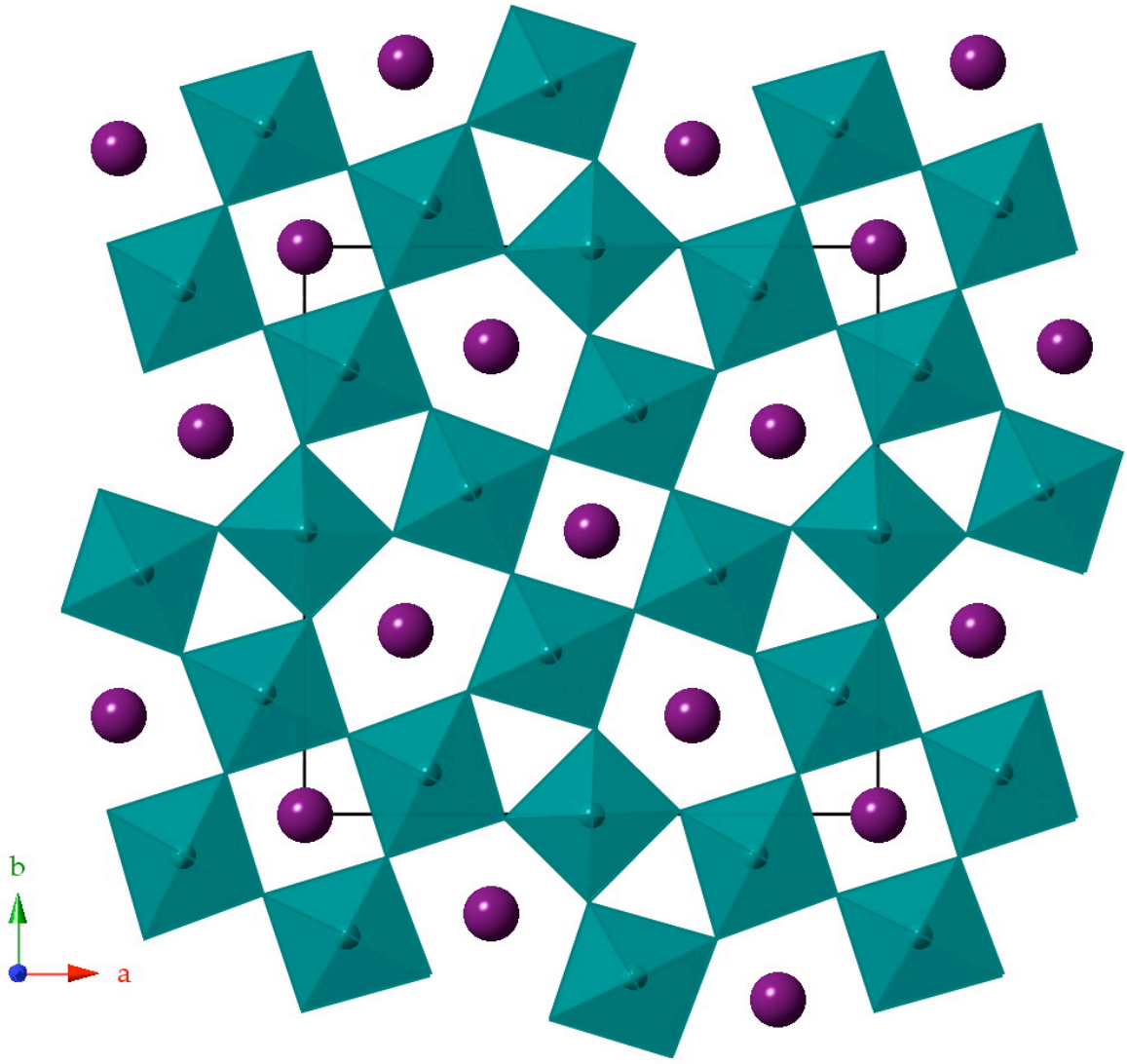

Figure 3.44: TTB structure of $K_3Cu_3Fe_2F_{15}$ viewed along the c-axis showing the randomly distributed [CuF_6] and [FeF_6] octahedra

The single crystal data agreed with the data reported by Blinc *et al*. The Cu^{2+} and Fe^{3+} ions were located in stoichiometric ratios on the two crystallographic (2c) and (8j) sites, Table 3.11. The bond lengths in the two sites showed no clear elongation in the axial M – F bond lengths as indicated in Table 3.12 and Figure 3.45, which would have indicated a Jahn-teller distortion of the Cu^{2+} site. Thus, the relative ratios were kept. Blinc and his co-workers came to the same conclusion with their analyses.

Table 3.11: Structural parameters for $K_3Cu_3Fe_2F_{15}$ from SCXRD at 150 K (a = 12.5787(6) Å, c = 3.9086(2) Å, and V = 618.43(5) Å^3, GOF = 1.098, wR_2 = 11.24%, R_1 = 4.94%) with anisotropic atomic displacement parameters

Atom	Site occupancy	x	y	z	U(eq)x100 Å^2
Fe1	0.4	0.5	0	0	1.22(3)
Cu1	0.6	0.5	0	0	1.22(3)
Fe2	0.4	0.42715(5)	0.28572(5)	0	1.23(2)
Cu2	0.6	0.42715(5)	0.28572(5)	0	1.23(2)
K1	1	0.5	0.5	-0.5	2.46(5)
K2	1	0.67465(12)	0.17465(12)	-0.5	3.97(6)
F1	1	0.5	0	-0.5	6.2(4)
F2	1	0.2819(3)	0.2181(3)	0	3.32(14)
F3	1	0.4288(5)	0.2895(4)	-0.5	4.68(16)
F4	1	0.5070(3)	0.1536(3)	0	3.47(11)
F5	1	0.3598(4)	0.4261(3)	0	3.49(11)

U(eq) is defined as one third of the trace of the orthogonalised U^{ij} tensor

Table 3.12: Bond lengths for $K_3Cu_3Fe_2F_{15}$ at 150 K obtained from by SCXRD

Bond	Bond length [Å]
[Cu1/Fe1] – F4 (x4)	1.934(4)
[Cu1/Fe1] – F1 (x2)	1.9543(1)
Average [Cu1/Fe1] – F*	1.941
[Cu2/Fe2] – F4	1.942(4)
[Cu2/Fe2] – F3 (x2)	1.9550(2)
[Cu2/Fe2] – F5	1.959(4)
[Cu2/Fe2] – F2	2.015(4)
[Cu2/Fe2] – F5	2.068(5)
Average [Cu2/Fe2] – F*	1.982

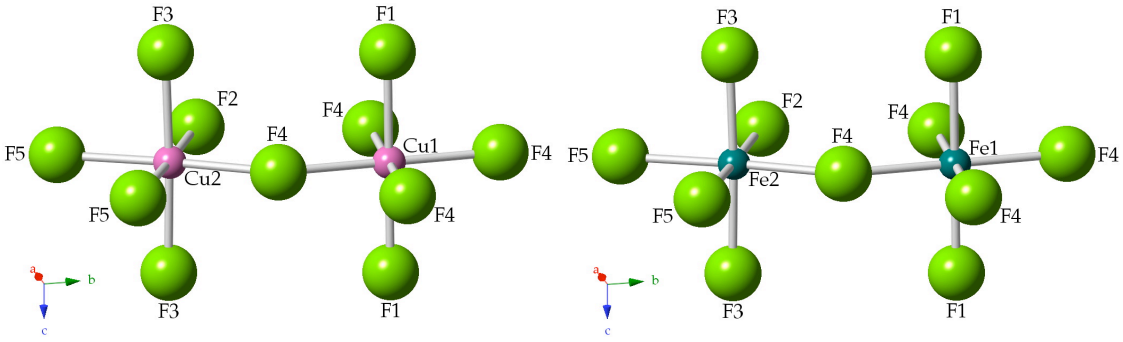

Figure 3.45: Coordination environments for the sites [Fe1/Cu1] and [Fe2/Cu2] in $K_3Cu_3Fe_2F_{15}$ obtained from the SCXRD data

This model did not agree with the powder Rietveld refinement data at 150 K. At that temperature, there was clear evidence that the TTB phase was orthorhombic, Figure 3.46, as the (660) peak in the tetragonal model clearly split into two peaks at low temperatures. This was the same type of splitting as observed in both of the K_xFeF_3 samples, and so the *P4/mbm* starting model was converted into the "*Cmmm*" orthorhombic distortion using the program ISODISTORT.[29]

For all refinements the following parameters were refined: the background (using a cosine Fourier series with 9 terms); the detector zero point; the scale factor; and the phase fractions. For the TTB phase, specifically, the following were also included: lattice parameters; isotropic atomic displacement parameters, which were constrained so that the [Cu1/Fe1] and [Cu2/Fe2] ion pairs each had the same values; pseudo-Voigt profile parameters - GW (for the Gaussian contribution) and LY (for the Lorentzian contribution). The lattice parameters and profile parameters, GV and LY, were also refined for the impurity phase $KFeF_3$, except at 300 K, where the profile parameters were constrained to those of the 250 K data set. Only the lattice parameters were refined for the CuO impurity phase. The profile parameters GW and LY were set to the default values given in GSAS.

The two impurity phases, K_2FeF_5 and α-Fe_2O_3, showed no abnormal behaviour. The major impurity was $KFeF_3$ with a 13% weight fraction, followed by α-Fe_2O_3 with a weight fraction of 1.8%. The TTB phase made up the remaining 85%. This ratio did not change throughout the temperature range

investigated, Figure 3.47. The lattice parameters for both of the phases changed continuously and gave no indication that there was a phase transition or other anomaly in the analysed temperature range, Figures 3.47. The impurities were found to be a good fit throughout the temperature range and are not discussed further in this chapter.

The lattice parameters for the TTB phase behaved in the same manner as the ones for the impurity phases. That is to say, that there were no outliers or changes in the rates of contraction. This can be confirmed in Figure 3.48.

The fact that the SCXRD data gave a contradictory result to the sPXRD refinements was of no further concern as the SCXRD data showed many systematic weaknesses in the diffraction data. It was apparent that the single crystal was not representative of the bulk material. No phase transition has been reported for this compound as yet, but the transition is in line with the other observed transitions in the pure iron analogues. The magnetic data reported by Blinc *et al*. showed no anomalies in the phase transition temperature range. This was an unexpected result, as the pure iron analogues showed deviations in these temperature ranges, even if they were minor.[12]

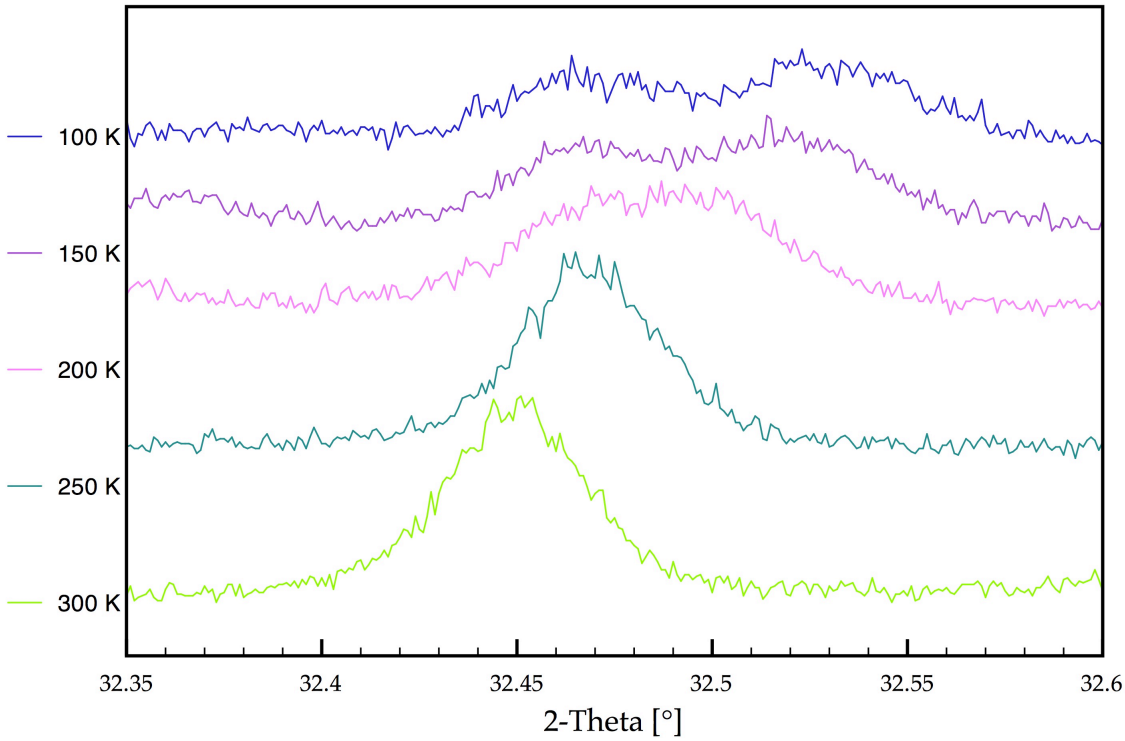

Figure 3.46: Excerpt from the sPXRD patterns of $K_3Cu_3Fe_2F_{15}$ as a function of temperature indicating the splitting of the "(660)" peak of the tetragonal model

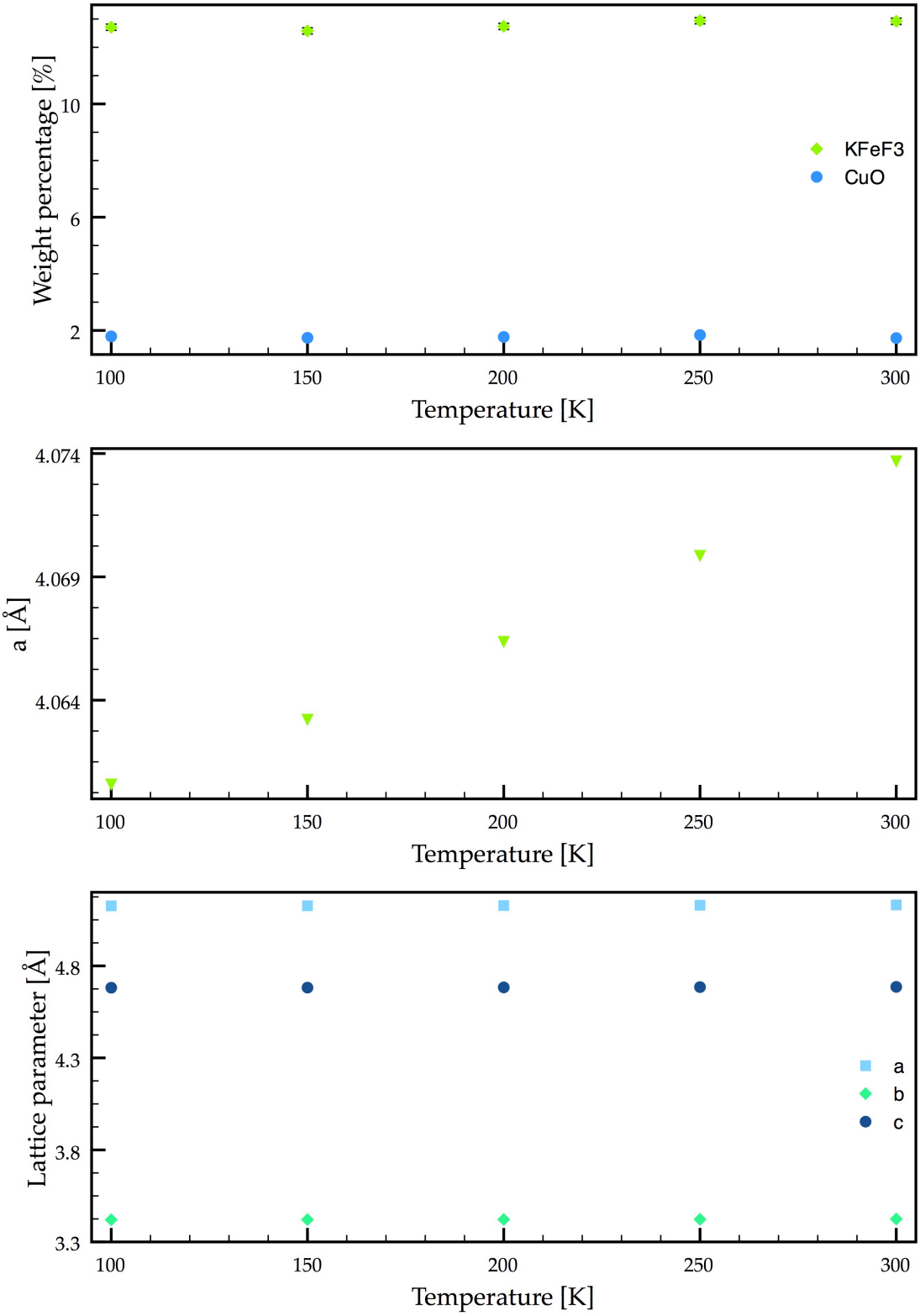

Figure 3.47: Weight fractions (top) for the impurity phases $KFeF_3$ and CuO, and their respective lattice parameters (middle) and (bottom) versus temperature

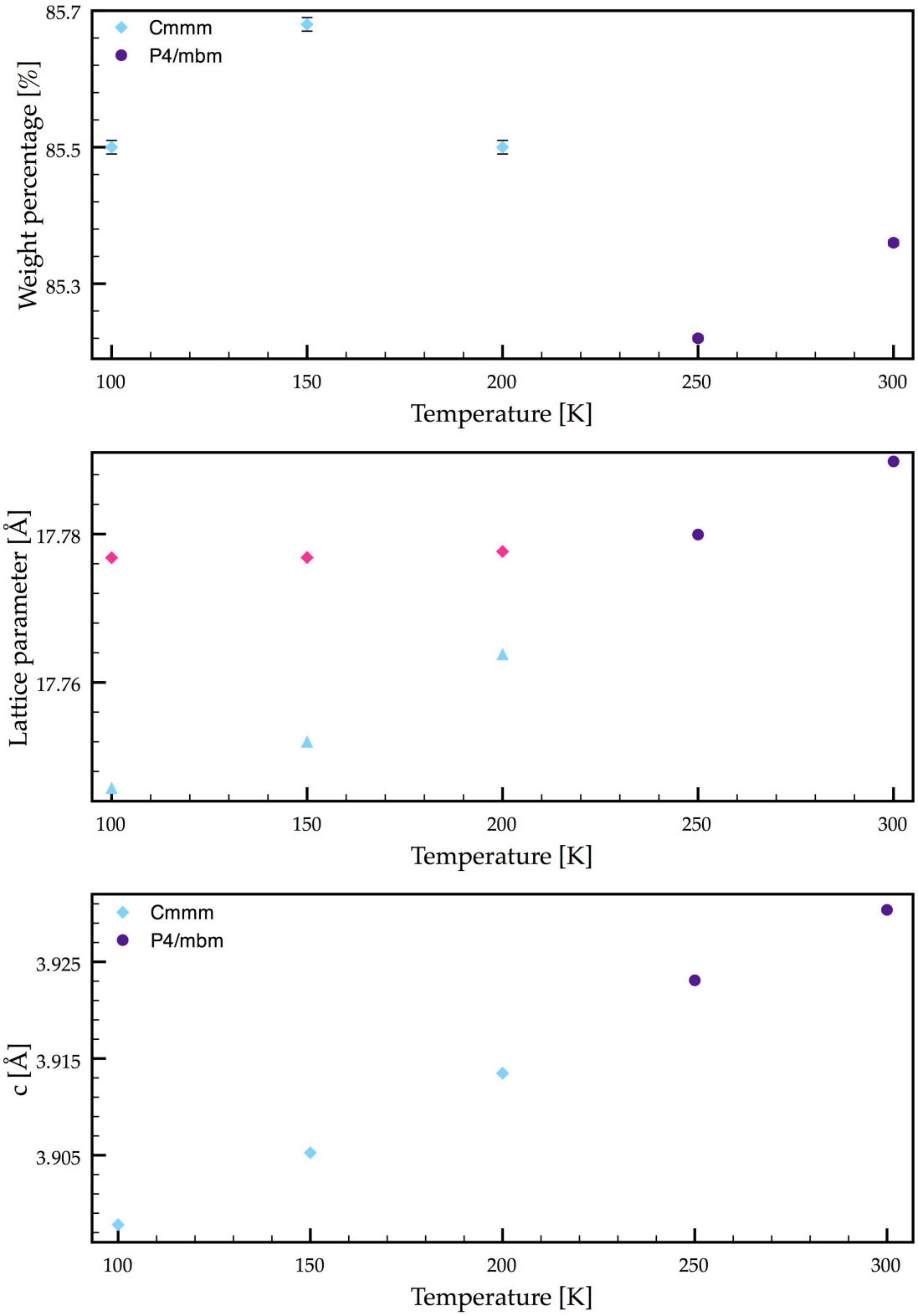

Figure 3.48: Weight fraction (top) for $K_3Cu_3Fe_2F_{15}$ and the lattice parameters a and b (middle) and c (bottom) for both phases, with the lattice parameter a multiplied by √2 for the P4/mbm to allow them to be plotted on the same scale as Cmmm

3.5 Discussion

The tetragonal model reported for $K_{0.58}FeF_3$ was the same as that reported in the literature.[8] Different models for the tetragonal phase in either the aforementioned centrosymmetric space group or the noncentrosymmetric space group *P4bm* have been reported, most of the reports agree that it should be reported as noncentrosymmetric. We found no evidence that the noncentrosymmetric model (e.g. *P4bm*) was better than the centrosymmetric one (*P4/mbm* in this instance). The appearance of a phase separation below 340 K was new and unexpected. This co-existence of the tetragonal and orthorhombic phases close to room temperature may well explain why there have been conflicting reports of the single crystal structure of this compound at room temperature. The "*Cmmm*" approximation model at low temperatures has not been reported for this family of solid solutions either. This orthorhombic distortion was distinct from that for the "*Pbam*" approximation model that showed a distortion of the [FeF_6] octahedra in the "perovskite" core, whereas the distortion in "*Cmmm*" was driven by a polarisation along the *c*-axis. This was the same type of distortion mode as that reported by Fabbrici *et al*.[17] in the FES structure in *Bbm2*. Further, they stated that they drew their conclusions from a comparison of their electron diffraction data with the electron diffraction data from the TTB compound $Ba_2NaNb_5O_{15}$ (BNN).[35] It is interesting to note that whilst BNN shows a quasi-commensurate modulation in the *ab* plane, they did not see any such evidence for the K_xFeF_3 samples analysed. We found tentative evidence of just such a distortion in our sample of $K_{0.58}FeF_3$.

The lower K^+ content sample, $K_{0.5}FeF_3$, showed many of the same characteristics as the $K_{0.58}FeF_3$ sample. At high temperatures, the centrosymmetric *P4/mbm* was the best model. But, even at 500 K, there was already a distinct phase separation, with the existence of a second tetragonal phase, $P4_2bc$. This second tetragonal phase showed clear charge-ordering leading to a doubling of the *c*-axis. This charge-ordered structure was also reported for the TTB compounds $K_{0.54}(Mn,Fe)F_3$ at room temperature, as well as for $KMnCrF_6$.[13, 20] This co-existence of both a charge-disordered and charge-ordered phase was something that Fabbrici *et al*. had suggested as models at

different temperatures, not as simultaneous events. The charge-ordered structure then went through a phase transition to the same orthorhombic approximation model as the higher K^+ content sample, in the space group "*Cmmm*". The standard *P4/mbm* model remained throughout, although it may be assumed that there would be some manner of orthorhombic or monoclinic distortion that could not be evidenced from the data. Consequently, the tetragonal model was kept.

It was interesting to note that both of the samples underwent the tetragonal to orthorhombic distortion at around 320 K. This is not the case for their reported Curie temperatures. These varied greatly with composition.[11] The phase separations for both samples seemed to be driven by two different factors: $K_{0.58}FeF_3$ showed a distortion of the "perovskite" octahedra in the *ab*-plane leading to the orthorhombic distortion that affected only the *a* and *b* lattice parameters; whereas $K_{0.5}FeF_3$ separated into two tetragonal phases, with one showing a random distribution of iron atoms, whilst the other showed a clear preference for one set of ions above another in the crystallographic sites. This difference in phase separations contradicted the conclusion that Fabbrici *et el*. came to, which was that all members of the TTB composition in the K_xFeF_3 solid solution would show the same structures.[17]

The copper-doped analogue, $K_3Cu_3Fe_2F_{15}$, was characterised in the same high temperature tetragonal model as the two previous samples. But, unlike the K_xFeF_3 solid solutions, there was no evidence of a phase separation. Also, there was no evidence for charge-ordering, which was clearly visible from the observed M – F bond lengths. The phase transition to the orthorhombic phase, on the other hand, was clearly related to that of the K_xFeF_3 solid solutions. The approximation model "*Cmmm*" was the best estimate for the low-temperature structure.

A summary of the phase separations and phase transitions for the three reported TTB structures is given in Figure 3.49.

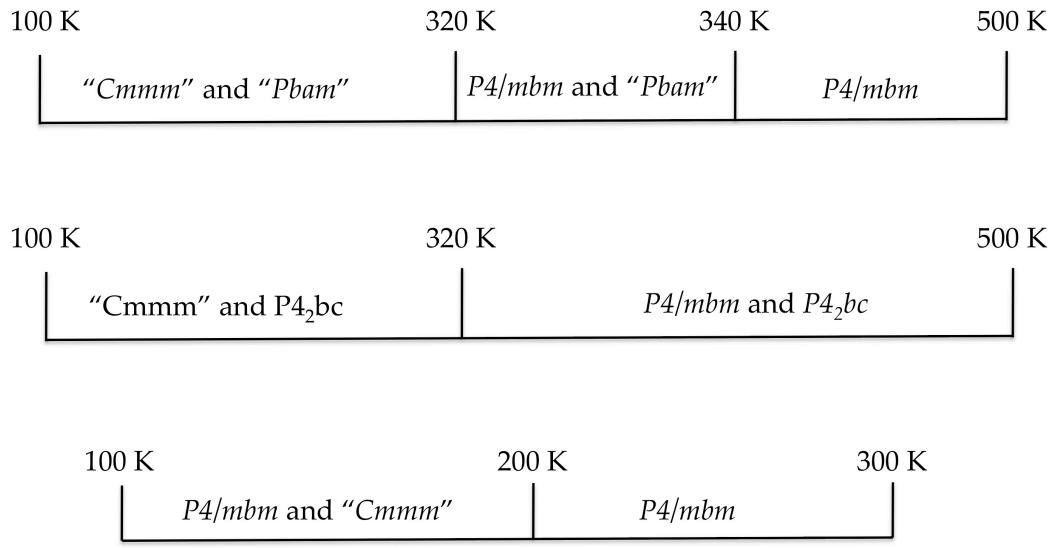

Figure 3.49: Summary of the phase separations and phase transitions as described in this chapter for the compounds $K_{0.58}FeF_3$ (top), $K_{0.5}FeF_3$ (middle), and $K_3Cu_3Fe_2F_{15}$ (bottom)

3.6 Conclusions

It has been shown that a centrosymmetric model just as well described the high temperature tetragonal model as a noncentrosymmetric model did. This does not exclude the possibility that the sample is noncentrosymmetric, merely that we could provide insufficient evidence to show it truly was the better model. Other analytical techniques, such as electrical measurements, could provide a better answer to that question. The phase separations for both solid solutions of K_xFeF_3 ($x = 0.58$ and $x \approx 0.5$) were new and well defined, at least in terms of lattice parameter metrics, throughout the entire temperature range. Although the tetragonal and orthorhombic phases coexisted for only 20 K in $K_{0.58}FeF_3$, they showed a clear and rapid growth of the "*Pbam*" phase from 0% to 10%. This weight percentage did not change as the tetragonal model went through a phase transition to the orthorhombic "*Cmmm*" approximation model. The phase separation for the $K_{0.5}FeF_3$ sample was already present at 500 K. The appearance of these two phases was interesting as the less abundant tetragonal phase, in the standard *P4/mbm* setting, showed a random distribution of the two iron ions in the unit cell, whilst the larger weight

fraction tetragonal model, $P4_2bc$, was charge-ordered. Both of these samples had a tetragonal to orthorhombic phase transition in the 320 K temperature range. In both cases, it was the *P4/mbm* phase that distorted into the "*Cmmm*" model. This same property was observed for $K_3Cu_3Fe_2F_{15}$, although there was no evidence for a phase separation for that composition.

3.7 References

1. P. B. Jamieson, S. C. Abrahams and J. L. Bernstein, *J. Chem. Phys.*, 1968, **48**, 5048-5057.
2. M. Francombe, *Acta Crystallogr.*, 1960, **13**, 131-140.
3. P. B. Jamieson, S. C. Abrahams and J. L. Bernstein, *J. Chem. Phys.*, 1969, **50**, 4352-4363.
4. R. R. Neurgaonkar, J. G. Nelson and J. R. Oliver, *Mater. Res. Bull.*, 1992, **27**, 677-684.
5. R. R. Neurgaonkar, J. G. Nelson, J. R. Oliver and L. E. Cross, *Mater. Res. Bull.*, 1990, **25**, 959-970.
6. A. Simon and J. Ravez, *C. R. Chim.*, 2006, **9**, 1268-1276.
7. J. Ravez, S. C. Abrahams and R. d. Pape, *J. Appl. Phys.*, 1989, **65**, 3987-3990.
8. R. de Pape, *Compt. Rend.*, 1965, **260**, 4527-4530.
9. A. M. Hardy and G. Ferey, *Acta Crystallogr., Sect. B: Struct. Sci*, 1973, **29**, 1654-1658.
10. S. C. Abrahams and J. Ravez, *Ferroelectrics*, 1992, **135**, 21 - 37.
11. J. Ravez, S. C. Abrahams, A. M. Mercier, L. Rabardel and R. d. Pape, *J. Appl. Phys.*, 1990, **67**, 2681-2683.
12. R. Blinc, G. Tavcar, B. Zemva, D. Hanzel, P. Cevc, C. Filipic, A. Levstik, Z. Jaglicic, Z. Trontelj, N. Dalal, V. Ramachandran, S. Nellutla and J. F. Scott, *J. Appl. Phys.*, 2008, **103**, 074114.
13. E. Banks, M. Shone, Y. S. Hong, R. F. Williamson and W. O. J. Boo, *Inorg. Chem.*, 1982, **21**, 3894-3897.
14. S. Ishihara, J. P. Rivera, E. Kita, Z. G. Ye, F. Kubel and H. Schmid, *Ferroelectrics*, 1994, **162**, 399-409.
15. J. Ravez, *J. Phys. III*, 1997, **7**, 1129-1144.

16. N. A. Hill, *J. Phys. Chem. B*, 2000, **104**, 6694-6709.
17. S. Fabbrici, E. Montanari, L. Righi, G. Calestani and A. Migliori, *Chem. Mater.*, 2004, **16**, 3007-3019.
18. F. Mezzadri, S. Fabbrici, E. Montanari, L. Righi, G. Calestani, E. Gilioli, F. Bolzoni and A. Migliori, *Phys. Rev. B: Condens. Matter* 2008, **78**, 064111.
19. R. Blinc, B. Zalar, P. Cevc, A. Gregorovic, B. Zemva, G. Tavcar, V. Laguta, J. F. Scott and N. Dalal, *J. Phys.: Condens. Matter*, 2009, **21**, 045902.
20. E. Banks, S. Nakajima and G. J. B. Williams, *Acta Crystallogr., Sect. B: Struct. Sci* 1979, **35**, 46-49.
21. R. Blinc, G. Tavcar, B. Zemva, E. Goreshnik, D. Hanzel, P. Cevc, A. Potocnik, V. Laguta, Z. Trontelj, Z. Jaglicic and J. F. Scott, *J. Appl. Phys.*, 2009, **106**, 023924.
22. R. Blinc, P. Cevc, A. Potocnik, B. Zemva, E. Goreshnik, D. Hanzel, A. GregoroviC, Z. Trontelj, Z. Jaglicic, V. Laguta, M. Perovic, N. S. Dalal and J. F. Scott, *J. Appl. Phys.*, 2010, **107**, 043511-043515.
23. A. R. West, in *Solid State Chemistry and Its Applications*, Wiley, Chichester, 1984, Chapter 3.
24. *General Structure Analysis System GSAS*, A. C. Larson and R. B. von Dreele, Report No. La-UR-86-748, 1987.
25. A. Le Bail, A. Desert and J. L. Fourouet, *J. Solid State Chem.*, 1990, **84**, 408-412.
26. N. Pailhe, A. Wattiaux, M. Gaudon and A. Demourgues, *J. Solid State Chem.*, 2008, **181**, 2697-2704.
27. R. Shannon, *Acta Crystallogr., Sect. A: Fundam. Crystallogr.*, 1976, **32**, 751-767.
28. N. E. Brese and M. O'Keeffe, *Acta Crystallogr., Sect. B: Struct. Sci.*, 1991, **47**, 192-197.
29. B. J. Campbell, H. T. Stokes, D. E. Tanner and D. M. Hatch, *J. Appl. Crystallogr.*, 2006, **39**, 607-614.
30. C. Filipic, Z. Kutnjak, R. Lortz, A. Torres-Pardo, M. Dawber and J. F. Scott, *J. Phys.: Condens. Matter*, 2007, **19**, 236206.
31. I. Levin, M. C. Stennett, G. C. Miles, D. I. Woodward, A. R. West and I. M. Reaney, *Appl. Phys. Lett.*, 2006, **89**, -.

32. J. Schneck, J. C. Toledano, C. Joffrin, J. Aubree, B. Joukoff and A. Gabelotaud, *Phys. Rev. B: Condens. Matter*, 1982, **25**, 1766.
33. A. Stergiou, I. Kerasiotis and C. Stergiou, *J. Optoelectron. Adv. Mater.*, 2007, **9**, 1772-1778.
34. N. Miyata, K. Tanaka and F. Marumo, *Acta Crystallogr., Sect. B: Struct. Sci.*, 1983, **39**, 561-564.
35. P. Labbe, H. Leligny, B. Raveau, J. Schneck and J. C. Toledano, *J. Phys.: Condens. Matter*, 1990, **2**, 25.

Chapter 4

The Structural Phase Transition of the S = ½ Kagome Fluoride $Cs_2ZrCu_3F_{12}$

4.1 A Brief Introduction to Frustrated Structures[1-3]

A frustrated system is defined as a system where preferred interactions of the magnetic moments or spins cannot be simultaneously satisfied and, as a result, the system cannot reach an energy minimum. A simple example to illustrate this is to look at a triangle and attempt to place an up or down spin on each vertex of the triangle so that each neighbouring pair have the opposite spin, Figure 4.1. It is easy to place the first two spins, but there is no possibility to place the third without causing one of the sides of the triangle to breach the preferred spin arrangement. This is the definition of frustration used in this thesis.

In these frustrated systems there are several different possible properties that arise as a consequence of this frustration. Notably, the spins can never order into a fully two-dimensional antiferromagnetic array; on each triangle there is one pair of parallel spins that interact. A more satisfying option is for the ordering of these interactions to be localised. These compounds are called valence bond solids (VBS), Figure 4.2.

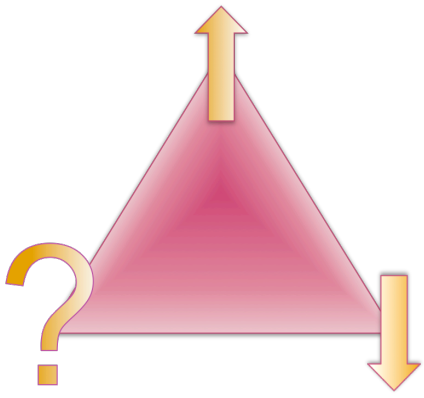

Figure 4.1: Frustrated spins on a triangle

The antiparallel pairs of spins are ordered in the same manner as a chemical bond. In these pairs, there are two possible arrangements for the spin pairs: up-down, and down-up. The observed antiparallel pair is thus an "average" or, more correctly, a quantum-superposition of these two states, which are thus doubly degenerate. An analogy can be drawn to the description of the bonding in benzene in terms of two resonance forms. In the VBS state the location of these spin pairs is fixed, and so the bonds within the structure define the pattern the spin pairs create. However, frustration is relieved due to the doubly degenerate nature of neighbouring spin-pairs, but as a consequence there is no long-range antiferromagnetic order. This "localised bonding" nature may break the lattice symmetry of the material and thus is a factor to consider when looking at the crystal structure of these compounds. If, rather than being fixed relative to each other, there is no particular preference for which spin pairs are formed, and they can be easily interchanged, then the material is referred to as a resonating valence bond solid (RVB) state. In this state, there are many possible long and short range spin-pairings, and these form a ground state with a degeneracy much greater than two-fold. Because the valence bonds are no longer defined in space, but continue to fluctuate amongst many degenerate possibilities, the compound is referred to as a spin liquid. In this type of material, the spins may order with their nearest neighbour, or one further away. This random ordering without any long-range order is analogous to the structural order within a liquid. The spin liquid is referred to as a quantum spin liquid (QSL) if the spin is close to or equal to ½. If this is not the case, it is referred to as a classical spin liquid (CSL). The liquid-like nature of the spin interactions does not affect the lattice symmetry of the material, as the bonds within the structure do not define them.

In a QSL, the magnetic fluctuations should still exist at absolute zero, and there will be no net magnetic moment as both the VBS and the QSL have an $S = 0$ ground state. These compounds are thus of particular interest in fundamental physics, but there are very few good model systems from which to understand these exotic electronic states. From the point of view of a solid state chemist there are therefore great opportunities both in the synthesis of candidate model systems, and in the crystallographic and chemical understanding of existing candidates. In this chapter, a comparison of two

isostructural S = ½ kagome compounds is made and a new insight is proposed into why one, $Cs_2ZrCu_3F_{12}$, orders antiferromagnetically at low temperatures whereas the other, $Rb_2SnCu_3F_{12}$, adopts a VBS ground state.

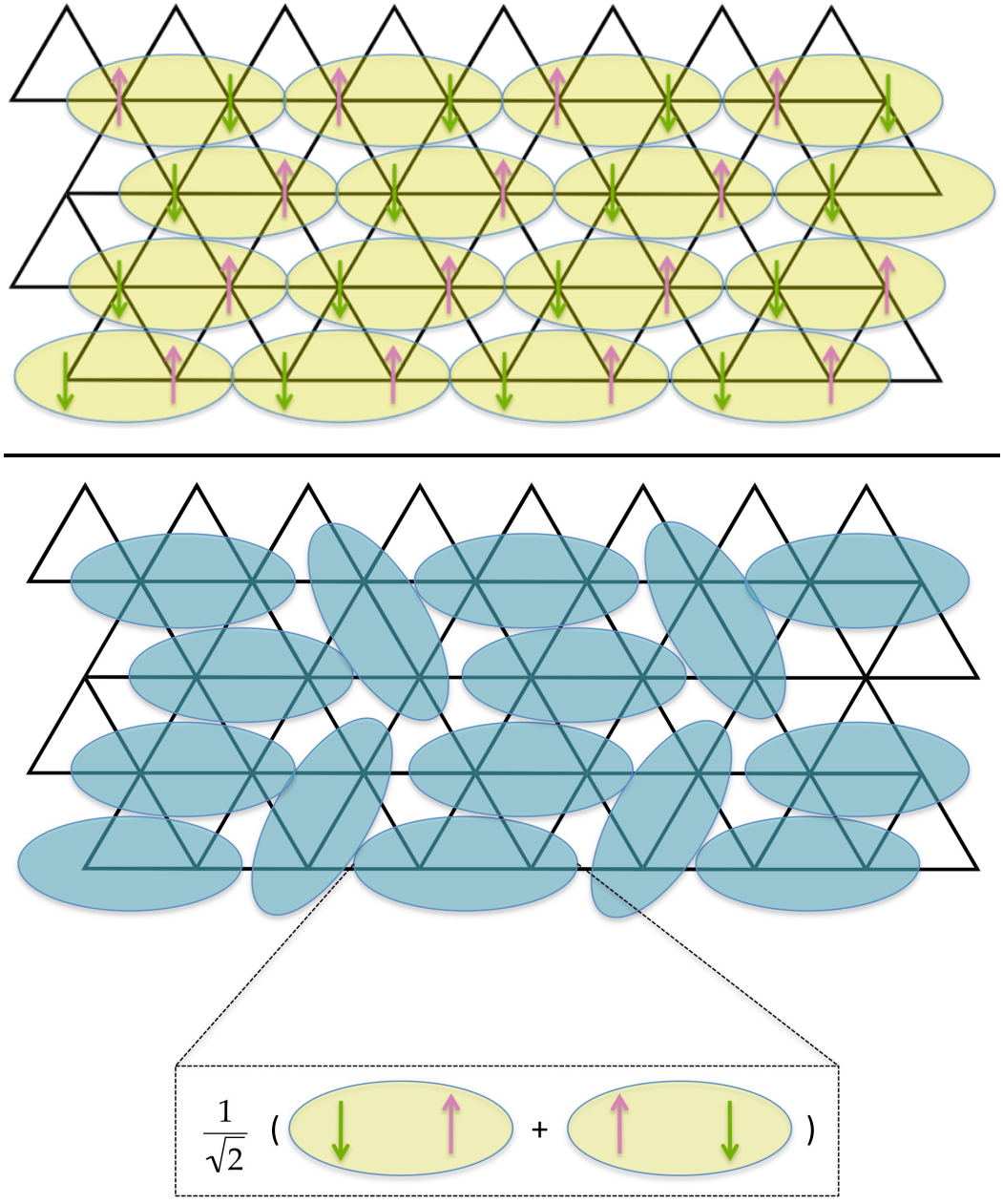

Figure 4.2: Antiferromagnetic arrangement of frustrated spins which can show long-range order in one dimension but not in two (top) and a valence bond solid showing localised pairs of ordered spins which are a quantum-superposition of two possible degenerate states (bottom)

4.2 Introduction to S = ½ Kagome Systems

The two-dimensional kagome system is defined and described in Chapter 1. An early example of such a kagome system was reported by Courbion *et al*.[4] They presented the crystal structure of $Cs_2NaAl_3F_{12}$ ($R\bar{3}m$, a = 7.310(5) Å, α = 57.45(10)°). They did not note that the structure was a kagome system, describing it instead as a distorted form of the pyrochlore structure of $KRbNiCrF_6$ with ⅔ disorder between cationic sites. Almost 15 years later, Le Bail *et al*.[5] presented two new analogues of this compound, $A_2NaAl_3F_{12}$ (A^+ = K, Rb). Unlike the caesium compound, these two samples crystallised in the monoclinic space group $P2_1/m$. The distortion to the monoclinic phase was attributed to the relatively small size of the K^+ and Rb^+ ions compared to the Cs^+ ion. This led the [AlF_6] octahedral layers to buckle to maintain the coordination numbers required by the alkaline metal ions. A further difference was observed for the two new analogues; by lowering the symmetry of the system to monoclinic, there were now two distinct A-sites. Englich *et al*.[6] then extended this family by reporting the structures of rhombohedral $Cs_2LiMn_3F_{12}$ ($R\bar{3}$); triclinic ($P\bar{1}$) $Cs_2NaMn_3F_{12}$, $Rb_2NaMn_3F_{12}$, and $Rb_2LiMn_3F_{12}$; and one example in monoclinic $C2/c$ for $Cs_2KMn_3F_{12}$. $Cs_2LiMn_3F_{12}$ was initially solved in $R\bar{3}m$, but it was found that the mirror plane in the space group was better omitted and so the final structure was solved in $R\bar{3}$. This allowed the [MnF_6] octahedra to be well modelled and show a clear Jahn-Teller distortion, with the axial Mn – F bond lengths 1.15 times longer than their equatorial counterparts. The net result was a pinwheel effect, where long bonds were alternated with short ones in the six-membered pinwheel, or "wind" wheel as they called it, Figure 4.3.

The three compounds $Cs_2NaMn_3F_{12}$, $Rb_2NaMn_3F_{12}$, and $Rb_2LiMn_3F_{12}$ were reported to be triclinic with pseudo-monoclinic or pseudo-rhombohedral symmetry. All three could be solved in monoclinic $P2_1/n$, but the [MnF_6] octahedra appeared compressed and a better fit was obtained by allowing the atoms the freedom to move more in the triclinic cell. The coordination environments of the Cs^+ and Rb^+ ions are most affected by this change, changing from 18 to 12. Magnetic measurements for $Cs_2KMn_3F_{12}$ showed antiferromagnetic ordering at low temperatures, but $Cs_2NaMn_3F_{12}$ did not.

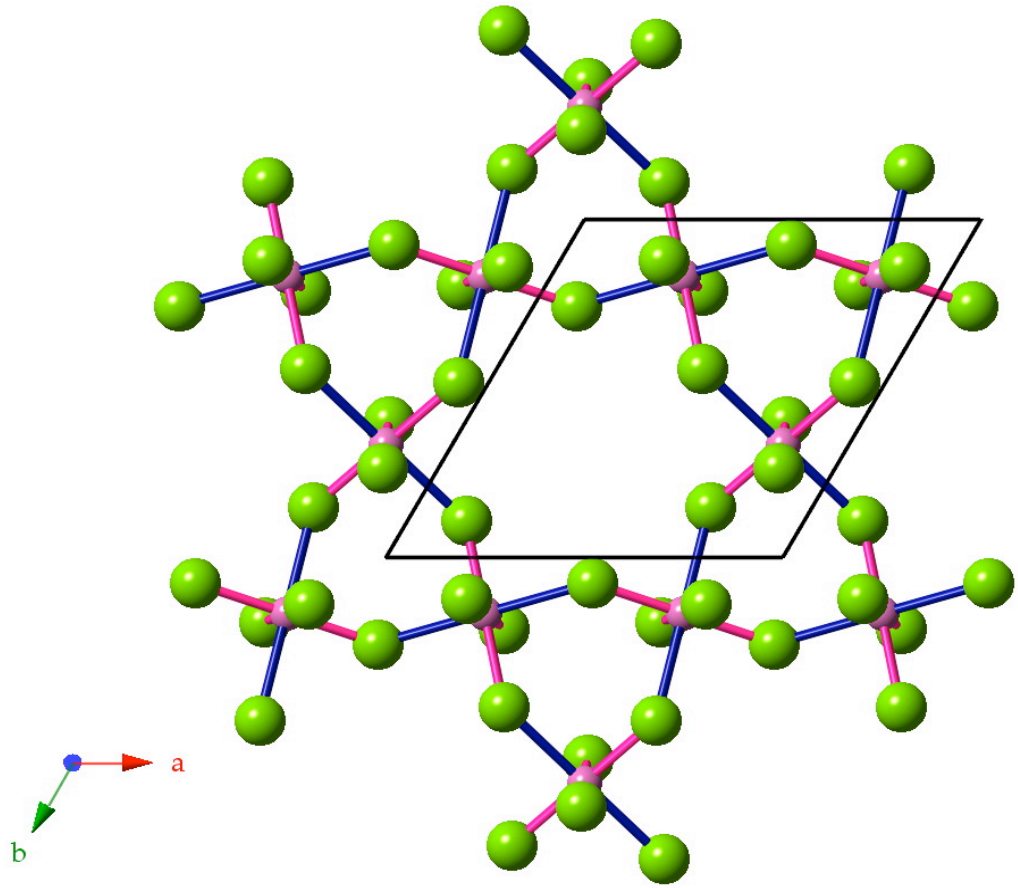

Figure 4.3: Pinwheel arrangement of Mn – F bonds in $Cs_2LiMn_3F_{12}$, with the shorter Mn – F bonds (~1.8 Å) in pink and longer Mn – F bonds (~2.2 Å) in blue

A further set of analogues was reported by Müller and Müller.[7] They reported the synthesis, characterisation and magnetic behaviour of $Cs_2MCu_3F_{12}$ (M^{4+} = Zr, Hf). $Cs_2ZrCu_3F_{12}$ ($R\bar{3}m$, a = 7.1661(6) Å, c = 20.464(2) Å) has Jahn-Teller distorted [CuF_6] octahedra that link only along the equatorial Cu – F bonds leading to the elongated bonds not affecting the six-membered channel. This regular arrangement of octahedra means that there is little distortion in the plane formed by these octahedra. $Cs_2HfCu_3F_{12}$ was solved from powder data and shown to be isostructural. Both compounds were reported to show antiferromagnetic behaviour from approximately 200 K downwards.

A decade later, condensed matter physicists then reinvestigated these compounds, as they seemed ideal candidates for RVB and QSL materials. Yamabe *et al.*[8] observed that $Cs_2MCu_3F_{12}$ (M^{4+} = Zr, Hf) showed structural phase transitions at approximately 210 K and 175 K, respectively. The structures of the low temperature phases could not be solved due to twinning. At the

structural transitions, there were also anomalies in the magnetic susceptibility. Below approximately 25 K, both samples ordered antiferromagnetically with weak ferromagnetic moments.

Morita *et al.*[9] then reported the synthesis and study of the antiferromagnet $Rb_2SnCu_3F_{12}$ ($R\bar{3}$, a = 13.917(2) Å, c = 20.356(3) Å), Figure 4.4. This compound has the same structure as $Cs_2ZrCu_3F_{12}$, with the difference that the a and b axes are doubled and the mirror plane removed. Two of the fluorine atoms were also delocalised and thus each was shown as two partially occupied sites. This compound did not show magnetic ordering at low temperatures, thus indicating that the ground state was disordered and the compound adopted a potential VBS state. This was confirmed when the compound was later found to exhibit a pinwheel VBS ground state.[10] The same authors also reported the structure of $Cs_2SnCu_3F_{12}$, which was found to be isostructural to $Cs_2ZrCu_3F_{12}$.[11] It underwent a phase transition at about 185 K. It was suggested that the low temperature structure of this compound might be similar to that of $Rb_2SnCu_3F_{12}$, i.e. with the a and b axes doubled, but the structure could not be determined due to twinning. It should be pointed out that, for each member of the $A_2BCu_3F_{12}$ family, the crystal structures have been reported at room temperature and only speculative comments about the nature of the low temperature phases have been made.

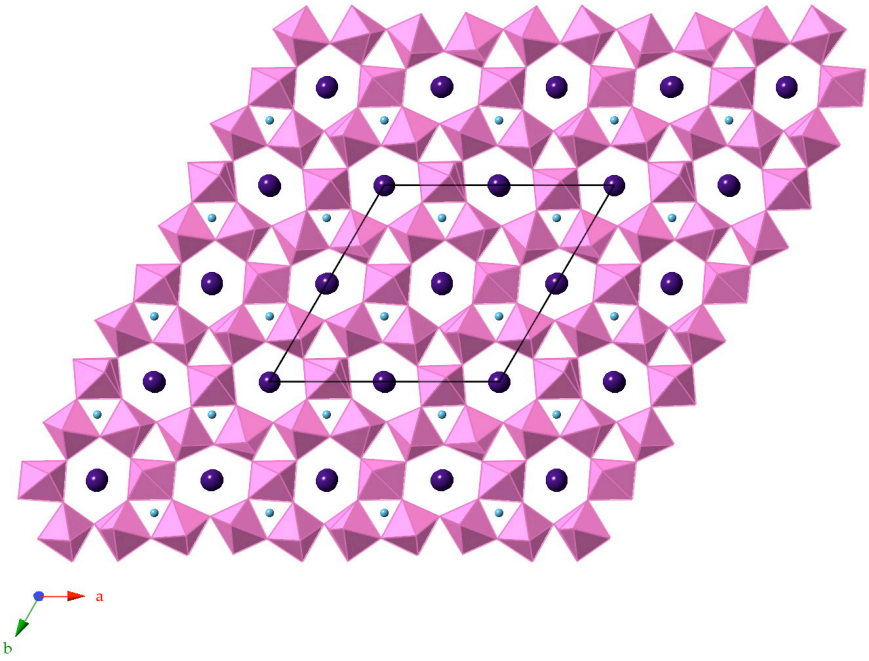

Figure 4.4: Kagome structure of $Rb_2SnCu_3F_{12}$ viewed along the c-axis

4.3 Experimental

4.3.1 Synthesis

$Cs_2ZrCu_3F_{12}$ was prepared by combining the 0.154 g (1.01 mmol) CsF, 0.152 g (1.50 mmol) CuF_2, and 0.084 g (0.50 mmol) ZrF_4 under an inert atmosphere and placing them in a closed Au tube. The tube was crimped shut and then dehydrated at 120 °C for 12 hours, and subsequently heated under argon to 750 °C for 12 hours. It was then cooled to 500 °C at 0.1 °C per minute. After that the sample was left to cool to room temperature in the furnace under flowing argon.

4.3.2 Single Crystal X-ray Diffraction

Data were collected in air at 295 K and at 125 K using a Rigaku SCXmini diffractometer. The same crystal was used for both measurements. The structures were solved by direct methods and refined using SHELXL-97.[12]

4.3.3 Synchrotron Powder X-ray Diffraction

Standard room temperature PXRD experiments were performed using a Stoe diffractometer with Ge monochromated Cu $K_{\alpha 1}$ radiation (λ = 1.54056 Å).[13] The high-resolution X-ray powder diffraction beamline I11 at the Diamond Light Source synchrotron (λ = 0.825558(2) Å) was used for all variable temperature high-resolution X-ray powder diffraction experiments between 300 K and 100 K. All diffraction data were analysed and refined using the GSAS software.[14] Parameters refined include the background coefficients, the detector zero point, instrumental parameters, lattice parameters, profile parameters, isotropic and anisotropic atomic displacement parameters, and atomic position parameters.

4.3.4 AC Impedance Spectroscopy Measurements

Dielectric (capacitance and loss) measurements were carried out in the frequency range 100 Hz - 10 MHz using an Agilent 4294A Impedance Analyser with an excitation voltage of 500 mV and in the temperature range between 50 K and 340 K in a closed cycle helium refrigerator with heating/cooling rates of 2 K/min. Electrodes were fabricated from silver paste applied to opposing faces of an agglomeration of single crystals. Due to the irregular geometry it was not possible to determine the precise electrode area and separation, but as a rough approximation these were 1 mm^2 on a sample of thickness 1 mm, respectively.

4.4 Results and Discussion

All cifs and powder XRD data are given in Appendix C.

4.4.1 The Crystal Structures of $Cs_2ZrCu_3F_{12}$

Pale blue single crystals of the desired compound were obtained from the solid state reaction. A suitable crystal was used for both room temperature (295 K) and low temperature (125 K) SCXRD measurements.

The room temperature (RT) structure was found to be rhombohedral and the same as that reported in the literature.[7] Crystal data and refinement details for the RT structure are given in Table 4.1. Two-dimensional copper-fluoride sheets extend in the *ab* plane and are connected to the other planes in the structure via $[ZrF_6]$ linking octahedra, Figure 4.5. The structural parameters for $Cs_2ZrCu_3F_{12}$ are given in Table 4.2. The Cu atoms form a perfectly flat plane, Figure 4.6, and the triangles formed by these atoms, consequently, do the same. There is only one Cu atom in the asymmetric unit and all triangles formed by the Cu atoms are equivalent and equilateral. Six fluorine atoms surround the Cu atoms, F1 occupying the equatorial positions in the kagome plane and F2 occupying the axial positions. The Cu1 – F2 bonds (2.331(6) Å) show significant Jahn-Teller distortion compared to the Cu1 – F1 bonds (1.892(2) Å). A list of

selected bond lengths in the structure is given in Table 4.3. The elongated bonds are not in the kagome plane and so do not lead to the pinwheel arrangement as seen in the Mn^{3+} based analogues shown before in Figure 4.3.

Table 4.1: SCXRD data and refinement details for the RT phase of $Cs_2ZrCu_3F_{12}$

Crystal system	Trigonal
Space group	$R\bar{3}m$
Unit cell parameters	$a = 7.1560(19)$ Å $c = 20.447(7)$ Å
Volume	906.8(5) $Å^3$
Z	3
ρ(calc)	4.261 Mg/m^3
Crystal size	0.03 x 0.06 x 0.16 mm^3
Goodness-of-fit on F^2	1.223
Final R indices [I>2sigma(I)]	$R_1 = 0.0474$, $wR_2 = 0.0993$
R indices (all data)	$R_1 = 0.0516$, $wR_2 = 0.1041$

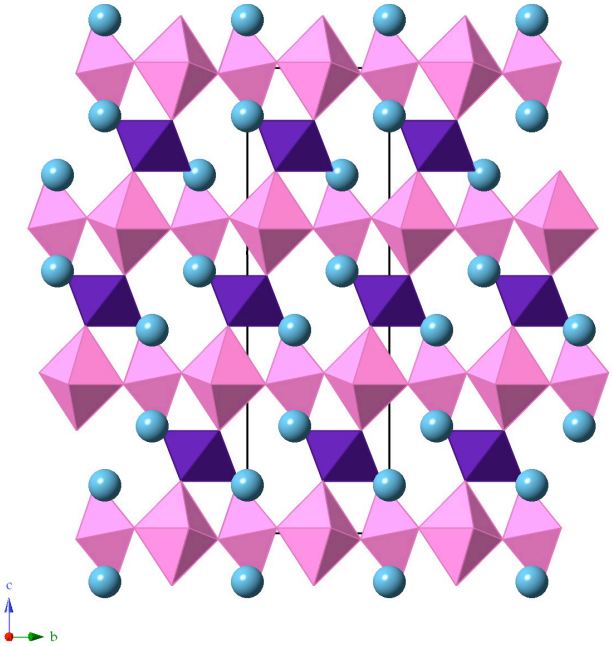

Figure 4.5: Layering of the copper-fluoride kagome layers (pink) in the rhombohedral form of $Cs_2ZrCu_3F_{12}$ with the layers connected via $[ZrF_6]$ linking octahedra (purple) viewed along the a-axis

Table 4.2: Structural parameters for RT phase of $Cs_2ZrCu_3F_{12}$ with isotropic atomic displacement parameters

Atom	Site	x	y	z	U(eq)x100 Å^2
Cu1	9e	0.5	0	0	1.8(1)
Zr1	3b	0.3333	-0.3333	0.1667	2.0(1)
Cs1	6c	0	0	0.1037(1)	4.0(1)
F1	18h	0.4096(9)	0.2048(4)	0.0124(3)	2.9(1)
F2	18h	0.4685(5)	-0.0630(10)	0.1124(3)	4.3(2)

U(eq) is defined as one third of the trace of the orthogonalized U^{ij} tensor

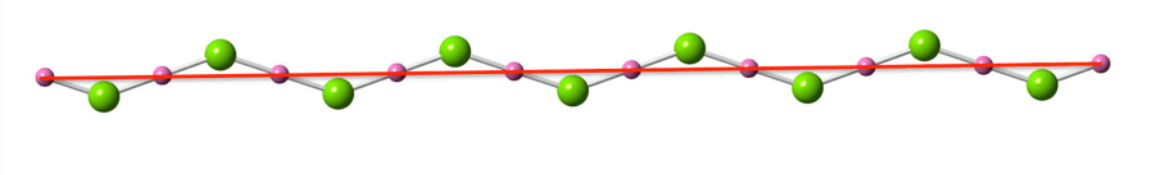

Figure 4.6: Projection along the copper-fluoride kagome layers (pink) in the rhombohedral form of $Cs_2ZrCu_3F_{12}$ showing the co-planar arrangement of the Cu atoms following the "ideal" kagome model

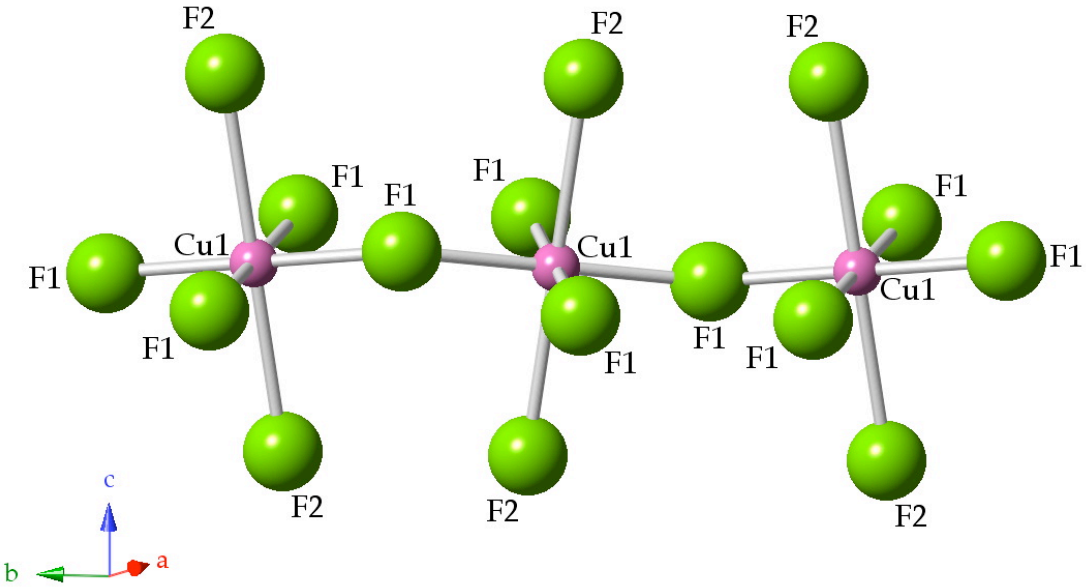

Figure 4.7: Positions and labels of the axial and equatorial fluorine atoms around the Cu1 site in the rhombohedral form of $Cs_2ZrCu_3F_{12}$

Table 4.3: Selected bond lengths from the SCXRD data for $Cs_2ZrCu_3F_{12}$ at RT

Bond	Bond length [Å]
Cu1 – F1 (x4)	1.892(2)
Cu1 – F2 (x2)	2.332(6)
Zr1 – F2 (x6)	2.009(6)
Cs1 – F1 (x3)	3.151(6)
Cs1 – F1 (x3)	3.475(6)
Cs1 – F2 (x3)	3.432(6)
Cs1 – F2 (x3)	3.604(2)

Although the Cu atoms themselves are co-planar in their arrangement, the [CuF_6] octahedra formed by them tilt so that the distance between the apical F atoms of two adjacent octahedra alternates between 2.90(1) Å and 4.25(1) Å, Figure 4.7.

The low temperature (LT) structure was solved at 125 K. This is significantly below the reported phase transition temperature based on the magnetic anomaly in the range of 225 to 210 K. The structure is found to be monoclinic and the best fit is obtained in $P2_1/m$. The crystal and refinement details are given in Table 4.4. Table 4.5 lists the structural parameters.

Table 4.4: SCXRD data and refinement details for the LT phase of $Cs_2ZrCu_3F_{12}$

Crystal system	Monoclinic	
Space group	$P2_1/m$	
Unit cell parameters	a = 7.798(15) Å	
	b = 7.212(14) Å	β = 93.97(2)°
	c = 10.351(19) Å	
Volume	580.7(19) Å^3	
Z	2	
ρ(calc)	4.436 Mg / m^3	
Goodness-of-fit on F^2	1.122	
Final R indices [I>2sigma(I)]	R_1 = 0.0489, wR_2 = 0.1022	
R indices (all data)	R_1 = 0.0620, wR_2 = 0.1087	

Table 4.5: Structural parameters for LT phase of $Cs_2ZrCu_3F_{12}$ with isotropic atomic displacement parameters

Atom	Site	x	y	z	U(eq)x100 Å^2
Cu1	2e	0.7835(2)	0.2500	0.2280(2)	1.3(1)
Cu2	2b	0.5000	0	0	1.4(1)
Cu3	2c	1.0000	0	0.5000	1.3(1)
Zr1	2e	0.2970(2)	0.2500	0.2401(1)	1.3(1)
Cs1	2e	0.0170(1)	0.7500	0.1494(1)	2.0(1)
Cs2	2e	0.5529(1)	0.7500	0.3756(1)	2.3(1)
F1	4f	0.7040(8)	0.0572(8)	0.1046(5)	1.8(1)
F2	4f	0.8597(8)	0.0517(8)	0.3432(5)	1.9(1)
F3	2e	0.5361(11)	0.2500	0.3251(8)	1.8(2)
F4	2e	1.0606(11)	0.2500	0.1476(7)	1.7(2)
F5	2e	0.3983(11)	0.2500	0.0373(8)	1.9(2)
F6	4f	0.3517(8)	-0.0185(8)	0.1718(6)	2.1(2)
F7	2e	0.9841(12)	0.2500	0.5598(8)	1.8(2)
F8	4f	0.7687(8)	-0.0739(9)	0.6169(6)	2.3(2)

U(eq) is defined as one third of the trace of the orthogonalized U^{ij} tensor

As is apparent from Figure 4.8, the kagome lattice has distorted considerably in going from the RT to the LT phase. The reason for this is immediately evident: the Zr^{4+} ion has changed from 6-coordinate in the RT phase to 7-coordinate in the LT phase. In order for this to occur, one of the in-plane F atoms (i.e. F1 in the rhombohedral phase, F5 in the monoclinic phase) has to move significantly from its original position to coordinate to the Zr^{4+}. The Cu^{2+} ion then follows so as to maintain its coordination number, Figure 4.9. The result is that there are now three separate Cu sites and these three are distorted to varying degrees. The net result is that the "ideal" kagome layer formed by the Cu ions is no longer flat. A line of fit drawn through the Cu^{2+} ions, Figure 4.10, highlights the deviations of the Cu^{2+} ions from this plane in the LT model when compared to the RT model. This results in two distinct triangles formed by the Cu^{2+} ions, Figure 4.11. Selected bond lengths of the LT

phase are given in Table 4.6. The Jahn-Teller distortion of the Cu – F bond is still observed out of the kagome plane, as in the RT structure.

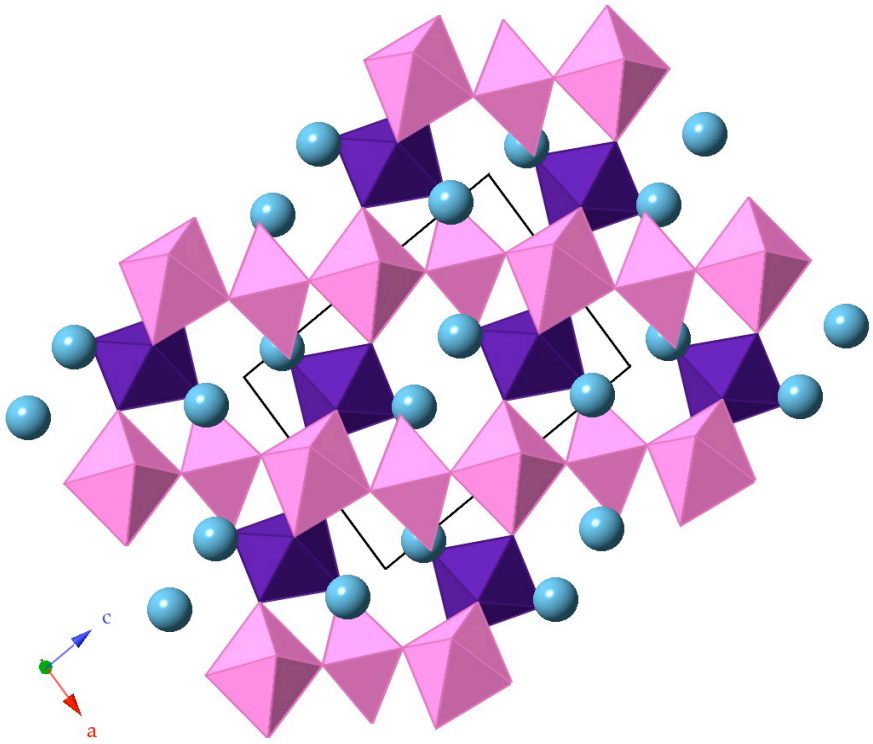

Figure 4.8: Layering of the copper-fluoride kagome layers (pink) in the monoclinic form of $Cs_2ZrCu_3F_{12}$ with the layers connected via $[ZrF_7]$ linking polyhedra (purple) viewed along the b-axis

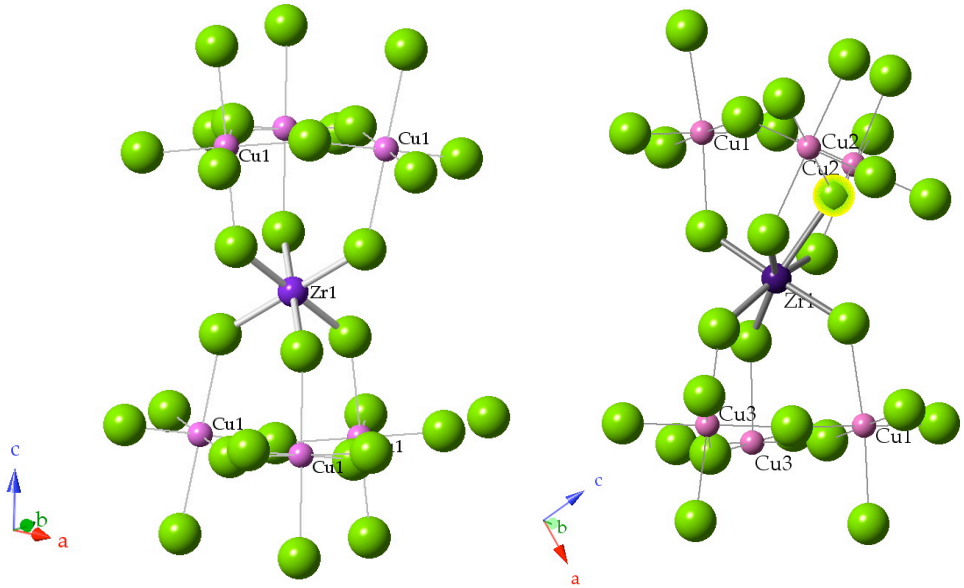

Figure 4.9: Coordination environment of the Zr^{4+} ion in the rhombohedral form of $Cs_2ZrCu_3F_{12}$ (left) and the monoclinic form (right) with the newly coordinated fluoride ion shown in yellow

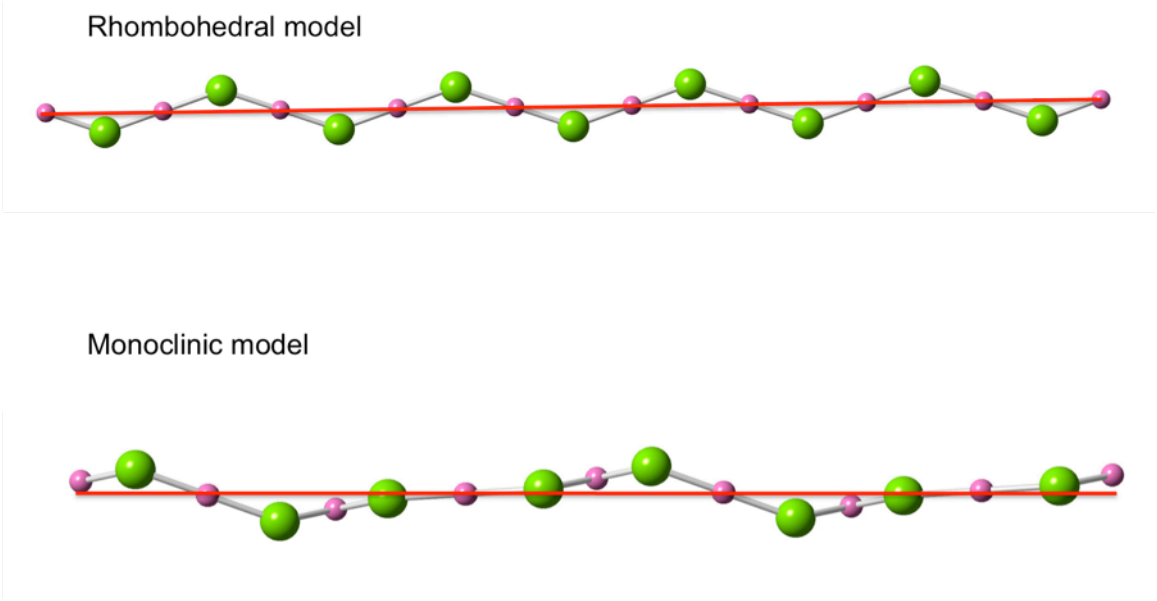

Figure 4.10: Projection along the copper-fluoride kagome layers (pink) in the rhombohedral forms of $Cs_2ZrCu_3F_{12}$ showing the co-planar arrangement of the Cu atoms following the "ideal" kagome model (top) and the monoclinic forms of $Cs_2ZrCu_3F_{12}$ showing the displaced arrangement of the Cu atoms (bottom)

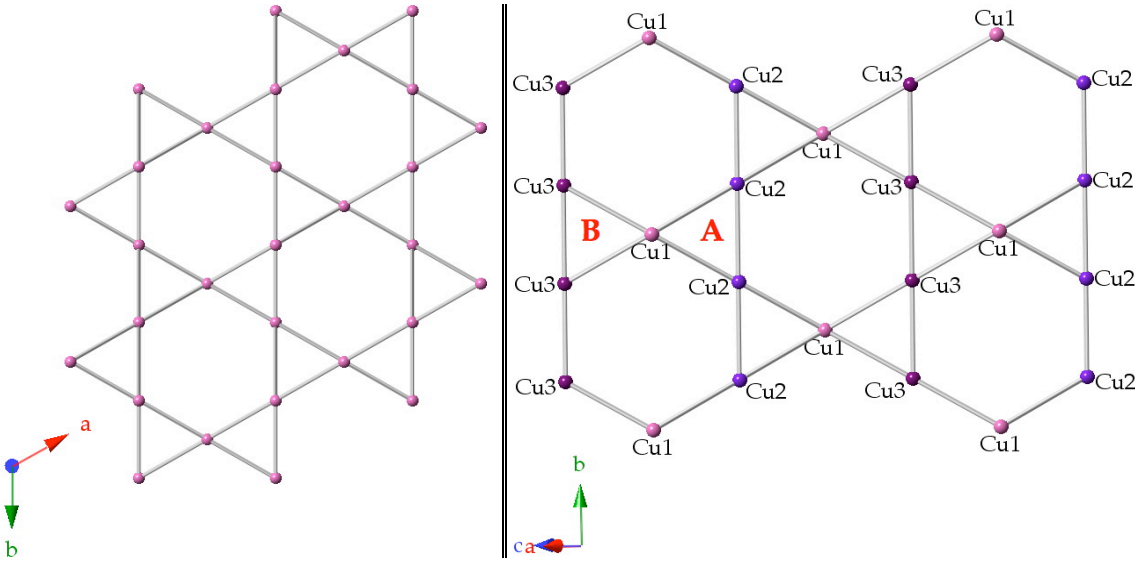

Figure 4.11: Cu grid arrangement in the RT phase (left) and LT phase (right) of $Cs_2ZrCu_3F_{12}$ showing the single triangle for RT and two distinct triangles for LT forms

Table 4.6: Selected bond lengths from the SCXRD data for the LT phase of $Cs_2ZrCu_3F_{12}$

Bond	Bond length [Å]
Cu1 – F1 (x2)	1.959(6)
Cu1 – F2 (x2)	1.930(6)
Cu1 – F3 (x2)	2.237(10)
Cu2 – F1 (x2)	1.906(6)
Cu2 – F5 (x2)	2.018(5)
Cu2 – F6 (x2)	2.191(7)
Cu3 – F2 (x2)	1.930(6)
Cu3 – F7 (x2)	1.913(4)
Cu3 – F8 (x2)	2.303(7)
Zr1 – F3	2.005(9)
Zr1 – F4	2.018(9)
Zr1 – F5	2.294(9)
Zr1 – F6 (x2)	2.115(7)
Zr1 – F8 (x2)	2.043(7)

The Cu octahedra tilt strongly out of the plane and so the average distance between the fluorine vertices of adjoining octahedra varies between 2.83(1) Å and 4.75(1) Å. Again, the alternating long-short separation between these points is observed.

4.4.2 Variable Temperature sPXRD Measurements on $Cs_2ZrCu_3F_{12}$

To obtain a better picture of the phase transition, high-resolution sPXRD data were collected in 10 K steps from 300 K to 125 K. The 300 K data were fitted very well using the rhombohedral model. All remaining peaks could be assigned to the impurity phase Cs_2ZrF_6 which was reported by Bode and Teufer ($P\bar{3}m1$, a = 6.41 Å, c = 5.01 Å).[15] For all refinements using only the rhombohedral model and this impurity phase, the following parameters were

refined: the background (using a shifted Chebyschev function with 12 terms); the detector zero point; the scale factor; and the phase fractions. For the rhombohedral phase, specifically, the following were also included: lattice parameters; atom positions; anisotropic atomic displacement parameters for the metal ions and isotropic atomic displacement parameters for the fluoride ions; pseudo-Voigt profile parameters - GW (for the Gaussian contribution) and LY (for the Lorentzian contribution); and all 34 order terms of the spherical harmonics ODF giving 113 ODF parameters. The lattice parameters, atom positions, isotropic atomic displacement parameters and profile parameters, GU and LX, were also refined for the impurity phase.

From the refinement it became immediately clear that there was a strong preferred orientation problem. The (h0l) peaks were underrepresented. A spherical harmonics correction using all available terms provided a good improvement for the fit, Figure 4.12. Figures 4.13 and 4.14 give detailed plots of the entire 2-theta region.

Table 4.7: Structural parameters for $Cs_2ZrCu_3F_{12}$ at 300 K using the $R\bar{3}m$ model (a = 7.165299(8) Å, c = 20.51025(3) Å, and V = 911.948(3) Å^3, χ^2 = 8.835, wR_p = 13.53%, R_p = 16.00%) with anisotropic displacement parameters for the metal ions and isotropic atomic displacement parameters for the fluoride ions, and spherical harmonics preferred orientation correction

Atom	x	y	z	(U_{11}, U_{22}, U_{33}, U_{12}, U_{13}, U_{23})x100 Å^2 **or** U_{iso}*x100 Å^2*
Cu1	-0.5	0	0	-0.36(9), -0.38(14), 0.35(11), -0.19(7), -0.111(7), -0.22(14)
Zr1	0.3333	-0.3333	0.1667	0.70(11), 0.70(11), 0.20(15), 0.35(5), 0, 0
Cs1	0	0	0.10400(11)	1.55(10), 1.55(10), 2.26(13), 0.77(5), 0, 0
F1	0.0520(12)	-0.04740(6)	0.1112(3)	*0.73(19)*
F2	-0.5878(9)	0.2061(5)	0.0109(3)	*1.5(2)*

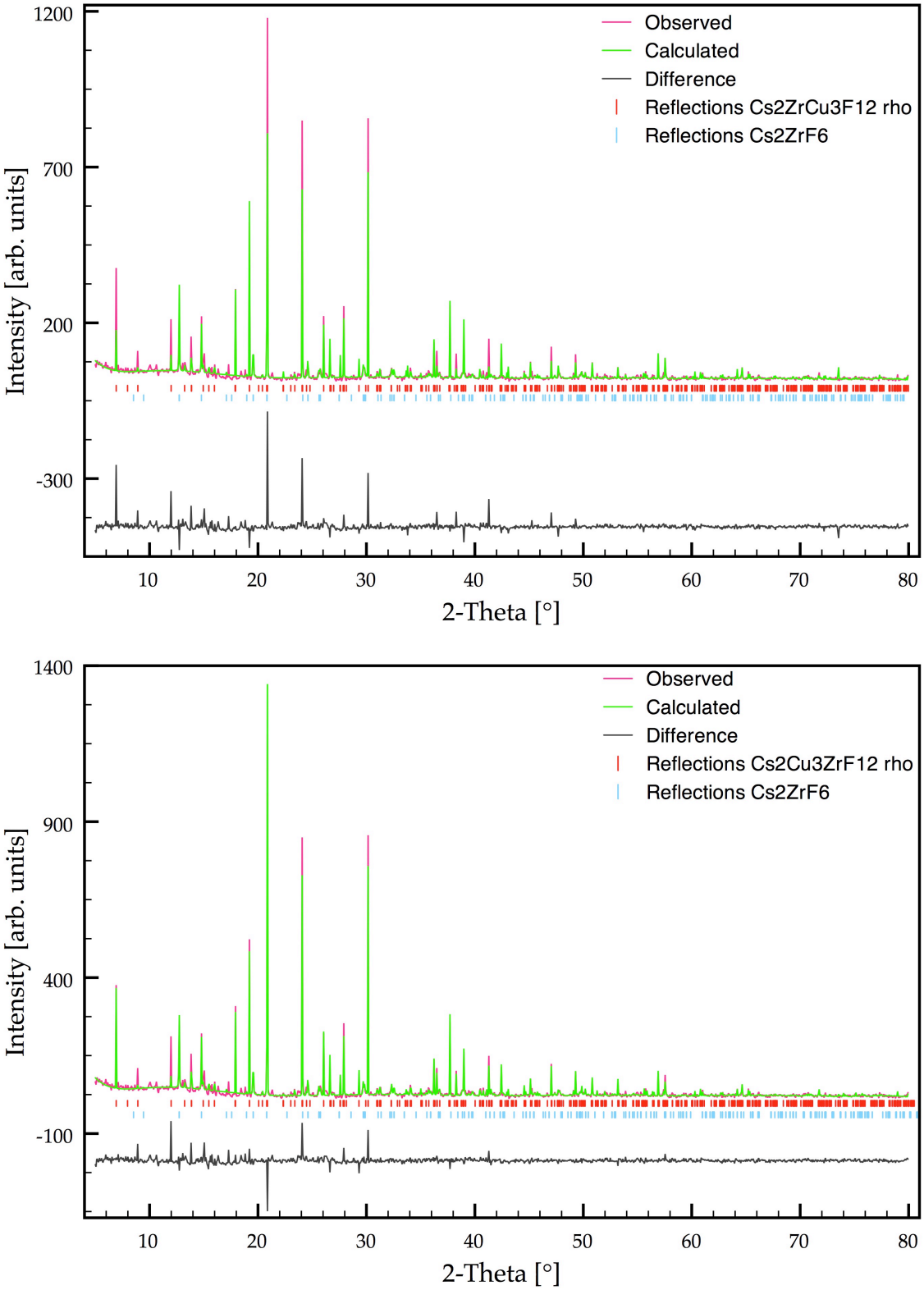

Figure 4.12: Rietveld plots for rhombohedral $Cs_2ZrCu_3F_{12}$ without any preferred orientation correction (top) and with spherical harmonic preferred orientation correction (bottom) at 300 K

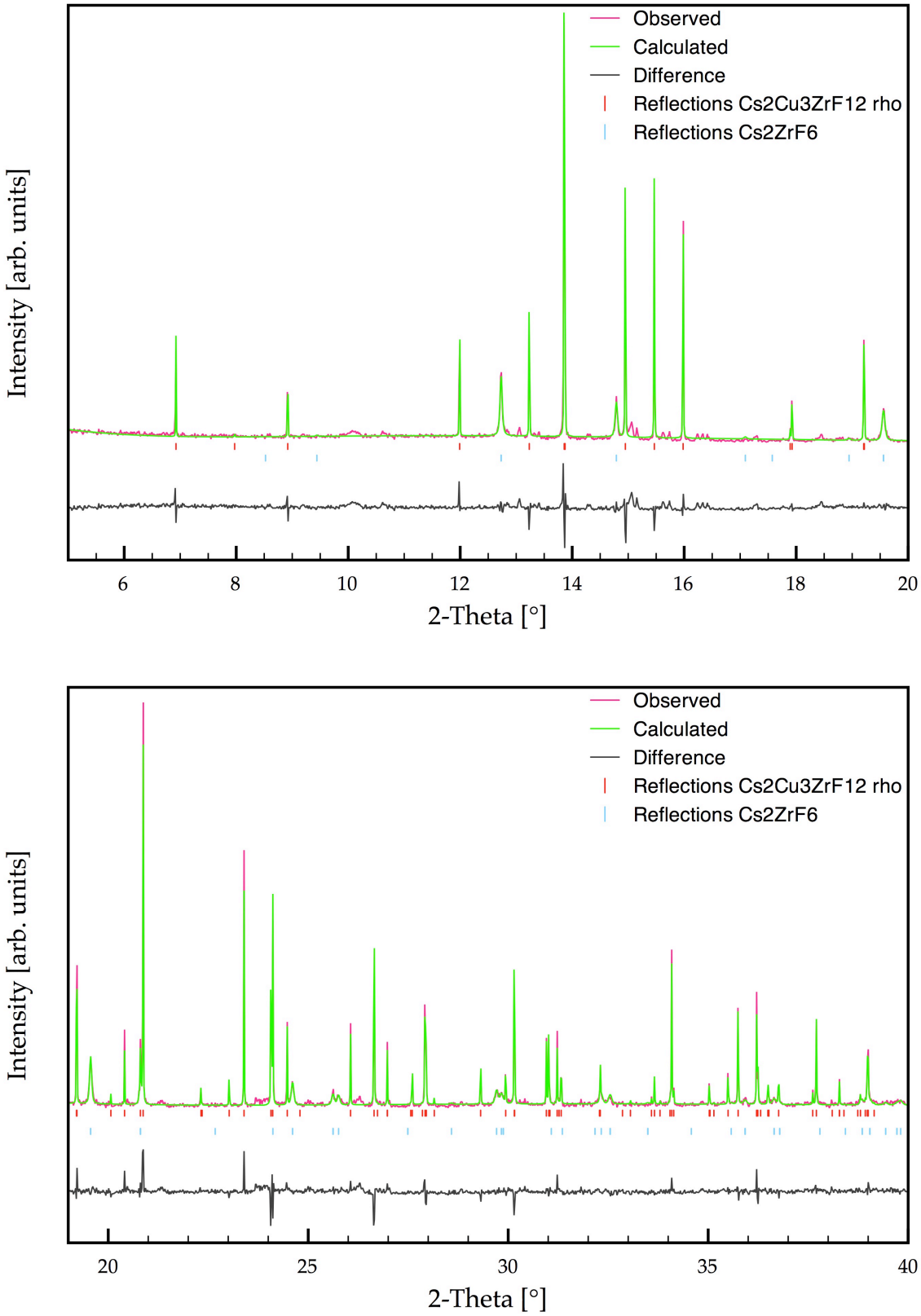

Figure 4.13: Detailed Rietveld plots for rhombohedral $Cs_2ZrCu_3F_{12}$ at 300 K showing the 5 to 20° 2-theta range (top) and the 20 to 40° 2-theta range (bottom)

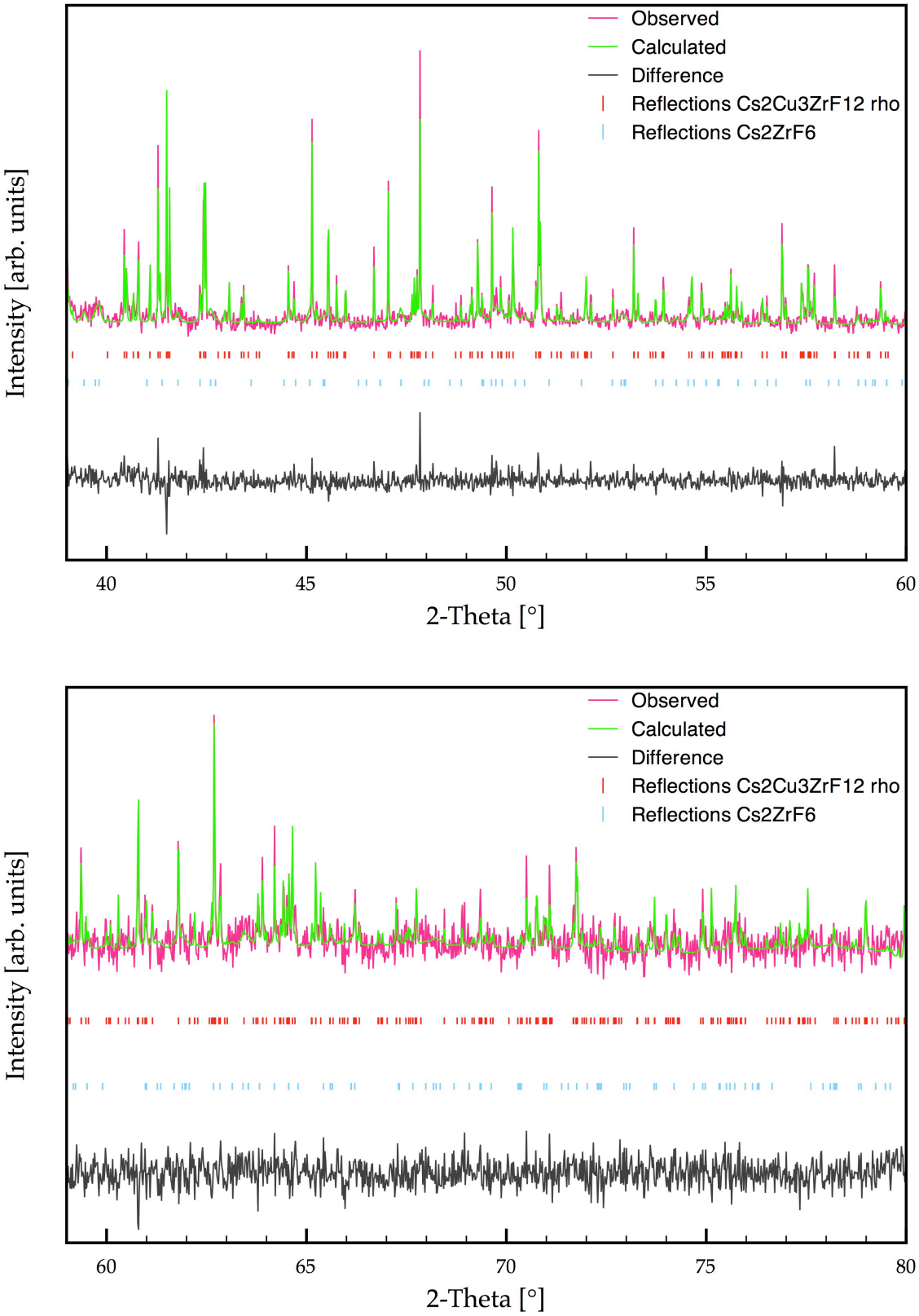

Figure 4.14: Detailed Rietveld plots for rhombohedral $Cs_2ZrCu_3F_{12}$ at 300 K showing the 40 to 60° 2-theta range (top) and the 60 to 80° 2-theta range (bottom)

The impurity was modelled with the given cif, but it was clear that the authors had reported only an approximate model, with the true symmetry probably being lower. Due to time constraints, no attempts were made to synthesise the compound and determine the correct structure.

The impurity, Cs_2ZrF_6, was found to show no outliers or anomalies in the lattice parameters over the complete temperature range, Figure 4.15. Below 210 K, it was necessary to fix the lattice parameters and profile parameters. This was done for the lattice parameters by subtracting the average of the lattice parameters from each subsequent temperature; and for the profile parameters by using the average of the readings up to that point. This was attributed to the poorly determined structural model for this material. The deviation in the weight percentage, as can be seen in Figure 4.15, was attributed to the same fixing of the lattice and profile parameters. This was evident as the observed deviation only began below 210 K, the temperature at which the aforementioned parameters were fixed. As the impurity compound did not affect any further aspects of the refinement, it will not be further discussed in this work.

The bond lengths Cu – F and Zr – F obtained from the sPXRD analyses differed considerably from those determined by the SCXRD data. Selected PXRD bond lengths are given in Table 4.8, along with the SCXRD data for reference. The main discrepancy appears to be due to the position of the F1 atom, presumably related to the preferred orientation problems in the sPXRD data.

Below 230 K the bond lengths obtained from the sPXRD data were disregarded as the bond lengths deviated notably. This was attributed to the phase transition and the co-existence of the two phases, in addition to the sudden decrease in the weight fraction of the rhombohedral phase. Thus, the atomic parameters were fixed and not refined once the phase transition began to appear.

The lattice parameters for the rhombohedral phase were plotted as a function of temperature, Figure 4.16. The weight percentage was also monitored over the same temperature range, Figure 4.16.

Table 4.8: Selected bond lengths [Å] for the rhombohedral phase of $Cs_2ZrCu_3F_{12}$ over the temperature range 300 K to 230 K obtained from Rietveld refinements of sPXRD data compared to the SCXRD data at 295 K

Temperature [K]	Cu1-F1	Cu1-F2	Zr1-F1
295 SCXRD	**1.892(2)**	**2.331(6)**	**2.009(6)**
300	1.8856(18)	2.304(5)	2.083(7)
290	1.8752(14)	2.305(4)	2.066(5)
280	1.8839(18)	2.301(4)	2.116(5)
270	1.8768(14)	2.309(5)	2.087(6)
260	1.8643(14)	2.300(4)	2.091(5)
250	1.8716(13)	2.312(4)	2.089(5)
240	1.8871(17)	2.298(4)	2.105(5)
230	1.8801(15)	2.305(4)	2.112(5)

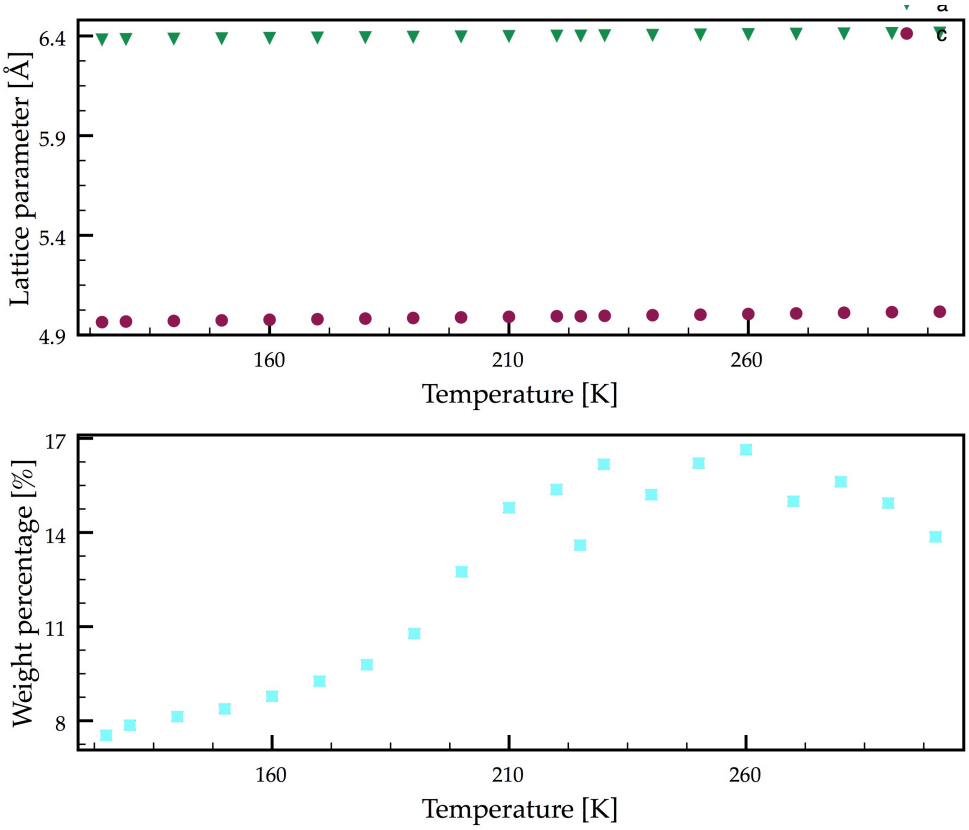

Figure 4.15: Lattice parameters a and c (top) for the impurity phase Cs_2ZrF_6 versus temperature, and (bottom) the weight percentage of the sample versus temperature

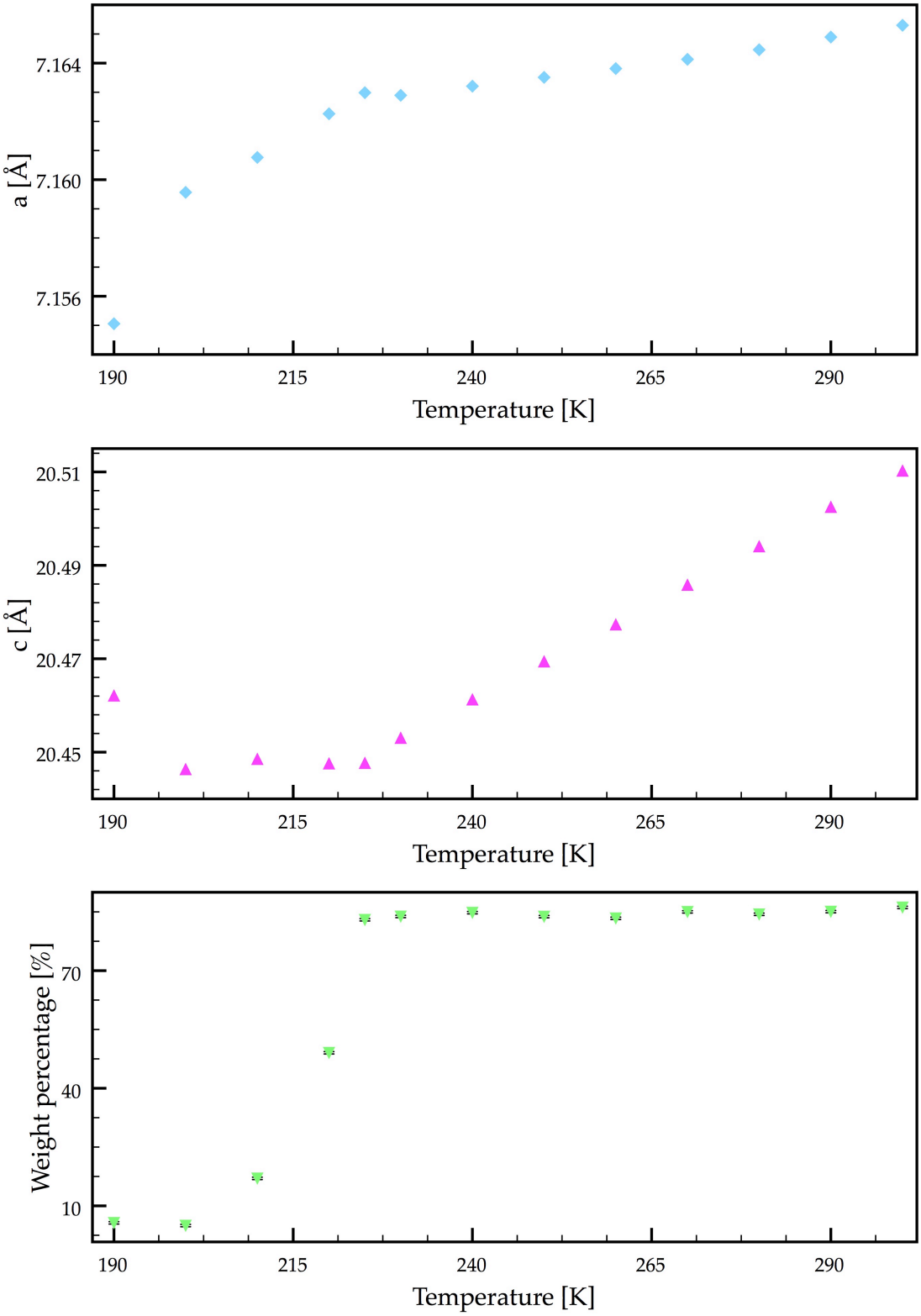

Figure 4.16: Lattice parameters a (top) and c (middle) for the rhombohedral phase of $Cs_2ZrCu_3F_{12}$ versus temperature, and (bottom) the weight percentage of this phase versus temperature

At 225 K, there was the first evidence of a phase transition occurring. This temperature agreed well with that reported by Ono *et al.*[16] The phase fraction of the rhombohedral phase dropped quickly from around 80% at 225 K to 0% at 180 K. The monoclinic phase in turn increased from 3% at 225 K to roughly 90% at 180 K. The discrepancy between the maximum amounts of each phase was attributed to the fixing of the Cs_2ZrF_6 impurity phase at low temperatures and the resultant compromise in fit. The co-existence of the two $Cs_2ZrCu_3F_{12}$ phases indicated a first-order phase transition, Figure 4.17. The powder patterns in this temperature range showed the first order phase transition very clearly, Figure 4.18. At 230 K, it was clear that there was only one $Cs_2ZrCu_3F_{12}$ phase, but by 210 K both phase could be clearly distinguished, and by 180 K only the monoclinic phase of $Cs_2ZrCu_3F_{12}$ remained. Throughout the phase transition, it was possible to refine the lattice parameters and profile coefficients for each phase, but not the full structural models. At low phase fractions (below 5%) the lattice parameters and profile coefficients were extrapolated from the previous data and fixed. Figure 4.19 is a Rietveld plot at 210 K showing the two phases. Figures 4.20 and 4.21 show detailed plots of the 210 K data.

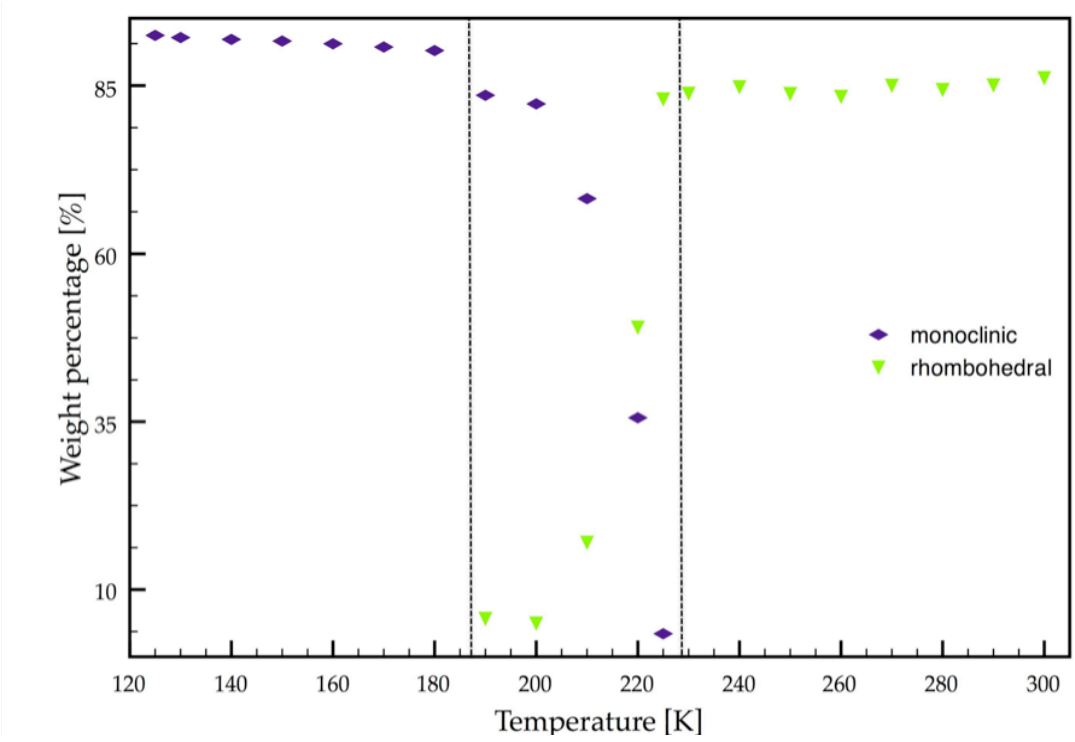

Figure 4.17: Weight fractions of the two phases of $Cs_2ZrCu_3F_{12}$ as a function of temperature showing the co-existence of the two phases during the phase transition

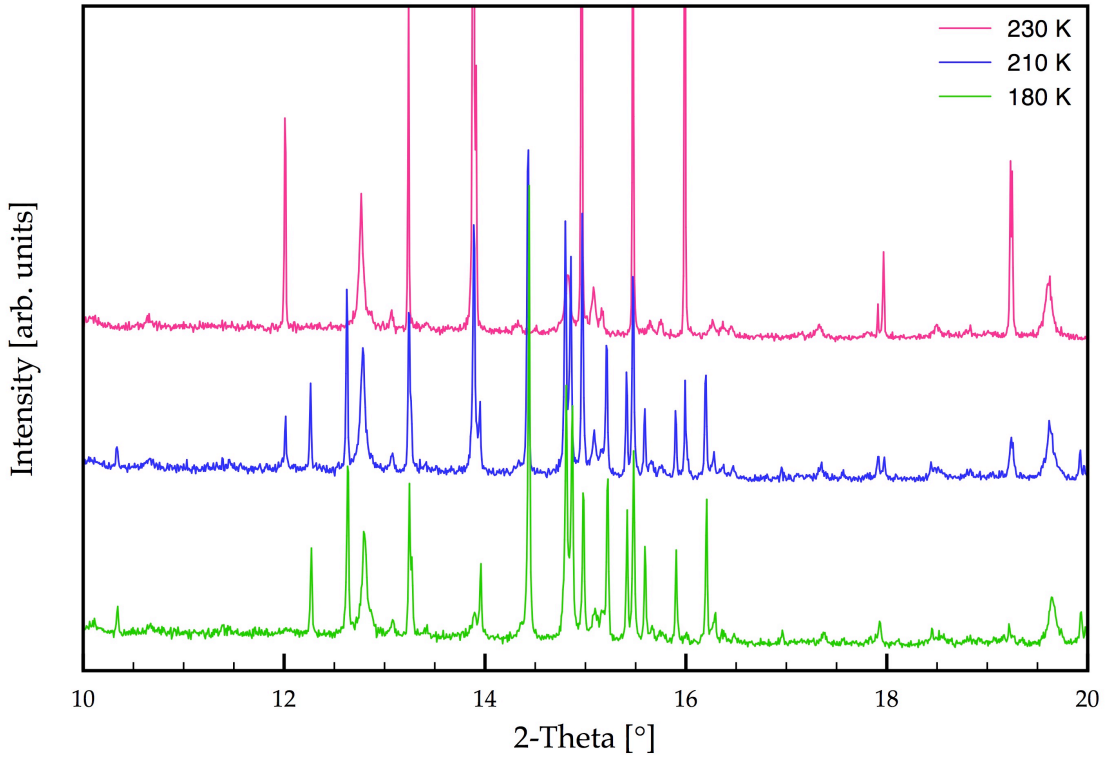

Figure 4.18: Plots of the observed data for $Cs_2ZrCu_3F_{12}$ before (pink), during (blue) and after (green) the phase transition

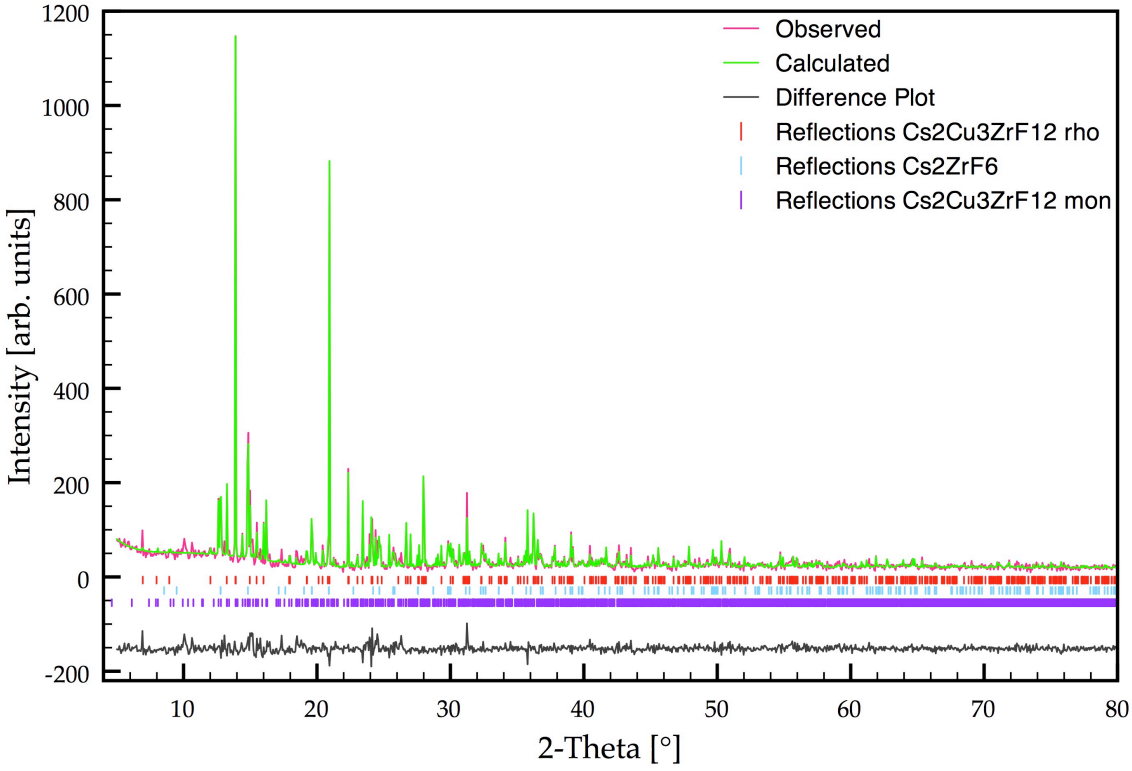

Figure 4.19: Rietveld plot for the two phases of $Cs_2ZrCu_3F_{12}$ showing the co-existence of the two phases at 220 K

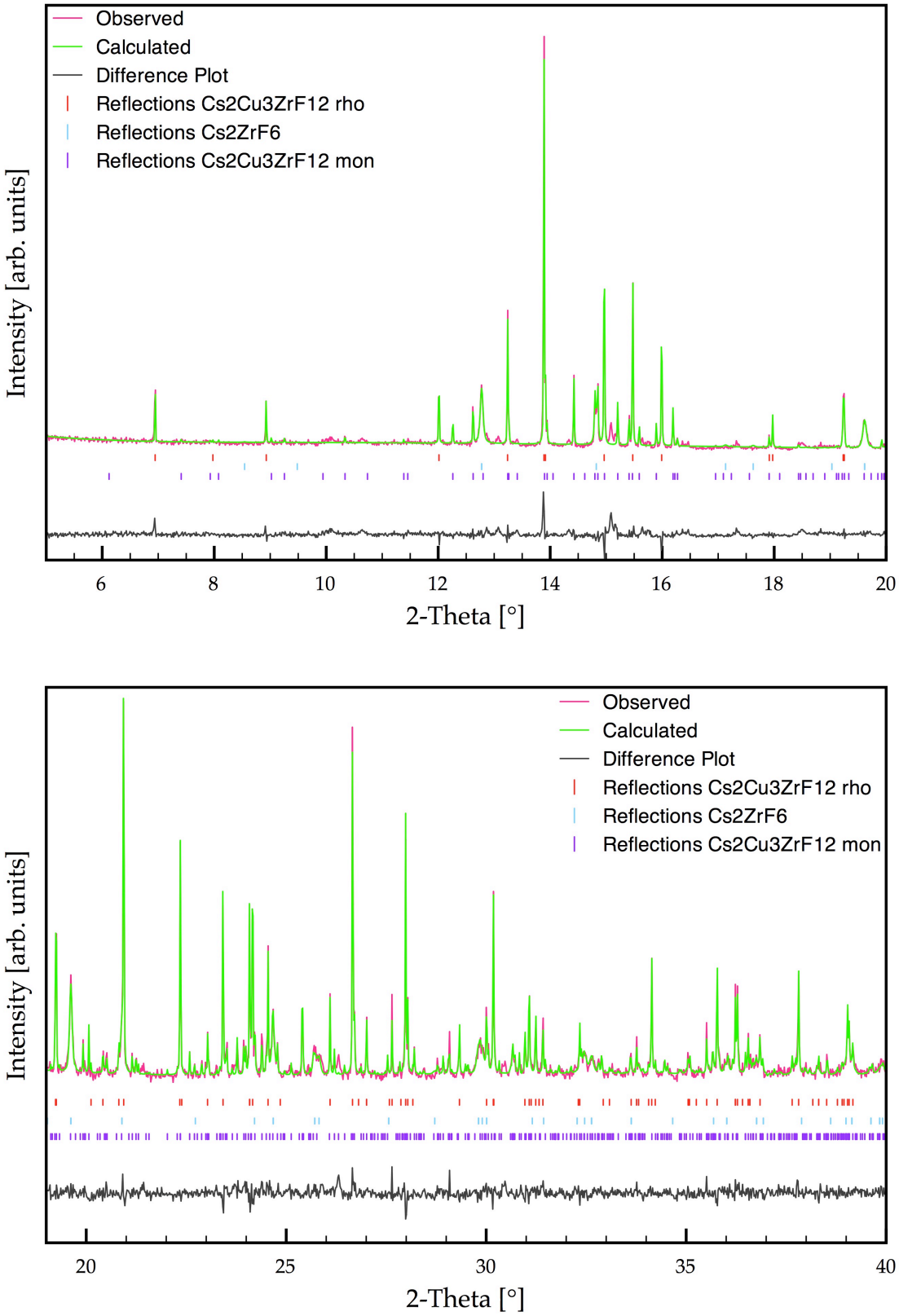

Figure 4.20: Detailed Rietveld plots for the phase transition of $Cs_2ZrCu_3F_{12}$ at 220 K showing the 5 to 20° 2-theta range (top) and the 20 to 40° 2-theta range (bottom)

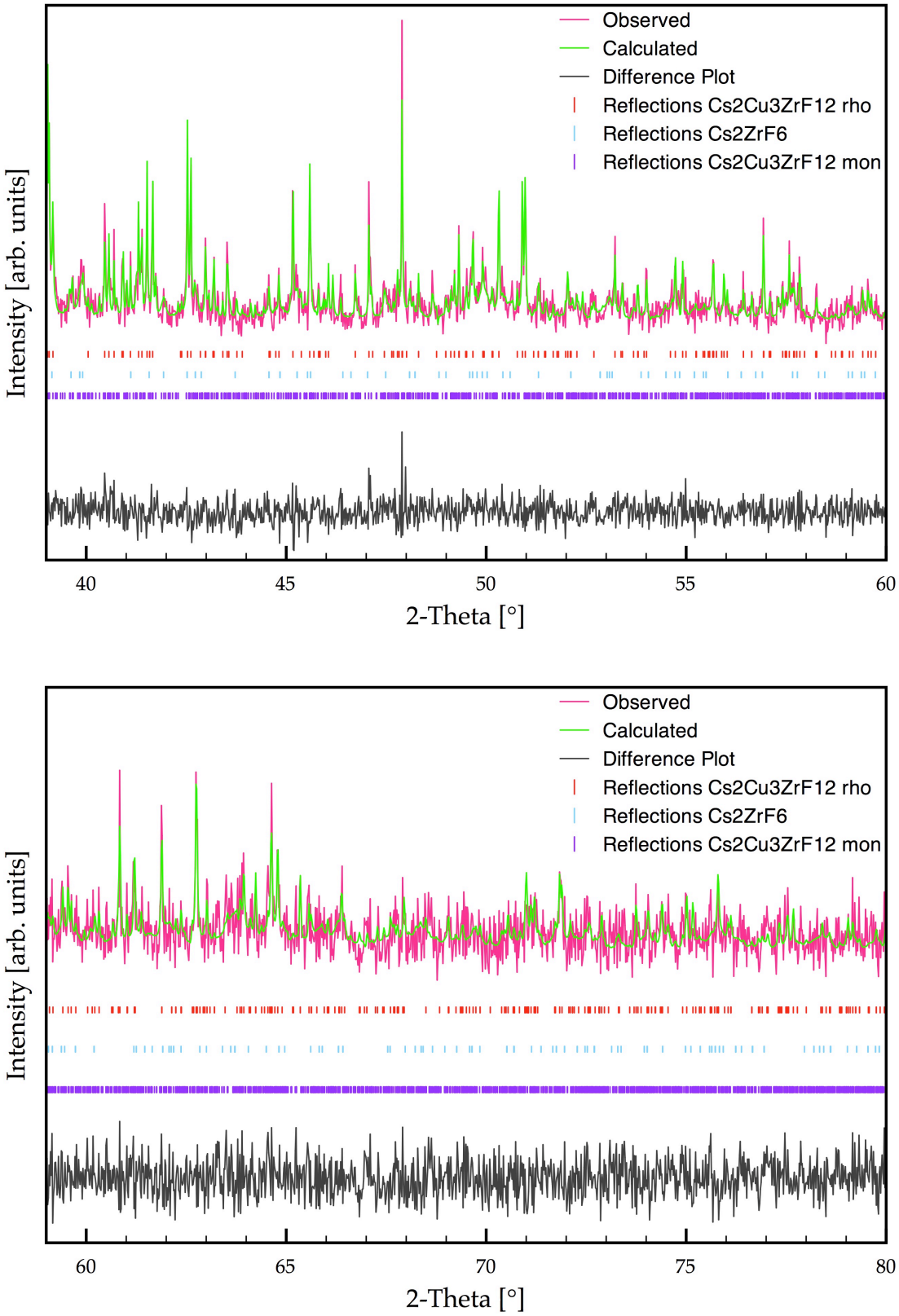

Figure 4.21: Detailed Rietveld plots for the phase transition of $Cs_2ZrCu_3F_{12}$ at 220 K showing the 40 to 60° 2-theta range (top) and the 60 to 80° 2-theta range (bottom)

The monoclinic phase fitted the experimental data well, Figures 4.22 to 4.24. The only problem was that the atom parameters (positions and atomic displacement parameters) could not be brought to converge and were thus fixed to the values of the SCXRD data. For the monoclinic phase, the following were refined: lattice parameters; pseudo-Voigt profile parameters - GW (for the Gaussian contribution) and LY (for the Lorentzian contribution); and all 34 order terms of the spherical harmonics ODF giving 168 ODF terms. All parameters, apart from the phase fraction, were fixed and extrapolated from the high temperature data for the impurity phase.

The lattice parameters for the monoclinic phase evolved continuously and showed no anomalies, Figure 4.25. The nonlinear behaviour of the values at 225 and 200 K were assigned to the low phase fraction of the sample and thus the refinement was rather approximate for these temperatures. The weight fraction of the phase grew in quickly from 225 K and stayed constant after that, as previously shown in Figure 4.17. The lattice parameters at 125 K (a = 7.73268(3) Å, b = 7.13917(3) Å, c = 10.24999(4) Å, β = 93.924(5)°) agreed well with those reported for the SCXRD data (a = 7.798(15) Å, b = 7.212(14) Å, c = 10.351(19) Å, β = 93.97(2)°).

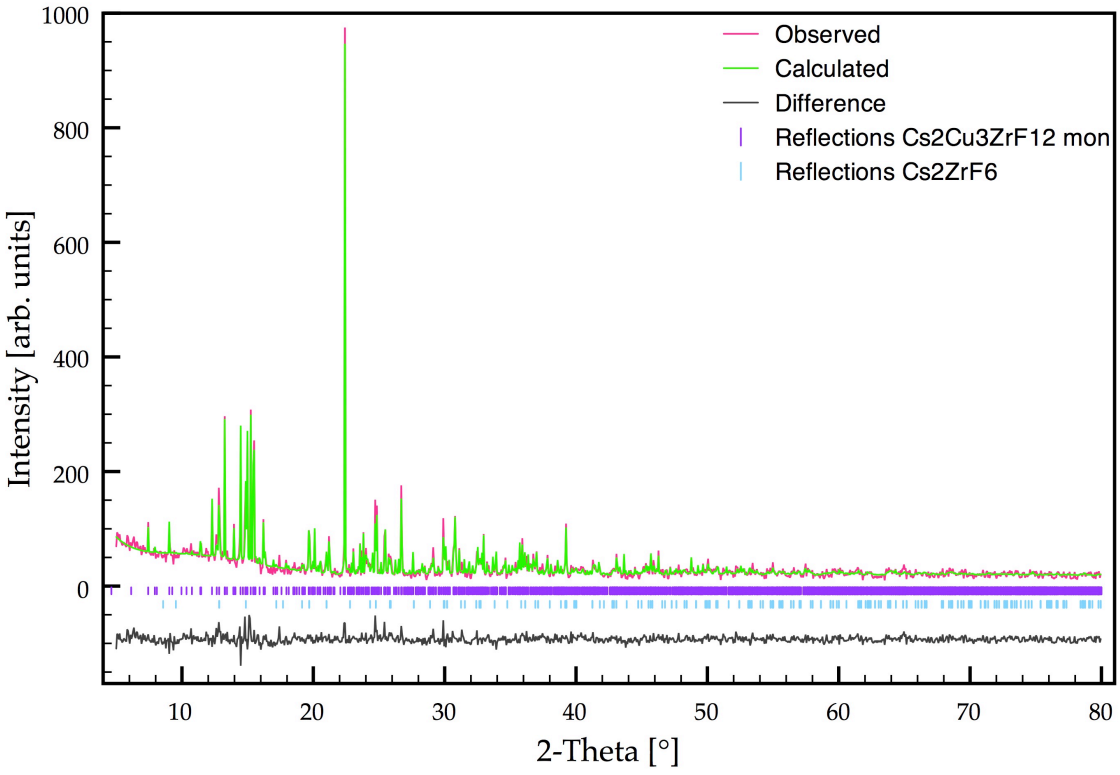

Figure 4.22: Rietveld plot of monoclinic $Cs_2ZrCu_3F_{12}$ at 125 K

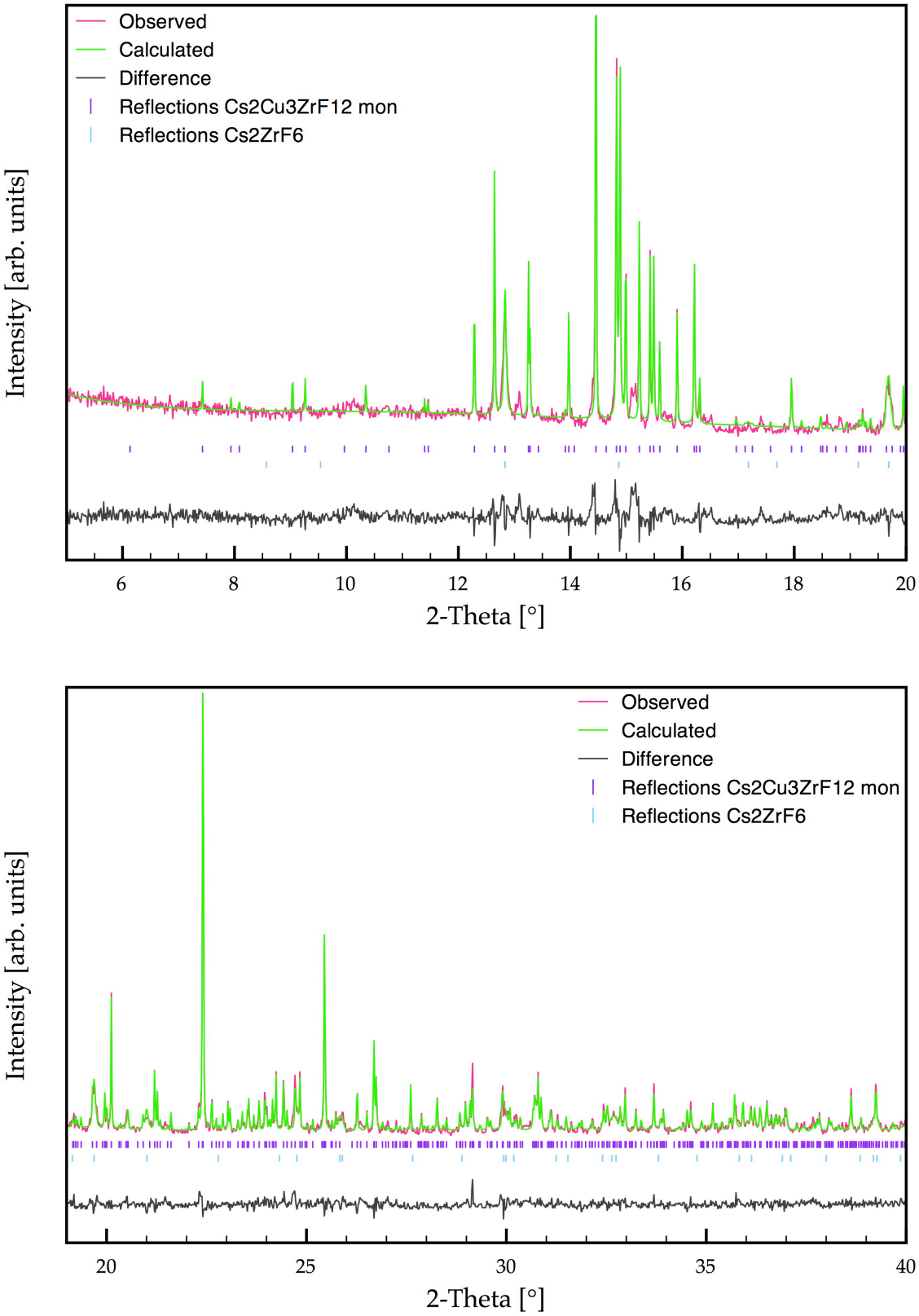

Figure 4.23: Detailed Rietveld plots for the monoclinic $Cs_2ZrCu_3F_{12}$ phase at 125 K showing the 5 to 20° 2-theta range (top) and the 20 to 40° 2-theta range (bottom)

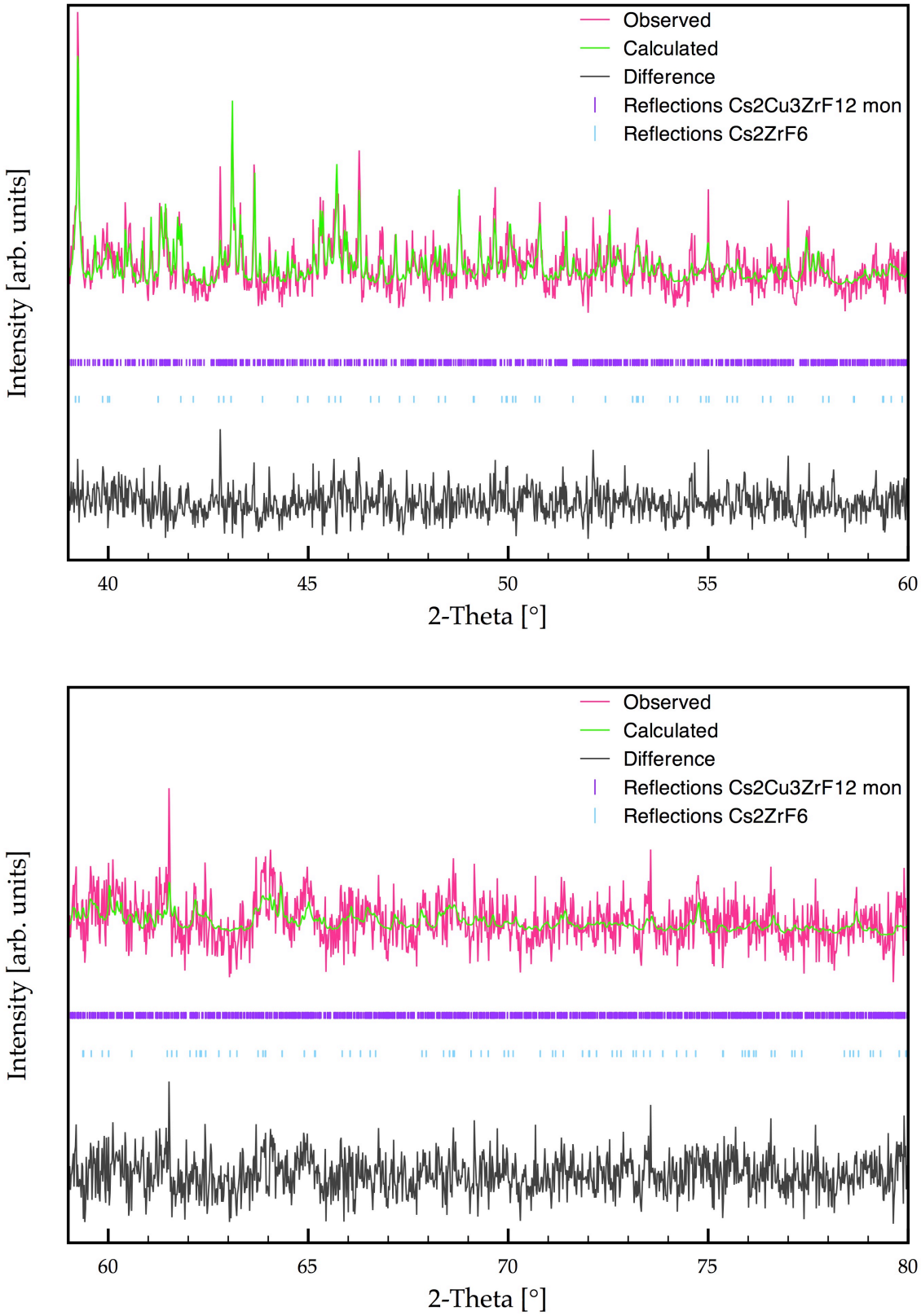

Figure 4.24: Detailed Rietveld plots for the monoclinic $Cs_2ZrCu_3F_{12}$ phase at 125 K showing the 40 to 60° 2-theta range (top) and the 60 to 80° 2-theta range (bottom)

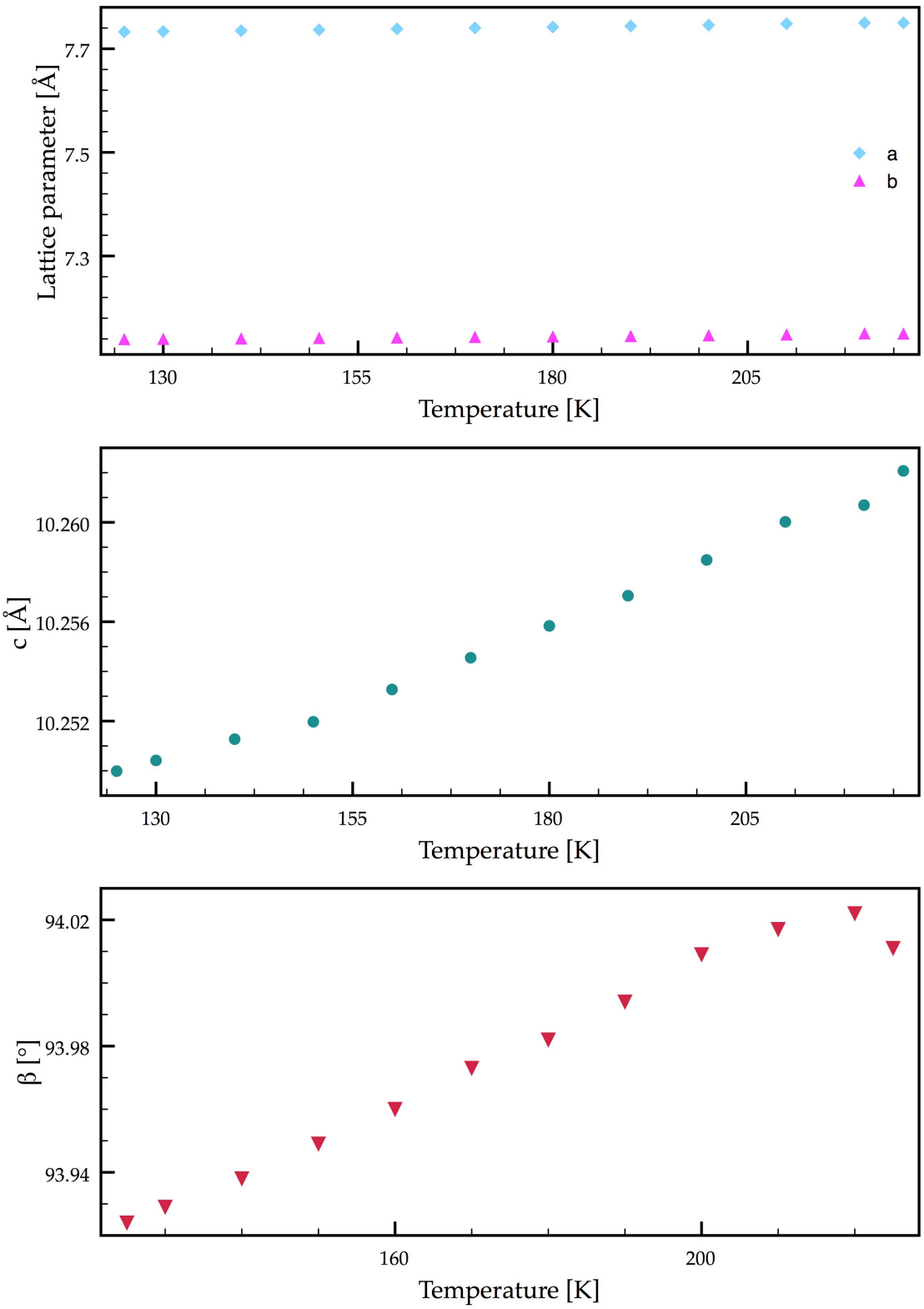

Figure 4.25: Lattice parameters a and b (top), and c (middle) for the monoclinic phase of $Cs_2ZrCu_3F_{12}$ versus temperature, and (bottom) the angle β of the unit cell versus temperature

In order to allow for a direct comparison of the two phases, the lattice parameters of the two phases were converted to an equivalent crystallographic setting. The transformation matrix to convert the rhombohedral model to the equivalent monoclinic model was found to be (⅓ ⅔ -⅓ ; -1 0 0; ⅔ ⅘ ⅓). This transformation matrix was then used to obtain the lattice parameters for the "pseudo-monoclinic" model corresponding to the rhombohedral phase. A plot of these is given in Figures 4.26 and 4.27. A clear break was seen in all of the parameters when passing through the phase transition. The only parameter that showed some relationship between the two phases was the *b* lattice parameter. This was not unexpected as it was the only parameter that remained unchanged during the matrix transformation. The abrupt change in lattice parameters at the phase transition mirrored the change in the structure due to the change in the coordination number of the Zr^{4+} ion and the resultant buckling of the kagome layers away from the ideal planar arrangement.

4.4.3 AC Impedance Spectroscopy Measurements on $Cs_2ZrCu_3F_{12}$

The sample was analysed by impedance spectroscopy and found to have a step in capacitance at the phase transition, Figure 4.28. In addition to this, there was clear evidence of hysteresis of approximately 10 K upon reheating the sample, supporting the conclusion of a first-order phase transition. When using several of the data points below the transition, and then several above, an approximation of the relative permittivity was found to be around 4.0 for the monoclinic model, and 4.5 for the rhombohedral model using the equation

$$C = \varepsilon' \varepsilon_0 \frac{A}{d} \qquad (4.1)$$

The equation relates the capacitance, C, to the dielectric constant, ε′, the permittivity of free space, ε_0, and the geometric factor (A/d). In the geometric factor, A denotes the area of the electrode and d the distance between the two electrodes. This geometric factor was approximated to be of the magnitude 1 cm. The ratio of the two relative permittivities was 0.89.

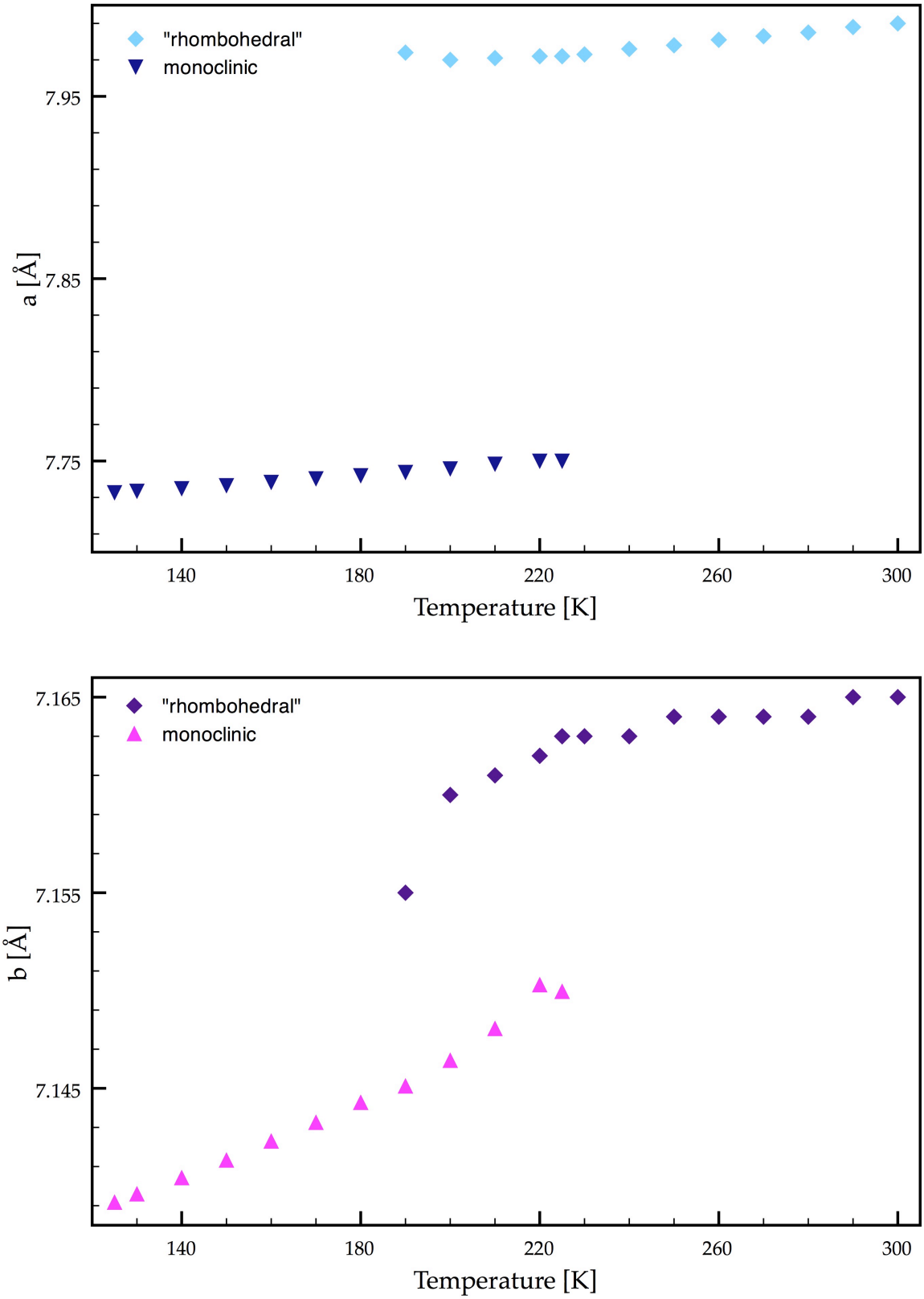

Figure 4.26: Comparative plots of the lattice parameters a (top) and b (bottom) for the two phases of $Cs_2ZrCu_3F_{12}$ set in the monoclinic phase

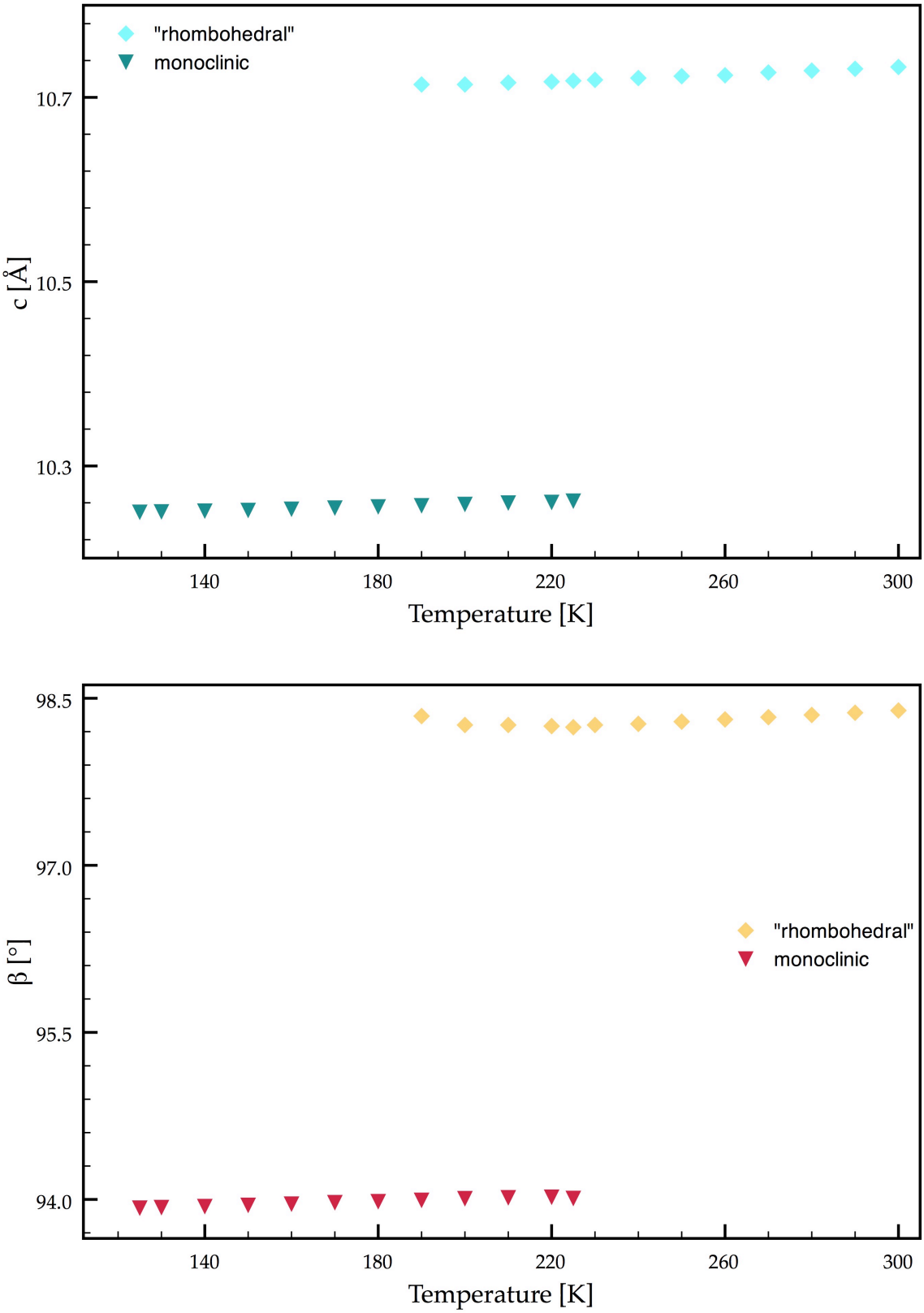

Figure 4.27: Comparative plots of the lattice parameter c (top) and the angle β (bottom) for the two phases of $Cs_2ZrCu_3F_{12}$ set in the monoclinic phase

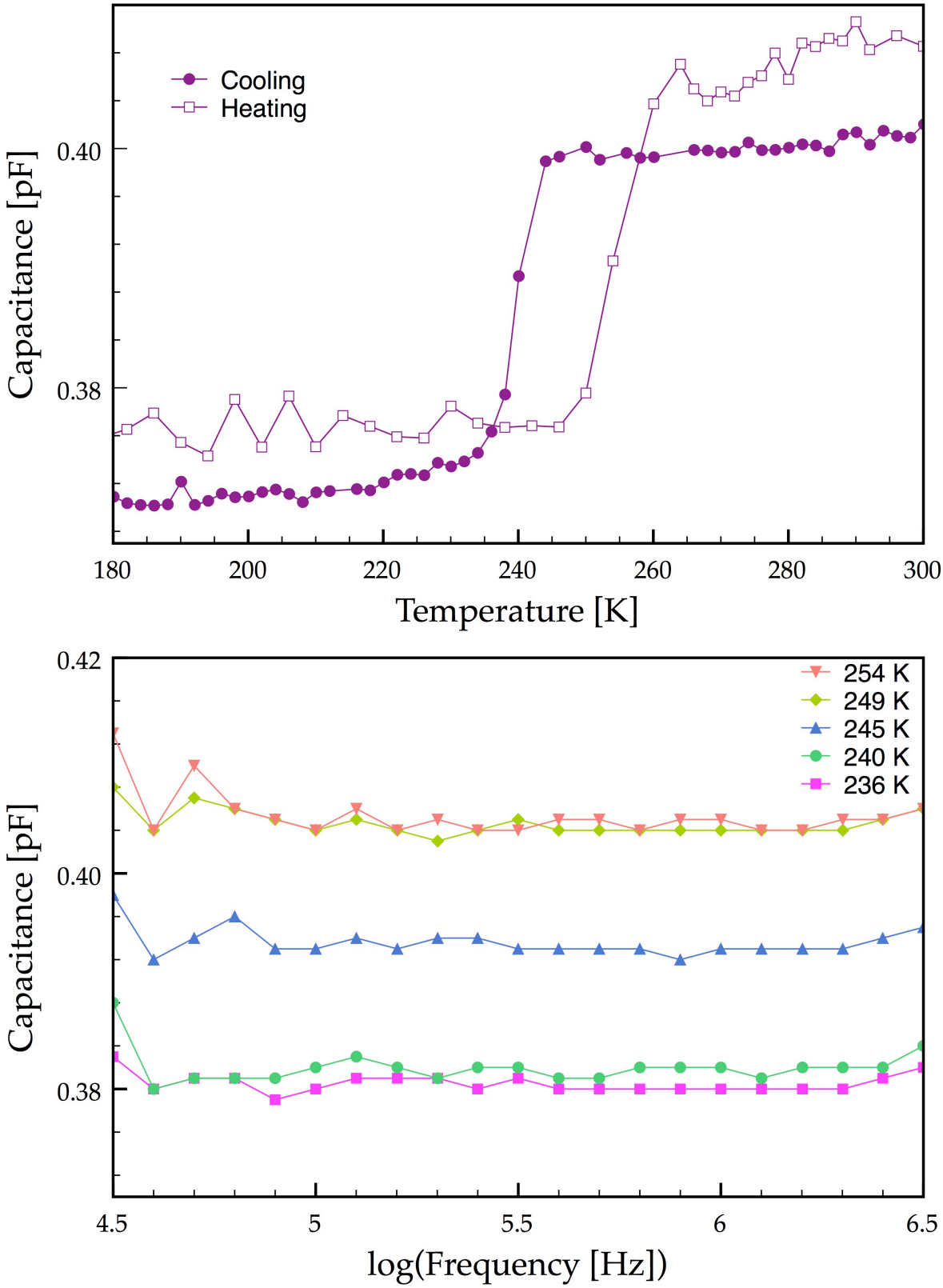

Figure 4.28: Capacitance dependence of $Cs_2ZrCu_3F_{12}$ versus temperature on both cooling and heating at 1 MHz (top), and (bottom) the capacitance versus the log of the frequency at selected temperatures above, during, and below the phase transition

The theoretical permittivity values were then calculated using the Clausius-Mosotti equation

$$\varepsilon' = \frac{\left(3V_m + 8\pi\alpha_D^T\right)}{\left(3V_m - 4\pi\alpha_D^T\right)} \qquad (4.2)$$

Here, V_m is the molar volume of the sample, taken from the SCXRD solutions, and α^T_D is the total dielectric polarisability, which is calculated from average values given by Shannon.[17] The polarisability of Cs^+ was 7.43 Å^3, 3.25 Å^3 for Zr^{4+}, 2.11 Å^3 for Cu^{2+}, and 1.62 Å^3 for F^-. The value for α^T_D was then summed as follows: $2xCs^+ + Zr^{4+} + 3xCu^{2+} + 12xF^-$; this gave a sum total of 43.88 Å^3. The calculated relative permittivities for the monoclinic and rhombohedral models were 5.7 and 6.2 respectively. The ratio of the two was 0.91, close to the observed ratio for the experimental data, indicating a good agreement of the calculated and observed values. The ratio was a better estimate of the fit of the values as the geometric factor, (A/d), in equation (4.1) was estimated at 1.0. This estimate was made from an inspection of the agglomerate crystals and the electrodes thereon. By taking the ratio of the numbers, this experimental error was eliminated.

A second set of measurements was then performed to verify that the observed change in capacitance was due to the phase transition. There was no change in the capacitance versus frequency as can be seen from Figure 4.28. The change could thus be attributed to the phase transition.

4.4.4 Comparison of $Cs_2ZrCu_3F_{12}$ and $Rb_2SnCu_3F_{12}$

As reported in the introduction to this chapter, several compounds of the form $A_2BCu_3F_{12}$ (A^+ = Cs, Rb; B^{4+} = Zr, Hf, Sn) have been synthesised to date. All three of the Cs analogues have been reported, whilst only $Rb_2SnCu_3F_{12}$ has been reported for the Rb group. All three Cs materials were reported in the aristotype rhombohedral form. Furthermore, all three showed magnetic susceptibility anomalies at lower temperatures that were attributed to a phase transition. From the magnetic and diffraction data, it became clear that the Zr

and Hf compounds underwent a first-order phase transition, whilst the Sn material seemed to undergo a second-order phase transition. There is no evidence of a phase transition for the Rb analogue.

Both $Cs_2ZrCu_3F_{12}$ and $Rb_2SnCu_3F_{12}$ crystallise in a rhombohedral form at room temperature, although the former in $R\bar{3}m$ and the latter in $R\bar{3}$. Thus, $Rb_2SnCu_3F_{12}$ has lost the mirror plane present in the $Cs_2ZrCu_3F_{12}$. The result is an increase in the unit cell to 2*a*, 2*a*, *c*, Figure 4.29. The $Rb_2SnCu_3F_{12}$ structure has two crystallographically distinct Cu^{2+} ions. This is due to there being some disorder amongst two of the axial out-of-plane fluorides. The net result is that there are now two distinct triangles being formed by the Cu^{2+} ions, Figure 4.30. The two triangles for $Rb_2SnCu_3F_{12}$ are dissimilar in that the one is formed by three Cu1 atoms and thus equilateral (triangle B) and the second triangle has different lengths for all three sides (triangle A), and thus no symmetry. A side-on view of the kagome layers indicates a further difference between the two structures, Figure 4.30. In the diagram, the Cu^{2+} ions for the $Rb_2SnCu_3F_{12}$ compound were drawn in different colours to indicate the different sites. The Cu – F – Cu angles consequently change from 142.1° for $Cs_2ZrCu_3F_{12}$ to between 123.9° and 138.4° for $Rb_2SnCu_3F_{12}$. These angles are comparable to the angles for the monoclinic distortion of $Cs_2ZrCu_3F_{12}$ which are between 126.7° and 142.7°.

Further, there is no evidence of a phase transition for $Rb_2SnCu_3F_{12}$. $Cs_2ZrCu_3F_{12}$, on the other hand, changes from rhombohedral to monoclinic. This is as a result of the change in coordination environment for the Zr^{4+} ion. At room temperature it adopted a six-fold coordination, which is a very unusual number for Zr^{4+}; it prefers higher coordination numbers such as 7 or 8.[18, 19] This preference for higher coordination numbers is not mirrored by Sn^{4+}; its favoured coordination number is 6.

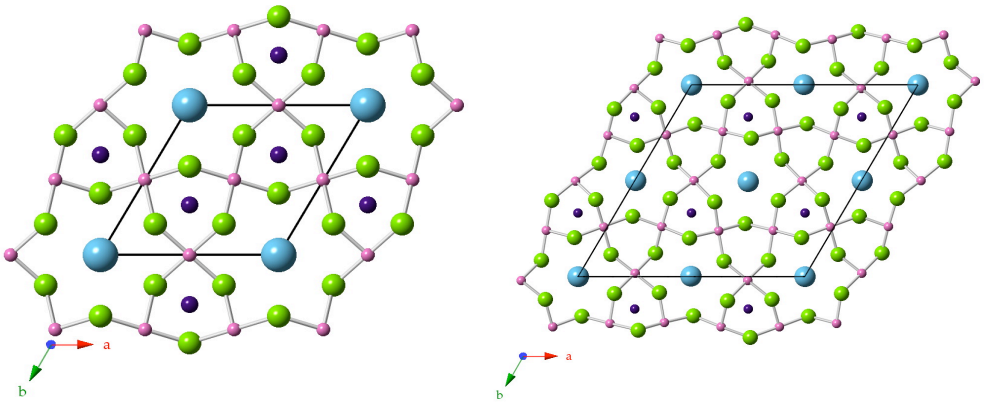

Figure 4.29: Kagome sheets and unit cells for $Cs_2ZrCu_3F_{12}$ (left) and $Rb_2SnCu_3F_{12}$ (right) indicating the doubling of the a and b axes for the latter

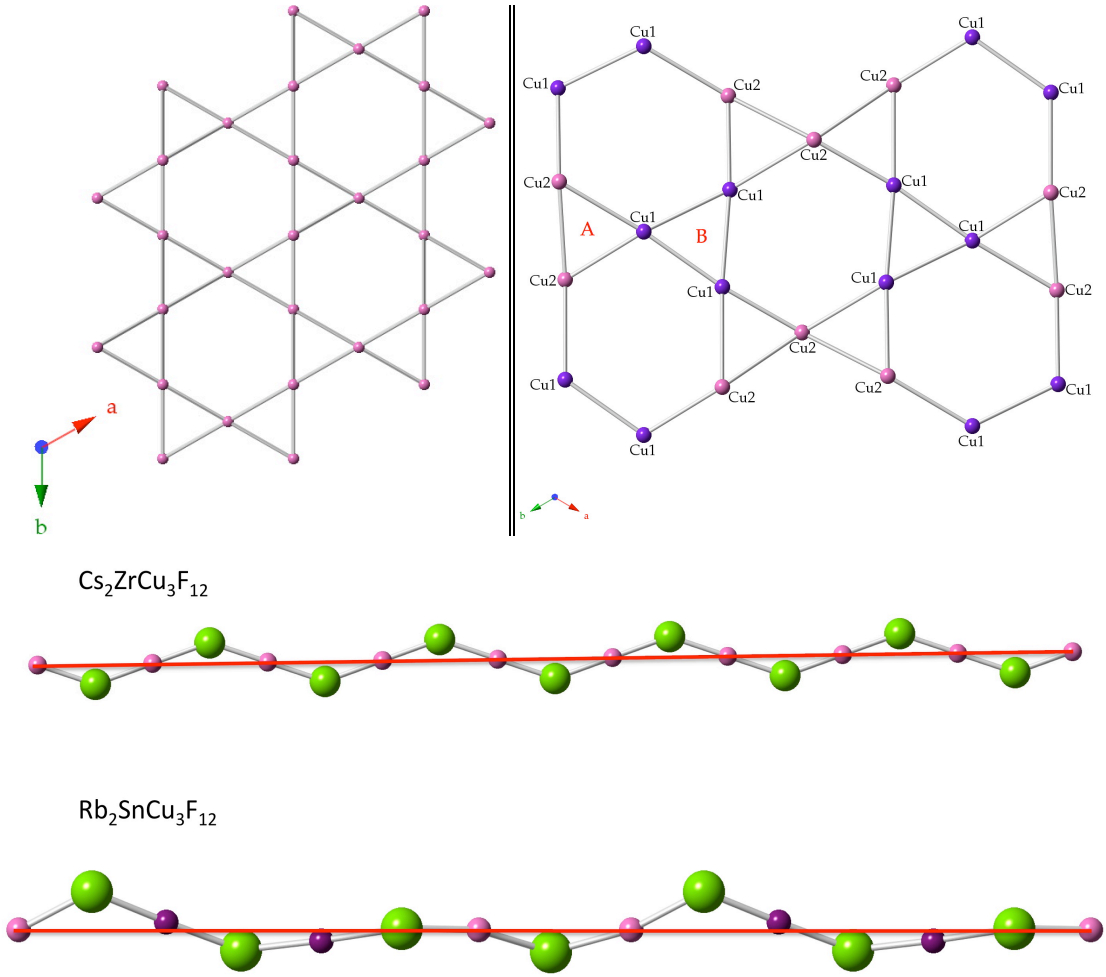

Figure 4.30: Cu kagome grid arrangement in the $Cs_2ZrCu_3F_{12}$ (top left) and $Rb_2SnCu_3F_{12}$ (top right) indicating the single triangle for $Cs_2ZrCu_3F_{12}$ and two distinct triangles for $Rb_2SnCu_3F_{12}$; the Cu layers are shown in a side-on view below (the two Cu sites are given in different colours in $Rb_2SnCu_3F_{12}$)

Whilst these two compounds are good examples of the difference between an "ideal" kagome lattice and a distorted one, the compound $Cs_2CeCu_3F_{12}$, as reported by Amemiya *et al.*[20] is an example of an extremely distorted kagome lattice, to the point that the layers seem to arrange themselves in a step-like manner, Figure 4.31. The side-on view of the layer is compared to the two aforementioned materials in Figure 4.32. This compound cannot be modelled in the high symmetry rhombohedral space groups, and is instead best described in the orthorhombic space group *Pnnm* (a = 11.0970(16) Å, b = 14.441(2) Å, c = 7.2970(11) Å). This buckling is attributed to the large Ce atom, whose coordination number is 8. The net result is that the compound shows only partial ferromagnetic ordering but is still antiferromagnetic below 3.0 K.

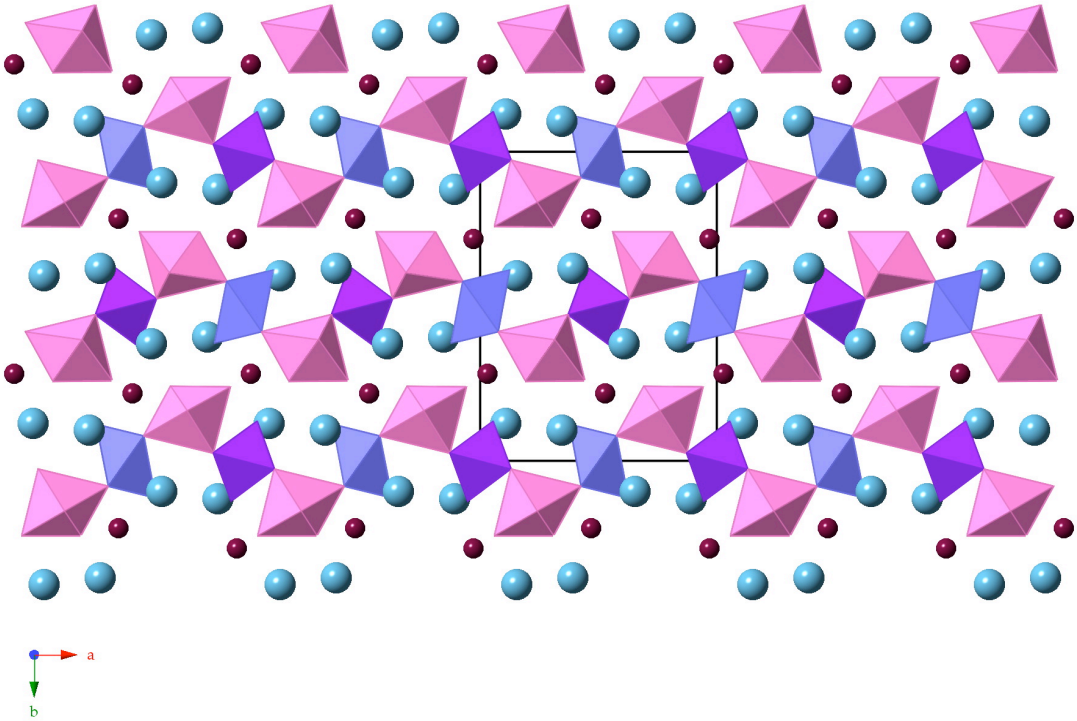

Figure 4.31: Kagome structure of $Cs_2CeCu_3F_{12}$ viewed along the c-axis showing the severely buckled kagome Cu-layers, with the three distinct Cu sites indicated in different colours

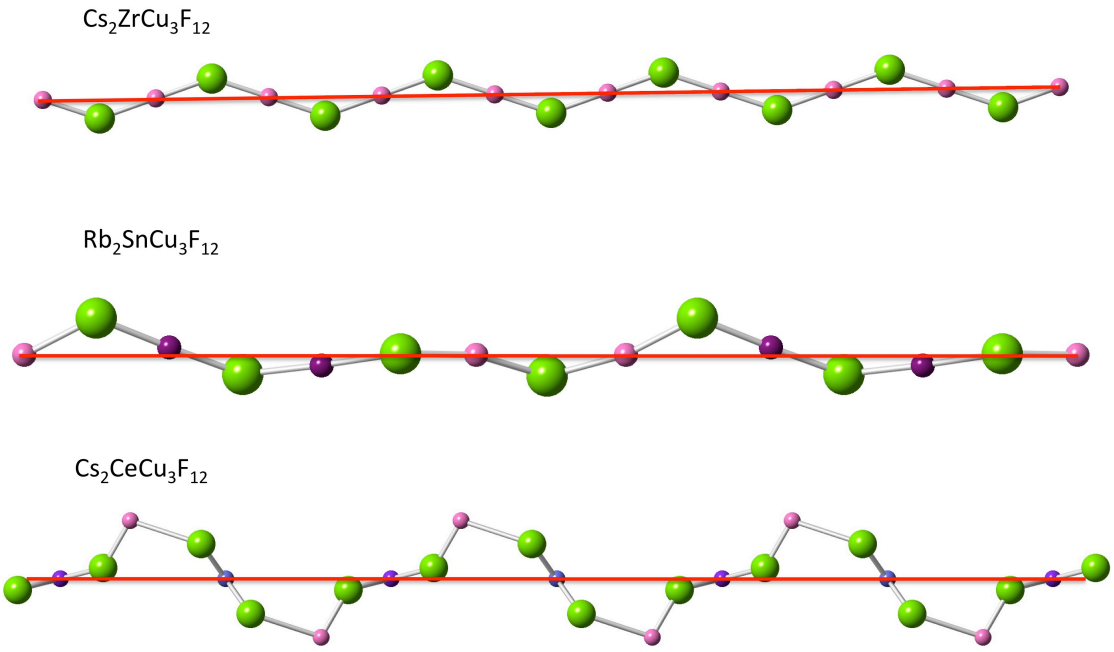

Figure 4.32: Side-on view of the Cu kagome layers for $Cs_2ZrCu_3F_{12}$ (top) $Rb_2SnCu_3F_{12}$ (middle) and $Cs_2CeCu_3F_{12}$ (bottom) with the crystallographically distinct Cu sites shown in different colours for the latter two compounds

4.5 Conclusions

The two phases of $Cs_2ZrCu_3F_{12}$ show the "ideal" and distorted kagome lattices well and indicate the consequence of tilting of these layers in the RT and LT structures. The catalyst for this buckling is the movement of one F atom towards the Zr^{4+} ion to increase its the coordination number from 6 to 7. The Cu^{2+} ion bonded to that F atom then also moves out of the plane to maintain its octahedral geometry. This leads to the generation of three crystallographically distinct Cu sites.

The change in lattice parameters in going from one phase to the other is very abrupt (first-order) as can be seen when the rhombohedral model is transformed into a pseudo-monoclinic form and the lattice parameters plotted as a function of temperature.

The electrical data shows an anomaly at the phase transition temperature. This anomaly occurs at the same temperature where an anomaly

has been reported in the magnetic susceptibility measurements. This supports the conclusion that both of these changes are a result of the structural change.

The change in coordination number is a likely driving force to explain why $Rb_2SnCu_3F_{12}$ is a VBS whilst $Cs_2ZrCu_3F_{12}$ is not.

Attempts have been made to synthesise the remaining members of the $A_2BCu_3F_{12}$ (A^+ = Cs, Rb; B^{4+} = Zr, Sn) family. Whilst successful, the desired products are the minor phase and work is ongoing to find a more successful synthetic route. A further isotypic family of materials that is to be synthesised is $A_2TiCu_3F_{12}$ (A^+ = Cs, Rb), where the $Cs_2TiCu_3F_{12}$ is deemed the most ideal potential candidate for a QSL.

This chapter has recently been accepted for publication in the journal *Chemistry of Materials* (Manuscript ID: cm-2011-01762f).

4.6 References

1. A. Harrison, *J. Phys.: Condens. Matter*, 2004, **16**, S553-S572.
2. L. Balents, *Nature*, 2010, **464**, 199-208.
3. F. L. Pratt, P. J. Baker, S. J. Blundell, T. Lancaster, S. Ohira-Kawamura, C. Baines, Y. Shimizu, K. Kanoda, I. Watanabe and G. Saito, *Nature*, 2011, **471**, 612-616.
4. G. Courbion, C. Jacoboni and R. de Pape, *Acta Crystallogr., Sect. B: Struct. Sci.*, 1976, **32**, 3190-3193.
5. A. Le Bail, Y. Gao, J. L. Fourquet and C. Jacoboni, *Mater. Res. Bull.*, 1990, **25**, 831-839.
6. U. Englich, C. Frommen and W. Massa, *J. Alloys Compd.*, 1997, **246**, 155-165.
7. M. Müller and B. G. Müller, *Z. Anorg. Allg. Chem.*, 1995, **621**, 993-1000.
8. Y. Yamabe, T. Ono, T. Suto and H. Tanaka, *J. Phys.: Condens. Matter*, 2007, **19**, 145253.
9. K. Morita, M. Yano, T. Ono, H. Tanaka, K. Fujii, H. Uekusa, Y. Narumi and K. Kindo, *J. Phys. Soc. Jpn.*, 2008, **77**, -.
10. K. Matan, T. Ono, Y. Fukumoto, T. J. Sato, J. Yamaura, M. Yano, K. Morita and H. Tanaka, *Nature Phys.*, 2010, **6**, 865-869.

11. T. Ono, K. Morita, M. Yano, H. Tanaka, K. Fujii, H. Uekusa, Y. Narumi and K. Kindo, *J. Phys.: Conf. Ser.*, 2009, **145**, 012005.
12. G. M. Sheldrick, *Acta Crystallogr., Sect. A: Found. Crystallogr.* , 2008, **64**, 112-122.
13. A. R. West, in *Solid State Chemistry and Its Applications*, Wiley, Chichester, 1984, Chapter 3.
14. *General Structure Analysis System GSAS*, A. C. Larson and R. B. von Dreele, Report No. La-UR-86-748, 1987.
15. H. Bode and G. Teufer, *Z. Anorg. Allg. Chem.*, 1956, **283**, 18-25.
16. T. Ono, K. Morita, M. Yano, H. Tanaka, K. Fujii, H. Uekusa, Y. Narumi and K. Kindo, *Phys. Rev. B: Condens. Matter*, 2009, **79**, 174407.
17. R. D. Shannon, *J. Appl. Phys.*, 1993, **73**, 348-366.
18. K. Adil, M. Leblanc, V. Maisonneuve and P. Lightfoot, *Dalton Trans.*, 2010, **39**, 5983-5993.
19. R. L. Davidovich, *Russ. J. Coord. Chem.*, 1998, **24**, 751-768.
20. T. Amemiya, M. Yano, K. Morita, I. Umegaki, T. Ono, H. Tanaka, K. Fujii and H. Uekusa, *Phys. Rev. B: Condens. Matter*, 2009, **80**, 100406.

Chapter 5

Exploratory Hydrothermal and Slow Evaporation Reactions on Metal Fluorides

5.1 Introduction to Hydrothermal Methods[1-3]

The term hydrothermal was originally coined by Sir Roderick Murchison to refer to the effect water had in the earth's crust at high temperatures and pressures. Hydrothermal reactions were then designed by geologists to mimic this behaviour and synthesise minerals. Schafthaul was the first to do this by making quartz crystals in 1845.[1] Since then, the hydrothermal method has been used to synthesise many new materials.[2] Particular successes have been achieved in the synthesis of zeolites, nanotubes and rods, and new oxides.[4]

Although much progress has been made in developing this method, it has focussed mostly on the materials that are used as the reaction vessels. Very little is known about the actual processes and mechanisms occurring during these reactions, and so the reactions are quite frequently referred to as "black-box" reactions, because the starting materials and the products are known, but the intermediate steps are a mystery.

Hydrothermal reactions, in this work, are referred to as reactions done in a closed system, a bomb autoclave, using an aqueous solvent and heating the system above 100 °C under autogeneous pressure. If a non-aqueous solvent is used, it is referred to as a solvothermal reaction.

The advantage of doing reactions in a hydrothermal manner is that the extreme pressure conditions and low reaction temperatures, allow for new compounds and also phases of known compounds to be made. The synthesis of meta-stable phases and compounds is also easily achieved. The addition of solvent to the reaction vessel allows for the inclusion of solvent molecules in the structure, something that is not possible in solid state reactions of the same starting materials. This solvent inclusion and the attainment of meta-stable

phases was the driving force behind the success of the zeolite syntheses using hydrothermal methods. Also, the reaction times for these reactions are much faster than their ambient pressure analogues. Because of this, it is simple to use this method as a high throughput approach to analysing a system of materials. Further, by changing the solvents, or adding reducing agents (such as ethylene glycol or ethanol), it is very easy to tailor these reactions.

The most reactions in the hydrothermal chemistry area initially focused on inorganic materials. Oxides were of particular interest as the starting materials were readily available. Also, in nature many of the observed minerals are oxides, such as quartz, corundum, and perovskite. All of these are readily synthesised using hydrothermal methods. Attempts were then made to synthesise previously unknown materials of a similar composition. This proved successful and so the field was expanded to include ever more complex and "exotic" materials. Many of these materials could be tailored to be open-framework materials, such as zeolites.[4, 5] These materials have large channels that allow other atoms or molecules to pass through them, and even coordinate to selected atoms within the zeolite.

An area of particular interest in the oxide hydrothermal field has been vanadium oxides.[3, 6] These materials can have the vanadium ion in a range of oxidation states (usually from +3 to +5) and thus allow for many different combinations with oxygen and other atoms. These materials can lead to 1-, 2-, or 3-dimensionally connected structures. Further to this work, much research has been done on vanadium oxyfluorides.[7-11] Examples of pure vanadium fluorides have also been reported.[12]

A further modification that has been done to these compounds is the addition of organic moieties.[13] The organic components can be "templating" agents that act as spacers within the structure, or as ligands, which form a part of the actual structure.[14-17] Only templating reactions are considered and discussed in this chapter. Many templates have been used in hydrothermal reactions, for example pyridine, bipyridyl, ethylene glycol, and imidazolates.

In this chapter, crystal structures of two previously unreported vanadium (oxy)fluorides, $BaVO_2F_3$ and $Sr_2V_2F_{10}.H_2O$, are presented. Several novel organic inorganic hybrid fluorides containing manganese or molybdenum are also reported.

5.2 Experimental

5.2.1 Synthesis

The experimental details for each sample reported are given in the section pertaining to that reaction. In all reactions done, HF is used not as a mineralising agent but rather as a source of fluoride ions as the remaining starting materials do not contain fluoride ions.

5.2.2 Single Crystal X-ray Diffraction

Data were collected in air at 125 K using a Rigaku SCXmini diffractometer. The structures were solved by direct methods and refined using SHELXL-97.[18]

5.2.3 Powder X-ray Diffraction

Standard room temperature PXRD experiments were performed using a Stoe diffractometer (in house) with Ge monochromated Cu K_{α_1} radiation (λ = 1.54056 Å).[19]

5.3 Results and Discussion

The primary focus of this work was to synthesise new inorganic and hybrid fluorides as potential ferroelectrics. By using an exploratory approach it was hoped that several noncentrosymmetric materials could be isolated and studied as possible candidates. This approach proved ultimately unsuccessful, and after an excess of 500 reactions only the compounds described in this chapter were isolated.

The general approach for the two inorganic systems was to initially use a 1:1 ratio for the two metal salts and then alter the amount of ethylene glycol and water added, but keeping the total volume of the two solvents added constant

at 5.0 mL. The amount of HF added was never altered. Initially all reactions were carried out at 160 °C for 24, 48, or 96 hours. The entire system was then repeated, but by changing the metal salt ratio to 1:2, and finally to 1:3.

The synthesis of the hybrid materials was as follows: the metal salt to template ratio was 1:1 or 2:1, in all cases. The solvents used were ethylene glycol, ethanol, methanol, or DMF. Each of the organic solvents was added to between 0 and 5.0 mL of water to make up a total volume of 5.0 mL in the 20 mL Teflon liners. These samples were only reacted for 24 hours and cooled to room temperature on a bench next to the oven. The reaction temperature ranged from 100 °C to 160 °C. The high temperature samples all degraded to give a black tar-like substance. This was attributed to a decomposition of the starting materials to form a polymer of some sort. Consequently, the high temperature approach was soon abandoned and most reactions attempted at 100 °C. Figure 5.1 indicates the organic templates used, and in the case of *o*-nitroacetanilide, the organic template moiety, 2-nitrobenzamium, that is changes to.

Selected data tables are given in Appendix A. All cifs and powder XRD data for each compound are given in Appendix D.

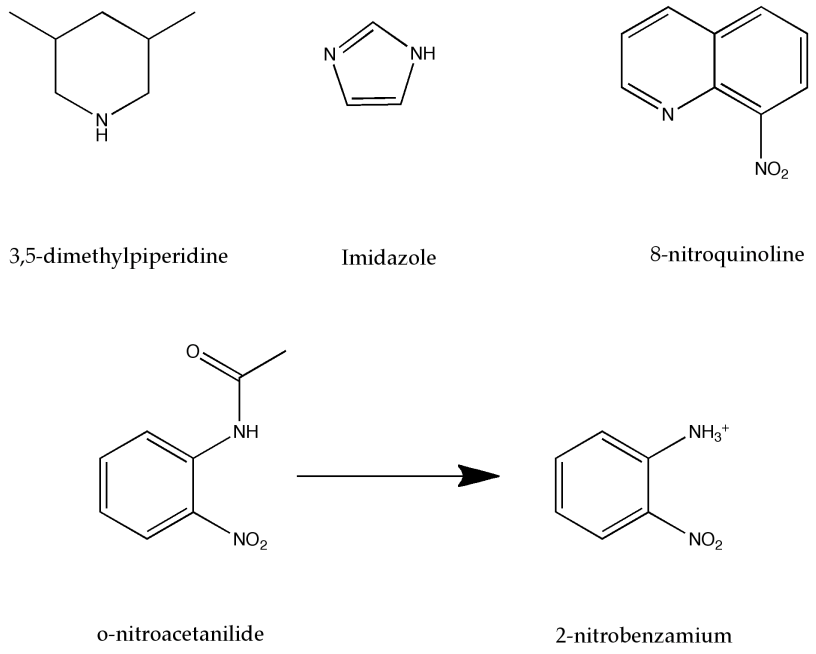

Figure 5.1: Organic templates used during the course of the hybrid reactions, and the "decomposition" product obtained in the case of o-nitroacetanilide

5.3.1 Synthesis and Crystal Structure of $Sr_2V_2F_{10}·H_2O$

$Sr_2V_2F_{10}·H_2O$: The compound was synthesised hydrothermally by combining 1.007 mmol V_2O_5 with 31 mmol (0.50 mL) of 48% HF and 2.976 mmol $SrCl_2$ in 110 mmol (2.0 mL) water and 90 mmol (5.0 mL) ethylene glycol. This mixture was reacted at 160 °C for 96 hours. The resultant green and black product, a mixture of green crystals and black powder, was washed with water to yield the product. The powder XRD pattern on the entire sample indicates that some impurities remain.

The SrF_2 - V_2O_5 system (in a mixture of water and ethylene glycol) was extensively studied and only one previously unreported product could be obtained from this study. The most common product of these reactions was SrF_2, with the V_2O_5 most likely being washed away during filtration. The new compound was $Sr_2V_2F_{10}·H_2O$, Figure 5.2, with crystal data given in Table 5.1. This compound is isostructural to $Sr_2Fe_2F_{10}·H_2O$ as reported by Le Meins *et al*.[20]

The compound crystallises in the orthorhombic space group *Cmca* with two crystallographically distinct V atoms, Figure 5.3. The one forms corner-sharing $[VF_5]_n$ octahedra that link up to form chains along the *a*-axis, whilst the second forms isolated $[VF_5(H_2O)]$ octahedra.

Table 5.1: SCXRD crystal data and refinement details for $Sr_2V_2F_{10}·H_2O$

Crystal system	Orthorhombic
Space group	*Cmca*
Unit cell parameters	a = 7.844(4) Å
	b = 19.883(9) Å
	c = 10.707(5) Å
Volume	1670.0(13) $Å^3$
Z	8
ρ(calc)	3.851 Mg/m^3
Goodness-of-fit on F^2	1.303
Final R indices [I>2sigma(I)]	R_1 = 0.0956, wR_2 = 0.1658
R indices (all data)	R_1 = 0.1238, wR_2 = 0.1746

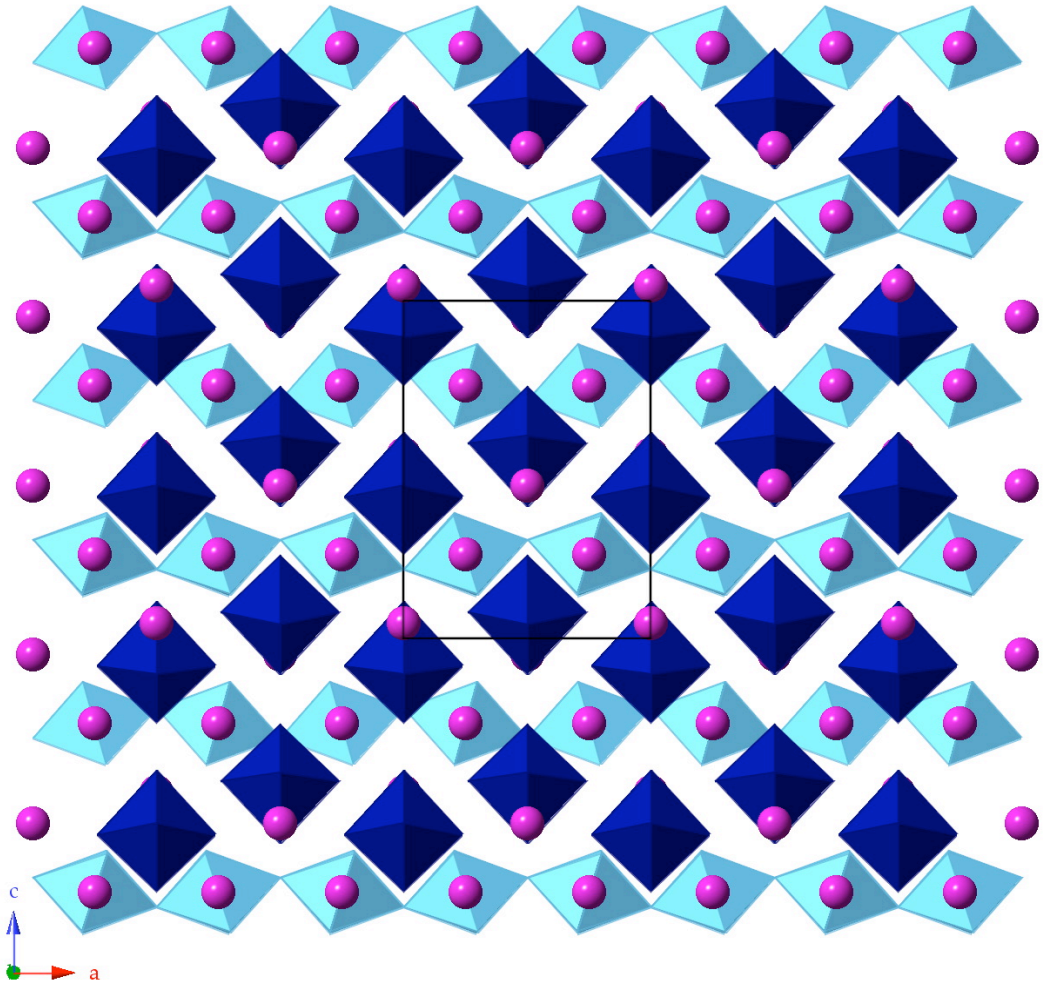

Figure 5.2: $Sr_2V_2F_{10}{\cdot}H_2O$ viewed along the b-axis indicating the two V octahedra in blue tones and the Sr sites in pink

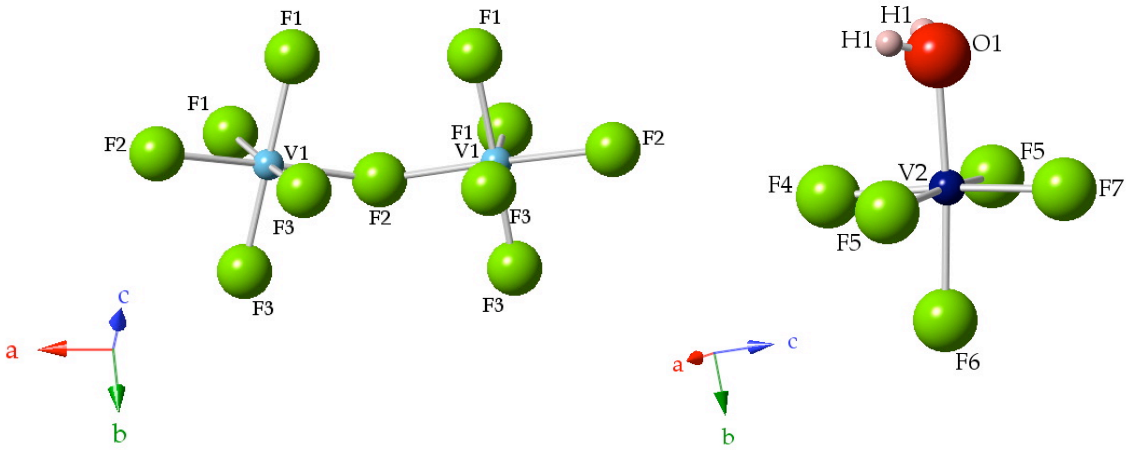

Figure 5.3: Corner-sharing $[VF_5]_n$ (left) and isolated $[VF_5(H_2O)]$ octahedra (right) of $Sr_2V_2F_{10}{\cdot}H_2O$

An analysis of the bond lengths and the resultant bond valence sums (BVS) for each of the V atoms indicates that both are in the +3 oxidation state, as summarised in Table 5.2. The same calculations confirm the +2 oxidation state for the two crystallographically distinct Sr atoms in the structure.

The Sr atoms form face-sharing $[SrF_{10}]$ polyhedra and isolated $[SrF_8]$ polyhedra. These two polyhedra types share faces with each other to form an ABA layer type arrangement that acts as a spacer between adjacent $[VF_5]_n$ layers, Figure 5.4.

The two V-centred octahedra are linked to one another by hydrogen bonds between the H1 site on the $[VF_5(H_2O)]$ monomers and the F3 site on the $[VF_5]_n$ chains. This hydrogen-bonding network is shown in Figure 5.5. The chains link to the isolated octahedra on alternating sides along the chain to allow for as many hydrogen bonds to be formed as possible, considering the steric interactions.

Table 5.2: Selected bond lengths and bond valence sums (BVS) for $Sr_2V_2F_{10}\cdot H_2O$

Bond	Bond length [Å]	Bond	Bond length [Å]
V1 – F1 (x2)	1.911(8)	V2 – F4	1.932(12)
V1 – F2 (x2)	2.017(3)	V2 – F5 (x2)	1.888(9)
V1 – F3 (x2)	1.903(8)	V2 – F6	2.004(11)
		V2 – F7	1.906(11)
		V2 – O1	2.001(13)
BVS, ∑ [V1]	3.152	BVS, ∑ [V2]	3.263

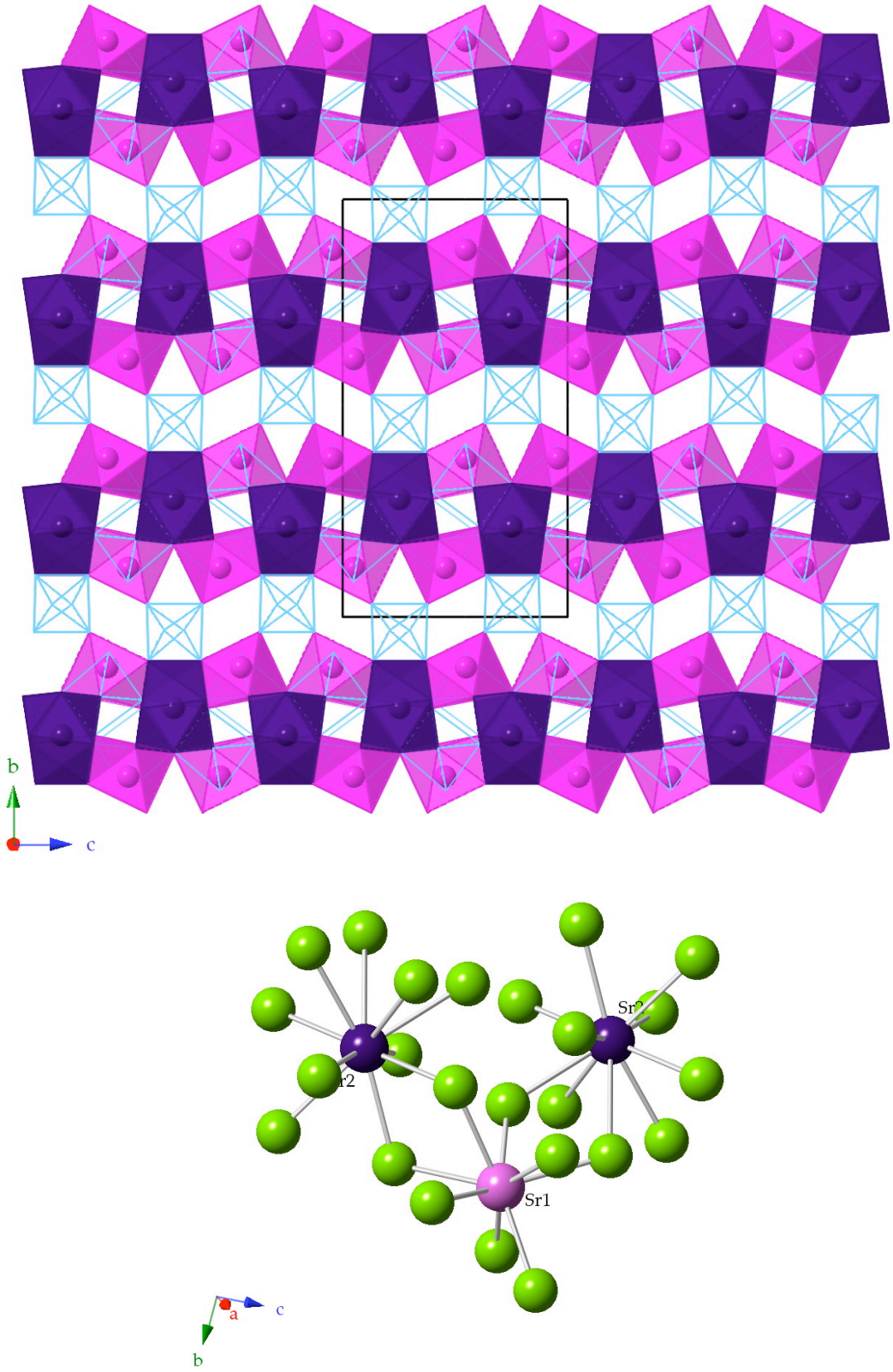

Figure 5.4: $Sr_2V_2F_{10}{\cdot}H_2O$ viewed along the a-axis indicating layers of SrF_{10} polyhedra (purple) and isolated SrF_8 polyhedra (pink), and the V sites as blue lines

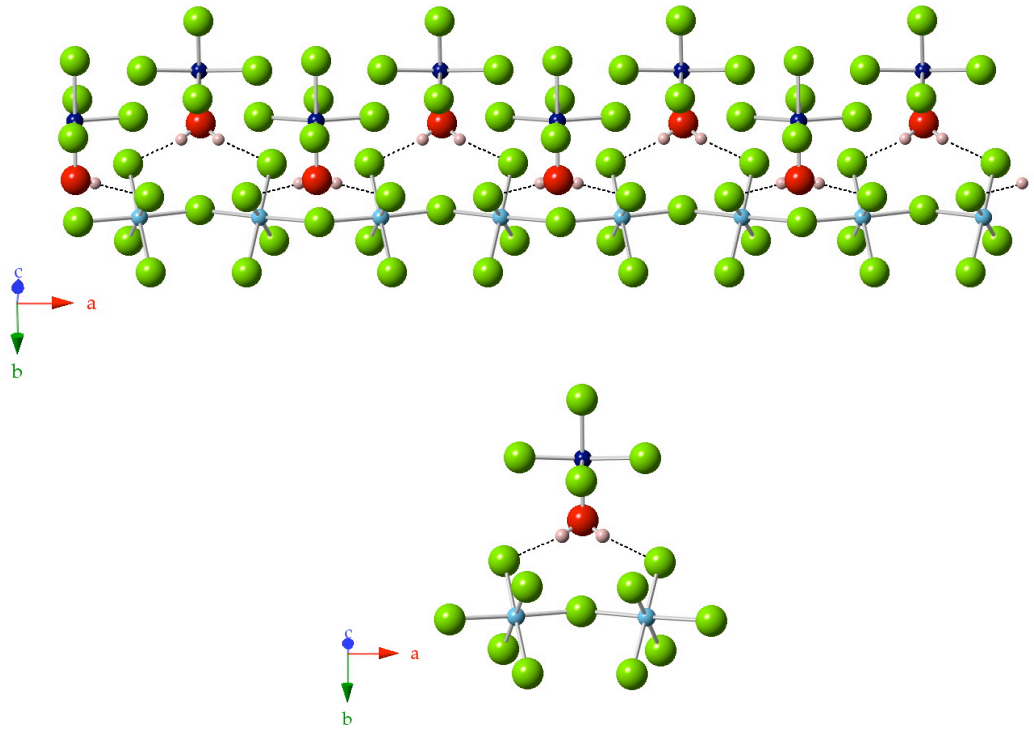

Figure 5.5: Hydrogen-bonding network in $Sr_2V_2F_{10}{\cdot}H_2O$ showing the connection of the isolated $[VF_5(H_2O)]$ monomers to the $[VF_5]_n$ chains (Sr atoms omitted for clarity)

5.3.2 Synthesis and Crystal Structure of $BaVO_2F_3$

$BaVO_2F_3$: The compound was synthesised hydrothermally by combining 1.007 mmol V_2O_5 with 31 mmol (0.50 mL) of 48% HF and 1.010 mmol $Ba(NO_3)_2$ in 277 mmol (5.0 mL) water. This mixture was reacted at 100 °C for 24 hours. The resultant yellow product, a mixture of crystals and powder, was washed with water to yield the product.

There are only two reported barium vanadium oxyfluorides in the ICSD. They are $Ba(VOF_4)$ and $Ba_3(V_2O_4F_8)$.[9, 10] In $Ba(VOF_4)$ the $[VOF_5]$ octahedra are linked together to form infinite chains, whilst $Ba_3(V_2O_4F_8)$ has isolated $[V_4(O,F)_{20}]^{8-}$ octahedra surrounded by Ba^{2+} ions.

$BaVO_2F_3$ crystallises in the cubic space group $P2_13$. The structure consists of isolated V-centred trigonal bipyramids, Figure 5.6. Crystal data are given in Table 5.3. Each $[V(O_{⅔}F_{⅓})_3F_2]$ unit has a disordered arrangement of the O and F atoms in its three equatorial positions. One of the axial fluorine atoms is also delocalised over three sites, Figure 5.7.

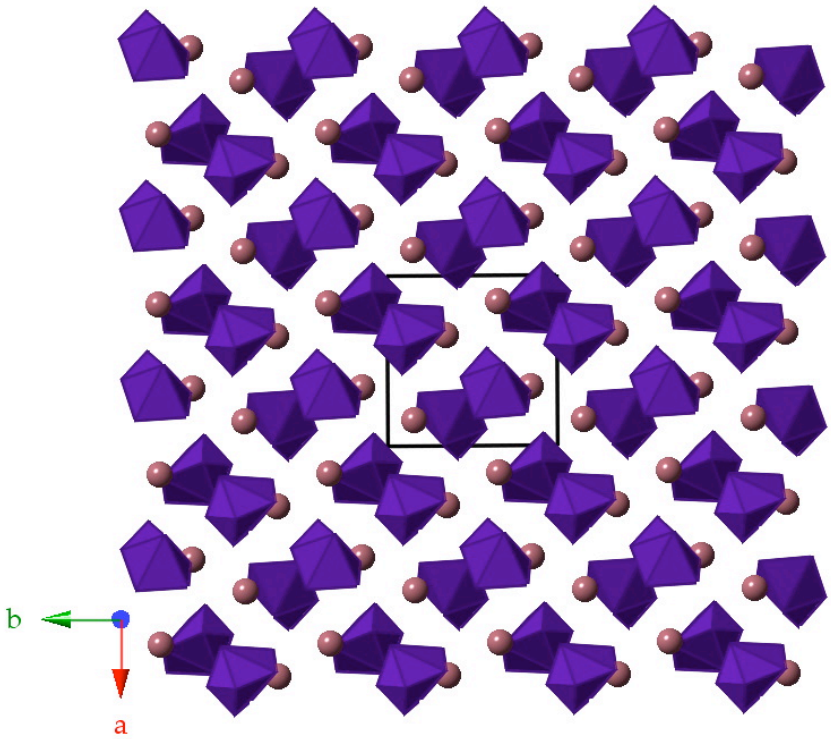

Figure 5.6: $BaVO_2F_3$ viewed along the c-axis, indicating the isolated disordered trigonal bipyramidal delocalised $[V(O_{⅔}F_{⅓})_3F_2]$ in purple

The geometry, the trigonal bipyramid, is quite rare in vanadium oxyfluorides. One such example is in the complex oxyfluoride ion $[V_{14}O_{36}F_4]^{8-}$ consisting of several different polyhedra, including two $[VO_4F]^{2-}$ trigonal bipyramids.[21] Two other reported examples are given by Welk *et al*. in $Cu(NC_5H_5)_4VOF_4$ and $[Cu(NC_5H_5)_4VOF_4][Cu(NC_5H_5)_4(H_2O)VOF_4]\cdot H_2O$.[22]

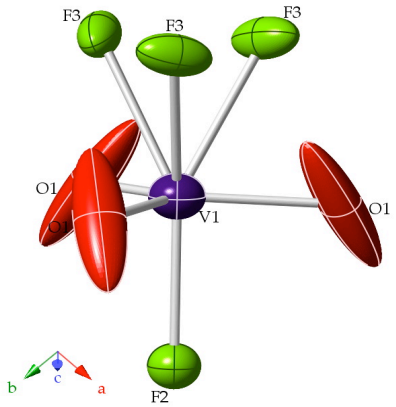

Figure 5.7: Coordination environment of the trigonal bipyramidal V site in $BaVO_2F_3$ indicating the delocalised O1/F1 site, with 50% probability displacement ellipsoids

Table 5.3: SCXRD crystal data and refinement details for $BaVO_2F_3$

Crystal system	Cubic
Space group	$P2_13$
Unit cell parameters	a = 7.521(3) Å
Volume	425.4(3) $Å^3$
Z	4
ρ(calc)	4.329 Mg/m^3
Goodness-of-fit on F^2	1.269
Final R indices [I>2sigma(I)]	R_1 = 0.0486, wR_2 = 0.1030
R indices (all data)	R_1 = 0.0486, wR_2 = 0.1030

Table 5.4: Selected bond lengths and bond valence sum (BVS) for $BaVO_2F_3$

Bond	Bond length [Å]
V1 – (O,F)1 (x3)	1.72(2)
V1 – F2	1.916(16)
V1 – F3	2.00(3)
BVS, ∑ [V1]	5.258

The equatorial (O,F) sites were assigned a statistical 2:1 ratio. This ratio supported the oxidation state calculated from the BVS sums that the V ion was in the +5 oxidation state, Table 5.4. There was no possibility of determining which of the three sites was occupied by the F and which by O atoms.

5.3.3 Synthesis and Crystal Structure of $(C_7NH_{16})_2[MnF_5(H_2O)]\cdot 2H_2O$

$(C_7NH_{16})_2[MnF_5(H_2O)]\cdot 2H_2O$: The hybrid material was synthesised by dissolving $Mn(CH_3CO_2)_3\cdot 2H_2O$ (0.9989 mmol, 0.2678 g) in 0.50 mL (11 mmol) HF and 5.0 mL (277 mmol) water, at 100 °C overnight. The amine 3,5-dimethylpiperidine (3.0 mmol, 0.40 mL) was then added to the solution and returned to the 100 °C oven for a further hour. The resultant mixture was allowed to cool to room temperature, and the brown crystals filtered, washed with ethanol, and dried at 60 °C.

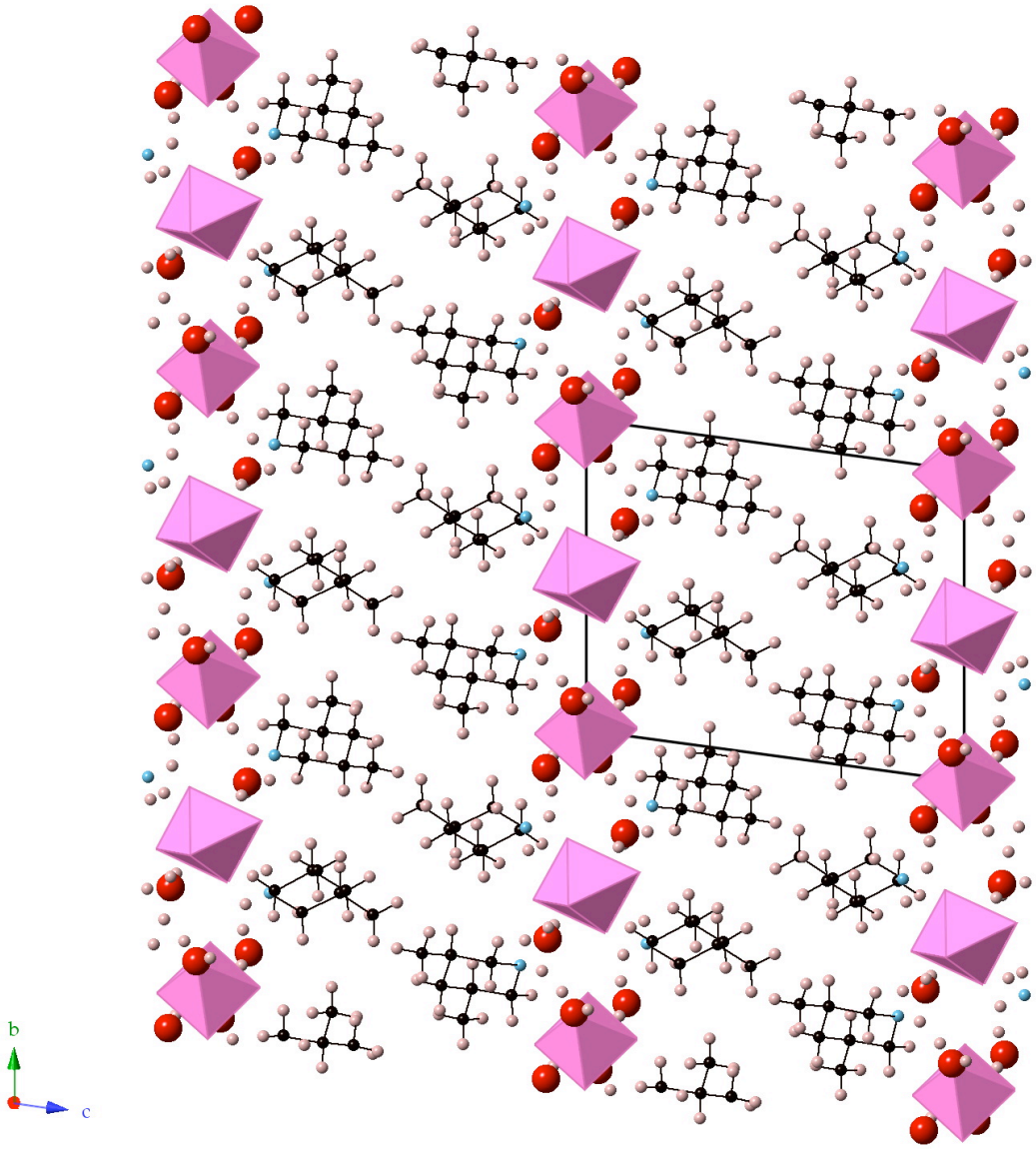

Figure 5.8: $(C_7NH_{16})_2[MnF_5(H_2O)]\cdot 2H_2O$ viewed along the a-axis indicating the two isolated Mn-centred octahedra and the organic template moiety, 3,5-dimethylpiperidine, separating these layers

This compound is shown in Figure 5.8, with crystal data summarised in Table 5.5. It is triclinic in space group $P\bar{1}$ with two Mn sites, one of which forms $[MnF_6]$ octahedra and the other $[MnF_4(H_2O)_2]$ octahedra, Figure 5.9. These two isolated octahedra alternate along a layer that is separated from the next inorganic layer by two 3,5-dimethylpiperidine moieties. Both of the Mn ions are found to be Mn^{3+} from BVS, Table 5.6.

Table 5.5: SCXRD crystal data and refinement details for $(C_7NH_{16})_2[MnF_5(H_2O)]\cdot 2H_2O$

Crystal system	Triclinic	
Space group	$P\bar{1}$	
Unit cell parameters	a = 7.470(3) Å	α = 93.48(2)°
	b = 11.153(5) Å	β = 104.755(17)°
	c = 13.666(6) Å	γ = 104.753(19)°
Volume	1055.1(8) Å^3	
Z	4	
ρ(calc)	1.361 Mg/m^3	
Goodness-of-fit on F^2	1.117	
Final R indices [I>2sigma(I)]	R_1 = 0.0723, wR_2 = 0.1360	
R indices (all data)	R_1 = 0.1108, wR_2 = 0.1467	

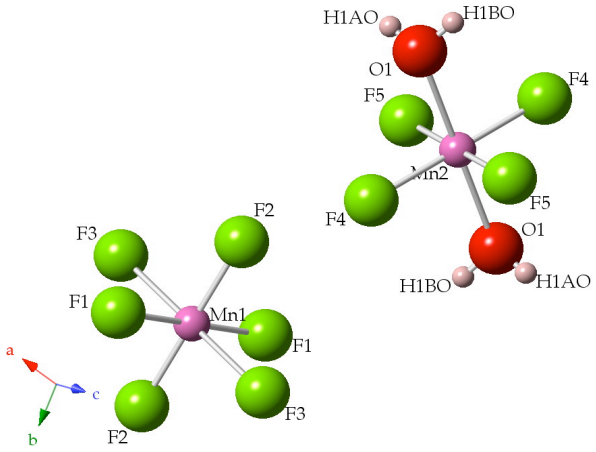

Figure 5.9: Isolated $[MnF_6]$ and $[MnF_4(H_2O)_2]$ octahedra of $(C_7NH_{16})_2[MnF_5(H_2O)]\cdot 2H_2O$

Table 5.6: Selected bond lengths and BVS for $(C_7NH_{16})_2[MnF_5(H_2O)]\cdot 2H_2O$

Bond	Bond length [Å]	Bond	Bond length [Å]
Mn1 – F1 (x2)	1.865(3)	Mn2 – F4 (x2)	1.878(3)
Mn1 – F2 (x2)	1.836(3)	Mn2 – F5 (x2)	1.821(3)
Mn1 – F3 (x2)	2.165(3)	Mn2 – O1 (x2)	2.202(4)
BVS, ∑ [Mn1]	2.902	BVS, ∑ [Mn2]	3.270

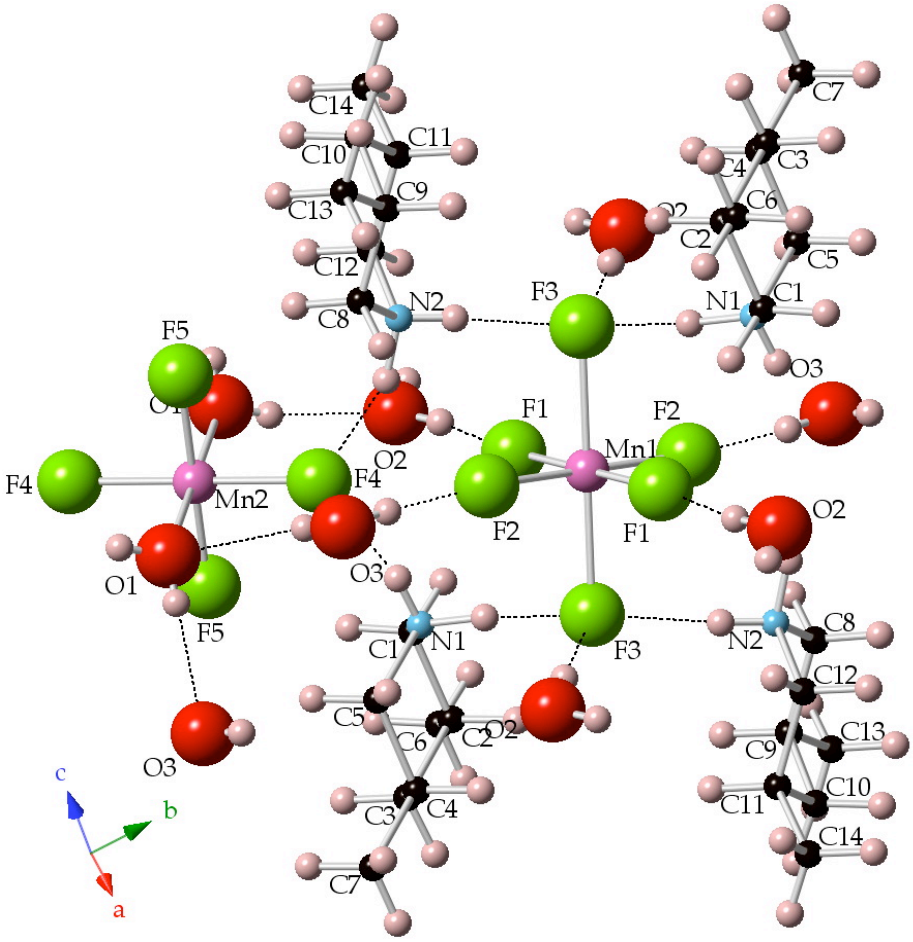

Figure 5.10: Hydrogen bonding network linking the [MnF_6] and [$MnF_4(H_2O)_2$] octahedra to the water molecules and amines moieties of $(C_7NH_{16})_2[MnF_5(H_2O)]\cdot 2H_2O$

The Mn-centred octahedra are linked to the water molecules and amides via hydrogen bonds, Figure 5.10. The two *trans* bonds of both octahedra are elongated (Table 5.6) and can be attributed to a Jahn-Teller distortion, which has also been observed for the piperazine-containing Mn^{3+} compounds $(pipH_2)_3[Mn_4F_{18}(H_2O)]\cdot(H_2O)$ and $(pipH_2)_4[Mn_2F_9]_2[MnF_4(H_2O)_2][MnF_4(HF)_2]$.[23, 24] The long *trans* bonds in the [MnF_6] octahedron are 2.165(3) Å long, whereas the remaining bonds are 1.836(3) Å to 1.865(3) Å in length. The *trans* bonds in the [$MnF_4(H_2O)_2$] octahedron are the bonds to the water molecules at 2.202(4) Å, whilst the remaining bonds are to fluorine atoms, and range from 1.821(3) Å to 1.878(3) Å in length. All of these values agree with those reported in the above-mentioned literature. A further example where this elongation of the axial bonds is observed is in the hybrid organic inorganic material bis(3-amino-1,2,4-triazolium(1+))pentafluoromanganate(III), or $(3\text{-triazH})_2[MnF_5]$.[25]

5.3.4 Synthesis and Crystal Structure of $(C_3N_2H_5)[Mn_2F_6(H_2O)_2]$

$(C_3N_2H_5)[Mn_2F_6(H_2O)_2]$: This hybrid material was synthesised by dissolving $Mn(CH_3CO_2)_3 \cdot 2H_2O$ (0.9970 mmol, 0.2673 g) in 1.0 mL (23 mmol) HF and 2.0 mL (110 mmol) water, at 60 °C in a sealed plastic polytop bottle. Once the metal salt had dissolved (after approximately 30 minutes) imidazole (3.030 mmol, 0.2062 g) was added and the solution returned to the 60 °C oven for a further 15 minutes. The resultant mixture was allowed to cool to room temperature and form crystals over several days. These pink crystals were filtered, washed with ethanol, and dried at 60 °C.

The SCXRD data collected for this sample was not of the best quality with an internal R-factor of almost 20%, but due to the interesting nature of the compound obtained, it is described below. Several further attempts have been made to synthesise this material again, but these have proven unsuccessful to date.

The material crystallises in the noncentrosymmetric orthorhombic space group $P2_1ca$. The Mn-centred octahedra form edge-sharing dimers that link along corners to octahedra above and below in a ladder-like manner along the *a*-axis, Figure 5.11. These ladders are isolated from one another by the imidazolium ions, Figure 5.12. The imidazolium ion could not be fully structurally determined. Whilst the hydrogen atoms could be geometrically added to the C atoms, this was not possible for one of the N sites. Consequently, no hydrogen-bonding network can be reported for this structure. The structural data for this compound are reported in Table 5.7.

There are two Mn sites in the compound, Figure 5.13. They link to one another by sharing edges. The Mn1 ion is calculated to be Mn^{2+}, whilst the Mn2 ion is Mn^{3+}, Table 5.8. The pink colour of the crystals is indicative of an Mn^{2+} ion. The Mn2-centred octahedron shows evidence of a Jahn-Teller distortion, and this supports the observed oxidation state for that ion. The Mn1-centred octahedron has two *cis* equatorial water molecules, Figure 5.13. It was only possible to place one of the two required protons in each of the water molecules, and this is attributed to the less than optimal data quality.

This mixed valence, in addition to the polar space group, makes this a suitable candidate for multiferroic studies.

Table 5.7: SCXRD crystal data and refinement details for $(C_3N_2H_5)[Mn_2F_6(H_2O)_2]$

Crystal system	Orthorhombic
Space group	$P2_1ca$
Unit cell parameters	a = 7.6817(10) Å b = 8.4273(11) Å c = 15.217(2) Å
Volume	985.1(2) Å^3
Z	4
ρ(calc)	2.198 Mg / m^3
Goodness-of-fit on F^2	1.064
Final R indices [I>2sigma(I)]	R_1 = 0.0792, wR_2 = 0.1569
R indices (all data)	R_1 = 0.1339, wR_2 = 0.1727

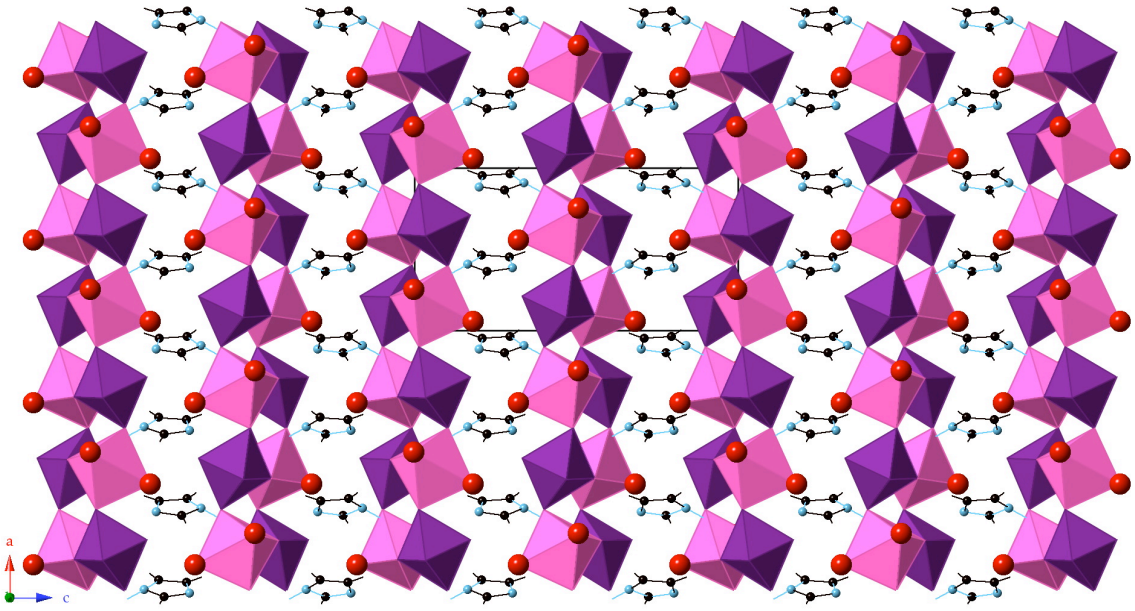

Figure 5.11: $(C_3N_2H_5)[Mn_2F_6(H_2O)_2]$ viewed along the b-axis indicating the ladders formed by the corner-sharing Mn-centred octahedra

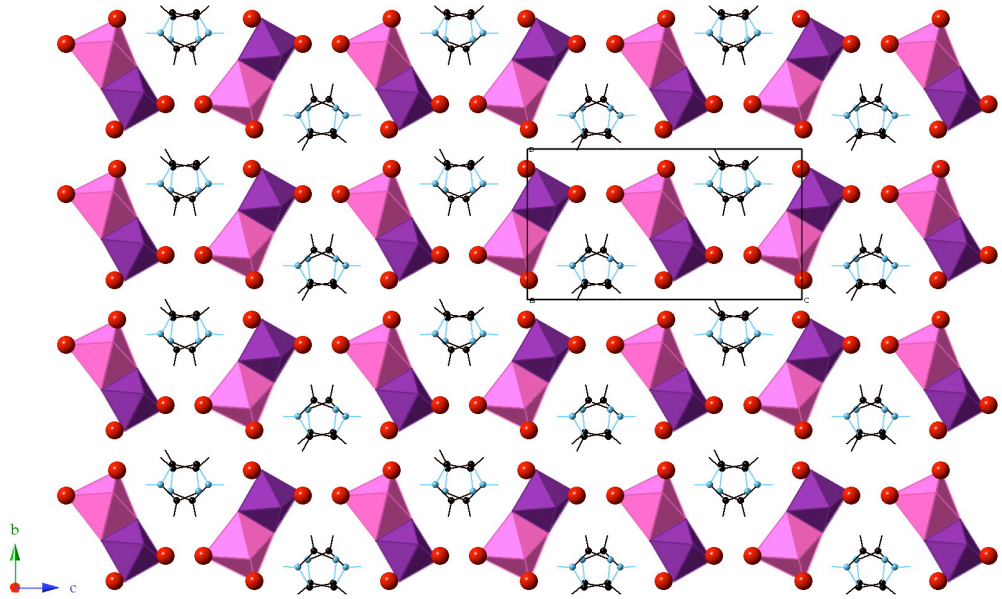

Figure 5.12: $(C_3N_2H_5)[Mn_2F_6(H_2O)_2]$ viewed along the a-axis indicating the imidazolium separating the ladders formed by the edge-sharing Mn-centred octahedra

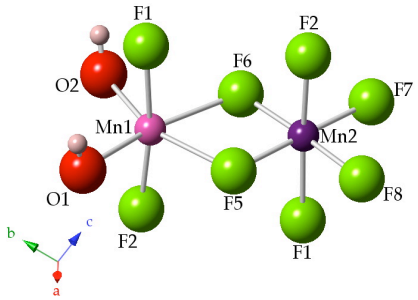

Figure 5.13: Edge-sharing Mn-centred dimer indicating the labelling scheme for $(C_3N_2H_5)[Mn_2F_6(H_2O)_2]$

Table 5.8: Selected bond lengths and BVS for $(C_3N_2H_5)[Mn_2F_6(H_2O)_2]$

Bond	Bond length [Å]	Bond	Bond length [Å]
Mn1 – F1	2.099(9)	Mn2 – F1	2.124(9)
Mn1 – F2	2.049(8)	Mn2 – F2	2.059(8)
Mn1 – F5	2.182(6)	Mn2 – F5	1.855(6)
Mn1 – F6	2.216(6)	Mn2 – F6	1.865(6)
Mn1 – O1	2.110(10)	Mn2 – F7	1.858(7)
Mn1 – O2	2.134(9)	Mn2 – F8	1.862(7)
BVS, ∑ [Mn1]	2.058	BVS, ∑ [Mn2]	2.955

5.3.5 Synthesis and Crystal Structure of $(C_7NH_{16})_2[MoF_4O_2]$

$(C_7NH_{16})_2[MoF_4O_2]$: This hybrid material was synthesised by dissolving MoO_3 (1.002 mmol, 0.1442 g) in 0.50 mL (11 mmol) HF and 5.0 mL (277 mmol) water, at 100 °C in a sealed plastic polytop bottle for three hours. 3,5-dimethylpiperidine (3.0 mmol, 0.40 mL) was added and the solution returned to the 60 °C oven for a further 12 hours. The resultant mixture was allowed to cool to room temperature and form crystals over several days.

$(C_7NH_{16})_2[MoF_4O_2]$ crystallises in the triclinic space group $P\bar{1}$, Table 5.9. The structure consists of isolated Mo-centred octahedral monomers separated by 3,5-dimethylpiperidine moieties, Figure 5.14. In the Mn analogue, $(C_7NH_{16})_2[MnF_5(H_2O)]\cdot 2H_2O$, reported in Section 5.3.3, monomers are also formed, but with two F atoms replaced by H_2O molecules to give $[MnF_4(H_2O)_2]$.

There are four different Mo sites, Figure 5.15. Each of the octahedra has four F atoms and two O atoms, in a mutually *cis* configuration. The $[MoF_4O_2]$ octahedra designated by the Mo1, Mo2, and Mo3 sites are found in the same plane, as seen in Figure 5.14. The Mo4 octahedron is found between these layers. They are linked to one another by hydrogen bonds between the octahedra and the template. Each of the Mo ions is Mo^{6+}, Table 5.10.

Table 5.9: SCXRD crystal data and refinement details for $(C_7NH_{16})_2[MoF_4O_2]$

Crystal system	Triclinic	
Space group	$P\bar{1}$	
Unit cell parameters	a = 13.967(6) Å	α = 78.374(13)°
	b = 14.322(6) Å	β = 89.077(13)°
	c = 21.9114(10) Å	γ = 69.357(9)°
Volume	4010(2) Å^3	
Z	8	
ρ(calc)	1.432 Mg/m^3	
Goodness-of-fit on F^2	1.009	
Final R indices [I>2sigma(I)]	R_1 = 0.0871, wR_2 = 0.1660	
R indices (all data)	R_1 = 0.2900, wR_2 = 0.2758	

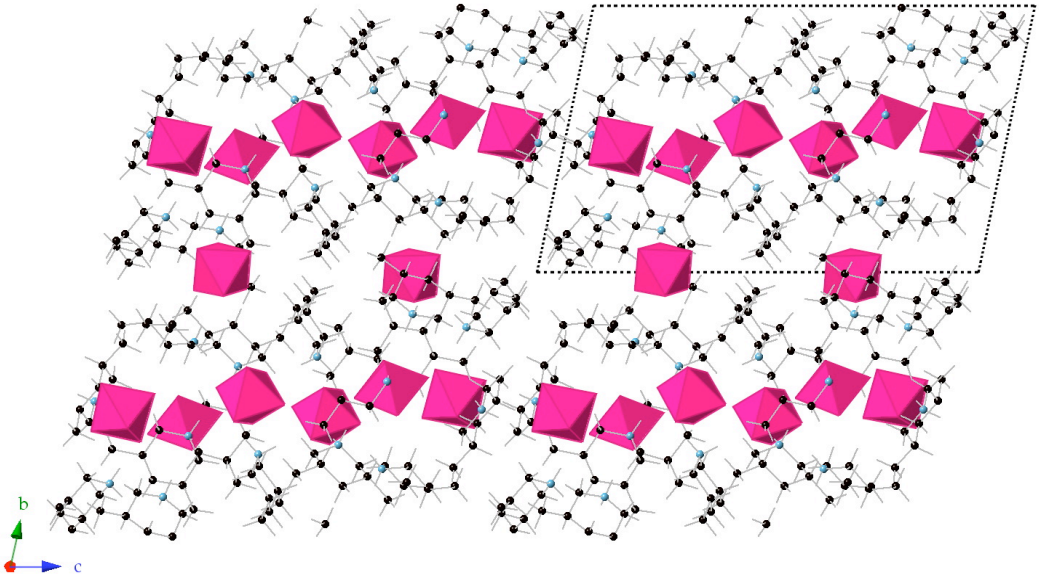

Figure 5.14: $(C_7NH_{16})_2[MoF_4O_2]$ viewed along the a-axis indicating the 3,5-dimethylpiperidine moieties separating the $[MoF_4O_2]$ monomers

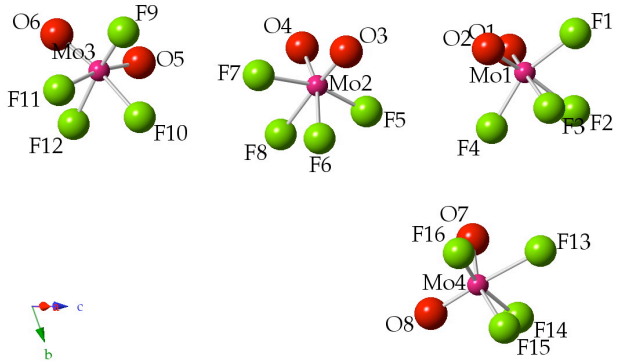

Figure 5.15: The four distinct $[MoF_4O_2]$ octahedra in $(C_7NH_{16})_2[MoF_4O_2]$

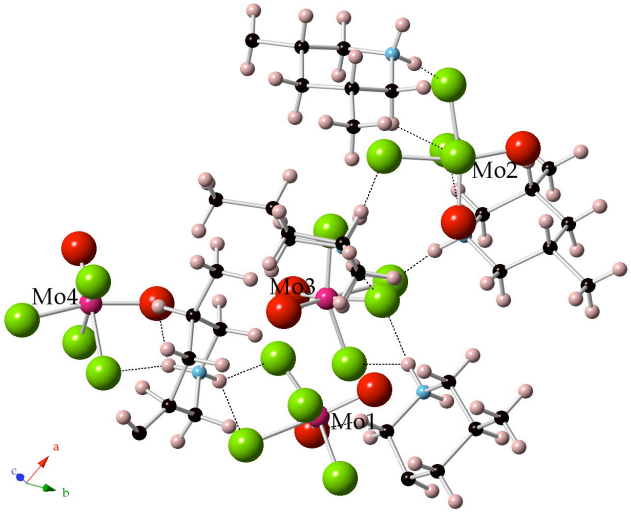

Figure 5.16: Hydrogen-bonding network in $(C_7NH_{16})_2[MoF_4O_2]$

Table 5.10: Selected bond lengths and BVS for $(C_7NH_{16})_2[MoF_4O_2]$

Bond	Bond length [Å]	Bond	Bond length [Å]
Mo1 – F1	1.922(5)	Mo2 – F5	1.858(5)
Mo1 – F2	2.038(5)	Mo2 – F6	2.050(4)
Mo1 – F3	2.122(5)	Mo2 – F7	1.998(4)
Mo1 – F4	1.928(5)	Mo2 – F8	2.098(4)
Mo1 – O1	1.695(6)	Mo2 – O3	1.714(5)
Mo1 – O2	1.678(6)	Mo2 – O4	1.743(5)
BVS, ∑ [Mo1]	5.998	BVS, ∑ [Mo2]	5.644
Bond	Bond length [Å]	Bond	Bond length [Å]
Mo3 – F9	1.909(5)	Mo1 – F13	2.157(5)
Mo3 – F10	2.078(5)	Mo1 – F14	1.960(5)
Mo3 – F11	2.114(5)	Mo1 – F15	1.993(5)
Mo3 – F12	1.928(5)	Mo1 – F16	1.852(5)
Mo3 – O5	1.689(6)	Mo1 – O7	1.784(6)
Mo3 – O6	1.712(6)	Mo1 – O8	1.684(6)
BVS, ∑ [Mo3]	5.847	BVS, ∑ [Mo4]	5.722

The hydrogen-bonding network observed for this material, Figure 5.16, links the four Mo-centred octahedra to one another via the linkers, or templates.

5.3.6 Synthesis and Crystal Structure of $(C_3N_2H_5)_2[Mo_2F_6O_4]$

$(C_3N_2H_5)_2[Mo_2F_6O_4]$: The hybrid material was synthesised by dissolving MoO_3 (1.123 mmol, 0.1617 g) and imidazole (0.986 mmol, 0.0671 g) in 0.50 mL (11 mmol) HF, 3.0 mL (166 mmol) water, and 2.0 mL (34 mmol) ethanol and then heating the mixture to 100 °C in a sealed plastic polytop bottle for 24 hours. The resultant mixture was allowed to cool to room temperature and form crystals over several days.

The crystal structure obtained indicates that the structure is monoclinic and crystallises in the centrosymmetric space group $P2_1/n$, Figure 5.17 and Table 5.11.

Unlike in the previous structure, where the Mo-centred octahedra are isolated, $(C_3N_2H_5)_2[Mo_2F_6O_4]$ forms dimers in the form of $[Mo_2F_6O_4]$, Figure 5.18. Each Mo is double-bonded to two O atoms and single-bonded to four F atoms. As in the previous structure, the two O atoms are equatorial and the two equatorial F atoms are shared between the two Mo-centred octahedra. This leads to the edge-sharing dimers formed. Both Mo ions are in the +6 oxidation state, Table 5.12.

In the Mn equivalent, the Mn octahedra form edge-sharing dimers that link up along their corners to form ladders as described in Section 5.3.4.

A further difference is that the dimers in the Mn compound form a herringbone-type arrangement as seen in Figure 5.12. In the Mo compound, the dimers align in a parallel manner and merely seem to rotate through 90° along the axis through the dimers. This can be seen in Figure 5.17.

Table 5.11: SCXRD crystal data and refinement details for $(C_3N_2H_5)_2[Mo_2F_6O_4]$

Crystal system	Monoclinic	
Space group	$P2_1/n$	
Unit cell parameters	a = 11.607(4) Å	
	b = 9.504(3) Å	β = 98.420(9)°
	c = 12.978(5) Å	
Volume	1416.2(9) Å^3	
Z	4	
ρ(calc)	1.862 Mg/m^3	
Goodness-of-fit on F^2	1.199	
Final R indices [I>2sigma(I)]	R_1 = 0.0518, wR_2 = 0.1696	
R indices (all data)	R_1 = 0.0643, wR_2 = 0.1956	

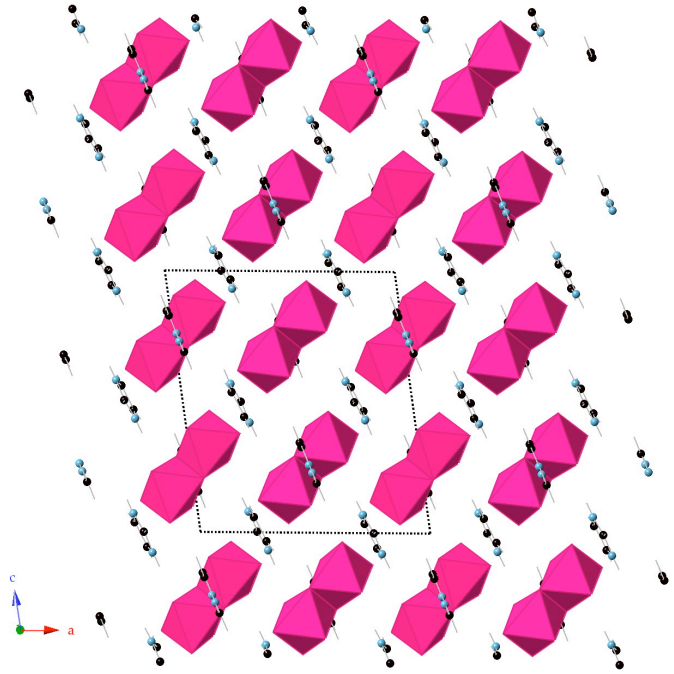

Figure 5.17: $(C_3N_2H_5)_2[Mo_2F_6O_4]$ viewed along the b-axis indicating the imidazolium ion separating the $[Mo_2F_6O_4]$ dimers

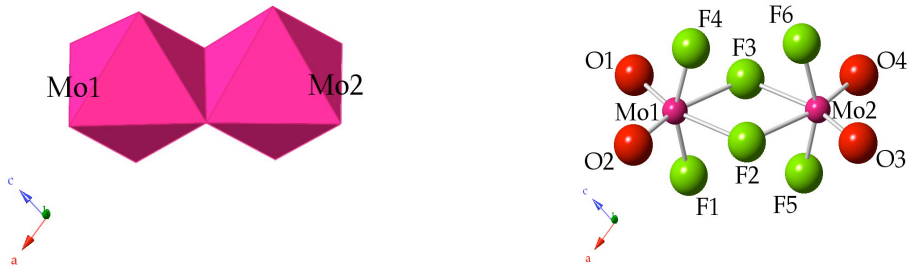

Figure 5.18: $[Mo_2F_6O_4]$ dimers with the labelling scheme shown on the right for $(C_3N_2H_5)_2[Mo_2F_6O_4]$

Table 5.12: Selected bond lengths and BVS for $(C_3N_2H_5)_2[Mo_2F_6O_4]$

Bond	Bond length [Å]	Bond	Bond length [Å]
Mo1 – F1	1.928(2)	Mo2 – F2	2.174(2)
Mo1 – F2	2.146(2)	Mo2 – F3	2.179(2)
Mo1 – F3	2.208(2)	Mo2 – F5	1.907(2)
Mo1 – F4	1.920(2)	Mo2 – F6	1.931(2)
Mo1 – O1	1.685(3)	Mo2 – O3	1.682(3)
Mo1 – O2	1.684(3)	Mo2 – O4	1.691(3)
BVS, ∑ [Mo1]	5.795	BVS, ∑ [Mo2]	5.795

5.3.7 Synthesis and Crystal Structure of $(C_9H_7N_2O_2)_2[Mo_2F_6O_4]$

$(C_9H_7N_2O_2)_2[Mo_2F_6O_4]$: The hybrid material was synthesised by dissolving MoO_3 (1.004 mmol, 0.1445 g) and 8-nitroquinoline (1.000 mmol, 0.1742 g) in 0.50 mL (11 mmol) HF and 5.0 mL (86 mmol) ethanol at 100 °C in a sealed plastic polytop bottle for 24 hours. The resultant mixture was allowed to cool to room temperature and form crystals over several days.

The compound is monoclinic in $P2_1/n$, and the sole Mo site forms a dimer with a symmetry-generated Mo site, Figure 5.19 and Table 5.13. This dimer is chemically identical to the one reported in Section 5.3.6. The two octahedra share an edge by sharing two equatorial F atoms. O atoms that form double bonds to the Mo atom occupy the remaining equatorial sites. The axial bonds are formed between the Mo atom and F atoms, Figure 5.20. As in the previous structure, the Mo ion is in the +6 oxidation state, Table 5.14

Attempts were made to determine if any hydrogen bonds were present in the sample, but none could be located.

Table 5.13: SCXRD crystal data and refinement details for $(C_9H_7N_2O_2)_2[Mo_2F_6O_4]$

Crystal system	Monoclinic	
Space group	$P2_1/n$	
Unit cell parameters	a = 7.3424(11) Å	
	b = 10.0706(15) Å	β = 90.743(6)°
	c = 15.079(2) Å	
Volume	1114.9(3) Å^3	
Z	4	
ρ(calc)	2.145 Mg/m^3	
Goodness-of-fit on F^2	1.068	
Final R indices [I>2sigma(I)]	R_1 = 0.0645, wR_2 = 0.0976	
R indices (all data)	R_1 = 0.1104, wR_2 = 0.1064	

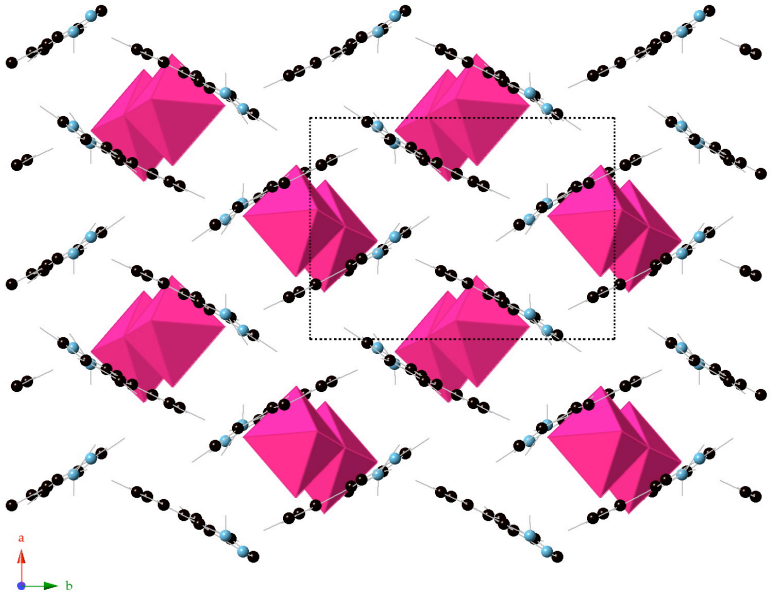

Figure 5.19: $(C_9H_7N_2O_2)_2[Mo_2F_6O_4]$ viewed along the c-axis indicating the 8-nitroquinoline moiety separating the $[Mo_2F_6O_4]$ dimers

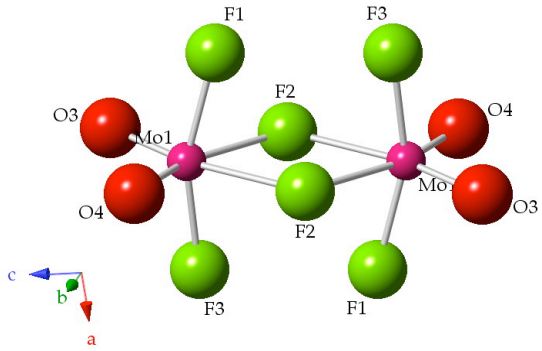

Figure 5.20: Edge-sharing $[Mo_2F_6O_4]$ dimers indicating the labelling scheme for $(C_9H_7N_2O_2)_2[Mo_2F_6O_4]$

Table 5.14: Selected bond lengths and BVS for $(C_9H_7N_2O_2)_2[Mo_2F_6O_4]$

Bond	Bond length [Å]
Mo1 – F1	1.939(3)
Mo1 – F2	2.131(3)
Mo1 – F2	2.176(3)
Mo1 – F3	1.924(3)
Mo1 – O3	1.688(4)
Mo1 – O4	1.689(4)
BVS, ∑ [Mo1]	5.775

5.3.8 Synthesis and Crystal Structure of $(C_6H_7N_2O_2)_2[Mo_2F_6O_4]$

$(C_6H_7N_2O_2)_2[Mo_2F_6O_4]$: The hybrid material was synthesised by dissolving MoO_3 (0.9990 mmol, 0.1438 g) and *o*-nitroacetanilide (1.001 mmol, 0.1804 g) in 0.50 mL (11 mmol) HF and 5.0 mL (277 mmol) H_2O at 100 °C in a sealed plastic polytop bottle for 24 hours. The resultant mixture was allowed to cool to room temperature and form crystals over several days.

The monoclinic structure crystallises in $P2_1/c$. This is the same space group as the previous two monoclinic structures ($P2_1/n$) but the unit cell axes have been chosen differently to give this alternative unit cell choice. Table 5.15 gives a summary of the crystallographic data, and the structure is given in Figure 5.21. The sole Mo site symmetry-generates a further Mo site that forms a dimer, Figure 5.22. As with the previous two samples reported in Sections 5.3.5 and 5.3.6, $(C_3N_2H_5)_2[Mo_2F_6O_4]$ and $(C_9H_7N_2O_2)_2[Mo_2F_6O_4]$ respectively, the dimers formed in this compound consist of two octahedra, each with two double-bonded O atoms occupying the equatorial positions and the remaining positions taken up by the F atoms. The two equatorial F atoms form the edge that is shared between the two octahedra. Also, as with the previous two examples, the Mo is in the +6 oxidation state, Table 5.16.

Table 5.15: SCXRD crystal data and refinement details for $(C_6H_7N_2O_2)_2[Mo_2F_6O_4]$

Crystal system	Monoclinic	
Space group	$P2_1/c$	
Unit cell parameters	a = 9.4305(7) Å	
	b = 6.6881(5) Å	β = 95.923(7)°
	c = 15.3947(11) Å	
Volume	965.79(12) Å^3	
Z	4	
ρ(calc)	2.229 Mg / m^3	
Goodness-of-fit on F^2	1.185	
Final R indices [I>2sigma(I)]	R_1 = 0.0402, wR_2 = 0.0843	
R indices (all data)	R_1 = 0.0660, wR_2 = 0.0919	

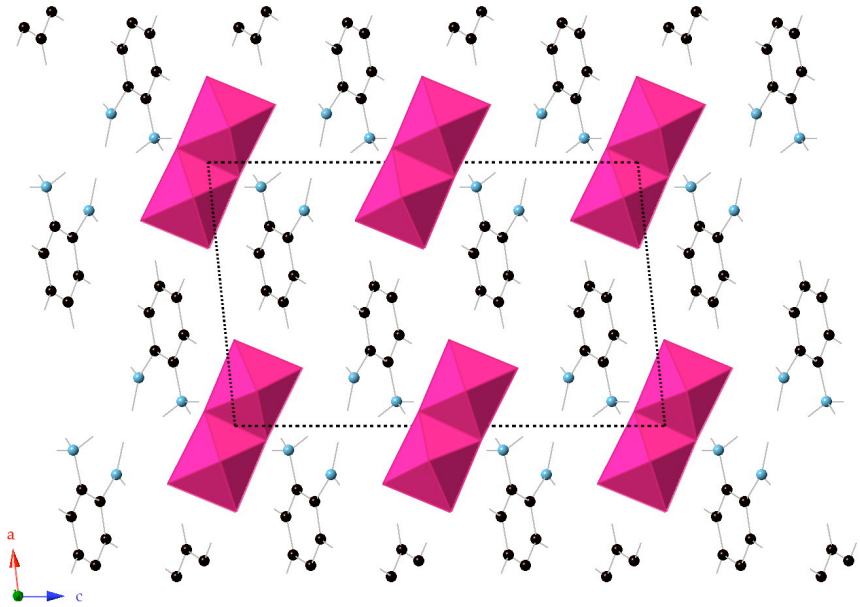

Figure 5.21: $(C_6H_7N_2O_2)_2[Mo_2F_6O_4]$ viewed along the b-axis indicating the 2-nitrobenzamium ion separating the $[Mo_2F_6O_4]$ dimers

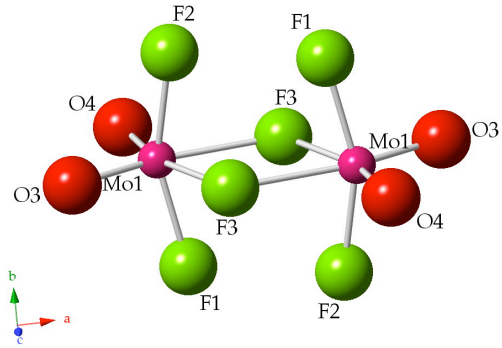

Figure 5.22: Edge-sharing $[Mo_2F_6O_4]$ dimers indicating the labelling scheme for $(C_6H_7N_2O_2)_2[Mo_2F_6O_4]$

Table 5.16: Selected bond lengths and BVS for $(C_6H_7N_2O_2)_2[Mo_2F_6O_4]$

Bond	Bond length [Å]
Mo1 – F1	1.916(2)
Mo1 – F2	1.951(2)
Mo1 – F3	2.147(2)
Mo1 – F3	2.194(2)
Mo1 – O3	1.687(3)
Mo1 – O4	1.686(3)
BVS, ∑ [Mo1]	5.998

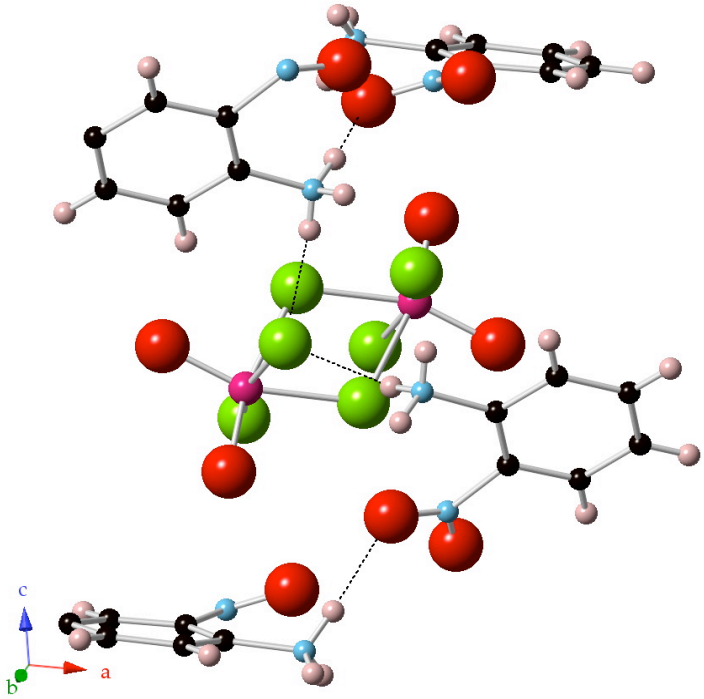

Figure 5.23: Hydrogen-bonding network between the $[Mo_2F_6O_4]$ dimers and the template indicating the helical arrangement of these bonds for $(C_6H_7N_2O_2)_2[Mo_2F_6O_4]$

The organic template starting material o-nitroacetanilide changed during the reaction by losing the acetyl group to become a 2-nitrobenzamium ion. This deacetylation leads the nitrogen group to take up two protons from the solution to become positively charged as a RNH_3^+ terminal group. The acetyl group takes up a proton to become acetic acid.

The hydrogen-bonding network for this compound shows that the Mo dimers are linked to the 2-nitrobenzamium ions via these hydrogen bonds and these bonds assume a helical arrangement, Figure 5.23.

5.4 Discussion

Although many attempts were made to synthesise different compounds in the studied systems, the products in all cases seemed unaffected by temperature, reactant ratio, solvent, and reaction time, as outlined at the beginning of the results chapter (Section 5.3).

The $[MF_4(H_2O)_2]$ octahedron is frequently encountered in manganate compounds.[26] The two water molecules occupy *trans* positions in the

octahedron, and this is the most common position for them to occupy. A fully fluorinated [MnF_6] octahedron is far less common. The co-existence of these two octahedra types has thus far not been reported for an organically templated Mn compound. In $(C_7NH_{16})_2[MnF_5(H_2O)]\cdot 2H_2O$, two octahedra are connected to the templates via extensive hydrogen-bonding networks. They do not share hydrogen-bonds with one another. This is atypical for Mn compounds which tend to form strong hydrogen-bonds between the apical water molecules and the F atoms on the neighbouring Mn octahedra.[26]

Chain structures have also been reported for the manganate compounds. These seem to be favoured by diammonium cations such as ethylenediamine.[27] The newly synthesised compound $(C_3N_2H_3)[Mn_2F_{10}]$ as reported in Section 5.3.4 is the first example of a ladder compound for an organically-templated manganese fluoride. Alas, the relatively high internal R-factor of the data has prevented a proper and detailed study of the ladders and the hydrogen-bonding network potentially connecting the Mn octahedra to the templates.

The $[Mo_2F_6O_4]$ dimers are not an unknown occurrence for Mo materials.[28] The O atoms are always found to be in a *cis* arrangement in the terminal equatorial positions, whilst two F atoms act as the bridging atoms. Previous work in this group by Aldous has shown that there are many different arrangements that the Mo atom can assume, although he reported no instances of the Mo-centred octahedra observed in this study.[29] In most cases, if there was sharing of atoms between octahedra, the most likely atom to be shared was an O atom. Only in the tetramer $[Mo_4O_8F_{10}]$ found in $(NH_4)_6[Mo_4O_8F_{10}]$ and $K_6Mo_4O_8F_{10}$, and in the *cis*-linked $[MoOF_3]_n$ octahedra in $(C_4H_{12}N_2)_{0.5}[MoOF_3]$ are the F atoms responsible for the bridging. No cases of O-bridging were observed in the work carried out for this thesis. The two Mo-centred octahedra described above from the work by Aldous are given in Figure 5.24.

The effect of the metal ion on the structure was observable for the templates imidazole and 3,5-dimethylpiperidine. The latter leads to the formation of monomers for both the Mn and Mo compounds (Sections 5.3.3 and 5.3.5, respectively); whilst imidazole leads to the formation of the interesting ladder structure for the Mn compound and the $[Mo_2F_4O_2]$ dimers for the Mo compound (Sections 5.3.2 and 5.3.5, respectively). A further point of interest is that the monomers are formed when non-aromatic templates are used, as in 3,5-

dimethylpiperidine. All aromatic and unsaturated hydrocarbons lead to the formation of dimers or ladders. Although no extensive study of this systematic difference has been made, it is possible that the delocalisation of the π-bonds may affect this formation.

From the Mo samples, it also becomes apparent that the addition of a nitrate group to the amine does not affect the dimer formation. The case of the *o*-nitroacetanilide shows that it is important to use stable nitrogen-containing hydrocarbons as starting materials as their decomposition may lead to undesirable products.

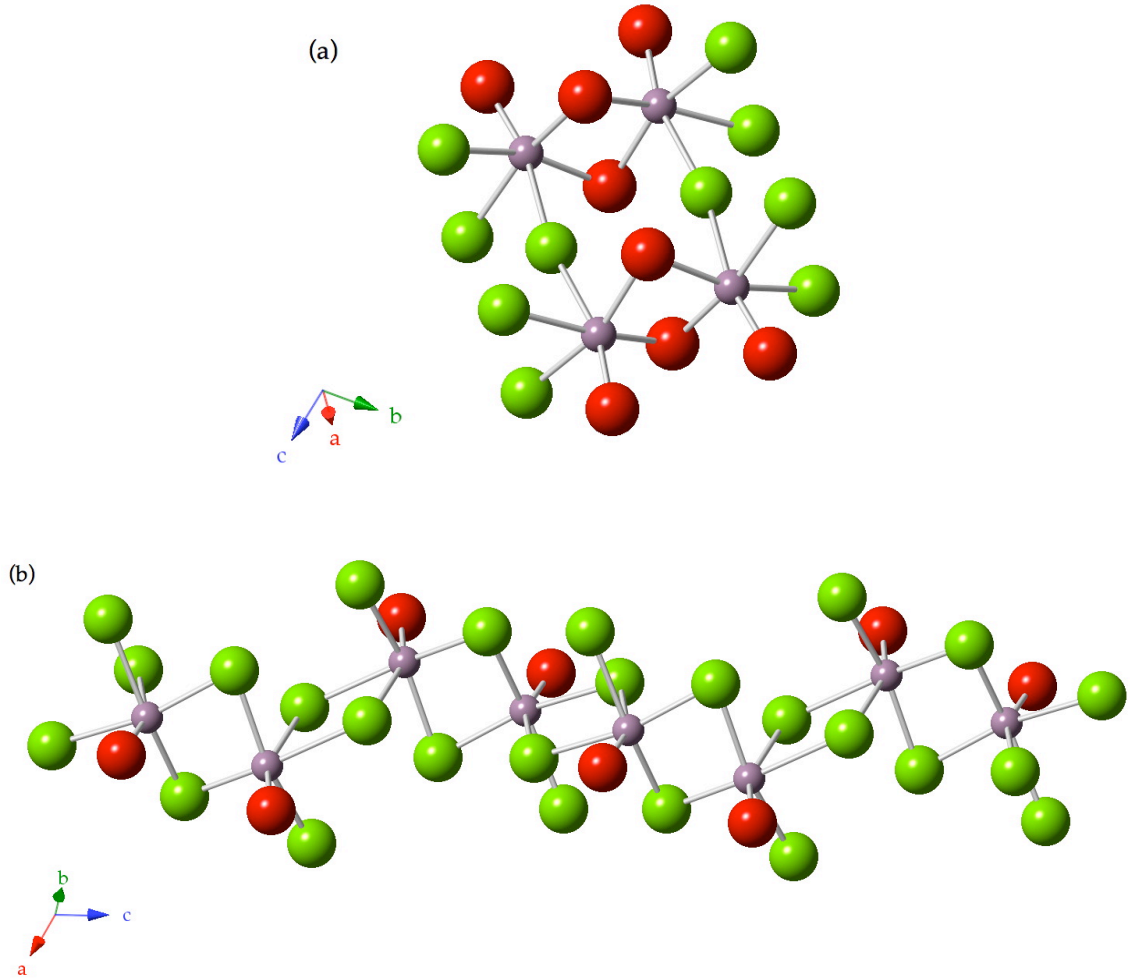

Figure 5.24: Fluorine-connected octahedra reported by Aldous[29] showing (a) the tetramer $[Mo_4O_8F_{10}]$ found in $(NH_4)_6[Mo_4O_8F_{10}]$, and (b) the cis-linked $[MoOF_3]_n$ octahedra in $(C_4H_{12}N_2)_{0.5}[MoOF_3]$

5.5 Conclusions

Although many reactions for the studied systems were performed, very few new structures were obtained. The new strontium structure, $Sr_2V_2F_{10}{\cdot}H_2O$, is isostructural to a known compound and of no further interest, as it is no candidate for electrical studies. The barium compound, $BaVO_2F_3$, although new, will not be ferroelectric, although piezoelectricity may be observed.

The Mn compounds were hard to analyse as all but two of the samples made were too twinned to obtain any useable crystals. The ladder structure, $(C_3N_2H_5)[Mn_2F_6(H_2O)_2]$, is of particular interest as it is polar and so is an ideal candidate for multiferroic studies, and attempts are being made to obtain a better sample.

The Mo hybrid materials show no particular promise for further study, but the uniformity in the results is interesting and may lead to a better starting point for further studies on other transition metals. The option of adding alkaline metals as counter-ions into this system also has yet to be explored and may yield some new and interesting results.

5.6 References

1. K. Byrappa and M. Yoshimura, *Handbook of Hydrothermal Technology*, William Andrew Publishing, Norwich, USA, 2001.
2. A. R. West, in *Solid State Chemistry and Its Applications*, Wiley, Chichester, 1984, Chapter 2.
3. T. Chirayil, P. Y. Zavalij and M. S. Whittingham, *Chem. Mater.* , 1998, **10**, 2629-2640.
4. A. K. Cheetham, G. Férey and T. Loiseau, *Angew. Chem., Int. Ed. Engl.*, 1999, **38**, 3268-3292.
5. S. Natarajan and S. Mandal, *Angew. Chem., Int. Ed. Engl.*, 2008, **47**, 4798-4828.
6. A. Mueller, R. Rohlfing, E. Krickemeyer and H. Boegge, *Angew. Chem.*, 1993, **105**, 916-918.
7. S. N. Achary, A. K. Tyagi and J. Kohler, *J. Solid State Chem.* , 2002, **165**, 74-78.

8. M. Leimkuhler and R. Mattes, *J. Solid State Chem.*, 1986, **65**, 260-264.
9. M. P. Crosnier-Lopez, H. Duroy and J. L. Fourquet, *Z. Anorg. Allg. Chem.*, 1993, **619**, 1597-1602.
10. M. P. Crosnier-Lopez, H. Duroy and J. L. Fourquet, *Z. Anorg. Allg. Chem.*, 1994, **620**, 309-312.
11. D. W. Aldous, R. J. Goff, J. P. Attfield and P. Lightfoot, *Inorg. Chem.*, 2007, **46**, 1277-1282.
12. D. W. Aldous, N. F. Stephens and P. Lightfoot, *Inorg. Chem.*, 2007, **46**, 3996-4001.
13. K. Adil, M. Leblanc, V. Maisonneuve and P. Lightfoot, *Dalton Trans.*, 2010, **39**, 5983-5993.
14. N. Buchholz, M. Leimkuhler, L. Kiriazis and R. Mattes, *Inorg. Chem.*, 1988, **27**, 2035-2039.
15. A. K. Cheetham, C. N. R. Rao and R. K. Feller, *Chem. Commun.*, 2006, 4780-4795.
16. D. W. Aldous, N. F. Stephens and P. Lightfoot, *Dalton Trans.* , 2007, 4207-4213.
17. P. Jain, V. Ramachandran, R. J. Clark, H. D. Zhou, B. H. Toby, N. S. Dalal, H. W. Kroto and A. K. Cheetham, *J. Am. Chem. Soc.*, 2009, **131**, 13625-13627.
18. G. M. Sheldrick, *Acta Crystallogr., Sect. A: Found. Crystallogr.* , 2008, **64**, 112-122.
19. A. R. West, in *Solid State Chemistry and Its Applications*, Wiley, Chichester, 1984, Chapter 3.
20. J.-M. Le Meins, A. Hemon-Ribaud and G. Courbion, *Acta Crystallogr., Sect. C: Cryst. Struct. Commun.*, 1997, **C53**, 1165-1166.
21. C. Ninclaus, D. Riou and G. Ferey, *Chem. Commun.*, 1997, 851-852.
22. M. E. Welk, C. L. Stern, K. R. Poeppelmeier and A. J. Norquist, *Cryst. Growth. Des.*, 2007, **7**, 956-961.
23. R. Stief and W. Massa, *Z. Anorg. Allg. Chem.*, 2004, **630**, 2502-2507.
24. R. Stief and W. Massa, *Z. Anorg. Allg. Chem.*, 2006, **632**, 797-800.
25. A. Ahmadi, R. Stief, W. Massa and J. Pebler, *Z. Anorg. Allg. Chem.*, 2001, **627**, 869-876.

26. U. Bentrup, M. Feist and E. Kemnitz, *Progr. Solid State Chem.*, 1999, **27**, 75-129.
27. U. Bentrup, L. Schroder and W. Massa, *Z. Naturforsch., B: Chem. Sci.*, 1992, **47**, 789-794.
28. J. Dirand, L. Ricard and R. Weiss, *Transition Met. Chem.*, 1975, **1**, 2-5.
29. D. Aldous, *Solvothermal Chemistry of Early Transition Metal Fluorides*, PhD thesis, University of St Andrews, 2008.

Chapter 6

Summary, Conclusions and Future Work

6.1 Summary

Several transition metal fluorides and oxyfluorides were synthesised and then analysed by sPXRD and SCXRD methods. Solid state methods were used to synthesise the tetragonal tungsten bronzes of K_xFeF_3 (where $x = 0.58$ and $x \approx 0.5$), as well as the two-dimensional kagome structure $Cs_2ZrCu_3F_{12}$.

Both of these compounds were subjected to variable temperature studies and found to exhibit phase transitions and the TTB structures also showed phase separations.

Hydrothermal methods were used to synthesise new transition metal fluorides and oxyfluorides of vanadium, manganese, and molybdenum. Various cationic species were used as counter-ions in these reactions, ranging from alkaline metals (barium and strontium) to organic templates such as imidazole and 3,5-dimethylpiperidine.

6.2 Conclusions

The results presented in Chapter 3 on selected fluoride TTBs shows that there is no clear indication from the sPXRD data alone that the K_xFeF_3 solid solutions are noncentrosymmetric. This is contradictory to the observed electrical measurements reported in the literature. The lack of evidence that the materials are noncentrosymmetric is not a confirmation that they are centrosymmetric, merely that there is insufficient evidence to show the noncentrosymmetric model is the better solution of the two. Other analytical techniques, such as further electrical measurements and electron microscopy may provide a better answer to that question. Centrosymmetric space groups have been used due to aforementioned lack of evidence for the noncentrosymmetric equivalents.

The phase separations observed for both investigated members of the K_xFeF_3 solid solution (i.e. x = 0.58 and x ≈ 0.5) are new and well characterised throughout the studied temperature range of 100 K to 500 K. The lattice parameters and phase fractions for each phase, as well as those for the observed impurities, confirm this.

The tetragonal models found above room temperature are in line with the reported variants of these materials. The same is true for the orthorhombic distortions seen at lower temperatures.

Although the tetragonal and orthorhombic phases in $K_{0.58}FeF_3$ are found to exist simultaneously in only a narrow temperature range of 20 K, they both show a clear and swift growth rate. The orthorhombic phase "*Pbam*" increases from 0% to 10% in this range, whilst the tetragonal phase *P4/mbm* decreases by the same amount. The two weight percentages then remain constant as the tetragonal phase, *P4/mbm*, undergoes a phase transition to the orthorhombic approximation model "*Cmmm*".

The phase separation is already present at 500 K for the $K_{0.5}FeF_3$ sample. Unlike the $K_{0.58}FeF_3$ sample, there are two tetragonal phases coexisting at this point, not one tetragonal and one orthorhombic. The tetragonal model in the standard *P4/mbm* setting shows no ordering of the Fe^{2+} and Fe^{3+} ions, whilst the more abundant tetragonal phase $P4_2bc$ shows charge ordering.

Both of the members of the K_xFeF_3 solid solution (x = 0.58 and x ≈ 0.5) show phase transitions for the standard *P4/mbm* model to an orthorhombic distortion. In both cases the "*Cmmm*" approximation model gives the most adequate description of this distortion. This same tetragonal to orthorhombic phase transition is observed for $K_3Cu_3Fe_2F_{15}$, although there is no evidence for a phase separation in this material.

The kagome structure presented in Chapter 4 shows that the two phases of $Cs_2ZrCu_3F_{12}$ possess the "ideal" and distorted kagome lattices at room temperature and below 225 K respectively. This indicates the result of the tilting of the kagome layers in these two structures. The change in the coordination number of the Zr^{4+} ion from 6 to 7 in going from the high temperature to the low temperature phase is the driving force for the buckling of the layers, as one of the F atoms in the layer must move significantly away from its original position to facilitate this change. The Cu^{2+} ion bonded to this F

atom then moves as well, as it too wishes to maintain its coordination number of 6. This leads to the generation of three crystallographically distinct Cu^{2+} sites and a buckling of the hitherto flat kagome layer.

The first order phase transition is clearly indicted in the abrupt change in lattice parameters in this temperature range (around 225 K) and the same conclusion is observed in the electrical data.

This electrical data also indicates that there is an anomaly at the phase transition temperature. This anomaly occurs at the same temperature where a further anomaly has been reported in the magnetic susceptibility measurements. The electrical data thus lends support to the conclusion that both of the anomalies arise as a result of the first-order phase transition in going from the high temperature rhombohedral model to the low temperature monoclinic model.

The hydrothermal reactions presented in Chapter 5 give a range of new materials. The strontium compound reported, $Sr_2V_2F_{10}{\cdot}H_2O$, is new and found to be isostructural to a known compound, $Sr_2Fe_2F_{10}{\cdot}H_2O$, and of no further interest, as it is apparent that it cannot be electrically or magnetically active. The new barium compound, $BaVO_2F_3$, cannot be ferroelectric as it crystallises in a cubic space group, but piezoelectricity may be observed.

Most attempts to synthesise new Mn compounds with various organic templates led to the formation of crystals but these were all extremely twinned and the data collected could not be solved. Two of the samples, though, have yielded new structures. The first of these, the ladder structure $(C_3N_2H_5)[Mn_2F_6(H_2O)_2]$, is of particular interest as it is polar and so this makes it an ideal candidate for multiferroic studies, and ongoing attempts are being made to produce a purer and more crystalline sample to determine its full structure and to perform electrical and magnetic measurements. The second hybrid material of a Mn compound, $(C_7NH_{16})_2[MnF_5(H_2O)]{\cdot}2H_2O$, crystallises in a centrosymmetric space group and is therefore not a suitable material for ferroic studies.

The Mo hybrid materials show no particular promise for further study as all of the obtained materials are centrosymmetric, but the uniformity in the results is interesting and may lead to a better starting point for further studies on other transition metal (oxy)fluorides.

6.3 Future Work

First and foremost all of the reaction processes must be optimised so that the impurities can be eliminated from the products. This is vitally important so that the electrical and magnetic measurements that can be done on these samples are not affected by these impurities.

For the TTB samples this seems to be problematic as the solid solutions seem to separate into two separate phases above room temperature irrespective of the composition. A more thorough and systematic study of the solid solution system is needed to determine if this is a general or intrinsic feature. This makes the interpretation of magnetic and electrical data more challenging. The magnetic and electrical measurements must be repeated though, to confirm the reports presented by other research groups. This solid solution is extremely composition dependent and so any physical measurements must be accompanied by a crystallographic analysis of the same sample to ascertain the exact composition of the material studied.

The kagome structures are easier to synthesise, as the starting materials seem less prone to oxidise during the reaction process. In order to fully understand the phases of these compounds, the remaining members of the $A_2BCu_3F_{12}$ (A^+ = Cs, Rb; B^{4+} = Zr, Sn) family must be synthesised. This has been met with limited success to date in so far as the materials have been synthesised, but they are the minor phase in the product material. Attempts to improve the synthetic route are underway. This is being done by changing the reactant starting ratios so that there is an excess of the alkaline fluoride, as it seems the most volatile of the starting materials. The reaction temperature and time are being investigated as well. A further isotypic family of materials that is to be synthesised is $A_2TiCu_3F_{12}$ (A^+ = Cs, Rb).

The hydrothermal work presented is best extended by the use of different transition metals with the reported organic templates. Particularly suitable candidates for this are vanadium and copper. The option of adding alkaline metals as counter-ions into this system also has yet to be explored and may yield some new and interesting results. It would be of interest to also extend the study of the Mo system with the various organic templates to

determine if there is an effect on the formation of monomers or dimers by the presence of aromatic versus saturated organic templates.

DUCK!

Appendix A

Table A.1: Crystal data and structure refinement for $Sr_2V_2F_{10}\cdot H_2O$

Identification code	srv4
Empirical formula	F10 H3O Sr2 V2
Formula weight	486.14
Temperature	93(2) K
Wavelength	0.71073 Å
Crystal system	Orthorhombic
Space group	*Cmca*
Unit cell dimensions	a = 7.844(4) Å α = 90°
	b = 19.883(9) Å β = 90°
	c = 10.707(5) Å γ = 90°
Volume	1670.0(13) $Å^3$
Z	8
Density (calculated)	3.851 Mg/m^3
Absorption coefficient	15.017 mm^{-1}
F(000)	1768
Crystal size	0.12 x 0.10 x 0.01 mm^3
Theta range for data collection	3.38 to 28.20°.
Index ranges	-8<=h<=10, -24<=k<=24, -9<=l<=12
Reflections collected	4764
Independent reflections	965 [R(int) = 0.1279]
Completeness to theta = 28.20°	87.3 %
Absorption correction	Multiscan
Max. and min. transmission	0.8643 and 0.2659
Refinement method	Full-matrix least-squares on F^2
Data / restraints / parameters	965 / 0 / 51
Goodness-of-fit on F^2	1.303
Final R indices [I>2sigma(I)]	R1 = 0.0956, wR2 = 0.1658
R indices (all data)	R1 = 0.1238, wR2 = 0.1746
Largest diff. peak and hole	1.931 and -2.593 e.$Å^{-3}$

Table A.2: Atomic coordinates (x 10^4) and equivalent isotropic displacement parameters (Å^{2}x 10^3) for $Sr_2V_2F_{10}\cdot H_2O$

U(eq) is defined as one third of the trace of the orthogonalized U^{ij} tensor

	x	y	z	U(eq)
O(1)	0	842(6)	440(12)	10(3)
F(1)	3007(10)	3968(4)	3656(7)	10(2)
F(2)	5000	4691(6)	2061(12)	20(3)
F(3)	2972(11)	336(4)	1267(7)	14(2)
F(4)	0	1787(6)	2467(11)	14(3)
F(5)	2398(11)	1885(4)	792(7)	13(2)
F(6)	0	2829(5)	1043(10)	7(2)
F(7)	0	1976(5)	-1097(10)	10(2)
V(1)	2500	4672(2)	2500	11(1)
V(2)	0	1842(2)	666(3)	7(1)
Sr(1)	5000	1191(1)	466(2)	6(1)
Sr(2)	2500	2828(1)	2500	9(1)

Table A.3: Anisotropic displacement parameters (Å^{2}x 10^3) for $Sr_2V_2F_{10}\cdot H_2O$

The anisotropic displacement factor exponent takes the form: $-2p^2[h^2a^{*2}U^{11} + ... + 2 h k a^* b^* U^{12}]$

	U^{11}	U^{22}	U^{33}	U^{23}	U^{13}	U^{12}
V(1)	19(2)	8(2)	7(2)	0	-2(2)	0
V(2)	6(2)	10(2)	6(2)	-1(1)	0	0
Sr(1)	6(1)	6(1)	6(1)	0(1)	0	0
Sr(2)	5(1)	11(1)	9(1)	0	0(1)	0

Table A.4: Crystal data and structure refinement for $BaVO_2F_3$

Identification code	bav10_sir92
Empirical formula	Ba F3 O2 V
Formula weight	277.28
Temperature	293(2) K
Wavelength	0.71073 Å
Crystal system	Cubic
Space group	$P2_13$

Unit cell dimensions	a = 7.521(3) Å α = 90 °
	b = 7.521(3) Å β = 90°
	c = 7.521(3) Å γ = 90°
Volume	425.4(3) $Å^3$
Z	4
Density (calculated)	4.329 Mg/m^3
Absorption coefficient	11.348 mm^{-1}
F(000)	488
Crystal size	0.150 x 0.150 x 0.150 mm^3
Theta range for data collection	4.69 to 27.58°.
Index ranges	-7<=h<=9, -8<=k<=8, -6<=l<=9
Reflections collected	2332
Independent reflections	314 [R(int) = 0.0598]
Completeness to theta = 27.58°	97.0 %
Absorption correction	Multiscan
Max. and min. transmission	1.0000 and 0.2621
Refinement method	Full-matrix least-squares on F^2
Data / restraints / parameters	314 / 0 / 28
Goodness-of-fit on F^2	1.269
Final R indices [I>2sigma(I)]	R1 = 0.0486, wR2 = 0.1030
R indices (all data)	R1 = 0.0486, wR2 = 0.1030
Absolute structure parameter	-0.1(2)
Largest diff. peak and hole	1.014 and -1.079 e.$Å^{-3}$

Table A.5: Atomic coordinates (x 10^4) and equivalent isotropic displacement parameters ($Å^2$x 10^3) for $BaVO_2F_3$

	x	y	z	U(eq)
Ba(1)	6542(1)	1542(1)	3458(1)	20(1)
V(1)	1682(4)	1682(4)	1682(4)	34(1)
O(1)	3330(30)	93(18)	1790(40)	132(12)
F(1)	3330(30)	93(18)	1790(40)	132(12)
F(2)	3152(12)	3152(12)	3152(12)	31(4)
F(3)	960(40)	-740(40)	840(40)	40(8)

Table A.6: Anisotropic displacement parameters (Å^{2}x 10^3) for $BaVO_2F_3$

The anisotropic displacement factor exponent takes the form: $-2p^2[h^2a^{*2}U^{11} + ... + 2 h k a^* b^* U^{12}]$

	U^{11}	U^{22}	U^{33}	U^{23}	U^{13}	U^{12}
Ba(1)	20(1)	20(1)	20(1)	2(1)	2(1)	-2(1)
V(1)	34(1)	34(1)	34(1)	-3(1)	-3(1)	-3(1)
O(1)	152(19)	19(6)	220(30)	2(10)	150(20)	6(10)
F(1)	152(19)	19(6)	220(30)	2(10)	150(20)	6(10)
F(2)	31(4)	31(4)	31(4)	-2(4)	-2(4)	-2(4)
F(3)	47(19)	31(15)	42(17)	14(13)	-23(14)	-14(14)

Table A.7: Crystal data and structure refinement for $(C_7NH_{16})_2[MnF_5(H_2O)]\cdot 2H_2O$

Identification code	mnn60	
Empirical formula	C14 H38 F5 Mn N2 O30	
Formula weight	216.20	
Temperature	125(2) K	
Wavelength	0.71073 Å	
Crystal system	Triclinic	
Space group	$P\bar{1}$	
Unit cell dimensions	a = 7.470(3) Å	α = 93.48(2)°
	b = 11.153(5) Å	β = 104.755(17)°
	c = 13.666(6) Å	γ = 104.753(19)°
Volume	1055.1(8) Å^3	
Z	4	
Density (calculated)	1.361 Mg/m^3	
Absorption coefficient	0.682 mm^{-1}	
F(000)	460	
Crystal size	0.12 x 0.03 x 0.03 mm^3	
Theta range for data collection	2.62 to 28.07°.	
Index ranges	-8<=h<=7, -12<=k<=14, -11<=l<=15	

Reflections collected	5235
Independent reflections	3549 [R(int) = 0.0501]
Completeness to theta = 28.07°	69.2 %
Absorption correction	Multiscan
Max. and min. transmission	0.9798 and 0.9226
Refinement method	Full-matrix least-squares on F^2
Data / restraints / parameters	3549 / 0 / 264
Goodness-of-fit on F^2	1.117
Final R indices [I>2sigma(I)]	R1 = 0.0723, wR2 = 0.1360
R indices (all data)	R1 = 0.1108, wR2 = 0.1467
Largest diff. peak and hole	0.565 and -0.363 e.$Å^{-3}$

Table A.8: Atomic coordinates (x 10^4) and equivalent isotropic displacement parameters ($Å^2$x 10^3) for $(C_7NH_{16})_2[MnF_5(H_2O)]\cdot 2H_2O$

	x	y	z	U(eq)
O(1)	2386(6)	9129(4)	319(4)	19(1)
O(2)	8427(8)	3134(4)	8984(3)	25(1)
O(3)	4213(7)	8606(4)	8926(3)	21(1)
F(1)	-7655(4)	4274(3)	-488(2)	20(1)
F(2)	-5279(4)	6446(3)	-513(2)	21(1)
F(3)	-5496(4)	5677(3)	1399(2)	20(1)
F(4)	1737(4)	11561(3)	34(2)	17(1)
F(5)	337(4)	10317(3)	1368(2)	18(1)
N(1)	-2616(7)	7845(4)	1747(4)	16(1)
N(2)	2333(7)	3398(5)	1609(4)	19(1)
Mn(1)	-5000	5000	0	13(1)
Mn(2)	0	10000	0	13(1)
C(1)	-808(8)	7883(5)	2521(4)	19(1)
C(2)	-1109(8)	7816(6)	3580(4)	26(1)
C(3)	-1991(9)	8848(6)	3830(4)	29(1)
C(4)	-3857(9)	8809(6)	3022(4)	26(1)
C(5)	-3471(8)	8856(5)	1979(4)	20(1)

C(6)	801(9)	7881(7)	4351(5)	35(2)
C(7)	-4745(10)	9828(6)	3253(5)	39(2)
C(8)	3447(8)	2902(5)	2475(4)	20(1)
C(9)	3772(9)	3686(6)	3480(4)	28(1)
C(10)	1869(9)	3790(6)	3626(4)	28(1)
C(11)	716(9)	4300(6)	2743(4)	30(2)
C(12)	446(8)	3490(5)	1738(4)	23(1)
C(13)	4882(10)	3131(7)	4357(5)	37(2)
C(14)	-1213(10)	4333(6)	2866(5)	37(2)

Table A.9: Anisotropic displacement parameters ($Å^2 x\ 10^3$) for

$(C_7NH_{16})_2[MnF_5(H_2O)]\cdot 2H_2O$

The anisotropic displacement factor exponent takes the form: $-2p^2[\ h^2 a^{*2} U^{11} + ... + 2\ h\ k\ a^*\ b^*\ U^{12}\ ]$

	U11	U22	U33	U23	U13	U12
O(1)	16(2)	18(2)	27(2)	6(2)	10(2)	7(2)
O(2)	18(3)	18(2)	43(3)	7(2)	11(2)	8(2)
O(3)	16(3)	14(2)	31(2)	5(2)	3(2)	3(2)
F(1)	14(2)	19(2)	26(2)	3(1)	6(1)	1(1)
F(2)	20(2)	15(2)	31(2)	9(1)	9(1)	6(1)
F(3)	21(2)	16(2)	22(2)	2(1)	11(1)	3(1)
F(4)	16(2)	12(2)	22(2)	4(1)	7(1)	-2(1)
F(5)	21(2)	15(2)	18(2)	5(1)	6(1)	1(1)
N(1)	16(3)	15(2)	15(2)	3(2)	3(2)	2(2)
N(2)	24(3)	15(3)	15(2)	2(2)	7(2)	1(2)
Mn(1)	10(1)	10(1)	19(1)	4(1)	5(1)	2(1)
Mn(2)	13(1)	11(1)	16(1)	3(1)	5(1)	1(1)
C(1)	18(3)	21(3)	22(3)	4(2)	10(2)	7(2)
C(2)	25(4)	31(3)	21(3)	4(3)	5(3)	10(3)
C(3)	34(4)	35(4)	17(3)	-2(3)	9(3)	7(3)
C(4)	32(4)	31(3)	17(3)	2(3)	9(3)	13(3)
C(5)	19(3)	25(3)	16(3)	7(2)	0(2)	9(2)

C(6)	34(4)	45(4)	25(3)	7(3)	3(3)	14(3)
C(7)	38(4)	42(4)	42(4)	3(3)	16(3)	17(3)
C(8)	16(3)	24(3)	23(3)	1(2)	6(2)	8(2)
C(9)	25(4)	34(4)	26(3)	3(3)	7(3)	11(3)
C(10)	30(4)	39(4)	16(3)	-3(3)	9(3)	9(3)
C(11)	27(4)	43(4)	23(3)	4(3)	11(3)	13(3)
C(12)	22(3)	26(3)	22(3)	10(2)	10(3)	6(3)
C(13)	34(4)	58(5)	21(3)	5(3)	8(3)	15(3)

Table A.10: Crystal data and structure refinement for $(C_3N_2H_5)[Mn_2F_6(H_2O)_2]$

Identification code	mnn18batch2
Empirical formula	C3 H9 F6 Mn2 N2 O2
Formula weight	328.95
Temperature	125(2) K
Wavelength	0.71073 Å
Crystal system	Orthorhombic
Space group	$P2_1ca$
Unit cell dimensions	a = 7.6817(10) Å
	b = 8.4273(11) Å
	c = 15.217(2) Å
Volume	985.1(2) $Å^3$
Z	4
Density (calculated)	2.218 Mg/m^3
Absorption coefficient	2.651 mm^{-1}
F(000)	628
Crystal size	0.27 x 0.05 x 0.04 mm^3
Theta range for data collection	3.61 to 27.48°.
Index ranges	-9<=h<=9, -10<=k<=10, -19<=l<=19
Reflections collected	9517
Independent reflections	2242 [R(int) = 0.1396]
Completeness to theta = 27.48°	99.8 %
Absorption correction	Multiscan

Max. and min. transmission	0.9014 and 0.5347
Refinement method	Full-matrix least-squares on F^2
Data / restraints / parameters	2242 / 1 / 61
Goodness-of-fit on F^2	1.118
Final R indices [I>2sigma(I)]	R1 = 0.1127, wR2 = 0.2140
R indices (all data)	R1 = 0.1710, wR2 = 0.2351
Absolute structure parameter	0.22(15)
Largest diff. peak and hole	2.076 and -1.376 e.$Å^{-3}$

Table A.11: Atomic coordinates (x 10^4) and equivalent isotropic displacement parameters ($Å^2$x 10^3) for $(C_3N_2H_5)[Mn_2F_6(H_2O)_2]$

	x	y	z	U(eq)
N(1)	-790(20)	2738(15)	1999(8)	13(3)
C(1)	-380(20)	1180(20)	2071(14)	21(5)
N(2)	-930(30)	2276(15)	3364(8)	16(3)
C(3)	-610(20)	3380(20)	2763(11)	21(5)
C(2)	-360(20)	950(30)	2940(15)	29(5)
Mn(1)	1556(4)	6567(3)	563(2)	14(1)
Mn(2)	1508(3)	3364(3)	-539(2)	6(1)
F(1)	-980(20)	7211(9)	108(5)	9(2)
F(2)	4026(18)	6239(8)	1011(5)	7(2)
F(7)	2322(15)	2701(12)	-1724(7)	12(2)
F(3)	740(30)	7000(20)	1754(13)	72(6)
F(5)	983(13)	4053(12)	585(7)	14(2)
F(4)	2281(16)	8714(14)	281(8)	27(3)
F(8)	540(20)	1300(20)	22(12)	69(5)
F(6)	2162(13)	5476(11)	-744(6)	10(2)

Table A.12: Crystal data and structure refinement for $(C_7NH_{16})_2[MoF_4O_2]$

Identification code	mon1a
Empirical formula	C14 H32 F4 Mo N2 O2
Formula weight	864.71

Temperature	125(2) K
Wavelength	0.71073 Å
Crystal system	Triclinic
Space group	$P\bar{1}$
Unit cell dimensions	a = 13.967(6) Å α = 78.374(13)°
	b = 14.322(6) Å β = 89.077(13)°
	c = 21.9114(10) Å γ = 69.357(9)°
Volume	4010(2) Å^3
Z	8
Density (calculated)	1.432 Mg/m^3
Absorption coefficient	0.696 mm^{-1}
F(000)	1792
Crystal size	0.20 x 0.20 x 0.20 mm^3
Theta range for data collection	0.95 to 32.28°.
Index ranges	-19<=h<=19, -20<=k<=19, -31<=l<=30
Reflections collected	52703
Independent reflections	25826 [R(int) = 0.1193]
Completeness to theta = 32.28°	90.7 %
Absorption correction	Multiscan
Max. and min. transmission	0.8733 and 0.8733
Refinement method	Full-matrix least-squares on F^2
Data / restraints / parameters	25826 / 0 / 829
Goodness-of-fit on F^2	1.009
Final R indices [I>2sigma(I)]	R1 = 0.0871, wR2 = 0.1660
R indices (all data)	R1 = 0.2900, wR2 = 0.2758
Largest diff. peak and hole	0.992 and -1.410 e.Å^{-3}

Table A.13: Atomic coordinates (x 10^4) and equivalent isotropic displacement parameters (Å^{2}x 10^3) for $(C_7NH_{16})_2[MoF_4O_2]$

	x	y	z	U(eq)
O(1)	2157(5)	5423(5)	1122(3)	65(2)
O(2)	710(7)	5453(6)	1912(3)	101(3)

O(3)	5713(4)	5301(4)	2446(3)	50(2)
O(4)	7607(4)	5364(4)	2473(3)	48(2)
O(5)	7418(6)	4966(5)	5087(3)	75(2)
O(6)	7523(6)	5588(6)	6151(4)	98(3)
O(7)	2314(5)	1097(4)	2640(3)	50(2)
O(8)	2778(5)	-603(5)	3513(3)	68(2)
F(1)	259(4)	5832(5)	654(3)	84(2)
F(2)	1593(5)	4060(4)	649(2)	80(2)
F(3)	188(4)	4134(4)	1469(2)	54(1)
F(4)	2076(4)	3643(4)	1834(3)	71(2)
F(5)	7224(4)	3939(5)	1962(2)	72(2)
F(6)	6512(3)	3318(3)	3053(2)	44(1)
F(7)	6830(3)	4725(3)	3538(2)	40(1)
F(8)	8365(3)	3383(3)	3017(2)	44(1)
F(9)	5709(4)	5671(4)	5722(2)	62(2)
F(10)	6474(4)	3740(4)	5672(2)	54(1)
F(11)	6587(4)	4329(4)	6720(2)	54(1)
F(12)	8274(4)	3552(5)	6131(3)	85(2)
F(13)	711(4)	875(4)	2187(2)	65(2)
F(14)	2528(4)	-661(4)	2296(3)	68(2)
F(15)	1118(4)	-887(4)	3011(3)	71(2)
F(16)	850(4)	797(4)	3400(2)	64(2)
N(2)	8818(6)	1580(6)	2611(3)	56(2)
N(3)	4897(5)	3536(5)	6325(3)	47(2)
N(5)	4431(5)	3857(5)	2897(3)	39(2)
N(6)	8557(5)	5151(6)	591(3)	51(2)
N(7)	1936(9)	7372(6)	2569(5)	102(4)
N(8)	1496(7)	2059(6)	1334(4)	65(2)
C(8)	8047(8)	-544(8)	3594(5)	82(4)
C(9)	8362(12)	66(10)	3011(6)	107(5)
C(10)	8520(10)	946(9)	3135(5)	83(4)
C(11)	8233(11)	1731(10)	2013(5)	95(4)
C(12)	8109(12)	841(11)	1863(6)	110(5)

C(13)	7503(10)	1051(10)	1259(6)	102(4)
C(14)	7733(8)	262(8)	2421(5)	68(3)
C(15)	4846(8)	1445(8)	7721(4)	72(3)
C(16)	4443(7)	2329(7)	7144(4)	54(2)
C(17)	5282(7)	2724(7)	6909(4)	52(2)
C(18)	4510(7)	3192(7)	5825(4)	50(2)
C(19)	3656(7)	2795(7)	6030(4)	51(2)
C(20)	3285(8)	2440(7)	5505(4)	63(3)
C(21)	4005(6)	1988(7)	6623(5)	54(3)
C(29)	4591(8)	1086(7)	3359(5)	72(3)
C(30)	4832(7)	2017(6)	2997(4)	53(2)
C(31)	4208(6)	2958(6)	3236(4)	42(2)
C(32)	4172(6)	4068(7)	2202(4)	47(2)
C(33)	4795(7)	3134(7)	1939(4)	53(2)
C(34)	4500(7)	3358(8)	1228(4)	61(3)
C(35)	4612(7)	2202(7)	2297(4)	54(2)
C(36)	6270(11)	7339(11)	957(6)	127(6)
C(37)	6850(9)	6508(9)	612(6)	80(3)
C(38)	7965(7)	5971(8)	911(4)	61(3)
C(39)	8080(6)	4371(7)	584(4)	52(2)
C(40)	6991(7)	4836(9)	303(5)	67(3)
C(41)	6542(9)	4021(11)	323(6)	109(5)
C(42)	6372(8)	5686(10)	623(5)	78(4)
C(43)	2340(20)	8022(15)	843(7)	252(16)
C(44)	1790(20)	8131(11)	1439(9)	204(14)
C(45)	2453(13)	7282(10)	1991(6)	117(6)
C(46)	924(11)	7263(9)	2515(7)	125(7)
C(47)	216(17)	8030(10)	1994(10)	172(11)
C(48)	-817(14)	7868(15)	1951(11)	239(15)
C(49)	710(20)	8045(11)	1403(9)	206(16)
C(50)	3903(11)	368(11)	701(7)	159(8)
C(51)	2786(13)	746(10)	884(8)	118(6)
C(52)	2573(8)	1647(9)	1163(5)	74(3)

C(53)	748(9)	2273(10)	805(6)	91(4)
C(54)	898(15)	1423(17)	487(12)	213(13)
C(55)	211(15)	1187(16)	321(13)	278(17)
C(56)	2035(16)	970(13)	353(9)	146(8)
N(4)	21(5)	5903(5)	7134(3)	43(2)
Mo(1)	1233(1)	4920(1)	1313(1)	40(1)
Mo(2)	6955(1)	4516(1)	2662(1)	44(1)
Mo(3)	7110(1)	4783(1)	5839(1)	45(1)
C(22)	729(7)	4264(7)	5903(5)	61(3)
C(23)	523(6)	5203(7)	6186(4)	46(2)
C(24)	263(7)	4987(7)	6856(5)	56(3)
C(25)	-897(7)	6759(7)	6797(4)	49(2)
C(26)	-707(7)	7054(7)	6124(4)	49(2)
C(27)	-1690(7)	7903(7)	5775(5)	62(3)
C(28)	-358(7)	6128(7)	5809(4)	54(3)
Mo(4)	1867(1)	81(1)	2939(1)	68(1)
N(1)	6992(5)	3170(5)	4565(3)	50(2)
C(1)	9635(7)	1343(8)	5267(5)	75(3)
C(2)	8485(7)	1785(6)	5182(4)	49(2)
C(3)	8139(6)	2720(6)	4640(4)	50(2)
C(4)	6501(7)	2429(6)	4513(4)	50(2)
C(5)	6827(6)	1499(6)	5021(4)	45(2)
C(6)	6344(7)	722(8)	4953(5)	69(3)
C(7)	8013(6)	1014(6)	5086(4)	45(2)

Table A.14: Anisotropic displacement parameters ($Å^2 x\ 10^3$) for

$(C_7NH_{16})_2[MoF_4O_2]$

The anisotropic displacement factor exponent takes the form: $-2p^2[\ h^2a^{*2}U^{11} + ... + 2\ h\ k\ a^*\ b^*\ U^{12}\ ]$

	U^{11}	U^{22}	U^{33}	U^{23}	U^{13}	U^{12}
O(1)	74(5)	64(4)	72(5)	-8(4)	11(4)	-47(4)
O(2)	172(9)	101(6)	74(5)	-61(5)	61(6)	-81(6)

O(3)	31(3)	56(4)	50(4)	8(3)	-7(3)	-10(3)
O(4)	42(3)	56(4)	44(3)	2(3)	7(3)	-24(3)
O(5)	105(6)	45(4)	76(5)	-10(4)	57(4)	-30(4)
O(6)	81(5)	109(6)	157(8)	-95(6)	52(5)	-62(5)
O(7)	73(4)	42(3)	42(3)	-13(3)	6(3)	-26(3)
O(8)	60(4)	72(5)	51(4)	0(4)	1(3)	-5(4)
F(1)	61(4)	84(4)	91(5)	33(4)	-26(3)	-35(3)
F(2)	135(6)	75(4)	48(3)	-23(3)	32(4)	-56(4)
F(3)	44(3)	58(3)	60(3)	0(3)	4(2)	-25(3)
F(4)	55(3)	70(4)	78(4)	18(3)	-14(3)	-28(3)
F(5)	77(4)	98(5)	40(3)	-24(3)	6(3)	-25(4)
F(6)	32(2)	41(3)	54(3)	-6(2)	2(2)	-11(2)
F(7)	40(3)	40(3)	35(2)	-5(2)	3(2)	-9(2)
F(8)	30(2)	47(3)	50(3)	-12(2)	3(2)	-6(2)
F(9)	64(4)	52(3)	46(3)	-4(3)	-1(3)	3(3)
F(10)	52(3)	59(3)	63(3)	-21(3)	19(3)	-31(3)
F(11)	65(3)	43(3)	40(3)	-8(2)	6(2)	-3(3)
F(12)	47(3)	81(4)	107(5)	-29(4)	-5(3)	8(3)
F(13)	71(4)	58(3)	57(3)	-12(3)	-8(3)	-11(3)
F(14)	71(4)	60(4)	68(4)	-33(3)	3(3)	-8(3)
F(15)	69(4)	47(3)	102(5)	-39(3)	16(3)	-17(3)
F(16)	71(4)	59(3)	64(4)	-30(3)	9(3)	-17(3)
N(2)	57(5)	56(5)	56(5)	-20(4)	9(4)	-18(4)
N(3)	36(4)	41(4)	58(5)	-5(4)	11(4)	-12(3)
N(5)	31(4)	37(4)	45(4)	-6(3)	-3(3)	-9(3)
N(6)	37(4)	60(5)	42(4)	2(4)	2(3)	-9(4)
N(7)	170(11)	21(4)	96(8)	-4(5)	-69(8)	-11(6)
N(8)	82(6)	51(5)	68(6)	-6(4)	22(5)	-33(5)
C(8)	79(8)	81(8)	101(9)	-2(7)	12(7)	-58(7)
C(9)	138(13)	102(11)	109(11)	1(9)	-16(10)	-87(10)
C(10)	140(11)	109(10)	42(6)	-10(6)	11(6)	-100(9)
C(11)	143(13)	98(10)	57(7)	-17(7)	-3(8)	-57(9)
C(12)	135(13)	100(11)	86(10)	-8(9)	-37(9)	-37(10)

C(13)	104(10)	91(10)	96(10)	-13(8)	-39(8)	-19(8)
C(14)	67(7)	64(7)	81(8)	-10(6)	-10(6)	-36(6)
C(15)	86(8)	61(7)	57(7)	10(5)	-8(6)	-25(6)
C(16)	51(6)	53(6)	52(6)	-3(5)	-7(5)	-14(5)
C(17)	52(6)	52(6)	43(5)	-2(4)	-7(4)	-14(5)
C(18)	44(5)	58(6)	46(5)	-9(5)	5(4)	-17(5)
C(19)	59(6)	42(5)	56(6)	-3(4)	17(5)	-27(5)
C(20)	76(7)	55(6)	61(6)	-14(5)	3(6)	-24(6)
C(21)	34(5)	46(5)	81(7)	-1(5)	4(5)	-20(4)
C(29)	71(7)	50(6)	93(8)	-6(6)	-8(6)	-24(6)
C(30)	50(6)	34(5)	71(7)	-5(5)	-17(5)	-13(4)
C(31)	37(5)	38(5)	47(5)	0(4)	-4(4)	-14(4)
C(32)	43(5)	55(6)	40(5)	-2(4)	-12(4)	-19(5)
C(33)	38(5)	71(7)	51(6)	-19(5)	-12(4)	-16(5)
C(34)	47(6)	85(8)	52(6)	-27(6)	-2(5)	-19(5)
C(35)	48(6)	54(6)	61(6)	-20(5)	-8(5)	-16(5)
C(36)	118(12)	108(11)	101(11)	-22(9)	34(9)	22(10)
C(37)	70(8)	69(8)	78(8)	-6(6)	18(6)	-4(7)
C(38)	53(6)	72(7)	53(6)	-9(5)	8(5)	-18(6)
C(39)	35(5)	76(7)	43(5)	1(5)	0(4)	-25(5)
C(40)	43(6)	96(9)	59(6)	-4(6)	-9(5)	-30(6)
C(41)	76(9)	153(13)	119(11)	-3(10)	-7(8)	-80(9)
C(42)	42(6)	112(10)	56(7)	6(7)	-6(5)	-11(7)
C(43)	580(50)	230(20)	51(9)	36(12)	-43(18)	-300(30)
C(44)	420(40)	51(9)	129(16)	46(9)	-150(20)	-104(16)
C(45)	215(18)	102(11)	69(9)	8(8)	-29(10)	-114(12)
C(46)	135(13)	79(9)	124(12)	-58(9)	-86(10)	33(9)
C(47)	230(20)	46(8)	190(20)	-44(11)	-139(19)	27(11)
C(48)	158(18)	190(20)	300(30)	-160(20)	-170(20)	86(15)
C(49)	400(40)	58(9)	125(16)	24(10)	-180(20)	-51(16)
C(50)	127(13)	110(12)	145(14)	26(10)	92(11)	41(10)
C(51)	129(14)	55(8)	150(15)	-18(10)	93(12)	-16(9)
C(52)	69(8)	76(8)	72(7)	5(6)	22(6)	-31(7)

C(53)	74(8)	111(10)	122(11)	-64(9)	0(8)	-52(8)
C(54)	145(17)	240(20)	380(30)	-250(30)	100(20)	-117(17)
C(55)	190(20)	210(20)	520(50)	-240(30)	-90(20)	-71(18)
C(56)	200(20)	98(13)	190(20)	-101(14)	74(17)	-70(14)
N(4)	37(4)	63(5)	39(4)	-19(4)	5(3)	-24(4)
Mo(1)	41(1)	45(1)	37(1)	-8(1)	1(1)	-18(1)
Mo(2)	36(1)	57(1)	33(1)	0(1)	5(1)	-15(1)
Mo(3)	47(1)	39(1)	55(1)	-12(1)	14(1)	-20(1)
C(22)	47(6)	68(7)	78(7)	-32(6)	16(5)	-24(5)
C(23)	38(5)	59(6)	54(6)	-24(5)	8(4)	-26(5)
C(24)	43(5)	52(6)	76(7)	-27(5)	11(5)	-12(5)
C(25)	47(5)	46(5)	58(6)	-14(5)	12(5)	-21(5)
C(26)	44(5)	67(6)	48(5)	-21(5)	2(4)	-28(5)
C(27)	53(6)	61(7)	72(7)	-15(5)	-7(5)	-19(5)
C(28)	48(6)	77(7)	57(6)	-37(5)	16(5)	-33(5)
Mo(4)	81(1)	41(1)	71(1)	-20(1)	-26(1)	-1(1)
N(1)	57(5)	36(4)	39(4)	-2(3)	12(4)	3(4)
C(1)	51(6)	62(7)	109(9)	-3(6)	-5(6)	-26(6)
C(2)	51(6)	38(5)	55(6)	-3(4)	1(5)	-14(4)
C(3)	48(6)	39(5)	52(6)	-7(4)	14(4)	-2(4)
C(4)	46(5)	42(5)	47(5)	-12(4)	1(4)	3(4)
C(5)	37(5)	39(5)	48(5)	-5(4)	1(4)	-3(4)
C(6)	53(6)	69(7)	82(8)	-14(6)	2(6)	-18(6)
C(7)	47(5)	25(4)	43(5)	6(4)	5(4)	2(4)

Table A.15: Crystal data and structure refinement for $(C_3N_2H_5)_2[Mo_2F_6O_4]$

Identification code	mo3aoff
Empirical formula	C6 H10 F6 Mo2 N4 O4
Formula weight	508.06
Temperature	125(2) K
Wavelength	0.71073 Å
Crystal system	Monoclinic

Space group	$P2_1/n$
Unit cell dimensions	a = 11.607(4) Å
	b = 9.504(3) Å β = 98.20(9)°
	c = 12.978(5) Å
Volume	1416.2(9) $Å^3$
Z	4
Density (calculated)	2.383 Mg/m^3
Absorption coefficient	1.862 mm^{-1}
F(000)	976
Crystal size	0.20 x 0.20 x 0.20 mm^3
Theta range for data collection	2.55 to 29.01°.
Index ranges	-15<=h<=14, -12<=k<=12, -17<=l<=17
Reflections collected	11458
Independent reflections	3255 [R(int) = 0.0969]
Completeness to theta = 29.01°	86.3 %
Absorption correction	Multiscan
Max. and min. transmission	0.7071 and 0.7071
Refinement method	Full-matrix least-squares on F^2
Data / restraints / parameters	3255 / 0 / 215
Goodness-of-fit on F^2	1.199
Final R indices [I>2sigma(I)]	R1 = 0.0518, wR2 = 0.1696
R indices (all data)	R1 = 0.0643, wR2 = 0.1956
Largest diff. peak and hole	1.893 and -2.049 $e.Å^{-3}$

Table A.16: Atomic coordinates (x 10^4) and equivalent isotropic displacement parameters ($Å^2$x 10^3) for $(C_3N_2H_5)_2[Mo_2F_6O_4]$

	x	y	z	U(eq)
O(1)	6106(3)	1527(3)	9652(2)	25(1)
O(2)	7300(3)	3501(3)	8782(2)	25(1)
O(3)	3728(3)	3564(3)	5342(2)	24(1)
O(4)	2562(3)	1543(3)	6189(2)	24(1)
F(1)	6642(2)	1123(2)	7707(2)	23(1)

F(2)	5458(2)	3407(2)	7074(2)	20(1)
F(3)	4413(2)	1549(2)	7894(2)	19(1)
F(4)	5053(2)	3962(2)	8967(2)	24(1)
F(5)	4792(2)	1108(2)	5955(2)	24(1)
F(6)	3229(2)	3858(2)	7315(2)	23(1)
N(1)	2824(4)	2857(5)	9313(4)	27(1)
N(2)	2218(4)	2906(5)	10798(3)	28(1)
Mo(1)	6075(1)	2530(1)	8578(1)	17(1)
Mo(2)	3796(1)	2514(1)	6392(1)	17(1)
C(1)	2415(5)	1517(5)	10583(4)	34(1)
C(2)	2815(5)	1487(5)	9655(4)	34(1)
C(3)	2466(4)	3696(6)	10014(3)	30(1)
N(3)	5128(4)	1347(5)	2583(3)	31(1)
N(4)	5215(4)	3544(5)	2299(4)	33(1)
C(4)	4902(5)	3392(5)	3267(4)	35(1)
C(5)	4851(4)	2006(5)	3444(4)	32(1)
C(6)	5352(5)	2280(5)	1892(4)	32(1)

Table A.17: Anisotropic displacement parameters ($Å^2 x\ 10^3$) for

$(C_3N_2H_5)_2[Mo_2F_6O_4]$

The anisotropic displacement factor exponent takes the form: $-2p^2[\ h^2a^{*2}U^{11} + ... + 2\ h\ k\ a^*\ b^*\ U^{12}\ ]$

	U^{11}	U^{22}	U^{33}	U^{23}	U^{13}	U^{12}
O(1)	33(2)	23(2)	20(1)	1(1)	7(1)	2(1)
O(2)	31(2)	21(1)	24(2)	-2(1)	5(1)	-2(1)
O(3)	32(2)	21(1)	21(1)	3(1)	7(1)	2(1)
O(4)	28(2)	20(1)	23(2)	-1(1)	4(1)	-3(1)
F(1)	29(1)	20(1)	22(1)	-3(1)	7(1)	5(1)
F(2)	26(1)	16(1)	18(1)	1(1)	8(1)	-1(1)
F(3)	25(1)	16(1)	17(1)	0(1)	6(1)	-1(1)
F(4)	30(1)	20(1)	22(1)	-6(1)	8(1)	0(1)
F(5)	33(1)	19(1)	21(1)	-5(1)	8(1)	3(1)

F(6)	29(1)	19(1)	23(1)	-3(1)	7(1)	5(1)
N(1)	33(2)	23(2)	28(2)	2(2)	12(2)	-4(2)
N(2)	37(2)	24(2)	26(2)	-3(2)	13(2)	3(2)
Mo(1)	22(1)	15(1)	15(1)	-1(1)	3(1)	0(1)
Mo(2)	22(1)	14(1)	16(1)	0(1)	3(1)	1(1)
C(1)	46(3)	23(2)	39(3)	6(2)	24(2)	1(2)
C(2)	44(3)	25(2)	39(3)	1(2)	23(2)	2(2)
C(3)	37(3)	21(2)	30(3)	3(1)	6(2)	0(2)
N(3)	39(2)	21(2)	33(2)	0(2)	1(2)	-4(2)
N(4)	43(3)	21(2)	35(2)	4(2)	11(2)	-4(2)
C(4)	43(3)	33(2)	34(3)	3(2)	18(2)	8(2)
C(5)	32(3)	28(2)	35(3)	-1(2)	11(2)	3(2)
C(6)	37(3)	32(2)	30(3)	-2(2)	10(2)	0(2)

Table A.18: Crystal data and structure refinement for $(C_9H_7N_2O_2)_2[Mo_2F_6O_4]$

Identification code	mo127
Empirical formula	C18 H14 F6 Mo2 N4 O8
Formula weight	360.11
Temperature	125(2) K
Wavelength	0.71073 Å
Crystal system	Monoclinic
Space group	$P2_1/n$
Unit cell dimensions	a = 7.3424(11) Å
	b = 10.0706(15) Å β = 90.743(6)°
	c = 15.079(2) Å
Volume	1114.9(3) $Å^3$
Z	4
Density (calculated)	2.145 Mg/m^3
Absorption coefficient	1.231 mm^{-1}
F(000)	704
Crystal size	0.49 x 0.03 x 0.02 mm^3
Theta range for data collection	3.07 to 27.47°.

Index ranges	-9<=h<=9, -13<=k<=12, -19<=l<=19
Reflections collected	9832
Independent reflections	2537 [R(int) = 0.1392]
Completeness to theta = 27.47°	99.4 %
Absorption correction	Multiscan
Max. and min. transmission	0.9758 and 0.5837
Refinement method	Full-matrix least-squares on F^2
Data / restraints / parameters	2537 / 0 / 172
Goodness-of-fit on F^2	1.068
Final R indices [I>2sigma(I)]	R1 = 0.0645, wR2 = 0.0976
R indices (all data)	R1 = 0.1104, wR2 = 0.1064
Largest diff. peak and hole	0.722 and -1.156 e.Å^{-3}

Table A.19: Atomic coordinates (x 10^4) and equivalent isotropic displacement parameters (Å^{2}x 10^3) for $(C_9H_7N_2O_2)_2[Mo_2F_6O_4]$

	x	y	z	U(eq)
F(2)	-112(5)	6139(3)	10285(2)	16(1)
O(4)	569(6)	7205(4)	8622(3)	20(1)
O(3)	864(6)	4766(4)	7970(3)	18(1)
Mo(1)	424(1)	5591(1)	8917(1)	12(1)
F(3)	-2188(4)	5478(4)	8835(2)	19(1)
F(1)	2875(4)	5457(4)	9402(2)	18(1)
O(2)	-2036(6)	2785(5)	7641(3)	25(1)
O(1)	241(6)	2076(4)	6869(3)	22(1)
C(8)	-1662(8)	3644(6)	6250(4)	14(1)
N(1)	-395(7)	2209(5)	5084(3)	13(1)
N(2)	-1121(7)	2778(5)	6971(3)	16(1)
C(6)	-3093(8)	5702(7)	5790(4)	19(1)
C(4)	-2048(8)	4155(6)	4675(4)	18(2)
C(2)	-970(8)	2621(7)	3557(4)	20(2)
C(3)	-1894(9)	3757(7)	3785(4)	22(2)
C(9)	-1352(8)	3312(6)	5353(4)	14(1)

C(7)	-2517(9)	4816(6)	6455(4)	19(2)
C(1)	-173(8)	1873(7)	4241(4)	18(1)
C(5)	-2879(9)	5364(6)	4923(4)	22(2)

Table A.20: Anisotropic displacement parameters ($Å^2 x\ 10^3$) for

$(C_9H_7N_2O_2)_2[Mo_2F_6O_4]$

The anisotropic displacement factor exponent takes the form: $-2p^2[\ h^2a^{*2}U^{11} + ... + 2\ h\ k\ a^*\ b^*\ U^{12}\ ]$

	U^{11}	U^{22}	U^{33}	U^{23}	U^{13}	U^{12}
F(2)	20(2)	13(2)	15(2)	0(1)	1(2)	2(2)
O(4)	26(3)	14(2)	18(2)	3(2)	-3(2)	-1(2)
O(3)	24(3)	15(3)	13(2)	-5(2)	2(2)	-5(2)
Mo(1)	14(1)	13(1)	10(1)	1(1)	-1(1)	-1(1)
F(3)	16(2)	24(2)	17(2)	4(2)	-4(1)	0(2)
F(1)	15(2)	21(2)	18(2)	2(2)	-2(1)	-1(2)
O(2)	34(3)	31(3)	11(3)	2(2)	7(2)	-6(2)
O(1)	25(3)	22(3)	18(3)	1(2)	-10(2)	5(2)
C(8)	13(3)	15(3)	15(3)	-1(3)	-7(2)	-2(3)
N(1)	15(3)	11(3)	14(3)	3(2)	-3(2)	-4(2)
N(2)	18(3)	14(3)	17(3)	-1(2)	-7(2)	-2(2)
C(6)	11(3)	12(3)	34(4)	-10(3)	-6(3)	0(3)
C(4)	13(3)	20(4)	21(3)	5(3)	-5(3)	-3(3)
C(2)	18(3)	30(4)	11(3)	-1(3)	0(3)	-6(3)
C(3)	18(4)	26(4)	23(4)	12(3)	-3(3)	-5(3)
C(9)	14(3)	11(3)	18(3)	2(3)	0(2)	-5(3)
C(7)	14(3)	21(4)	23(4)	-2(3)	-5(3)	-4(3)
C(1)	15(3)	21(4)	18(4)	-2(3)	1(3)	-7(3)
C(5)	19(4)	17(4)	29(4)	6(3)	-6(3)	-3(3)

Table A.21: Crystal data and structure refinement for $(C_6H_7N_2O_2)_2[Mo_2F_6O_4]$

Identification code	mo132
Empirical formula	C12 H14 F6 Mo2 N4 O8
Formula weight	324.08
Temperature	125(2) K
Wavelength	0.71073 Å
Crystal system	Monoclinic
Space group	$P2_1/c$
Unit cell dimensions	a = 9.4305(7) Å b = 6.6881(5) Å β = 95.923(7)° c = 15.3947(11) Å
Volume	965.79(12) $Å^3$
Z	4
Density (calculated)	2.229 Mg/m^3
Absorption coefficient	1.407 mm^{-1}
F(000)	632
Crystal size	0.13 x 0.10 x 0.08 mm^3
Theta range for data collection	3.26 to 27.47°.
Index ranges	-12<=h<=12, -8<=k<=8, -19<=l<=19
Reflections collected	9550
Independent reflections	2202 [R(int) = 0.0566]
Completeness to theta = 27.47°	99.7 %
Absorption correction	Multiscan
Max. and min. transmission	0.8958 and 0.8382
Refinement method	Full-matrix least-squares on F^2
Data / restraints / parameters	2202 / 0 / 157
Goodness-of-fit on F^2	1.185
Final R indices [I>2sigma(I)]	R1 = 0.0402, wR2 = 0.0843
R indices (all data)	R1 = 0.0660, wR2 = 0.0919
Largest diff. peak and hole	0.620 and -0.870 $e.Å^{-3}$

Table A.22: Atomic coordinates (x 10^4) and equivalent isotropic displacement parameters ($Å^2$x 10^3) for $(C_6H_7N_2O_2)_2[Mo_2F_6O_4]$

	x	y	z	U(eq)
O(3)	6732(3)	113(4)	4818(2)	20(1)
O(4)	7806(3)	-165(4)	3292(2)	22(1)
F(1)	8679(3)	2853(4)	4418(2)	21(1)
F(2)	8661(2)	-2805(3)	4566(2)	16(1)
F(3)	9445(2)	102(4)	5687(2)	16(1)
N(2)	931(4)	-4936(8)	3817(3)	16(1)
Mo(1)	8293(1)	40(1)	4374(1)	12(1)
O(1)	612(3)	-1999(5)	2651(2)	20(1)
O(2)	2223(4)	339(4)	2718(2)	29(1)
N(1)	1832(4)	-1355(5)	2876(2)	17(1)
C(1)	2863(4)	-2756(6)	3323(3)	13(1)
C(2)	2425(4)	-4485(6)	3716(3)	11(1)
C(3)	3440(5)	-5884(7)	4027(3)	16(1)
C(4)	4879(5)	-5537(7)	3953(3)	20(1)
C(5)	5300(5)	-3773(7)	3580(3)	21(1)
C(6)	4296(5)	-2362(7)	3276(3)	19(1)

Table A.23: Anisotropic displacement parameters ($Å^2$x 10^3) for

$(C_6H_7N_2O_2)_2[Mo_2F_6O_4]$

The anisotropic displacement factor exponent takes the form: $-2p^2[h^2a^{*2}U^{11} + ... + 2 h k a^* b^* U^{12}]$

	U^{11}	U^{22}	U^{33}	U^{23}	U^{13}	U^{12}
O(3)	17(2)	18(2)	26(2)	5(2)	5(1)	2(2)
O(4)	29(2)	22(2)	14(2)	2(1)	-2(1)	-4(2)
F(1)	20(1)	11(1)	31(2)	3(1)	1(1)	0(1)
F(2)	16(1)	11(1)	19(1)	1(1)	-2(1)	-1(1)
F(3)	12(1)	24(1)	11(1)	-1(1)	2(1)	0(1)
N(2)	16(2)	18(2)	14(2)	4(2)	3(2)	0(2)

Mo(1)	12(1)	10(1)	13(1)	2(1)	0(1)	0(1)
O(1)	18(2)	25(2)	15(2)	0(1)	-1(1)	5(2)
O(2)	38(2)	11(2)	41(2)	11(1)	17(2)	4(1)
N(1)	24(2)	16(2)	12(2)	1(2)	7(2)	5(2)
C(1)	16(2)	14(2)	8(2)	0(2)	0(2)	2(2)
C(2)	9(2)	13(2)	10(2)	-4(2)	0(2)	-2(2)
C(3)	21(3)	16(2)	12(2)	2(2)	3(2)	-3(2)
C(4)	18(2)	25(3)	18(2)	-4(2)	-1(2)	8(2)
C(5)	14(2)	32(3)	18(2)	-9(2)	2(2)	-4(2)
C(6)	23(2)	20(2)	15(2)	-2(2)	7(2)	-7(2)